On the photophoretic force exerted on mm- and sub-mm-sized particles

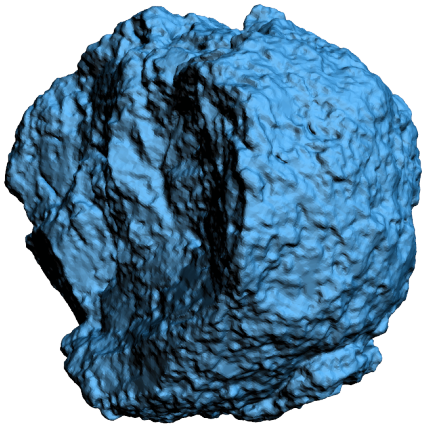

Christoph Lösche

A thesis accepted by the doctorate board
for the degree of

Dr. rer. nat.

Faculty of Physics, University of Duisburg-Essen, Germany
first reviewer: Prof. Dr. Gerhard Wurm
second reviewer: PD. Dr. Hubert Klahr
oral exam: 2015-10-13

Für meine Eltern und Yue.

Das Heiligste, das der Deutsche hat, ist die Arbeit.

Kurt Tucholsky (1890 — 1935)

Abstract

Two major forces caused by directed illumination act on a particle suspended in a gas: radiation pressure and photophoresis, the latter arising from interaction of gas atoms/ molecules with the particle surface. Photophoresis leads to momentum transfer as for the general case the gas atoms/molecules leave the surface at a speed, that correlates with the temperature and gas accommodation differences across this surface. It is also a candidate to transport particles in basically optically thin parts of protoplanetary disks, especially at the inner edge and at the optical surface. To model the transport and resulting effects in detail it is necessary to quantify the photophoretic strength for different particle classes as a fundamental input.

In this work photophoresis exerted on perfectly spherical particles and those with star-convex domain is investigated, essentially in pressure domains where the mean free path of the gas atoms/molecules is larger than the characteristic length of the suspended particle. Two new high-quality approximations with unprecedented accuracy, valid for longitudinal photophoresis on spheres resulting from directed illumination are introduced, one temperature-difference-based, the other based on the parameters light flux, radius, and thermal conductivity, as well as thermal radiation along the Stefan-Boltzmann law to account for the case that the sphere's temperature considerably exceeds the gas temperature. For the homogeneous non-spherical particles investigated, an almost perfect equality of the mean absolute force — averaged over 100 equally distributed directions of illumination — with the force acting on a sphere with the same volume but all other parameters kept constant is found and discussed. An effective thermal conductivity in terms of the phothophoretic strength is also introduced. Both variables, the radius of a volume-equivalent sphere and the effective thermal conductivity, enable to describe the mean value of the total photophoretic force exerted on star-convex particles with the same approximations derived for spheres. The new findings are compared and applied to the results of drop tower experiments and possible transport and size-sorting scenarios are briefly discussed for the minimum mass solar nebula.

Zusammenfassung

Zwei durch direkte Beleuchtung hervorgerufene Kräfte wirken auf von Gas umgebenen Teilchen: Strahlungsdruck und Photophorese, Letzteres herrührend von Wechselwirkungen zwischen Gas und Partikeloberfläche. Photophorese führt zu Impulsübertrag zwischen Gas und Teilchen, da im Allgemeinen Gasteilchen, die von der Teilchenoberfläche kurzzeitig adsorbiert wurden, diese mit einer Geschwindigkeit verlassen, die mit der Oberflächentemperatur oder der Akkommodation korreliert. Sie ist auch ein Kandidat um Teilchentransport in optisch dünnen Bereichen protoplanetarer Scheiben, besonders am inneren Rand oder der optischen Oberfläche zu erklären. Um jenen Transport zu modellieren und die sich daraus ergebenen Effekte detailliert zu verstehen, ist es notwendig, die photophoretische Kraft für verschiedene Partikelklassen zu quantifizieren.

In der vorliegenden Arbeit wird die Photophorese auf Kugeln und realistische, näherungsweise sphärischen Objekte untersucht, insbesondere in Druckbereichen, in denen die mittlere freie Weglänge der Gasteilchen größer als die charakteristische Länge des Partikels ist. Dabei werden zwei neue und ziemlich genaue Näherungen für longitudinale Photophorese auf Kugeln gezeigt. Eine der Näherungen ist temperaturunterschiedsbasierend, die andere hängt von den Eingangsparametern Bestrahlungsintensität, Radius und Wärmeleitfähigkeit ab, wobei auch thermische Abstrahlung nach dem Stefan-Boltzmann-Gesetz berücksichtigt wird, um Oberflächentemperaturen, die die des Gases übersteigen, ebenso einfließen zu lassen. Für die nicht-sphärischen Teilchen homogener Zusammensetzung, die untersucht wurden, fand sich eine nahezu perfekte Übereinstimmung des mittleren Kraftbetrags — gemittelt über einhundert gleichmäßig verteilte Eintrahlungsrichtungen — mit derjenigen Kraft, die auf eine Kugel gleichen Volumens wirken würde, blieben alle weiteren Parameter gleich. Eine auf die photophoretische Kraft bezogene effektive Wärmeleitfähigkeit wurde ebenso eingeführt. Beide Größen, das Volumen, ausgedrückt durch einen Radius, und die effektive Wärmeleitfähigkeit ermöglichen die Berechnung des Mittelwertes der photophoretischen Kraft auf ein Teilchen mit sternförmigem Gebiet mithilfe derselben Näherungen, die für Kugeln Gültigkeit besitzen. Alle neuen Erkenntnisse werden auf die Ergebnisse von Fallturmexperimenten bezogen und mögliche Transport- und Größensortierungsszenarios werde kurz erklärt anhand des minimum mass solar nebula.

Glossary

Notation

(1.23)	...	Equation number 23 in chapter 1
X	...	a scalar
$\mathbf{X}$	...	a vector with components X_i
$\underline{\mathbf{X}}$	...	a tensor
$\check{\mathbf{X}}$	...	flux of X
$\mathbf{r}$	...	position vector
$\mathbf{n}$, $\mathbf{t}$	...	normal and tangential vector
$\mathbf{v}$, v	...	velocity and speed, $v = \|\mathbf{v}\|_2$
$v_\mathbf{n}$	...	normal speed $v_\mathbf{n} := \mathbf{v} \cdot \mathbf{n}$, analogous for speed along x, y, z and tangent $\mathbf{t}$
$X^{(\pm)}$	...	X for gas particles leaving a surface ($+$, i.e. $\mathbf{v} \cdot \mathbf{n} > 0$) or impinging it ($-$, i.e. $\mathbf{v} \cdot \mathbf{n} < 0$)
$\|\mathbf{a}\|_n$	...	n-norm, $\|\mathbf{a}\|_2$ is the euclidean norm.

$$\|\mathbf{a}\|_n = \left(\sum_i |a_i|^n \right)^{1/n} \tag{0.1}$$

$\|f\|_{L_n}$	...	n norm for a function with measure $\mathrm{d}\mu$, $\|f\|_{L_n} = \left(\int |f(x)|^n \, \mathrm{d}\mu \right)^{1/n}$.
x, y, z	...	coordinates in a Cartesian coordinates
r	...	radius in a spherical coordinate system
φ, ξ	...	azimuth angles in a spherical coordinate system
ϑ, ζ	...	polar angle in a spherical coordinate system
$\mathbf{e}_z$	...	unit vector, here in z-direction...
$\boldsymbol{\partial_i}$	...	coordinate vector fields of a surface with respect to the parametrization, see. sec. 3.1.1.1
Π	...	parameter set, e.g., $[0, 2\pi] \times [0, \pi]$
$\mathrm{d}\mathbf{A}$	...	infinitesimal (surface) area element $\mathrm{d}\mathbf{A} = \mathbf{n} \, \mathrm{d}A$ $\mathrm{d}A = \mathrm{d}x \, \mathrm{d}y = r \, \sin\vartheta \, \mathrm{d}\vartheta \, \mathrm{d}\varphi \ldots$
$\mathrm{d}^3 r \equiv \mathrm{d}V$	...	infinitesimal volume in (3-dim.) position-space $\mathrm{d}V = \mathrm{d}x \, \mathrm{d}y \, \mathrm{d}z = r^2 \sin\vartheta \, \mathrm{d}r \, \mathrm{d}\vartheta \, \mathrm{d}\varphi \ldots$
$\mathrm{d}^3 v$	...	infinitesimal volume in (3-dim.) velocity-space
$\mathrm{d}^6 V = \mathrm{d}^3 v \, \mathrm{d}^3 r$	...	infinitesimal volume in (6-dim.) phase-space
∂V	...	border of a volume V

$\boldsymbol{\nabla}_r \equiv \boldsymbol{\nabla}$, $\boldsymbol{\nabla}_v$ ... gradient for position space and velocity space

$\frac{\partial X}{\partial \mathbf{a}}$ ... directional derivative of X in direction of $\mathbf{a}$, $\frac{\partial X}{\partial \mathbf{a}} := \boldsymbol{\nabla} X \cdot \mathbf{a}$

P_ν, Q_ν ... Legendre polynomials of first and second kind with degree ν

P_ν^μ, Q_ν^μ ... Associated Legendre polynomials of first and second kind with degree ν and order μ

$J_{\nu+1/2}$, $Y_{\nu+1/2}$ ... Bessel functions of first and second kind with degree $\nu + 1/2$

Y_ν^μ ... spherical harmonic of degree ν and order μ

$\int f(x)\,\mathrm{d}x \equiv \int \mathrm{d}x f(x)$ ... integral notation

f^* ... complex conjugate of a variable or function f

$\Re f\, \Im f$ ... real and imaginary part of f

$\mathbf{a} \cdot \mathbf{b}$ ... scalar product for two real vectors $\mathbf{a} \cdot \mathbf{b} = \sum_i a_i\, b_i$

$\mathbf{X} \otimes \mathbf{Y}$ ... tensor or dyadic product, see (2.33)

$(f\,,\,g) = (g\,,\,f)^*$ ... scalar product for two complex-valued functions $f(\vartheta, \varphi)$, $g(\vartheta, \varphi)$ defined on the unit sphere,

$$(f\,,\,g) = \int_0^{2\pi} \int_0^{\pi} f(\vartheta, \varphi)\, g^*(\vartheta, \varphi)\, \sin\vartheta\, \mathrm{d}\vartheta\, \mathrm{d}\varphi \tag{0.2}$$

$(f\,,\,g)_{[a,b]}$ ... scalar product for two functions f, g defined on $[a, b]$ (in case of the real-valued (associated) Legendre polynomials, $(f\,,\,g)_{[-1,1]} = (g\,,\,f)_{[-1,1]}$),

$$(f\,,\,g)_{[a,b]} = \int_a^b f(x)\, g^*(x)\, \mathrm{d}x. \tag{0.3}$$

$\overline{v^n}$, $\overline{v_j^n}$ ... the n-th moment of both the speed and the j-th component of the velocity $\mathbf{v}$ ($\int f(\mathbf{v})\, \mathrm{d}^3 v = 1$), see (2.28)

v_{rms} ... root mean squared speed, denoted by 'rms', defined as $v_{\mathrm{rms}} := \sqrt{\overline{v^2}}$

$\overline{\mathbf{a}}$ ... component-wise average along (2.28b), also see (2.29)

$\Theta(x)$ ... Heaviside function, equal to 0 for $x < 0$ and 1 for $x \geq 0$

$\delta_{\nu,\mu}$ ... Kronecker delta, equal to 1 if $\nu = \mu$, otherwise 0

$\delta(x)$ ... delta distribution

Variables

Unless stated otherwise, the following variables denote the physical properties listed here.

F_{phot}	...	photophoretic force	
$\tilde{F}^{(i)}$	...	i-th approximation of F_{phot}	
t	...	time	
A	...	(surface) area	
V	...	volume	$V = \int_V \mathrm{d}V$
ρ	...	mass density	
m, M	...	mass and molar mass	
k	...	thermal conductivity	
k_{B}	...	Boltzmann constant	
c_p, c_V	...	specific heat capacity at constant pressure and volume, respectively	
c_0	...	speed of light (in vacuum)	
E, E_0	...	electromagnetic wave at amplitude E_0 of the E-part	
I	...	intensity of an electromagnetic wave at amplitude E_0	$I = \langle S_{\text{poynting}} \rangle_t$, $I = c_0\, \epsilon_0\, E_0^2/2$ (SI), $I = c_0\, E_0^2/8\pi$ (cgs)
q	...	volumetric heat source function	
B	...	normalized volumetric heat source function	see (3.52)
A_I	...	absorption cross section	see (2.3)
$\mathbf{r}^*_{OQ}$	...	source asymmetry	see (2.4)
D_{th}	...	thermal diffusivity	$D_{\text{th}} = \frac{k}{\rho\, c_p}$
T	...	temperature	
T_∞	...	temperature far away from an object	
$\sigma(\mathbf{r}, \mathbf{v})$	...	(stationary) velocity distribution function	
$n(\mathbf{r})$	...	(stationary) spatial particle density	see (2.24)
$\tilde{n}$	...	complex refractive index	
N	...	(gas) particle count	
$\mathfrak{p}$	...	momentum	
p	...	pressure	
p^*	...	characteristic pressure	see (2.141b)
$\underline{\mathbf{\Pi}}$	...	pressure tensor	see (2.32b)
$\mathcal{E}$	...	translational energy	
h	...	heat transfer coefficient	
l	...	characteristic length	
Kn	...	Knudsen number	see (2.76)
A_{s}	...	scattering cross section	
α	...	accommodation coefficient (if not explicitly denoted otherwise, it is the thermal AC)	see sec. 2.8.1
η_{dyn}, η_{kin}	...	dynamic and kinematic viscosity	$\eta_{\text{kin}} = \frac{\eta_{\text{dyn}}}{\rho}$
Pr	...	Prandtl number	$Pr = \frac{\eta_{\text{kin}}}{D_{\text{th}}} = \frac{\eta_{\text{dyn}}\, c_p}{k}$

Contents

Published work

During this doctorate, the following peer reviewed articles and proceedings were published:

- Loesche, C. and Wurm, G. (2012). Thermal and photophoretic properties of dust mantled chondrules and sorting in the solar nebula. A&A, 545:A36.

- Loesche, C., Wurm, G., Teiser, J., Friedrich, J. M., and Bischoff, A. (2013). Photophoretic Strength on Chondrules. 1. Modeling. ApJ, 778(2):101.

- Loesche, C., Teiser, J., Wurm, G., Hesse, A., Friedrich, J. M., and Bischoff, A. (2014). Photophoretic Strength on Chondrules. 2. Experiment. ApJ, 792(1):73.

- Loesche, C., Friedrich, J. M., Teiser, J., and Wurm, G. (2011). Calculations on Photophoretic Motion of Chondrules in the Early Solar System and Temperature Distributions in Illuminated Chondrules. Meteoritics and Planetary Science Supplement, volume 74, page 5260.

Talks and Posters:

- Loesche, C. and Wurm, G. and Teiser, J. and Friedrich, J.M. (2011). Calculations on Photophoretic Motion of Chondrules in the early solar system and temperature distributions in illuminated chondrules. Talk and Abstract, 7th Planet Formation Workshop, Goettingen (Germany).

- Loesche, C. and Friedrich, J.M. and Teiser, J. and Wurm, G. (2011). Calculations on photophoretic motion of chondrules in the early solar system and temperature distributions in illuminated chondrules. Poster and Abstract, 74th Annual Meeting of the Meteoritical Society, London (UK).

- Loesche, C. and Wurm, G. and Teiser, J. and Friedrich, J.M. and Bischoff, A. (2012). Moving and Sorting Chondrules by Photophoresis. Talk and Abstract, Planet Formation and Evolution, Munich (Germany).

- Loesche, C. and Wurm, G. and Friedrich, J.M. and Teiser, J. and Bischoff, A. (2012). Moving and Sorting Chondrules by Photophoresis. Poster and Abstract, Paneth Kolloquium, Noerdlingen (Germany).

- Loesche, C. and Wurm, G. and Teiser, J. and Friedrich, J.M. and Bischoff, A. (2014). Photophoretic strength on chondrules: model and experiment. Poster and Abstract, Planet Formation and Evolution, Kiel (Germany).

- Loesche, C. and Wurm, G. and Teiser, J. and Friedrich, J.M. and Bischoff, A. (2014). Photophoretic strength on chondrules: model and experiment. Poster and Abstract, 5th annual meeting of the SPP1385, Heidelberg (Germany).

1

INTRODUCTION

Disks consisting of solids and gas give birth to planetary systems, as it is widely accepted. Many aspects of the formation process are still not well understood, though analysis of matter from the early solar system like primitive chondrites give hints. Chondrites contain chondrules as major components and calcium-aluminum-rich inclusions (CAIs), also in the same chondrite, and are embedded in a fine-grained matrix consisting of silicate dust (Hewins 1996). Both have different histories; CAIs condensed directly from the gas phase and are amongst the oldest materials radiometrically dated due to their high condensation temperature (Wadhwa et al. 2007 and Amelin et al. 2002). Chondrules likely formed by the melting of dust agglomerates, but other processes are also eligible for chondrule formation. However, it is well known, that chondrules formed within a few million years after the first CAIs (Scott 2007).

The inhomogeneous composition of many meteorites gives evidence for radial mixing of solid particles in the early solar system; particles forming at different times and in different places within the solar nebula can be found in the same meteorite. But the complementarity of matrix and chondrules, the fact that volatile elements depleted in chondrules are enriched in the matrix, restricts the relative transport of chondrules and dust (Klerner and Palme 1999 and Hezel and Palme 2010). The existence of meteorites with chondrules of different sizes, which implies the acting of a size-sorting mechanism (Liffman 2005 and Kuebler et al. 1999 and Scott et al. 1996 and Cuzzi et al. 1996 and Hughes 1978), gives evidence for more local transport. For instance, the chondrules of the carbonaceous, geochemically related CR-CH-CB-chondrite clan vary considerably in size from $< 100\,\mu$m (CH-chondrites) up to about cm-size (CB-chondrites) (Weisberg et al. 2010, 1995 and Krot et al. 2005 and Bischoff et al. 1993a,b).

Further evidence for radial transport can be inferred from cometary studies. Comets largely consist of ice and, thus, must have formed in outer parts of the solar system. In several comets, refractory minerals have been found by remote sensing (Sitko et al. 2004 and Wooden et al. 2004), and samples of comet Wild 2, collected by the Stardust spacecraft also contain high-temperature minerals, which likely formed close to the sun (Brownlee et al. 2006 and Zolensky et al. 2006).

Many different scenarios have been proposed until today to explain this radial redistribution and transport of solid particles. The latter one is strongly coupled to the gas dynamics in protoplanetary disks. Such a disk is shown in Figure 1.1. Turbulence drives gas flow (Cuzzi et al. 2003 and Bockelée-Morvan et al. 2002), and small particles cou-

ple well to gas movements, eventually leading to a random radial redistribution of solid particles. Klahr and Lin (2001, 2005) discuss the formation of dust rings in a gas disk, supporting concentration and size sorting in the Kuiper belt. cm- and mm-sized particles can be concentrated by streaming instabilities in zonal flows (Dittrich et al. 2013). Some models that take into account the vertical structure of the disk describe a radial outflow of particles due to pressure gradients within protoplanetary disks (Ciesla 2007 and Keller and Gail 2004), whilst other models employ additional processes such as X-winds. The X-wind model is based on ionized gas, that couples to the magnetic field of the central star and the inner disk. Particles in the vicinity of the star can be driven up an outward (Shu et al. 1997, 1996). However, all transport models strongly depend on the assumed underlying disk model and its parameters.

The background behind this work is photophoresis in the free molecular flow regime and the transport based on it, introduced earlier in Krauss and Wurm (2005) and Wurm and Krauss (2006). Photophoresis has been known for almost 200 years, particularly since Fresnel (1825). Whilst radiation pressure is a direct interaction between photons and particles, not necessarily suspended in a gaseous environment, photophoresis needs at least a thin gas, as the light heats up the particle, and the ensuing interaction with the gas propels the particle in a certain direction. For rarefied gases, i.e. in the free molecule regime, this effect can be understood as a momentum balance across the particle's surface. Gas atoms or molecules impinging the surface take thermal energy and the particle must balance the reflected gas particle's higher translation energy, that means, for a nonuniform thermal energy transfer across the surface (realized by, e.g., a varying temperature), the particle is subject to the so-called photophoretic force, as a direct result from the momentum balance. Basically, the effect is described kinetically. As the pressure rises, the interaction gets more complicated. Then an interface layer, the so-called Knudsen layer is mediating between the particle and the rest of the gas.

In the next chapter, the heat transfer equation and its solution ansatz for spheres is very briefly discussed, directly followed by a short introduction and recapitulation in gas kinetics, where photophoresis can easily be derived. Gas-surface interactions also play a role in the field of photophoresis, e.g. thermal accommodation, succeeded by the introduction of accommodation coefficients. Eventually, photophoresis in non-free-molecule regimes (*fm*) is discussed. The subsequent chapter is devoted to the general description of *fm*-photophoresis acting on star-convex particles, including several approximation equations for spheres, that incorporate solutions of special heat transfer problems. Chapter 4 then uses old and new findings for studies on onion-shell particles and chondrules in computer models as well as drop tower experiments. Possible transport and sorting scenarios are sketched in ch. 5.

In certain regions in protoplanetary disks, considering photophoresis is meaningful. One location is the surface of the disk. Both, calculations and laboratory experiments demonstrate that particles can be photophoretically transported at higher levels of disks near the optical surface. Here, stellar as well as thermal radiation emitted from the disk can induce photophoresis (van Eymeren and Wurm 2012 and Wurm and Haack 2009). Another location, where photophoresis undoubtfully acts is the inner edge of a disk. Early in the disk's history, that may be close to the sublimation radius, but a number of transition disk with large inner clearings have also been observed (Sicilia-Aguilar et al. 2008 and D'Alessio et al. 2005), where particle transport by photophoresis should be

considered (Moudens et al. 2011 and Haack and Wurm 2007). Particle recycling by more complex photophoretic processes that are capable of disassembling larger dusty bodies can also take place at the disk's edge (de Beule et al. 2013 and Kelling and Wurm 2013, 2011 and Wurm 2007). Several studies also showed, that photophoresis can lead to enhanced particle concentrations and enhance growth rates at the inner edge of the dust disk (Krauss and Wurm 2005 and Wurm et al. 2006). Furthermore, photophoresis can also drive the inner edge of the dust disk further out (Krauss et al. 2007 and Moudens et al. 2011). As it strongly depends on thermal and optical particle properties, photophoresis is a general transport mechanism, but it can also lead to particle sorting by separation near the inner edge (Wurm et al. 2013 and Loesche and Wurm 2012 and Wurm and Krauss 2006).

Dust aggregates, solid particles such as chondrules or CAIs, and dust-mantled particles are three materials with differing properties (Wurm et al. 2010 and von Borstel and Blum 2012 and Steinbach et al. 2004 and Rohatschek and Zulehner 1985). Loesche and Wurm (2012) showed, that sorting within a class is also possible, e.g. properties of dust-mantled chondrules were studied in detail (sec. 4.1). Loesche et al. (2013, 2014) focused on photophoretic properties of bare chondrules of realistic shape without dust mantles. Previous experimental data considering photophoresis on chondrules exist, but shows large scatter, also for the same chondrule (Wurm et al. 2010 and Hesse et al. 2011). Thus, it was important to shed some light on the detailed influence of particle properties (Loesche et al. 2013) and temporal evolution (Loesche et al. 2014). Complex particle composition and realistic particle shape are particularly major deviations from the usual assumption of the material homogeneity and perfect sphericity. Sec. 4.2 discusses the influence of particle composition and shape on the photophoretic force, both obtained by X-ray tomography. The heat transfer is modeled with COMSOL, mostly also employed for the in situ calculation of the photophoretic force, especially on the non-spherical particles. Sec. 4.3 explains the results of drop tower experiments with the temporal evolution of the photophoretic force for spinning particles and those heating up to stationary temperature.

1.1 Model of Hayashi et al. (1985)

For demonstration purposes, the simple model by Hayashi et al. (1985) is used to reproduce the gas density of a protoplanetary disk (Figure 1.2)

$$\rho(a) = 1.4 \times 10^{-6} \left(\frac{a}{1\,\mathrm{AU}}\right)^{-11/4} \mathrm{kg/m^3} \tag{1.1}$$

and the temperature at the radial position a

$$T_{\mathrm{gas}}(a) = 280 \left(\frac{L}{L_{\mathrm{sun}}}\right)^{1/4} \left(\frac{a}{1\,\mathrm{AU}}\right)^{-1/2} \mathrm{K}\,, \tag{1.2}$$

where L_{sun} is today's sun luminosity, and L the respective luminosity at the evolutionary stage. However, only scaling factors are introduced if it is set $L = L_{\mathrm{sun}}$. For the light flux at the radial position a it can be deduced (not considering absorption)

$$I(a) = \frac{L}{4\pi\, a^2}\,. \tag{1.3}$$

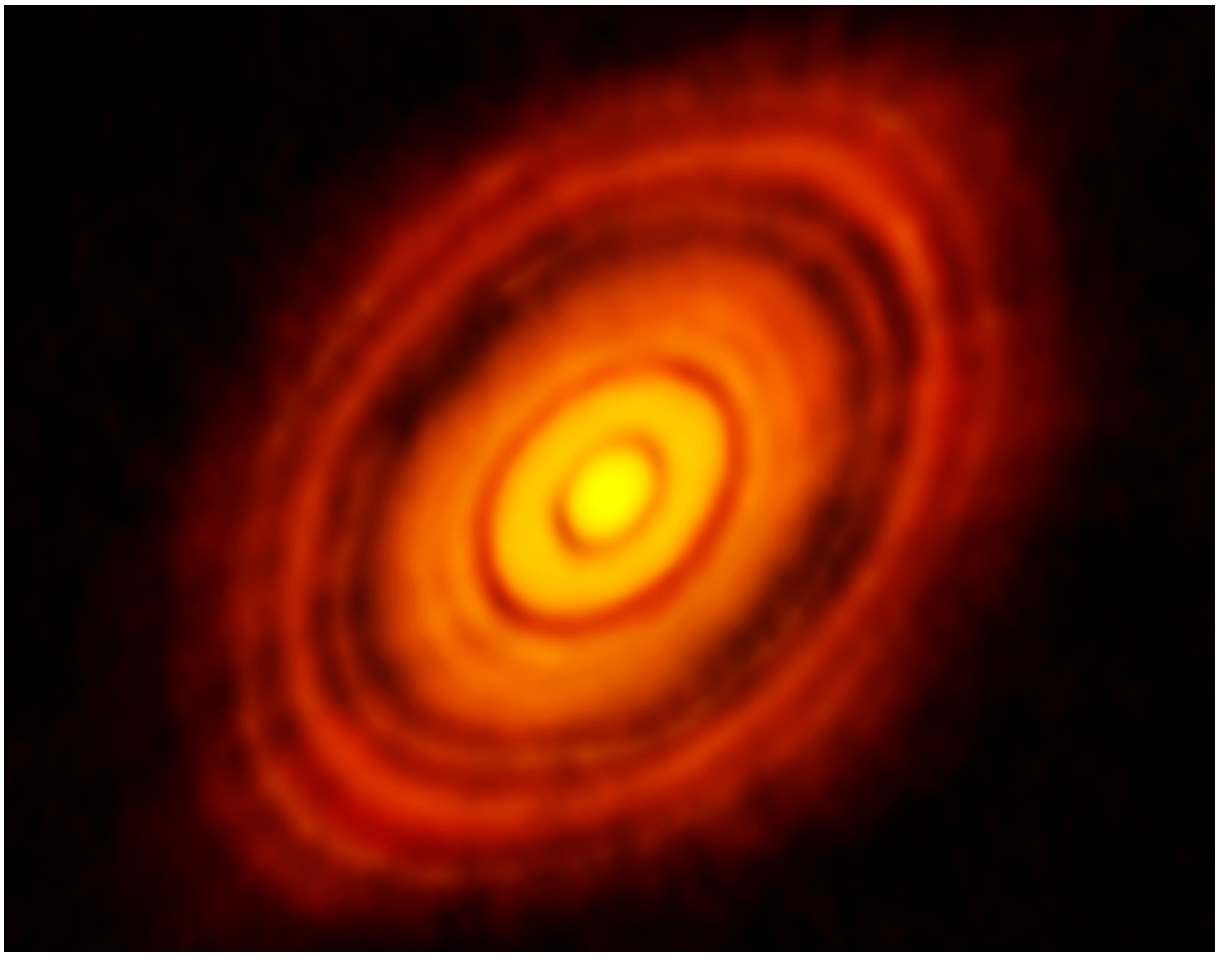

Figure 1.1: The Protoplanetary Disk of HL Tauri from ALMA, 2014-11-10. From http://apod.nasa.gov/apod/ap141110.html. Last visit: 2015-04-14.

With the perfect gas equation the pressure reads

$$p = \frac{\rho}{M_{\text{gas}}} R_{\text{gas}} T \ , \tag{1.4}$$

with R_{gas} and M_{gas} being the gas constant and its molar mass, respectively. Often, the ratio $\frac{R_{\text{gas}}}{M_{\text{gas}}} = 3551\,\text{J/kg K}$ is used for a Hydrogen-Helium gas mixture.

1.2 Chondrules

Primitive meteorites contain a lot of small ingeneous, basically spherical objects, which were given the name chondrule, a name derived from a ancient greek word with the meaning grain. First descriptions go back 200 years ago. Their origin is still not entirely understood, but it is believed, that "they were made by some pervasive process that formed melted silicate droplets" in the "disk of gas and solids that formed the Sun and planets 4.5 billion years ago" (Hewins et al. 2011). Two extracted chondrules from the Bjurböle chondrite (L/LL4-chondrite type) are shown in Figure 1.3. Chondrules consist of silicate material that was melted before forming the chondrite together with the matrix

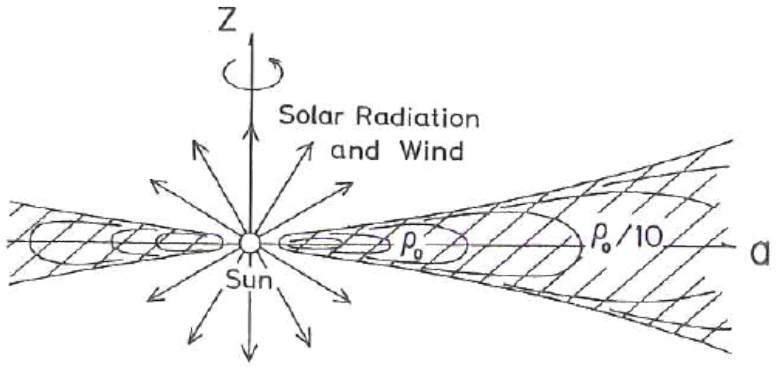

Figure 1.2: The sun and the surrounding solar nebula. Solid curvlinear contours represent constant density. From Hayashi et al. (1985).

material (Hewins 1996), and possibly CAIs and dark inclusions. Different types (abbreviated by one or two capital letters) with different degrees of alternation (e.g., diffusion processes that smeared out the chondrite structures, all indicated by numbers) exist and some of them are discussed in Hewins (1996). A concise collection about chondrules and the protoplanetary disk is given by Hewins et al. (2011).

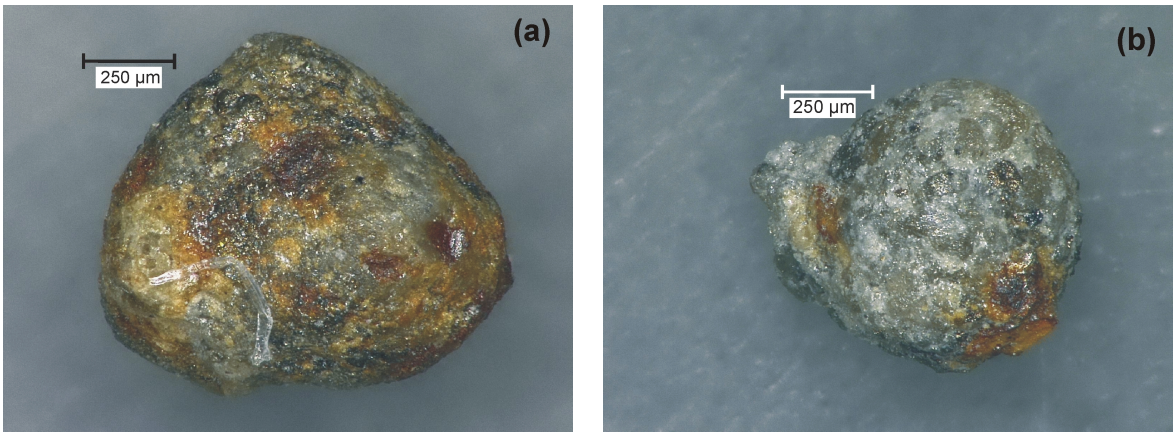

(a) Chondrule 13 in Table 4.4. **(b)** Chondrule 10 in Table 4.4.

Figure 1.3: Real chondrules (photographies by Jens Teiser).

2

BASICS OF PHOTOPHORESIS

The photophoretic force is a result from illumination of a particle suspended in gas (also fluids). Illumination leads to a non-uniform heat-up and hence a corresponding temperature distribution at the surface. Free molecular flow implies that all gas particle interact individually with the particle. Gas particles striking the surface of the particle are either reflected specularly (fraction $1-\alpha$) or diffusely (fraction α). If the specular reflection is constant across the particle's surface, then on average no net momentum is transferred. The other fraction of the gas particles, α, takes an average momentum related to the surface temperature; as the surface temperature increases the leaving gas particles which are in thermal equilibrium with the surface have a higher average speed and momentum conservation leads to a net momentum transfer between particle and those gas particles. The total force on the particle is the integral over the total particle surface of the local pressure induced by the interaction at the local temperature and in the free molecular flow regime as will be derived below

$$\mathbf{F} = -\frac{1}{2}\int_{\partial V} p\left(1+\sqrt{1+\alpha\left(\frac{T}{T_{\text{gas}}}-1\right)}\right)\,\mathrm{d}\mathbf{A}\ .$$

α is the thermal accommodation coefficient which will be defined in sec. 2.8.1, T represents the local temperature on the particle surface, and T_{gas} and p are the gas temperature and pressure far away from the particle, respectively.

2.1 Heat transfer problem

For the photophoresis arising from temperature differences across a particle's surface, the latter one has to be known. This knowledge can be gained through the solution of the respective heat transfer problem. In this section a brief description of possible solutions in the context of photophoresis are given. Unless stated otherwise, the notation and variables from the glossary are used. The spherical coordinate system in Figure 2.1 is used.

$\mathbf{r}$ denotes the position vector in the three-dimensional space[1]. The governing equation for heat transfer processes is the (time-dependent) heat transfer equation, which reads

$$\boldsymbol{\nabla}\cdot k\boldsymbol{\nabla}T + q = \rho\, c_p\, \partial_t T\ , \tag{2.1}$$

[1] $\mathbf{r} = r\,\mathbf{e}_r = x\,\mathbf{e}_x + y\,\mathbf{e}_y + z\,\mathbf{e}_z$

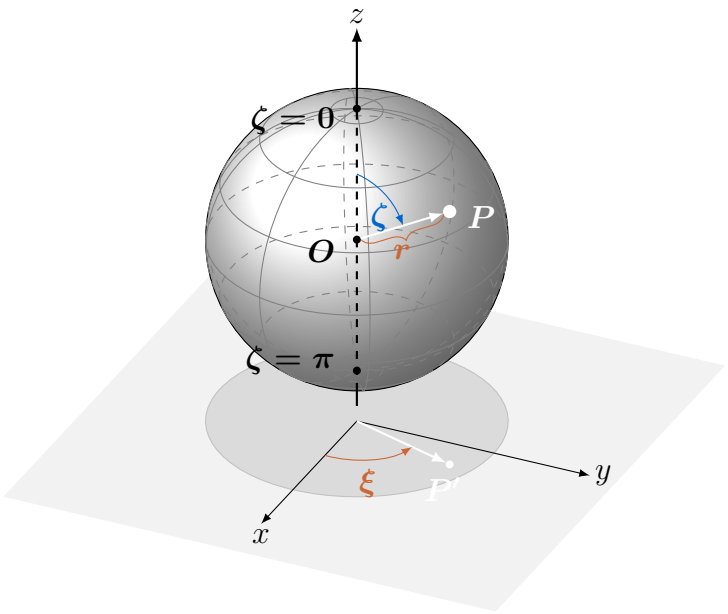

Figure 2.1: Ordinary spherical coordinate system used: $(r, \xi, \zeta) \in \mathbb{R}^+ \times [0, 2\pi] \times [0, \pi]$.

for the temperature T (k thermal conductivity, c heat capacity, ρ mass density). The inhomogeneity of the differential equation q is the volumetric heat source function, also called "source function". All involved variables can be dependent on position $\mathbf{r}$, time t and/or temperature T. For stationary processes it is $\partial_t T = 0$, and the equation becomes

$$\boldsymbol{\nabla} \cdot k \boldsymbol{\nabla} T = -q \; . \tag{2.2}$$

q allows the definition of the absorption cross section A_I for directed illumination at light flux I

$$A_I \, I = \int_V q \, \mathrm{d}V \; . \tag{2.3}$$

For later purposes, the pressure-regime-independent "source asymmetry" needs to be declared (Zulehner and Rohatschek 1990)

$$\mathbf{r}^*_{OQ} = \frac{1}{I \, A_I \, l} \int_V q \, \mathbf{r} \, \mathrm{d}V \; , \tag{2.4}$$

introducing the characteristic length l of the body absorbing the radiation.

A heat transfer problem involves boundary conditions to adequately describe the respective process. A few of them are used in the next chapter. To solve the resulting system of (partial) differential equations a separation ansatz is used, composing the solution of single functions depending on all independent variables, such as t, r, ζ, ξ: $T = \Gamma(t) R(r) \Theta(\zeta) \Phi(\xi)$. The spatial differential equation involves a Laplace equation, whose eigenfunctions are spherical harmonics in spherical symmetry, or Bessel functions in cylinder symmetry, thus each solution can be represented in eigenfunctions. An example is given in the next section.

2.1.1 Heat conduction within a homogeneous, solid sphere: temporal evolution

In spherical coordinates, the heat equation (2.1) reads

$$\frac{1}{r^2}\frac{\partial}{\partial r}\left(k\,r^2\frac{\partial T}{\partial r}\right)+\frac{1}{r^2\,\sin\zeta}\frac{\partial}{\partial\zeta}\left(k\,\sin\zeta\frac{\partial T}{\partial\zeta}\right)+\frac{1}{r^2\,\sin^2\zeta}\frac{\partial}{\partial\xi}\left(k\,\frac{\partial T}{\partial\xi}\right)+q=\rho\,c_p\,\frac{\partial T}{\partial t}\;. \tag{2.5}$$

For the case of constant thermal conductivity, the thermal diffusivity is $D_{\mathrm{th}}=\frac{k}{\rho\,c_p}$ and the previous equation turns to

$$\frac{1}{r^2}\frac{\partial}{\partial r}\left(r^2\frac{\partial T}{\partial r}\right)+\frac{1}{r^2\,\sin\zeta}\frac{\partial}{\partial\zeta}\left(\sin\zeta\frac{\partial T}{\partial\zeta}\right)+\frac{1}{r^2\,\sin^2\zeta}\frac{\partial^2 T}{\partial\xi^2}+\frac{q}{k}=\frac{1}{D_{\mathrm{th}}}\frac{\partial T}{\partial t}\;. \tag{2.6}$$

For simplification, the variable μ can be defined as

$$\mu=\cos\zeta\;, \tag{2.7}$$

and the above equation reads

$$\frac{\partial^2 T}{\partial r^2}+\frac{2}{r}\frac{\partial T}{\partial r}+\frac{1}{r^2}\frac{\partial}{\partial\mu}\left[\left(1-\mu^2\right)\frac{\partial T}{\partial\mu}\right]+\frac{1}{r^2\,\left(1-\mu^2\right)}\frac{\partial^2 T}{\partial\xi^2}+\frac{q}{k}=\frac{1}{D_{\mathrm{th}}}\frac{\partial T}{\partial t}\;. \tag{2.8}$$

Using the new independent variable (Hahn and Özişik 2012)

$$V=r^{1/2}\,T\;, \tag{2.9}$$

the heat equation (2.8) for a constant thermal conductivity transforms into

$$\frac{\partial^2 V}{\partial r^2}+\frac{1}{r}\frac{\partial V}{\partial r}-\frac{1}{4}\frac{V}{r^2}+\frac{1}{r^2}\frac{\partial}{\partial\mu}\left[\left(1-\mu^2\right)\frac{\partial V}{\partial\mu}\right]+\frac{1}{r^2\,\left(1-\mu^2\right)}\frac{\partial^2 V}{\partial\xi^2}+\frac{q\,r^{1/2}}{k}=\frac{1}{D_{\mathrm{th}}}\frac{\partial V}{\partial t}\;. \tag{2.10}$$

The solution scheme that has to be employed, depends on the respective symmetry of the system. Different schemes are summarized in Table 2.1.

Here, the separation of variables ansatz for the general case $T=T(r,\mu,\xi,t)$ (with separation variable $-\lambda^2$), concerning the transformation (2.9), is

$$V(r,\mu,\xi,t)=\Gamma(t)\,R(r)\,M(\mu)\,\Phi(\xi)\;. \tag{2.11}$$

The ensuing decoupled equations are (Hahn and Özişik 2012)

$$\frac{\mathrm{d}\Gamma}{\mathrm{d}t}+D_{\mathrm{th}}\,\lambda^2\Gamma=0 \tag{2.12a}$$

$$\frac{\mathrm{d}^2\Phi}{\mathrm{d}\xi^2}+m^2\Phi=0 \tag{2.12b}$$

$$\frac{\mathrm{d}^2 R}{\mathrm{d}r^2}+\frac{1}{r}\frac{\mathrm{d}R}{\mathrm{d}r}+\left[\lambda^2-\left(n+\frac{1}{2}\right)^2\frac{1}{r^2}\right]R=0 \tag{2.12c}$$

$$\frac{\mathrm{d}}{\mathrm{d}\mu}\left[\left(1-\mu^2\right)\frac{\mathrm{d}M}{\mathrm{d}\mu}\right]+\left[n(n+1)-\frac{m^2}{1-\mu^2}\right]M=0\;. \tag{2.12d}$$

Decoupling the time from the spatial part in (2.10) yields a separated form of the Helmholtz equation in spherical coordinates. However, Hahn and Özişik (2012) also give the solutions of each differential equation. C_n denote constants. The first equation has the general solution

$$\Gamma(t) = C_1 \, \mathrm{e}^{-D_{\mathrm{th}} \lambda^2 t} \tag{2.13a}$$

and the second one

$$\Phi(\xi) = C_2 \, \cos(m\,\xi) + C_3 \, \sin(m\,\xi) \; , \tag{2.13b}$$

for integers m, to satisfy 2π periodicity. The Bessel differential equation of order $n + \frac{1}{2}$ (2.12c) has the solution of a linear combination of the Bessel functions of the first and second kind (linearly independent) of degree $n + \frac{1}{2}$

$$R(r) = C_4 \, J_{n+\frac{1}{2}}(\lambda\, r) + C_5 \, Y_{n+\frac{1}{2}}(\lambda\, r) \; , \tag{2.13c}$$

and the associated Legendre differential equation (2.12d) the solution

$$M(\mu) = C_6 \, P_n^m(\mu) + C_7 \, Q_n^m(\mu) \tag{2.13d}$$

with the linearly independent Associated Legendre functions of the first and second kind with degree n and order m.

Table 2.1: Solution Schemes for the Heat equation in spherical coordinates. Taken from page 185, Hahn and Özişik (2012).

Variables	Equation to Solve	Transforms	Expected Equations
$T(r)$	(2.6) or (2.8)	None	Cauchy equation
$T(r,\mu)$	(2.8)	None	Cauchy equation in r, Legendre equation in μ
$T(r,\mu,\xi)$	(2.8)	None	Cauchy equation in r, Associated Legendre in μ
$T(r,t)$	(2.6) or (2.8)	$U(r,t) = r\,T(r,t)$	$\frac{\partial^2 U}{\partial r^2} + \frac{r\,q}{k} = \frac{1}{D_{\mathrm{th}}}\frac{\partial U}{\partial t}$
$T(r,\mu,t)$	(2.10)	$V = r^{1/2}\,T$	Bessel equation in r, Legendre equation in μ
$T(r,\mu,\xi,t)$	(2.10)	$V = r^{1/2}\,T$	Bessel equation in r, Associated Legendre in μ

2.1.2 Heat conduction within a homogeneous, solid sphere: steady-state

In the context of this work, the ansatz for steady-state problem of a homogeneous ($k =$ const) solid sphere with radius r_0 is often employed (in different variations, though). The considerations on page 221, and following, in Hahn and Özişik (2012) are briefly restated here. For $q = 0$, symmetry in ξ, and steady-state, the heat equation (2.8) is a remnant of the Laplace equation and reads

$$\frac{\partial^2 T}{\partial r^2} + \frac{2}{r}\frac{\partial T}{\partial r} + \frac{1}{r^2}\frac{\partial}{\partial \mu}\left[\left(1-\mu^2\right)\frac{\partial T}{\partial \mu}\right] = 0 \; , \tag{2.14}$$

then the separation ansatz with the separation constant $n(n+1)$ is

$$T(r,\mu) = R(r)M(\mu) \;, \tag{2.15}$$

turning (2.14) into the two ordinary differential equations

$$\frac{r^2}{R}\left(\frac{\mathrm{d}^2R}{\mathrm{d}r^2} + \frac{2}{r}\frac{\mathrm{d}R}{\mathrm{d}r}\right) = n(n+1) \tag{2.16a}$$

$$-\frac{1}{M}\frac{\mathrm{d}}{\mathrm{d}\mu}\left(\left(1-\mu^2\right)\frac{\mathrm{d}M}{\mathrm{d}\mu}\right) = n(n+1) \;, \tag{2.16b}$$

where (2.16b) is simply (2.12d) for $m = 0$ and has the general solution (along (2.13d), $P_n^0 = P_n$, $Q_n^0 = Q_n$)

$$M(\mu) = C_1\, P_n(\mu) + C_2\, Q_n(\mu) \;, \tag{2.17a}$$

which are the Legendre polynomials of the first and second kind. (2.16a) has the general solution

$$R(r) = C_3\, r^n + C_4\, r^{-n-1} \;. \tag{2.17b}$$

The temperatures at $r \to 0$ and $\mu \to \pm 1$ shall be finite. Furthermore, a Neumann boundary condition ($\mathbf{n} = \mathbf{n}_\mathrm{S}$, which is the normal of a sphere)

$$k\left.\frac{\partial T}{\partial \mathbf{n}}\right|_{r=r_0} = k\left.\frac{\partial T}{\partial r}\right|_{r=r_0} = f\left(T\big|_{r=r_0}\right) \;, \tag{2.18}$$

e.g.,

$$k\left.\frac{\partial T}{\partial r}\right|_{r=r_0} = -h\left(T\big|_{r=r_0} - T_\infty\right) \tag{2.19}$$

is often used in the following calculations, where h denotes the heat transfer coefficient. As the Legendre polynomials of the second kind are infinite at $\mu = \pm 1$ and $r^{-n-1} \xrightarrow{r\to 0} \infty$ diverges, it is $C_2 = C_4 = 0$, and thus

$$M(\mu) = C_1\, P_n(\mu) \tag{2.20a}$$

$$R(r) = C_3\, r^n \;. \tag{2.20b}$$

The general solution is the sum over all partial solutions (2.20a) and (2.20b) as

$$\boxed{T(r,\cos\zeta) = \sum_{\nu=0}^{\infty} C_\nu\, r^\nu\, P_\nu(\cos\zeta) \;.} \tag{2.21}$$

The coefficients C_ν can be obtained through the Neumann boundary condition. Generally, for a function $f(x)$ defined in $[-1,1]$, the expansion coefficients C_ν in $f(x) = \sum_{\nu=0}^{\infty} C_\nu P_\nu(x)$ can be obtained by evaluating the integrals

$$C_\nu = \frac{2\nu+1}{2}\left(f\,,\, P_\nu\right)_{[-1,1]} \;. \tag{2.22}$$

2.2 Classical kinetic gas theory

At this point, the assumption is that the gas here is an ideal gas (structureless, punctform particles with no interaction) in thermal equilibrium. In sec. 2.4, this will already be modified towards more realistic assumptions (theory of binary collisions to introduce the Boltzmann equation) allowing to describe the evolution from a non-equilibrium state towards an equilibrium state.

2.2.1 Notation

For N gas particles, the particle density is denoted with $\sigma(\mathbf{r}, \mathbf{v}, t)$, which is the basis for a statistical description of a thermodynamical system. In principle, each gas particle with the coordinate $\mathbf{r}_i = (r_i^{(1)}, r_i^{(2)}, r_i^{(3)})$ and velocity $\mathbf{v}_i = (v_i^{(1)}, v_i^{(2)}, v_i^{(3)})$ is described by a six-dimensional vector $(r_i^{(1)}, r_i^{(2)}, r_i^{(3)}, v_i^{(1)}, v_i^{(2)}, v_i^{(3)})$ (phase space), rendering $\mathbf{r}_i$ and $\mathbf{v}_i$ independent statistical variables. Usually, momentums $\mathbf{p}_i$ are used instead of velocities, but this will not make any difference here.

In thermodynamic equilibrium there is always the same average number of particles with a certain velocity at a certain point in space, and the particle density is subsequently stationary. The number of particles in a certain velocity 'cell' $\mathbf{v}, \mathrm{d}^3v$ in a certain position 'cell' $\mathbf{r}, \mathrm{d}^3r$ (to be exact, this is a probability) is therefore

$$\mathrm{d}^6N = \sigma(\mathbf{r}, \mathbf{v})\, \mathrm{d}^3r\, \mathrm{d}^3v \qquad \text{with the normalization} \int \mathrm{d}^6N = N\ , \tag{2.23}$$

where the spatial particle density n has been introduced, defined as

$$n(\mathbf{r}) \equiv \sigma(\mathbf{r}) = \int \sigma(\mathbf{r}, \mathbf{v})\, \mathrm{d}^3v\ . \tag{2.24}$$

In the case of a homogeneous system it is

$$\partial_{\mathbf{r}}\sigma(\mathbf{r}, \mathbf{v}) = 0 \quad \Longrightarrow \quad n(\mathbf{r}) = n = \frac{N}{V}\ . \tag{2.25}$$

Now, f denotes the one-particle density, thus it is also a probability function, defined as (including the non-stationary case)

$$f(\mathbf{r}, \mathbf{v}, t) \overset{(2.24)}{=} \frac{1}{n(\mathbf{r}, t)}\sigma(\mathbf{r}, \mathbf{v}, t)\ . \tag{2.26}$$

The distribution average of a physical variable $a(\mathbf{r}, \mathbf{v}, t)$ is defined as

$$\overline{a}(\mathbf{r}, t) \overset{(2.26)}{=} \frac{1}{n(\mathbf{r}, t)} \int \mathrm{d}^3v\, \sigma(\mathbf{r}, \mathbf{v}, t)\, a(\mathbf{r}, \mathbf{v}, t)\ . \tag{2.27}$$

It is necessary, to introduce moments of velocity distribution, given by the general definition (n-th moment of a probability function f)

$$\overline{v^n}(\mathbf{r}, t) = \int \mathrm{d}^3v\, f(\mathbf{r}, \mathbf{v}, t)\, v^n \quad \overset{(2.26)}{\Longrightarrow} \quad \overline{v^n}(\mathbf{r}, t) = \frac{1}{n(\mathbf{r}, t)} \int \mathrm{d}^3v\, \sigma(\mathbf{r}, \mathbf{v}, t)\, v^n \tag{2.28a}$$

$$\overline{v_j^n}(\mathbf{r}, t) = \int \mathrm{d}^3v\, f(\mathbf{r}, \mathbf{v}, t)\, v_j^n \quad \overset{(2.26)}{\Longrightarrow} \quad \overline{v_j^n}(\mathbf{r}, t) = \frac{1}{n(\mathbf{r}, t)} \int \mathrm{d}^3v\, \sigma(\mathbf{r}, \mathbf{v}, t)\, v_j^n\ . \tag{2.28b}$$

To keep up with the notation, a component-wise averaged velocity $\overline{\mathbf{v}^{(i)}}$ for a subspace (i) is defined along (2.28b) as

$$\overline{\mathbf{v}^{(i)}}(\mathbf{r},t) = \int\limits_{(i)} \mathrm{d}^3v\, f^{(i)}(\mathbf{r},\mathbf{v},t)\,\mathbf{v}\ . \tag{2.29}$$

2.2.2 The pressure of an ideal gas

The pressure of a gas is a result of momentum transfer from the gas particles (atoms, molecules) upon impinging a surface, e.g. the receptacle's walls or a suspended particle. The force on a surface element $\mathrm{d}\mathbf{A}$ with normal $\mathbf{n}$ caused by a gas particle with the momentum $\mathfrak{p} = m\mathbf{v}$ is

$$\begin{aligned}\mathrm{d}\mathbf{F} &= \frac{\mathrm{d}\mathfrak{p}}{\mathrm{d}t}\,\mathrm{d}^6N = \frac{\mathrm{d}\mathfrak{p}}{\mathrm{d}t}\sigma\,\mathrm{d}^3r\,\mathrm{d}^3v \\ &= \frac{\mathrm{d}\mathfrak{p}}{\mathrm{d}t}\otimes\mathbf{v}\cdot\,\mathrm{d}\mathbf{A}\,\sigma\,\mathrm{d}t\,\mathrm{d}^3v \\ &= \sigma\, m\,\mathbf{v}\otimes\mathbf{v}\cdot\,\mathrm{d}\mathbf{A}\,\mathrm{d}^3v\ ,\end{aligned} \tag{2.30}$$

with $\mathrm{d}\mathbf{A} = \mathrm{d}A\,\mathbf{n}$ and the normal speed $v_\mathbf{n} = \mathbf{v}\cdot\mathbf{n}$. This consideration is now rewritten in its integral form, introducing the pressure tensor (kinetic stress tensor) $\underline{\mathbf{\Pi}}$ which depends on σ.

The wall of a receptacle containing a gas or the surface ∂V of a particle suspended in the effectively infinite gas introduces a boundary condition that manifests itself in a notable discontinuity of the velocity distribution σ. Gas particles impinging ($\mathbf{v}\cdot\mathbf{n} < 0$, denoted as $-$) and leaving ($\mathbf{v}\cdot\mathbf{n} > 0$, denoted as $+$) have to be distinguished, and thus, have to be described by their own velocity distribution. In other words, this introduces the two velocity half-spaces $+$ and $-$, where the physical variables are piecewisely defined on, e.g. σ as

$$\sigma(\mathbf{r},\mathbf{v},t)|_{\partial V} = \begin{cases}\sigma^-(\mathbf{r},\mathbf{v},t) & \mathbf{n}\cdot\mathbf{v} < 0 \\ \sigma^+(\mathbf{r},\mathbf{v},t) & \mathbf{n}\cdot\mathbf{v} > 0\ .\end{cases} \tag{2.31}$$

Following the idea in (2.30), Hidy and Brock (1970) describes the net force acting on a surface area as

$$\mathrm{d}\mathbf{F} = -\mathrm{d}\mathbf{A}\cdot\left(\underline{\mathbf{\Pi}}^+ + \underline{\mathbf{\Pi}}^-\right) \tag{2.32a}$$

with

$$\underline{\mathbf{\Pi}}^{(i)}(\mathbf{r},t) = \int\limits_{(i)} \mathrm{d}^3v\,\sigma^{(i)}(\mathbf{r},\mathbf{v},t)\,m\,\mathbf{v}\otimes\mathbf{v}\ . \tag{2.32b}$$

In Cartesian coordinates, the tensor product yields

$$\mathbf{v}\otimes\mathbf{v} \;=\; \begin{pmatrix} v_x^2 & v_xv_y & v_xv_z \\ v_xv_y & v_y^2 & v_yv_z \\ v_xv_z & v_yv_z & v_z^2 \end{pmatrix}\ . \tag{2.33}$$

Any flux of a variable X in the subspace (i) is given by

$$\breve{\mathbf{X}}^{(i)}(\mathbf{r},t) = n^{(i)}(\mathbf{r},t)\,\overline{X^{(i)}\,\mathbf{v}^{(i)}}(\mathbf{r},t) = \int\limits_{(i)} \mathrm{d}^3v\,\sigma^{(i)}(\mathbf{r},\mathbf{v},t)\,\mathbf{v}\,X(\mathbf{r},\mathbf{v},t)\;. \tag{2.34}$$

With the first moment of the velocity, the particle flux $\breve{\mathbf{N}}$ can be represented as

$$\breve{\mathbf{N}}^{(i)}(\mathbf{r},t) \overset{(2.29)}{=} n^{(i)}(\mathbf{r},t)\,\overline{\mathbf{v}^{(i)}}(\mathbf{r},t)\;. \tag{2.35}$$

Subsequently, the net transfer of translational energy $\mathcal{E}$ can be defined (Hidy and Brock 1970)

$$\mathrm{d}\mathcal{E} = \mathrm{d}\mathbf{A}\cdot\left(\breve{\boldsymbol{\mathcal{E}}}^{+} + \breve{\boldsymbol{\mathcal{E}}}^{-}\right) \tag{2.36a}$$

with

$$\breve{\boldsymbol{\mathcal{E}}}^{(i)}(\mathbf{r},t) = \int\limits_{(i)} \mathrm{d}^3v\,\sigma^{(i)}(\mathbf{r},\mathbf{v},t)\,\mathbf{v}\,\frac{1}{2}m\,v^2\;. \tag{2.36b}$$

At the surface, a particle flux continuity condition is necessary, i.e. in this model, impenetrability of the surface

$$\begin{aligned} 0 &= \mathbf{n}\cdot\left[\breve{\mathbf{N}}^{+}(\mathbf{r},t) + \breve{\mathbf{N}}^{-}(\mathbf{r},t)\right] \\ &\overset{(2.35)}{=} \mathbf{n}\cdot\left[n^{+}(\mathbf{r},t)\,\overline{\mathbf{v}^{+}}(\mathbf{r},t) + n^{-}(\mathbf{r},t)\,\overline{\mathbf{v}^{-}}(\mathbf{r},t)\right] \qquad (2.37a) \\ &\overset{(2.28a)}{=} \mathbf{n}\cdot\left[\int\limits_{+}\mathrm{d}^3v\,\sigma^{+}(\mathbf{r},\mathbf{v},t)\,\mathbf{v} + \int\limits_{-}\mathrm{d}^3v\,\sigma^{-}(\mathbf{r},\mathbf{v},t)\,\mathbf{v}\right] \\ &\overset{(2.28b)}{\Longrightarrow} n^{+}\,\overline{v^{+}_{\mathbf{n}}} = -n^{-}\,\overline{v^{-}_{\mathbf{n}}}\;. \qquad (2.37b) \end{aligned}$$

Example: Corresponding to (2.32) and with no further specified velocity distributions $\sigma^{(\pm)}$, the total force acting on the surface of a sphere with radius r_0 is (mixing Cartesian components v_x, v_y, v_z with spherical coordinates components v_r, v_ξ, v_ζ)

$$\begin{aligned} \mathbf{F} = -2\pi\,r_0^2\,m\int\limits_0^{\pi}\mathrm{d}\zeta\,\sin\zeta\cdot \qquad (2.38) \\ \cdot\left(\int\limits_{+}\mathrm{d}^3v\,\sigma^{+}(\mathbf{r},\mathbf{v},t)\,v_r\begin{pmatrix}v_x\\v_y\\v_z\end{pmatrix} + \int\limits_{-}\mathrm{d}^3v\,\sigma^{-}(\mathbf{r},\mathbf{v},t)\,v_r\begin{pmatrix}v_x\\v_y\\v_z\end{pmatrix}\right)\;. \end{aligned}$$

For the force in z-component it is $v_z \overset{(A.4c)}{=} v_r\cos\zeta - v_\zeta\,\sin\zeta$, hence

$$\begin{aligned} F_z = -2\pi\,r_0^2\,m\int\limits_0^{\pi}\mathrm{d}\zeta\,\sin\zeta\cdot \qquad (2.39) \\ \cdot\left(\int\limits_{+}\mathrm{d}^3v\,\sigma^{+}(\mathbf{r},\mathbf{v},t)\,v_r\,(v_r\cos\zeta - v_\zeta\,\sin\zeta) + \int\limits_{-}\mathrm{d}^3v\,\sigma^{-}(\mathbf{r},\mathbf{v},t)\,v_r\,(v_r\cos\zeta - v_\zeta\,\sin\zeta)\right)\;, \end{aligned}$$

being in agreement with Hidy and Brock (1967) and Beresnev et al. (1993), Equation (1) and (13), respectively.

No gas-surface interaction except specular reflection at thermodynamic equilibrium: In a thermodynamic equilibrium the system is stationary, homogeneous and isotropic, thus σ is just a function of v or v^2, respectively:

$$\sigma = \sigma(v^2) \,, \tag{2.40}$$

and — because of no characterized direction in an arbitrary chosen Cartesian system — each velocity component is

$$\overline{v_x^2} = \overline{v_y^2} = \overline{v_z^2} = \frac{1}{3}\overline{v^2} \,. \tag{2.41}$$

Here, the second moment of both the speed and velocity components have been used along its definition in (2.28). For a Maxwell-Boltzmann velocity distribution, both means $\overline{v}$ and $\overline{v^2}$ will also be explicitly calculated in (2.60a) and (2.60b), respectively. Isotropy implies that for every Cartesian velocity component σ is symmetric around 0, thus it is $\overline{\mathbf{v}} \overset{(2.29)}{=} 0$.

As the boundary of the receptacle or the suspended particle divides the velocity space in two half-spaces '+' and '−' at each surface point, the pressure tensors $\underline{\mathbf{\Pi}}^{(i)}$ have to be discussed separately. The tensor $\mathbf{v} \otimes \mathbf{v}$ also consists of mixed terms of the velocity components, e.g., $v_y\, v_z$. Averaging them with an isotropic velocity distribution yields subsequently zero, too

$$\int\limits_{(i)} \mathrm{d}^3 v\, \sigma^{(i)}(v^2)\, v_y\, v_z = 0 \,. \tag{2.42}$$

Hence, the main diagonal components are the only non-zero elements in the pressure tensor, and they have the same value

$$\underline{\mathbf{\Pi}}^{(i)} \overset{(2.41)}{=} m\, n^{(i)}\, \frac{1}{3}\overline{v^{(i)2}} \begin{pmatrix} 1 & 0 & 0 \\ 0 & 1 & 0 \\ 0 & 0 & 1 \end{pmatrix} \,. \tag{2.43}$$

If the surface is expected to perfectly reflect impinging gas particles and if there is no exchange of energy between gas particles and surface, it is

$$\frac{1}{n^+}\sigma^+(v^2) = \frac{1}{n^-}\sigma^-(v^2) = \sigma_0(v^2) \Longrightarrow \overline{v^{(i)2}} = \frac{1}{2}\overline{v^2} \tag{2.44}$$

and the mass transfer boundary condition (2.37b) yields

$$0 = \mathbf{n} \cdot \left[\int\limits_{+} \mathrm{d}^3 v\, \sigma^+(v^2)\, \mathbf{v} + \int\limits_{-} \mathrm{d}^3 v\, \sigma^-(v^2)\, \mathbf{v} \right] \overset{\overline{v_\mathbf{n}^+} = -\overline{v_\mathbf{n}^-}}{=} \overline{v_\mathbf{n}^+} \left(n^+ - n^-\right) \Longrightarrow n^+ = n^- = n \,. \tag{2.45}$$

With all three considerations, both pressure tensors for impinging and leaving particles yield

$$\underline{\mathbf{\Pi}}^{(i)} \overset{(2.44)\,(2.45)}{=} \frac{1}{6} m\, n\, \overline{v^2}\, \mathbb{1} \,, \tag{2.46}$$

and the force on the surface is

$$\mathrm{d}\mathbf{F} = -\mathrm{d}\mathbf{A} \cdot \left(\underline{\mathbf{\Pi}}^{+} + \underline{\mathbf{\Pi}}^{-}\right) = -m\,n\,\frac{1}{3}\overline{v^2}\,\mathrm{d}\mathbf{A}\ . \tag{2.47}$$

Subsequently, the total pressure is

$$\boxed{\frac{dF}{dA} = p = m\,n\,\frac{1}{3}\overline{v^2}\ .} \tag{2.48}$$

In terms of average kinetic energy (for real gas particles this is only the translation energy) and the ideal gas equation

$$\bar{\mathcal{E}} = \frac{1}{2}m\,\overline{v^2} \tag{2.49}$$

$$p = n\,k_{\mathrm{B}}\,T \tag{2.50}$$

the pressure yields

$$p = \frac{2}{3}n\,\bar{\mathcal{E}} \tag{2.51}$$

$$\bar{\mathcal{E}} = \frac{3}{2}k_{\mathrm{B}}T\ . \tag{2.52}$$

Notation: A normal vector $\mathbf{n}$ must not be confused with the spatial gas densities n or $n^{(i)}$. Generally, the total of a vector $\mathbf{a}$ is just written as $a := \|\mathbf{a}\|_2$, but this does not make any sense in case of a normal vector, which has always the length $\|\mathbf{n}\|_2 = 1$.

Example: For a sphere at temperature T and the assumption $T^{+} = T$, the ordinary force caused by air pressure on one half of the sphere (e.g. $\mathbf{e}_z$) is expected to have the value $F_z = \pi\,r_0^2\,p$ ($\mathbf{n}_{\mathrm{S}}$ defined by (A.1)):

$$\mathbf{F} = 2\pi\ r_0^2\,p\int_0^{\pi/2}\left(\frac{1}{2}+\frac{1}{2}\right)\mathbf{n}_{\mathrm{S}}\sin\zeta\,\mathrm{d}\zeta = \pi r_0^2\,p\begin{pmatrix}0\\0\\1\end{pmatrix}\ . \tag{2.53}$$

2.3 The Maxwell-Boltzmann velocity distribution

The specific shape of the velocity distribution for an ideal gas in thermal equilibrium can be deduced from aforementioned symmetry assumptions. The fact, that v_x, v_y and v_z are independent stochastic variables with the same second moments, i.e. the isotropy condition

$$\overline{v_x^2} = \overline{v_y^2} = \overline{v_z^2} = \frac{1}{3}\overline{v^2}\ , \qquad (2.41)$$

implies, that $\tilde{\sigma}(v^2)$ can be factorized after the velocity components

$$\tilde{\sigma}(v^2) \sim \tilde{\sigma}(v_x^2)\,\tilde{\sigma}(v_y^2)\,\tilde{\sigma}(v_z^2)\ , \tag{2.54}$$

which can only be achieved with the exponential function

$$\tilde{\sigma}(v_i^2) \sim \mathrm{e}^{-a\,v_i^2} \ . \tag{2.55}$$

The normalization factor of $\tilde{\sigma}(v^2)$ will subsequently be dependent of a, whilst the latter one can be determined by calculating the second moment $\overline{v^2}$, which — on the other hand — is

$$\overline{v^2} \overset{(2.52)}{=} \frac{3k_\mathrm{B}\,T}{m} \ , \tag{2.56}$$

yielding

$$a = \frac{m}{2k_\mathrm{B}\,T} \ . \tag{2.57}$$

Thus, the Maxwell-Boltzmann velocity distribution $\sigma_0(\mathbf{v})$ is given by

$$\sigma_0(\mathbf{v}) = \left(\frac{m}{2\pi k_\mathrm{B} T}\right)^{3/2} \mathrm{e}^{-\frac{mv^2}{2k_\mathrm{B}T}} \ , \tag{2.58}$$

which is normalized as

$$\int \mathrm{d}^3v\,\sigma_0(\mathbf{v}) = \int\limits_{-\infty}^{\infty} \mathrm{d}x \int\limits_{-\infty}^{\infty} \mathrm{d}y \int\limits_{-\infty}^{\infty} \mathrm{d}z\,\sigma_0(\mathbf{v}) = \int\limits_0^{2\pi} \mathrm{d}\xi \int\limits_0^{\pi} \sin\zeta \mathrm{d}\zeta \int\limits_0^{\infty} \mathrm{d}v\,v^2\sigma_0(\mathbf{v}) = 1 \ . \tag{2.59}$$

For a Maxwell-Boltzmann velocity distribution $\sigma_0(\mathbf{v})$, the mean and mean-squared values of the gas speed are

$$\overline{v} \overset{(2.28a)}{=} \int \mathrm{d}^3v\,\sigma_0(\mathbf{v})\,v = \sqrt{\frac{8k_\mathrm{B}T}{\pi\,m}} \tag{2.60a}$$

$$\overline{v^2} \overset{(2.28a)}{=} \int \mathrm{d}^3v\,\sigma_0(\mathbf{v})\,v^2 = v_\mathrm{rms}^2 = \frac{3k_\mathrm{B}T}{m} \tag{2.60b}$$

and the mean normal speed for gas particles impinging a wall with normal $\mathbf{n}$, yields (again, averaged with $\sigma_0(\mathbf{v})$)

$$|\overline{v_\mathbf{n}^{(\pm)}}| = \left|\overline{\mathbf{n}\cdot\mathbf{v}^{(\pm)}}\right| \overset{(2.28a)}{=} \sqrt{\frac{k_\mathrm{B}T}{2\pi\,m}} \ . \tag{2.60c}$$

Obviously, the following relation exists for this special distribution

$$v_\mathrm{rms} = \mathrm{const}\,\overline{v_\mathbf{n}} \tag{2.60d}$$

2.4 The Boltzmann equation

2.4.1 Towards equilibrium

To describe a process leading from a non-equilibrium state to an equilibrium state for a an ideal gas, interactions of gas particles are necessary. The easiest type of interaction are binary collisions, which take place when two gas particles meet within their scattering cross sections. For instance, discrete elastic collisions with finite impulses (hard spheres

model) can well approximate the strong repulsive forces for atoms/molecules being close to each other (Cercignani 1988).

In the context of statistics, the collision integral $\left(\frac{\partial\sigma}{\partial t}\right)_{\text{coll}}$ describing the collisions is memory-less, i.e. it is only determined by the particle density at the examined moment, leading to an irreversible description of the gas evolution. The principal equation that describes this evolution for not too small times is called the Boltzmann equation. It is a nonlinear and closed integro-differential equation for the particle density in an effective approximation of a one-body theory, since there are only binary collisions. It has the form

$$\boxed{\frac{\partial\sigma}{\partial t} + \mathbf{v}\cdot\boldsymbol{\nabla}_r\sigma + \frac{\mathbf{F}_{\text{ext}}}{m}\cdot\boldsymbol{\nabla}_v\sigma = \left(\frac{\partial\sigma}{\partial t}\right)_{\text{coll}}} \,. \tag{2.61}$$

For adequately rarefied media the duration of binary collisions is small compared to the time the gas particles need to travel on their paths. In dense systems with many gas particles, this is not the case anymore as many-body effects have a considerable influence and a many-body theory has to be employed. Hence, the Boltzmann equation only describes sufficiently thin media. The term $\mathbf{v}\cdot\boldsymbol{\nabla}_r\sigma$ describes convection due to spatial inhomogeneities in the particle density as well as $m^{-1}\mathbf{F}_{\text{ext}}\cdot\boldsymbol{\nabla}_v\sigma$ for external force fields $\mathbf{F}_{\text{ext}}$. For an accurate description of the gas evolution certain boundary conditions have to be developed. A brief overview is given in sec. 2.7.

2.4.2 Background

For homogeneous systems in a non-equilibrium state with the velocity distribution $\sigma(\mathbf{v},t)$ those binary collisions can be balanced. The difference of the gas particle number for an arbitrary small time step is

$$\frac{\partial\sigma(\mathbf{v}_1,t)}{\partial t}\,\mathrm{d}t\,\mathrm{d}^3v_1 = \mathrm{d}^3v_1\,[\sigma(\mathbf{v}_1,t+\mathrm{d}t)-\sigma(\mathbf{v}_1,t)] = N^+ - N^- \,. \tag{2.62}$$

N^- denotes the number of gas particles within this time step whose velocity changes from $\mathbf{v}$, d^3v to another velocity due to a collision, N^+ denotes the number of particles whose velocity changes to $\mathbf{v}$, d^3v due to a collision. If there are d^3N_1 particles with velocity $\mathbf{v}_1$, d^3v_1 and d^3N_2 particles with velocity $\mathbf{v}_2$, d^3v_2, some of them will collide within a sufficiently small time step and have the velocities $\mathbf{v}_1'$, d^3v_1 and $\mathbf{v}_2'$, d^3v_2. It can be assumed, that the number of collisions is proportional to the particle number densities $\mathrm{d}N_i$ (corresponding to (2.23), it is $\mathrm{d}^6N_i = \sigma(\mathbf{v}_i,t)\,\mathrm{d}^3v_i$) as well as to $\mathbf{v}_i'$, d^3v_i and the time step $\mathrm{d}t$

$$c(\mathbf{v}_1\to\mathbf{v}_1',\mathbf{v}_2\to\mathbf{v}_2')\,\mathrm{d}^3v_1'\,\mathrm{d}^3v_2'\,\mathrm{d}N_1\,\mathrm{d}N_2\,\mathrm{d}t \,. \tag{2.63}$$

In this general definition the four velocities are independent from each other and the collision integral kernel $c(\mathbf{v}_1\to\mathbf{v}_1',\mathbf{v}_2\to\mathbf{v}_2')$ is the probability density for a collision, where gas particle 1 undergoes a velocity change from $\mathbf{v}_1$ to $\mathbf{v}_1'$, and gas atom/molecule 2 changes its velocity from $\mathbf{v}_2$ to $\mathbf{v}_2'$. c meets two elementary symmetry relations:

$$c(\mathbf{v}_1\to\mathbf{v}_1',\mathbf{v}_2\to\mathbf{v}_2') = c(\mathbf{v}_2\to\mathbf{v}_2',\mathbf{v}_1\to\mathbf{v}_1') \tag{2.64a}$$
$$c(\mathbf{v}_1\to\mathbf{v}_1',\mathbf{v}_2\to\mathbf{v}_2') = c(\mathbf{v}_1'\to\mathbf{v}_1,\mathbf{v}_2'\to\mathbf{v}_2) \tag{2.64b}$$
$$c(\mathbf{v}_1\to\mathbf{v}_1',\mathbf{v}_2\to\mathbf{v}_2') = c(\mathbf{v}_2'\to\mathbf{v}_2,\mathbf{v}_1'\to\mathbf{v}_1) \,. \tag{2.64c}$$

The first relation is only formal nature (relabeling), the second one results from the *Principle of Detailed Balance*, introduced by Boltzmann. It is formulated "for kinetic systems which are decomposed into elementary processes (collisions, or steps, or elementary reactions). At equilibrium, each elementary process should be equilibrated by its reverse process", which is based on microscopic reversibility (Gorban and Yablonsky 2011). The third symmetry relation can be decomposed into the two other ones before.

The collision numbers from above can be expressed by means of the kernel as

$$N^- = \mathrm{d}t\,\mathrm{d}v_1 \int \mathrm{d}^3v_2 \int \mathrm{d}^3v_1' \int \mathrm{d}^3v_2'\, \sigma(\mathbf{v}_1,t)\,\sigma(\mathbf{v}_2,t)\,c(\mathbf{v}_1 \to \mathbf{v}_1', \mathbf{v}_2 \to \mathbf{v}_2') \tag{2.65a}$$

$$N^+ = \mathrm{d}t\,\mathrm{d}v_1 \int \mathrm{d}^3v_2 \int \mathrm{d}^3v_1' \int \mathrm{d}^3v_2'\, \sigma(\mathbf{v}_1',t)\,\sigma(\mathbf{v}_2',t)\,c(\mathbf{v}_1' \to \mathbf{v}_1, \mathbf{v}_2' \to \mathbf{v}_2)\ , \tag{2.65b}$$

and thus (2.62) reads

$$\begin{aligned}\frac{\partial\sigma(\mathbf{v}_1,t)}{\partial t} &= -\int \mathrm{d}^3v_2 \int \mathrm{d}^3v_1' \int \mathrm{d}^3v_2' \,[\sigma(\mathbf{v}_1,t)\,\sigma(\mathbf{v}_2,t)\,c(\mathbf{v}_1 \to \mathbf{v}_1', \mathbf{v}_2 \to \mathbf{v}_2') - \\ &\quad -\sigma(\mathbf{v}_1',t)\,\sigma(\mathbf{v}_2',t)\,c(\mathbf{v}_1' \to \mathbf{v}_1, \mathbf{v}_2' \to \mathbf{v}_2)] \\ &\overset{(2.64b)}{=} -\int \mathrm{d}^3v_2 \int \mathrm{d}^3v_1' \int \mathrm{d}^3v_2'\, c(\mathbf{v}_1 \to \mathbf{v}_1', \mathbf{v}_2 \to \mathbf{v}_2') \times \\ &\quad \times [\sigma(\mathbf{v}_1,t)\,\sigma(\mathbf{v}_2,t) - \sigma(\mathbf{v}_1',t)\,\sigma(\mathbf{v}_2',t)]\ ,\end{aligned} \tag{2.66}$$

often also abbreviated as

$$\frac{\partial\sigma}{\partial t} = \left(\frac{\partial\sigma}{\partial t}\right)_{\mathrm{coll}} \tag{2.67}$$

with the collision integral

$$\boxed{\begin{aligned}\left(\frac{\partial\sigma}{\partial t}\right)_{\mathrm{coll}} &= -\int \mathrm{d}^3v_2 \int \mathrm{d}^3v_1' \int \mathrm{d}^3v_2'\, c(\mathbf{v}_1 \to \mathbf{v}_1', \mathbf{v}_2 \to \mathbf{v}_2') \times \\ &\quad \times [\sigma(\mathbf{v}_1,t)\,\sigma(\mathbf{v}_2,t) - \sigma(\mathbf{v}_1',t)\,\sigma(\mathbf{v}_2',t)]\ .\end{aligned}} \tag{2.68}$$

In the hard spheres model with specular reflection

$$\mathbf{v}_1' = \mathbf{v}_1 - \mathbf{n}(\mathbf{n}\cdot(\mathbf{v}_1 - \mathbf{v}_2)) \tag{2.69a}$$

$$\mathbf{v}_2' = \mathbf{v}_2 + \mathbf{n}(\mathbf{n}\cdot(\mathbf{v}_1 - \mathbf{v}_2))\ , \tag{2.69b}$$

the velocities $\mathbf{v}_1$, $\mathbf{v}_1'$, $\mathbf{v}_2$ and $\mathbf{v}_2'$ are related by conservation of momentum and energy

$$m\,\mathbf{v}_1 + m\,\mathbf{v}_2 = m\,\mathbf{v}_1' + m\,\mathbf{v}_2' = \text{const.} \tag{2.70a}$$

$$\frac{1}{2}m\,\mathbf{v}_1^2 + \frac{1}{2}m\,\mathbf{v}_2^2 = \frac{1}{2}m\,\mathbf{v}_1'^2 + \frac{1}{2}m\,\mathbf{v}_2'^2 = \text{const.}\ , \tag{2.70b}$$

and c can subsequently be composed of delta distributions. With the scattering cross section A_s the collision integral is (Cercignani 1988)

$$\left(\frac{\partial\sigma}{\partial t}\right)_{\mathrm{coll}} = -\int \mathrm{d}^3v_2\, A_\mathrm{s}\,\|\mathbf{v}_1 - \mathbf{v}_2\|_2\,[\sigma(\mathbf{v}_1,t)\,\sigma(\mathbf{v}_2,t) - \sigma(\mathbf{v}_1',t)\,\sigma(\mathbf{v}_2',t)]\ . \tag{2.71}$$

σ is stationary, if

$$\sigma(\mathbf{v}_1, t)\,\sigma(\mathbf{v}_2, t) - \sigma(\mathbf{v}_1', t)\,\sigma(\mathbf{v}_2', t) = 0\ , \tag{2.72}$$

i.e. both addends yield the same constant value, hence $\sigma(\mathbf{v}_1, t)\,\sigma(\mathbf{v}_2, t)$ depends on invariants: for binary collisions conservation of momentum and energy (2.70) apply, so that the product of the two distributions is a function f of translation energy and momentum

$$\sigma(\mathbf{v}_1)\,\sigma(\mathbf{v}_2) = f(\mathbf{v}_1 + \mathbf{v}_2, \mathbf{v}_1^2 + \mathbf{v}_2^2) \Longrightarrow \ln\sigma(\mathbf{v}_1) + \ln\sigma(\mathbf{v}_2) = \ln f(\mathbf{v}_1 + \mathbf{v}_2, \mathbf{v}_1^2 + \mathbf{v}_2^2)\ . \tag{2.73}$$

The argumentation is similar to the one in sec. 2.3: σ is an exponential function, whose exponent is linear in the momentum and the energy

$$\sigma(\mathbf{v}_1) = b\,\mathrm{e}^{-a(\mathbf{v}_1-\mathbf{u})^2}\ . \tag{2.74}$$

For resting gases it is $\mathbf{u} = 0$. Factors b and a are independent of $\mathbf{u}$, thus they yield the same values like for the Maxwell-Boltzmann velocity distribution, which was already derived in sec. 2.3, and σ is

$$\sigma(\mathbf{v}) = \sigma_0(\mathbf{v} - \mathbf{u}) = \left(\frac{m}{2\pi k_\mathrm{B} T}\right)^{3/2} \mathrm{e}^{-\frac{m(\mathbf{v}-\mathbf{u})^2}{2k_\mathrm{B}T}}\ . \tag{2.75}$$

2.5 The Knudsen number

The dimensionless Knudsen number Kn for gaseous media is defined as

$$\boxed{Kn = \frac{\text{mean free path of the gas } \lambda}{\text{characteristic length } l}\ .} \tag{2.76}$$

The characteristic length l could be the spherical particle's radius in an effectively infinite gaseous medium, such as the atmosphere or the gas in a protoplanetary disk. For wind tunnels l is, e.g., the diameter of a pipe. The mean free path λ is generally defined as

$$\lambda = \frac{1}{n\,A_\mathrm{s}}\ . \tag{2.77}$$

For Knudsen numbers in the effectively infinite medium the limit $Kn \to \infty$ defines the so-called free-molecule regime (*fm*). For experiments, Knudsen numbers $Kn \geq 10$ are regarded as being in this regime, and the considerations below still hold and introduce only a minor error. The transition regime comprises the range $0.25 \lesssim Kn \lesssim 10$. The definition is based on experiments as well as theoretical studies, but the lower bound is not fixed and can have different values for different transfer processes on (aerosol) particles. In the limit $Kn \to 0$ the medium is in the so-called continuum regime (*co*) (Hidy and Brock 1970). In parts of the continuum regime, i.e. for small Knudsen number, such as $Kn \ll 1$ (Rohatschek 1995), the continuum regime theory is extended with a slip-flow boundary condition (see Figure 2.2b). Hidy and Brock (1970) state, that generally, for the slip-flow regime as sub-regime no fixed bound can be given. For both extreme cases $Kn \to \infty$ and $Kn \to 0$ mathematical descriptions of transport processes to suspended particles

are easier to find compared in the case of the transition regime, hence in the latter one empirical methods are applied. Figure 2.2b shows the particular regime for a particle's characteristic length l over mean free path λ of the gas molecules and/or atoms.

In many phenomena, such as natural and technological ones, micron-sized particles and smaller ones (fine dust) are subject of transfer processes, e.g., heat transfer processes. This plays a role in especially the atmosphere where those particles are said to have the "greatest potential health and economic hazard" (Hidy and Brock 1970). It is also stated that "all atmospheric processes involving particles" in the lower atmosphere take place in the *fm* and the transition Knudsen regimes. Thus in the past decades there has been research on transfer processes such as *photophoresis* (Rohatschek 1956b,a, 1984 and Orr and Keng 1964 and Hidy and Brock 1967, 1970 and Tong 1973, 1975 and Yalamov et al. 1978 and Yalamov and Khasanov 1998 and Kerker and Cooke 1982 and Pluchino 1983 and Keh 2001 and Keh and Hsu 2005 and Beresnev et al. 2003c,a,b and Cheremisin et al. 2005, 2011 and Cheremisin and Kushnarenko 2013 and Wurm and Krauss 2008 and Soong et al. 2010 and Chang and Keh 2012 and Shvedov et al. 2012). The explanation what this terms means will be given below. It will be discussed for the free-molecule regime where the theory is exact within the restrictions imposed. For this discussion, gas-surface boundary conditions are introduced, including so-called accommodation coefficients.

Hereafter, unless otherwise stated, all considerations apply in the free-molecule regime.

2.6 Free molecular flow

2.6.1 Gas velocity distribution

If the Boltzmann equation (2.61) is applied in the *fm* regime, it is recommendable to introduce the dimensionless version of this equation (Hidy and Brock 1970):

$$\frac{\partial\tilde{\sigma}}{\partial\tilde{t}} + \tilde{\mathbf{v}}\cdot\boldsymbol{\nabla}_{\tilde{r}}\tilde{\sigma} + \tilde{\mathbf{F}}_{\text{ext}}\cdot\boldsymbol{\nabla}_{\tilde{v}}\tilde{\sigma} = \frac{0.707}{\pi}Kn^{-1}\left(\frac{\partial\tilde{\sigma}}{\partial\tilde{t}}\right)_{\text{coll}} . \tag{2.78a}$$

The dimensionless variables have the definitions (again, l denotes the characteristic length, $\overline{v}$ the mean gas speed, e.g., calculated for a Maxwell-Boltzmann-distribution in (2.60a))

$$\tilde{\mathbf{r}} = \frac{\mathbf{r}}{l} \tag{2.78b}$$

$$\tilde{\mathbf{v}} = \left(\frac{m}{2k_{\text{B}}T}\right)^{1/2}\mathbf{v} \tag{2.78c}$$

$$\tilde{t} = \frac{\overline{v}}{l}t \tag{2.78d}$$

$$\tilde{\sigma} = n\left(\frac{m}{2\pi k_{\text{B}}T}\right)^{3/2}\sigma \tag{2.78e}$$

$$\tilde{\mathbf{F}}_{\text{ext}} = \frac{l}{\overline{v}^2\,m}\mathbf{F}_{\text{ext}} . \tag{2.78f}$$

In the *fm* regime the mean free path of the gas particles is much larger than the characteristic length l, subsequently there are no collisions between gas particles on the scale of l

$$\frac{\partial\tilde{\sigma}}{\partial\tilde{t}} + \tilde{\mathbf{v}} \cdot \boldsymbol{\nabla}_{\tilde{r}}\tilde{\sigma} + \tilde{\mathbf{F}}_{\text{ext}} \cdot \boldsymbol{\nabla}_{\tilde{v}}\tilde{\sigma} = 0 \,, \tag{2.79}$$

as it is $Kn \to \infty$ for the free-molecule regime and hence, the collision term vanishes. Plus, with isolation from external forces (i.e. $\tilde{\mathbf{F}}_{\text{ext}} = 0$), the dimensionless Boltzmann equation (2.78a) turns into

$$\frac{\partial\tilde{\sigma}}{\partial\tilde{t}} + \tilde{\mathbf{v}} \cdot \boldsymbol{\nabla}_{\tilde{r}}\tilde{\sigma} = 0 \,, \tag{2.80}$$

and the gas particle's trajectories are straight lines. For instance, in the case of a suspended particle in an effectively infinite gaseous medium, in the vicinity of the particle, the gas particles go straight unless intercepted by the suspended particle itself. Furthermore, the particle does not alter the velocity distribution function $\sigma^-(\mathbf{v})$ of impinging gas particles, as gas particles leaving the surface do not collide with impinging gas particles themselves (on the same scale l). This is illustrated in Figure 2.2a. Thus the temperatures T^- and T_∞ can be identified in the *fm* regime

$$T^- \xrightarrow{Kn\to\infty} T_\infty \tag{2.81a}$$

$$T_{\text{gas}} \xrightarrow{r\to\infty} T_\infty \,. \tag{2.81b}$$

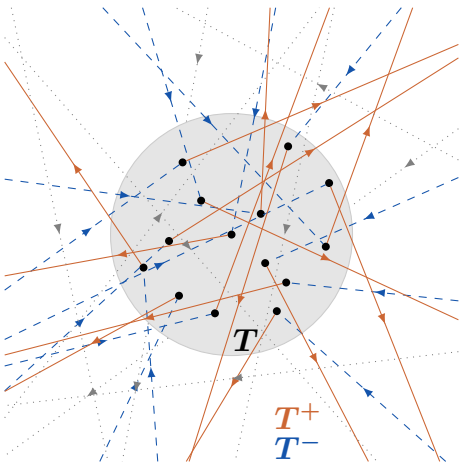

(a) Gas particle trajectories in the free-molecule regime. Blue dashed and orange indicate impinging (−) and leaving (+) gas particles, respectively. Dotted lines denote trajectories of gas particles missing the particle.

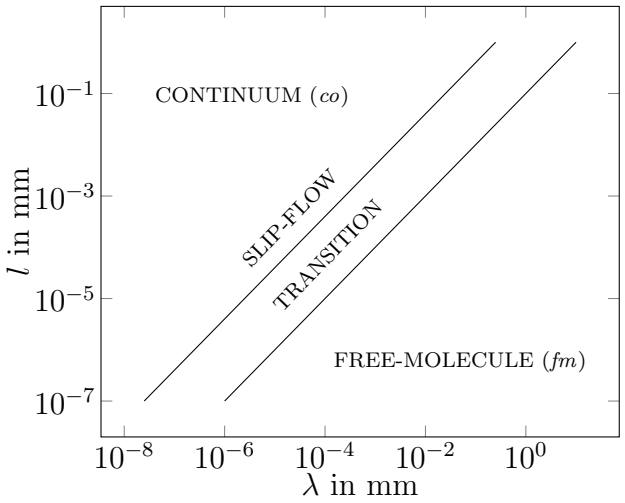

(b) Knudsen regimes.

Figure 2.2: Knudsen regimes and the model of a suspended particle in the free-molecule regime.

2.6.2 The pressure of gas — photophoresis

The following considerations are made for a single particle suspended in an effectively infinite gaseous medium, and the velocity distribution σ of a gas particle is a solution of the Boltzmann equation (2.61). An energy and momentum transfer between the gas and the suspended particle can only happen through binary collisions from gas molecules or atoms with the particle. Including those transfer processes, the pressure/force on the particle will be different from the result obtained in the adiabatic case (2.48). Clearly, a particle with non-constant temperature across the surface will somehow be subject to a non-zero net force.

The incident gas particles have the temperature T^-, those leaving the suspended particle have the temperature T^+, whereas the particle itself has the temperature T (Figure 2.2a). The spatial gas densities for the fraction of the gas which has not collided with the particle yet is n, those already impinged the particle are denoted with n^+. However, for the further derivation it is not necessary to know the exact form of the subjacent basic distribution σ within the borders of this model.

If the surface temperature T is higher than the (constant) gas temperature T^-, it is

$$T^- \leq T^+ \leq T \; . \tag{2.82}$$

Furthermore, if the temperature difference between particle and gas arises from heating by radiation and it is $T^- < T^+$, this is called *photophoresis*.

For a given velocity distribution function for the velocity half-spaces, the force on the surface ∂V can be obtained with the very general kinetic equation (2.32). This equation was used in Beresnev et al. (1993) (Equation (13)) and in Yalamov et al. (1976a) (Equation (14)). It has to be noted, that in Yalamov et al. (1976a) the equation describes the total force on the particle, i.e. not only the photophoretic force but also the drag force acting on the particle moving with velocity $\mathbf{u}$ relative to the gas, because the distribution function $\sigma^- = \sigma^-(\mathbf{v} + \mathbf{u})$ was used (see sec. 3.3.2 for discussion). $\mathbf{u}$ is the photophoretic drift velocity for a total force of zero.

At the surface at least one boundary condition has to be applied, e.g., the mass continuity condition at the surface

$$n^+ \left|\overline{v_{\mathbf{n}}^+}\right| = n \left|\overline{v_{\mathbf{n}}^-}\right| \quad \Longrightarrow n^+ = n \left|\frac{\overline{v_{\mathbf{n}}^-}}{\overline{v_{\mathbf{n}}^+}}\right| \; . \tag{2.37b}$$

Furthermore, accommodation descriptions (sec. 2.8) such as thermal or momentum accommodation can be applied, depending on the complexity of the given σ. Different scenarios are discussed in sec. 3.3.

For the case the velocity distributions σ^- and σ^+ are isotropic, (2.32) simplifies to

$$\mathbf{F} = -\frac{1}{3} \int_{\partial V} m\, n\, \overline{v^{(-)2}}\, \mathrm{d}\mathbf{A} \left(1 + \left|\frac{\overline{v_{\mathbf{n}}^-}}{\overline{v_{\mathbf{n}}^+}}\right| \frac{\overline{v^{(+)2}}}{\overline{v^{(-)2}}} \right) \; . \tag{2.83}$$

For an isolated, thermally equilibrated, effectively infinite gas in the free-molecule regime (Figure 2.2b) the (dimensionless) Gaussian velocity distribution

$$\tilde{\sigma}(\tilde{\mathbf{v}}) = \mathrm{e}^{-\frac{m\tilde{v}^2}{2k_\mathrm{B}T}} \tag{2.84}$$

solves the (dimensionless) Boltzmann equation (2.80). Corresponding to (2.58), the velocity distributions for the gas particles impinging the surface (−) and those leaving it (+) have the form

$$\sigma^-(\mathbf{v}) = n\,\sigma_0^-(\mathbf{v}) \overset{(2.58)}{=} n\left(\frac{m}{2\pi k_\mathrm{B} T^-}\right)^{3/2} \mathrm{e}^{-\frac{mv^2}{2k_\mathrm{B}T^-}} \tag{2.85a}$$

$$\sigma^+(\mathbf{v}) = n^+\,\sigma_0^+(\mathbf{v}) \overset{(2.58)}{=} n^+\left(\frac{m}{2\pi k_\mathrm{B} T^+}\right)^{3/2} \mathrm{e}^{-\frac{mv^2}{2k_\mathrm{B}T^+}}\,, \tag{2.85b}$$

thus the ratios for both normal speeds and the mean squared speeds are

$$\left|\frac{\overline{v_\mathbf{n}^-}}{\overline{v_\mathbf{n}^+}}\right| \overset{(2.60c)}{=} \sqrt{\frac{T^-}{T^+}} \tag{2.86a}$$

$$\frac{\overline{v^{(+)2}}}{\overline{v^{(-)2}}} \overset{(2.60b)}{=} \frac{T^+}{T^-} \tag{2.86b}$$

$$\frac{\overline{v^{(-)2}}}{\overline{v^2}} \overset{(2.60b)}{=} \frac{1}{2}\frac{T^-}{T}\,, \tag{2.86c}$$

and the equation for the photophoretic force (2.83) reads

$$\begin{aligned}\mathbf{F} &\overset{(2.83)}{\underset{(2.86)}{=}} -\frac{1}{6}\int_{\partial V} \mathrm{d}\mathbf{A}\left(1+\sqrt{\frac{T^+}{T^-}}\right) m\,n\,\overline{v^2} \\ &\overset{(2.48)}{=} -\frac{1}{2}\int_{\partial V} \mathrm{d}\mathbf{A}\,p\left(1+\sqrt{\frac{T^+}{T^-}}\right)\,.\end{aligned} \tag{2.87}$$

The last equation is essential for this work on photophoresis in the free-molecule regime, driven by a non-constant temperature of a particle (often simply referred to as 'temperature gradient') that is embedded in a gas with constant temperature T^-. Just to emphasize, T^- is the temperature of the unscattered gas particles, thus effectively those ones far away from the particle. This equation is widely used, for instance in Rohatschek and Zulehner (1985) and Rohatschek (1995). In Equation (7) in Tong (1973), Equation (6) in Hidy and Brock (1967), and Equation (11) in Tehranian et al. (2001), (2.87) is used in the special case of a sphere with rotationally-symmetric surface temperature (thus only the z component contributes).

Photophoresis is not only restricted to single particles but was also studied for aerosol agglomerates and their coagulation by Kuepper et al. (2014) and Cheremisin and Kushnarenko (2013).

2.7 Surface boundary conditions

In the following I will introduce coefficients subdividing the gas particles interacting with a body into two fractions. As stated in sec. 2.2.2, the presence of a particle at temperature T in the effectively infinite gaseous medium imposes a boundary condition on the solution of the Boltzmann equation, represented by the velocity distribution $\sigma^+(\mathbf{v})$ at the particle

surface. Formally, a probability function $\tilde{P}\left(\tilde{\mathbf{v}} \to \mathbf{v}\right)$ — also called scattering kernel — can be introduced, describing the reflection of an impinging particle with $\tilde{\mathbf{v}}$ and leaving with a velocity in the cell $\mathbf{v}$, $\mathrm{d}^3 v$. Correspondingly, the velocity distribution for the leaving gas particles then is described by the boundary condition (Hidy and Brock 1970 and Cercignani and Lampis 1971)

$$\boxed{\sigma^+(\mathbf{v}) = \int_- \frac{|\mathbf{n}\cdot\tilde{\mathbf{v}}|}{|\mathbf{n}\cdot\mathbf{v}|}\,\tilde{P}\left(\tilde{\mathbf{v}} \to \mathbf{v}\right)\,\sigma^-(\tilde{\mathbf{v}})\,\mathrm{d}^3\tilde{v}\;.} \tag{2.88}$$

$\tilde{P}$ as a probability function must be positive and satisfy a normalization condition as well as additionally a reciprocity relation (microscopic reversibility condition), which both read (Cercignani and Lampis 1971 and Lord 1991)

$$\int_{\mathbf{n}\cdot\mathbf{v}>0} \tilde{P}\left(\tilde{\mathbf{v}} \to \mathbf{v}\right)\,\mathrm{d}^3 v = 1\;, \tag{2.89}$$

$$|\mathbf{n}\cdot\tilde{\mathbf{v}}|\;\mathrm{e}^{\frac{-m\,\tilde{v}^2}{2k_\mathrm{B}T}}\;\tilde{P}\left(\tilde{\mathbf{v}} \to \mathbf{v}\right) = |\mathbf{n}\cdot\mathbf{v}|\;\mathrm{e}^{\frac{-m\,v^2}{2k_\mathrm{B}T}}\;\tilde{P}\left(-\mathbf{v} \to -\tilde{\mathbf{v}}\right)\;. \tag{2.90}$$

Reciprocity is a necessary condition which ensures microreversibility and compliance with Boltzmann's H-Theorem (sec. A.4) (Kuščer 1971 and Cercignani 1988). Retrieving $\tilde{P}\left(\tilde{\mathbf{v}} \to \mathbf{v}\right)$ remains a problem though. Historically, the first approach was to come up with the transition condition

$$\sigma^+(\mathbf{v}) = \varepsilon\,\sigma^{(0)+}(\mathbf{v}) + (1-\varepsilon)\,\sigma^-(\mathbf{v}^+)\;, \tag{2.91}$$

where

$$\mathbf{v}_0^+ = \mathbf{v} - 2\mathbf{n}(\mathbf{n}\cdot\mathbf{v}) \tag{2.92}$$

denotes the gas particle's velocity after the specular, adiabatic reflection with a body or wall. This condition was conceived by Maxwell (Maxwell 1890), and initially based on works of Kundt and Warburg (1875). Maxwell assumed that for low pressures a fraction $0 \leq \varepsilon \leq 1$ of gas molecules scatters diffusely at a surface and leave with a Maxwell-Boltzmann velocity distribution

$$\sigma^{(0)^+}(\mathbf{v}) = n^+\,\sigma_0(\mathbf{v}) = n^+\left(\frac{m}{2\pi k_\mathrm{B}T}\right)^{3/2}\mathrm{e}^{-\frac{mv^2}{2k_\mathrm{B}T}} \tag{2.93}$$

at the temperature T of the surface, whilst the rest $(1-\varepsilon)$ scatters only specularly with $\sigma^-(\mathbf{v}_0^+)$.

The scattering integral kernel for the Maxwell boundary condition is [2]

$$\tilde{P}_\mathrm{M}\left(\tilde{\mathbf{v}} \to \mathbf{v}, \varepsilon\right) = \sqrt{\frac{2\pi\,m}{k_\mathrm{B}T}}\,\varepsilon\;|\mathbf{n}\cdot\mathbf{v}|\;\sigma_0(\mathbf{v}) + (1-\varepsilon)\;\delta\left(\tilde{\mathbf{v}} - \mathbf{v}_0^+\right)\;, \tag{2.94}$$

which was also cited by Sharipov (2001, 2002, 2003b) and Sazhin et al. (2008). This kernel predicts both isotropic surface scattering of the thermalized gas particles and Dirac's delta function-like adiabatic scattering of the specularly reflected gas particles, which is sketched in Figure 2.3.

[2] written as $\tilde{P}_\mathrm{M}$, M for Maxwell

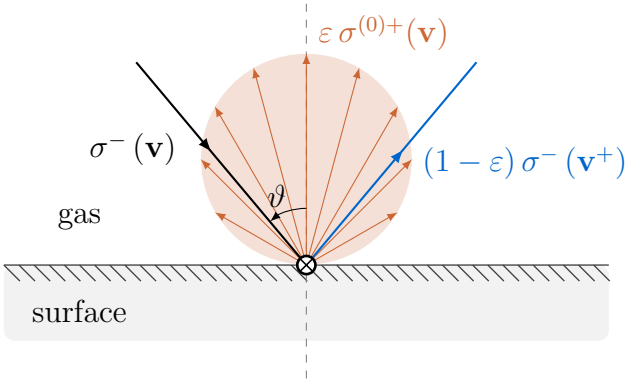

Figure 2.3: Specular and diffuse reflection with the Maxwell kernel. Not true to scale.

Maxwell (1878) also suggested a more general way for the thermal interaction of gas particles with a solid's surface, essentially described by a linear combination of simple kernels like the three kernels $\tilde{P}_0$, $\tilde{P}_1$ and $\tilde{P}_2$, which will be briefly discussed. The first one describes full accommodation, i.e. diffuse scattering:

$$\begin{aligned}\tilde{P}_0\left(\tilde{\mathbf{v}} \to \mathbf{v}\right) &= \tilde{P}_{\mathrm{M}}\left(\tilde{\mathbf{v}} \to \mathbf{v}, 1\right) \\ &= \sqrt{\frac{2\pi\, m}{k_{\mathrm{B}} T}}\; |\mathbf{n}\cdot\mathbf{v}|\; \sigma_0(\mathbf{v})\;.\end{aligned} \tag{2.95}$$

This kernel essentially takes account for vibrating surface atoms that can exchange energy with the impinging gas particles. Furthermore, on average the gas particles leave in thermal equilibrium with the solid's surface at temperature T (described by $\sigma_0(\mathbf{v}) = \left(\frac{m}{2\pi k_{\mathrm{B}} T}\right)^{3/2} \mathrm{e}^{-\frac{mv^2}{2k_{\mathrm{B}}T}}$). Another possibility, and that is the opposite of the kernel above, is adiabatic and specular reflection in case of a perfectly smooth and solid surface, described by the kernel

$$\begin{aligned}\tilde{P}_1\left(\tilde{\mathbf{v}} \to \mathbf{v}\right) &= \tilde{P}_{\mathrm{M}}\left(\tilde{\mathbf{v}} \to \mathbf{v}, 0\right) \\ &= \delta\left(\tilde{\mathbf{v}} - \mathbf{v}_0^{+}\right)\;.\end{aligned} \tag{2.96}$$

This kernel is rather of academic use and leaves a quite nonphysical smack. On the other hand, handling the delta distribution for the description of the non-diffuse scattered outgoing gas particles is the easiest, compared to other kernels. For a more realistic reflection of the gas particles only a small modification of the kernel describing specular reflection has to be made. It can be assumed, that the perfectly smooth and solid surface is microscopically rough. Subsequently, the impinging gas particle will still be reflected adiabatically (i.e., retain their speed), but scattered into different direction, which is described by the kernel (Struchtrup 2013)

$$\tilde{P}_2\left(\tilde{\mathbf{v}} \to \mathbf{v}\right) = \frac{|\mathbf{n}\cdot\mathbf{v}|}{\pi\,\tilde{v}^3}\,\delta\left(\tilde{v} - v\right)\;. \tag{2.97}$$

Cercignani and Lampis (1971) mathematically constructed scattering kernels $\tilde{P}_{\mathrm{CL}}$ with two or three parameters ε_i for the calculation of σ^{+} by employing (2.88), which are

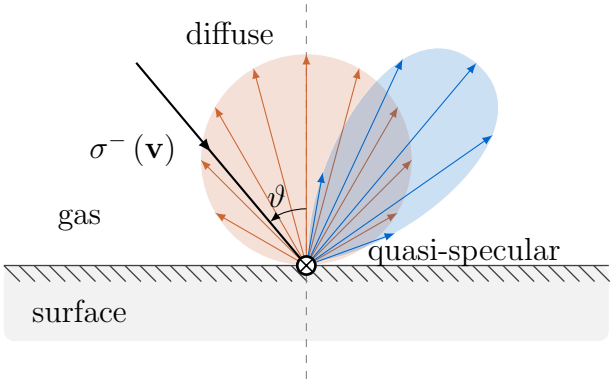

Figure 2.4: High vacuum experiments show quasi-specular scattering for clean solid surfaces whereas the diffuse scattering share or cosine scattered (both centered to the surface normal) share increases with surface contamination (Moe and Moe 2005). Not true to scale.

alternatives to the 'old' kernel $\tilde{P}_{\mathrm{M}}$ (2.94) based on Maxwell's work (Maxwell 1890). This publication is written in a very formal and mathematically rigorous way and is a mayor contribution in the field of gas-surface scattering. Hence I will explicitly refer to the writing itself and refrain from too detailed descriptions.

The motivation to find or construct new kernels arose from contradictions in experimental measurements. Earlier experiments could not confirm the predictions by the Maxwell kernel $\tilde{P}_{\mathrm{M}}$ (Hurlbut 1989, 1986 and Hinchen and Shepherd 1967 and Hinchen and Foley 1965 and Kuhlthau and Bishara 1965). Also Cercignani and Lampis (1971) wrote:

> However, this [Mawell] model is unrealistic because, for a given monochromatic beam, there would be a sharp maximum in the number of molecules per unit angle at the angle corresponding to specular reflection, a situation contradicted by experiments.

Poiseuille flow and the thermomolecular pressure difference as well as thermal transpiration/creep (Sharipov 2001, 2002 and Sazhin et al. 2008) cannot be successfully described, as values of accommodation coefficients (introduced below in sec. 2.8) are ambiguous. Most importantly, molecular beam scattering experiments show, that the non-diffuse fraction of the scattered beam is indeed of a plume-like shape which points into the direction of the specular reflection (Struchtrup 2013), as shown in Figure 2.4, rather than the single specularly reflected beam predicted by the Maxwell kernel $\tilde{P}_{\mathrm{M}}$, which also Cercignani and Lampis (1971) found nonphysical. The plume-like quasi-specular scattering can be described by the CL kernel with its two parameters.

For the CL kernel the velocity of the impinging gas particles is subdivided into the surface-tangential part (index t) and the normal part (index n). The kernel with the two parameters $-1 \leq \varepsilon_1 \leq 1$ and $0 \leq \varepsilon_2 \leq 1$ is ($v_\mathbf{n} \equiv \mathbf{n} \cdot \mathbf{v}$)

$$\begin{aligned}\tilde{P}_{\mathrm{CL}}\left(\tilde{\mathbf{v}} \to \mathbf{v}, \varepsilon_1, \varepsilon_2\right) &= \tilde{P}_\mathrm{t}\left(\tilde{\mathbf{v}}_\mathbf{t} \to \mathbf{v}_\mathbf{t}, \varepsilon_1\right) \times \tilde{P}_\mathrm{n}\left(\tilde{v}_\mathbf{n} \to v_\mathbf{n}, \varepsilon_2\right) \\ &= \frac{m^2\, \mathbf{n}\cdot\mathbf{v}}{2\pi\, \varepsilon_1\, \varepsilon_2\, (2-\varepsilon_2)\, (k_\mathrm{B}T)^2}\, I_0\left(\frac{m\sqrt{1-\varepsilon_2}}{k_\mathrm{B}\, T\, \varepsilon_2}\, v_\mathbf{n}\, \tilde{v}_\mathbf{n}\right) \times \\ &\times \exp\left(-\frac{m}{2k_\mathrm{B}\, T}\frac{v_\mathbf{n}^2 + (1-\varepsilon_2)\, \tilde{v}_\mathbf{n}^2}{\varepsilon_2} - \frac{m}{2k_\mathrm{B}\, T}\frac{\left(\mathbf{v}_\mathbf{t} - (1-\varepsilon_1)\, \tilde{\mathbf{v}}_\mathbf{t}\right)^2}{\varepsilon_1\, (2-\varepsilon_1)}\right)\,,\end{aligned} \tag{2.98}$$

where I_0 is the modified Bessel function of the first kind and 0-th order. The definition can be found in (A.5).

Lord (1991) extended their model to the cases of diffuse scattering with incomplete accommodation by the construction of the so-called Cercignani–Lampis–Lord (CLL) scattering kernel, which only uses one parameter $0 \leq \varepsilon \leq 1$

$$\begin{aligned}\tilde{P}_{\mathrm{CLL}}\left(\tilde{\mathbf{v}} \to \mathbf{v}, \varepsilon\right) &= \frac{2\sqrt{2k_\mathrm{B}T}\cos\zeta}{\pi\, \varepsilon\sqrt{1-\varepsilon}\sqrt{m}\,\tilde{v}}\, I_1\left(\frac{m}{k_\mathrm{B}\, T}\frac{\sqrt{1-\varepsilon}}{\varepsilon} v\, \tilde{v}\right) \times \\ &\times \exp\left(\frac{m}{2k_\mathrm{B}\, T}\frac{v^2 + (1-\varepsilon)\tilde{v}^2}{\varepsilon}\right)\,,\end{aligned} \tag{2.99}$$

(2.100)

with I_1 denoting the modified Bessel function of the first kind and first order.

Another kernel was proposed by Epstein (1967). It is based on the Maxwell kernel, with the parameter $\varepsilon = \varepsilon(\mathbf{v})$ as a function of the velocity of the incoming gas particles, and conservation of the Maxwell-Boltzmann distribution σ_0 on the particle's surface. The kernel is (Epstein 1967)

$$\tilde{P}_\mathrm{E}\left(\tilde{\mathbf{v}} \to \mathbf{v}, \varepsilon(\mathbf{v})\right) = \frac{\mathbf{n}\cdot\mathbf{v}\, \sigma_0(\mathbf{v})\, \varepsilon(\mathbf{v})\, \varepsilon(\tilde{\mathbf{v}})}{\int\limits_+ \mathbf{n}\cdot\mathbf{v}\, \sigma_0(\mathbf{v})\, \varepsilon(\mathbf{v})\, \mathrm{d}^3v} + (1-\varepsilon(\mathbf{v}))\, \delta\left(\tilde{\mathbf{v}} - \mathbf{v}_0^+\right)\,. \tag{2.101}$$

In the same publication, Epstein also suggested a particular form for $\varepsilon(\mathbf{v})$ with three parameters λ_1, λ_2 and B as

$$\varepsilon(\mathbf{v}) = \mathrm{e}^{-\frac{m\,\tilde{v}}{2k_\mathrm{B}\,\lambda_1}} + B\left(1 - \mathrm{e}^{-\frac{m\,\tilde{v}}{2k_\mathrm{B}\,\lambda_2}}\right)\,. \tag{2.102}$$

λ_1 and λ_2 account for the slowly and fast incident gas particles, respectively. Borman et al. (1988) also suggested another function. Other functions for $\varepsilon(\mathbf{v})$ only have to be smooth and meet the condition $0 \leq \varepsilon(\mathbf{v}) \leq 1$ (Sazhin et al. 2008).

In Sazhin et al. (2008) the authors numerically studied thermal creep through short and long capillaries using the Maxwell, Epstein and CL kernel. Their comparison with experimental data suggested, that the predictions made with the Maxwell kernel are less accurate than those made with the other two kernels. Molecular dynamics (MD) simulations were employed by Daun et al. (2009) to study the quality of the Maxwell and the CLL kernel theoretically. They also found out, that the Maxwell kernel is rather insufficient for accurate descriptions of gas-surface interactions, which is displayed in

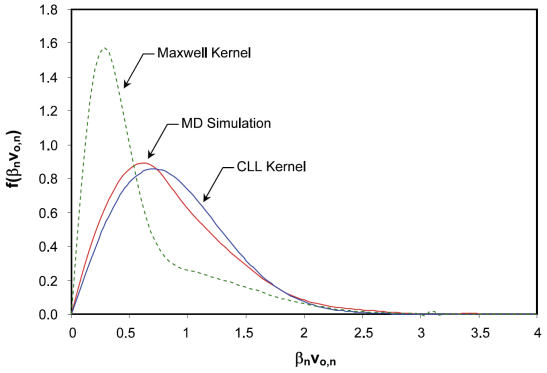

(a) normal speed distribution

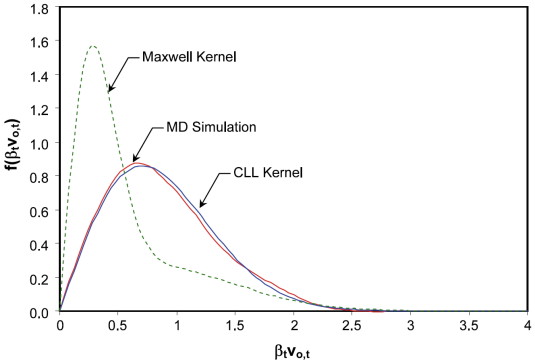

(b) tangential speed distribution

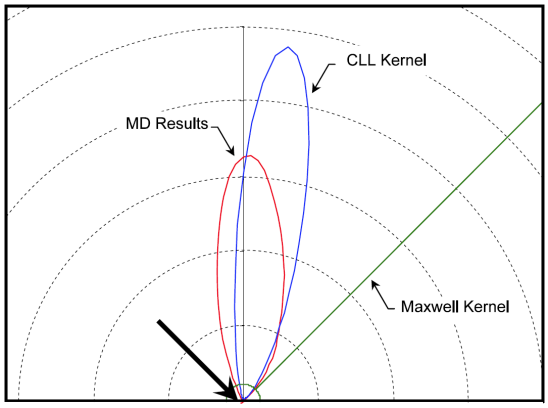

(c) incidence plane: directional scattering probability

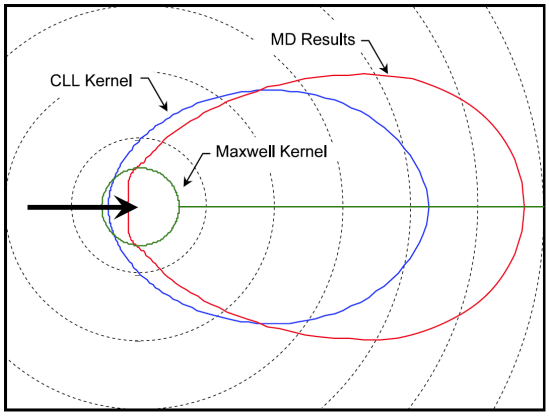

(d) from above: directional scattering probability

Figure 2.5: The Cercignani–Lampis–Lord (CLL) and the Maxwell scattering kernel and alongside of molecular dynamics (MD) results from Daun et al. (2009). For these pictures, $\beta = \sqrt{\frac{m}{2k_\mathrm{B}((1-\alpha)T^- + \alpha T)}}$ and the indices 'n' and 't' refer to normal and tangential motion, the index 'o' on the axes of two top figures denote the scattered gas particles (Daun et al. 2009). The deviation of the Maxwell scattering kernel from the MD simulations and the CLL kernels are obvious.

Figure 2.5. Woronowicz and Rault (1994) confirmed a better agreement of CLL kernel (Lord 1991) in Direct Monte Carlo Simulations than the Maxwell kernel. Sharipov (2002, 2003a,b) employed the CL kernel for studies on the "Plane flow between two parallel plates", "Slip and jump coefficients" and "Poiseuille flow and thermal creep through a long tube". The results are in good agreement with the findings in experiments cited in the respective publication.

Recently, Struchtrup (2013) suggested a modified Maxwell kernel with three parameters ε_i. It includes velocity-dependent accommodation and — by simplification — also isotropic scattering due to thermal activation. The latter one enables to differentiate momentum and energy accommodation coefficients, which are identical in the original Maxwell kernel and thus could not describe experimental findings. Accommodation coefficients are introduced in the subsequent section.

2.8 Accommodation coefficients α

For $\varphi(\mathbf{v})$ being a function of the gas particle velocity, e.g. the momentum or the kinetic energy, the functional $\alpha(\varphi)$ called *accommodation coefficient* is defined by (Sharipov 2002)

$$\alpha(\varphi) = \frac{\int\limits_{-} \varphi(\tilde{\mathbf{v}})\ |\tilde{\mathbf{v}}\cdot\mathbf{n}|\ \sigma^{-}(\tilde{\mathbf{v}})\,\mathrm{d}^3\tilde{v} - \int\limits_{+} \varphi(\mathbf{v})\ |\mathbf{v}\cdot\mathbf{n}|\ \sigma^{+}(\mathbf{v})\,\mathrm{d}^3 v}{\int\limits_{-} \varphi(\tilde{\mathbf{v}})\ |\tilde{\mathbf{v}}\cdot\mathbf{n}|\ \sigma^{-}(\tilde{\mathbf{v}})\,\mathrm{d}^3\tilde{v} - \int\limits_{+} \varphi(\mathbf{v})\ |\mathbf{v}\cdot\mathbf{n}|\ \sigma^{(0)+}(\mathbf{v})\,\mathrm{d}^3 v} \tag{2.103}$$

$$\overset{(2.88)}{=} \frac{\int\limits_{-} \varphi(\tilde{\mathbf{v}})\ |\tilde{\mathbf{v}}\cdot\mathbf{n}|\ \sigma^{-}(\tilde{\mathbf{v}})\,\mathrm{d}^3\tilde{v} - \int\limits_{-} |\tilde{\mathbf{v}}\cdot\mathbf{n}|\ \sigma^{-}(\tilde{\mathbf{v}}) \int\limits_{+} \varphi(\mathbf{v})\ \tilde{P}(\tilde{\mathbf{v}}\to\mathbf{v},\varepsilon_i)\ \mathrm{d}^3 v\,\mathrm{d}^3\tilde{v}}{\int\limits_{-} \varphi(\tilde{\mathbf{v}})\ |\tilde{\mathbf{v}}\cdot\mathbf{n}|\ \sigma^{-}(\tilde{\mathbf{v}})\,\mathrm{d}^3\tilde{v} - \int\limits_{-} |\tilde{\mathbf{v}}\cdot\mathbf{n}|\ \sigma^{-}(\tilde{\mathbf{v}}) \int\limits_{+} \varphi(\mathbf{v})\ \tilde{P}_0(\tilde{\mathbf{v}}\to\mathbf{v})\ \mathrm{d}^3 v\,\mathrm{d}^3\tilde{v}}\,.$$

At first sight, this definition seems to be unhandy and unwieldy. But this definition makes it possible to analytically interpret the parameters physically which occur in the scattering kernels $\tilde{P}(\tilde{\mathbf{v}}\to\mathbf{v},\varepsilon_i)$ to be investigated.

There are several types of accommodation coefficients, each associated with the transfer process to be described: mass, evaporation, momentum (α_m), energy. For poly-atomic gases the latter ones also have partial energy accommodation coefficients for translational, vibrational and rotational energy defined (Goodman 1980). Energy accommodation coefficients are also called *thermal accommodation coefficients* (see sec. 2.8.1), which are of particular interest in the context of *fm* photophoresis. Because of that, hereafter I will only use α or 'accommodation coefficient' when addressing the thermal accommodation coefficient.

For instance, according to this definition of α, if $\tilde{P}(\tilde{\mathbf{v}}\to\mathbf{v},\varepsilon_i) = \tilde{P}_\mathrm{M}(\tilde{\mathbf{v}}\to\mathbf{v},\varepsilon)$, then $\alpha(\varphi) = \varepsilon$ for all functions $\varphi(\mathbf{v})$. Thus, in literature, when the Maxwell-Kernel is introduced, ε is not called a parameter but accommodation coefficient right away. Otherwise, this means, that for this kernel and the resulting distribution function $\sigma^+(\mathbf{v})$, e.g., the momentum and the energy accommodation coefficient are identical, which is usually not the case for other kernels. As experiments showed, energy accommodation coefficients have to be distinguished from the momentum accommodation coefficients to prevent ambiguities, as described in the previous section upon introduction of the CL kernel. The CL kernel is capable to do so. Once again, by making use of the definition of α, it becomes

clear why the CL kernel does not predict the momentum and energy accommodation coefficients to be identical. For $\varphi(\mathbf{v}) = m\, v_{\mathbf{t}_i}$ ($v_{\mathbf{t}_i}$ is the velocity parallel to one of the tangents $\mathbf{t}_1$ or $\mathbf{t}_2$) it is $\alpha(\varphi) = \varepsilon_1$, and for $\varphi(\mathbf{v}) = \frac{1}{2} m\, v_{\mathbf{n}}^2$ it is $\alpha(\varphi) = \varepsilon_2$ (Sharipov 2002). Subsequently, ε_1 is the tangential momentum accommodation coefficient, whereas ε_2 is the normal translational energy accommodation coefficient. Both, tangential momentum accommodation coefficient and tangential translational energy accommodation coefficient can also be related to each other. According to Lord (1991), the tangential kinetic energy accommodation coefficient is equal to $\varepsilon_1\,(2 - \varepsilon_1)$.

As in general, (2.103) also depends upon the distribution function of the impinging gas particles $\sigma^-(\mathbf{v})$, Cercignani (1988) gives another definition of α that restricts σ^- somewhat. With two functions $\varphi(\mathbf{v})$ and $\psi(\mathbf{v})$ he puts [3]

$$(\varphi\,,\,\psi)_{L_2} = \int\limits_{+} \varphi(\mathbf{v})\,\psi(\mathbf{v})\,\sigma^{(0)+}(\mathbf{v})\,|\mathbf{n}\cdot\mathbf{v}|\,\mathrm{d}^3 v \tag{2.104}$$

and uses the linear operator A [4]

$$A\,g = \frac{1}{\sigma^{(0)+}(\mathbf{v})\,|\mathbf{n}\cdot\mathbf{v}|} \int\limits_{+} P(-\tilde{\mathbf{v}} \to \mathbf{v})\,g(\tilde{\mathbf{v}})\,\sigma^{(0)+}(\tilde{\mathbf{v}})\,|\mathbf{n}\cdot\tilde{\mathbf{v}}|\,\mathrm{d}^3\tilde{v}\ . \tag{2.105}$$

If the reciprocity of P holds, A is symmetric with respect to the scalar product above $(A\,\varphi\,,\,\psi)_{L_2} = (\varphi\,,\,A\,\psi)_{L_2}$. With the help of the parity operators

$$R\,\varphi = \varphi(-\mathbf{v}) \tag{2.106a}$$

$$R_{\mathbf{n}}\,\varphi = \varphi(\mathbf{v} - 2\mathbf{n}(\mathbf{n}\cdot\mathbf{v})) \tag{2.106b}$$

$$R_{\mathbf{t}}\,\varphi = \varphi(-\mathbf{v} + 2\mathbf{n}(\mathbf{n}\cdot\mathbf{v}))\ , \tag{2.106c}$$

Cercignani (1988) restricts φ to $R_{\mathbf{n}}\,\varphi = \varphi$ and defines ψ by

$$\sigma^-(\mathbf{v}) = \sigma^{(0)+}[1 + R\,\psi] \qquad (\mathbf{n}\cdot\mathbf{v} < 0)\ , \tag{2.107}$$

and (2.103) reads

$$\alpha(\varphi,\psi) = \frac{(R\,\varphi\,,\,\psi)_{L_2} - (\varphi\,,\,A\,\psi)_{L_2}}{(R\,\varphi\,,\,\psi)_{L_2}} \tag{2.108a}$$

$$= 1 - \frac{(A\,\varphi\,,\,\psi)_{L_2}}{(R\,\varphi\,,\,\psi)_{L_2}} \tag{2.108b}$$

$$= 1 - \frac{(A\,\varphi\,,\,\psi)_{L_2}}{(R_{\mathbf{t}}\,\varphi\,,\,\psi)_{L_2}}\ . \tag{2.108c}$$

The accommodation coefficients have to be determined empirically by numerical simulations (e.g. Molecular Dynamics Simulations by Daun et al. (2009)) and experiments (e.g. cooling processes of aerosols by Daun et al. (2008)).

[3] in a Hilbert space with functions for $\mathbf{v}\cdot\mathbf{n} > 0$ and the measure $\sigma^{(0)+}(\mathbf{v})\,|\mathbf{n}\cdot\mathbf{v}|$ and the accompanying norm $\|f\|_{L_2} = \left(\int\limits_{+} |f(\mathbf{v})|^2\,\sigma^{(0)+}(\mathbf{v})\,|\mathbf{n}\cdot\mathbf{v}|\,\mathrm{d}^3 v\right)^{1/2}$

[4] A defines a contraction mapping in L_2

2.8.1 Thermal accommodation coefficient

Historically, Knudsen (1911) introduced the name accommodation coefficient[5] and formally defined it exactly as

$$\alpha = \frac{T^- - T^+}{T^- - T} \,. \tag{2.109}$$

I recapitulate, that T^- denotes the temperature of the gas particles striking the surface at temperature T and, T^+ the temperature of the gas particles leaving the surface after interaction. Historically, this gave reason to call it thermal accommodation coefficient as α was defined by temperatures. Smoluchowski von Smolan (1898a,b) confirmed the theory of Maxwell and Knudsen experimentally under certain conditions and von Smoluchowski (1911) used the same equation to describe heat transfer between two cylinders slotted into each other. As stated in the previous section, the parameter ε in the Maxwell's velocity distribution (2.91) for the scattered gas particles is also the (kinetic) energy accommodation coefficient.

The general case in a potential non-equilibrium state between gas and surface is (Goodman 1974)

$$\alpha_{\text{non-EQ}}\left(\overline{\mathcal{E}^-}, \mathcal{E}\right) = \frac{\overline{\mathcal{E}^-} - \overline{\mathcal{E}^+}}{\overline{\mathcal{E}^-} - \mathcal{E}} \,. \tag{2.110}$$

$\mathcal{E}$ is the energy of those scattered gas particles being in equilibrium with the surface at temperature T as (c_V denotes the molecular heat capacity of the gas)

$$\mathcal{E} = \left(c_V + \frac{1}{2}k_\text{B}\right) T \,. \tag{2.111}$$

The additional addend in the brackets arises from streaming corrections of the average kinetic energy of gas particles striking a surface, considering that faster gas particles hit the surface also faster than slower ones (see Goodman and Wachman (1976), p.24 and following pages). In the context of (2.110) the incident gas is not required to have a velocity distribution σ^- corresponding to a thermal equilibrium at temperature T^- (Goodman 1974). For this general case, Goodman and Wachman (1976) defines an effective temperature $T_\text{eff}^\pm$ for the incident and leaving gas particles by

$$\overline{\mathcal{E}^\pm} = \left(c_V + \frac{1}{2}k_\text{B}\right) T_\text{eff}^\pm \,, \tag{2.112}$$

modifying (2.110) to

$$\alpha_{\text{non-EQ}}\left(T_\text{eff}^-, T\right) = \frac{T_\text{eff}^- - T_\text{eff}^+}{T_\text{eff}^- - T} \,. \tag{2.113}$$

Of course, the relation (2.112) also holds for a gas in a thermodynamic equilibrium, and $T_\text{eff}^\pm$ becomes $T^\pm$.

The thermal accommodation coefficient for the special case of thermal equilibrium — using (2.110) — can be defined (Goodman 1974) as

$$\boxed{\alpha_\text{EQ}\left(T^-\right) = \lim_{T \to T^-} \frac{T^- - T^+}{T^- - T} \,.} \tag{2.114}$$

[5] "Akkommodationskoeffizient" on page 597 of Knudsen (1911)

In this definition, experiments showed, that it is always $0 \leq \alpha_{\mathrm{EQ}} \leq 1$. For the general definition of the thermal accommodation coefficient (2.110), i.e., the non-equilibrium case, this is only given, if the incident gas particles have an equilibrium velocity distribution (Goodman 1974).

The gas itself — apart from its temperature — obviously determines the value of α, thus it makes a difference if the thermal accommodation coefficient is measured for molecular oxygen with, e.g., quartz, or if the gas is a mixture of helium and molecular hydrogen. Furthermore, the solid material also takes responsibility for the value of α. Even the small-scale geometry of the surface accounts for α. Rohatschek (1984) emphasizes the point, that a rough surface gives opportunity for multiple gas particle collisions with the surface before leaving the suspended particle again, resulting in a higher thermal accommodation coefficient than for the same material with a smooth surface. In the same publication he discussed the assumption of $\Delta\alpha = 0.1$ for the different surface structures of the same material.

An example of empirical values for α is shown in Table 2.2. Goodman and Wachman (1967) proposed an equation in closed form to calculate the thermal accommodation coefficient for monatomic gas-solid systems depending on a few system parameters. The subjacent basis are experimental data and a lattice theory. Goodman (1968) refined the theory of the lattice vibrations, normal to the solid's surface. He discusses the theory on an n-dimensional lattice with several central and non-central spring constants, the n-dimensional continuum, the one-dimensional lattice with surface impurity as well as the n-dimensional lattice with surface impurities. A concise summary of theories is given in Goodman (1980) where the author discusses classical theories like the "Hard-Spheres Model", the "Lattice Model", a modified lattice model, "Flat-Surface Cubes Models" as well as "Statistical 'Heat-Bath' Approaches" alongside with quantum theory-based models, such as "Devonshire Theory and Before", the "Close-Coupling Formalism" and "First-Order One-Phonon" models and their "Unitary Corrections". He also gave a glance over experimental approaches and data. Daun et al. (2008) used laser-induced incandescence (LII) to deduce the thermal accommodation coefficient for aerosols (soot with monatomic/polyatomic gases). A nanosecond laser pulse heats up aerosols up to 3000-3600 K and α can be measured by the cool-down of the aerosols. They, e.g., found out, that for monatomic gases α increases with the atomic mass ratio of gas and surface atoms.

It can be concluded, that theories for the thermal accommodation coefficient are rather complex and the experimental determination is, too. Thus I did not intend to explain the physical background more thoroughly but just to give a short overview about where to find an introduction into the thermal accommodation coefficient in literature.

2.8.2 Conclusion: *fm*-photophoresis with thermal accommodation

With (2.114) it is

$$T^{+} = T^{-} + \alpha \left(T - T^{-} \right) . \tag{2.115}$$

Table 2.2: Thermal accommodation coefficients for different gases and materials (excerpt from Wachman (1962) and Hidy and Brock (1967)).

Gas	Solid	α
Air	machined bronze	$0.91 - 0.94$
Air	polished cast iron	$0.87 - 0.93$
Air	etched aluminum	$0.89 - 0.97$
Air	machined aluminum	$0.95 - 0.97$
O_2	bright Pt	0.808
Kr	Pt	$0.634 - 0.705$
Ar	Pt	$0.640 - 0.649$
N_2	W	0.35
He	Na	0.090
Ne	K	0.199
He	W	0.017

Inserting this into (2.87) yields the equation for the photophoretic force in the free molecular flow regime with thermal accommodation:

$$\boxed{\mathbf{F} = -\frac{1}{2} \oint_{\partial V} p \left(1 + \sqrt{1 + \alpha \left(\frac{T}{T^-} - 1 \right)} \right) \mathrm{d}\mathbf{A} \, .} \tag{2.116}$$

This equation is, e.g., used by Rohatschek (1995) and Loesche and Wurm (2012) and Loesche et al. (2013).

In chapter 3, (2.87) (and (2.116) as special case) will be discussed for spheres, e.g., with rotational symmetric temperature around the z-axis. For directed illumination and spheres larger than the wavelength of light this results in a force parallel or anti-parallel to the light. The general solution on chondrules is given, together with other solutions.

2.9 Systematization: types of photophoresis

2.9.1 $\Delta\alpha$- and ΔT-photophoresis

The accommodation coefficient α does not only depend on the two temperatures T^- and T, but also on the material, of course. Hence, even for a suspended particle at constant temperature which is different from the gas' temperature a net momentum transfer between particle and gas is possible, ensuing in the particle's motion. This can be achieved by strong local variations of α across the particle's surface. This is called $\Delta\alpha$-photophoresis. For the opposite case, i.e. $\alpha = \text{const}$ and a temperature gradient exists, this is called ΔT-photophoresis. Both cases are extremes, the usual photophoresis constitutes of both, variation of temperature and accommodation coefficient at each point of the particle's surface.

2.9.2 Longitudinal photophoresis: positive and negative

Photophoresis depends on the temperature distribution across a particle's surface. This temperature distribution itself depends on the absorption properties of the particle. As most particles are good absorbers to radiation, *positive photophoresis* prevails, which only describes the fact that the force acts in the same direction as the radiation. Parankiewicz (1918) made an early report about this phenomenon. Conversely, if the force points towards the radiation source, this is called *negative photophoresis*. This can happen for weakly or moderately absorbing particles with the size being in the same magnitude as the radiation wavelength (refraction inside of a prolate ellipsoid, Figure 2.6). For instance in focused radiation beams theses two types of photophoresis can alternate periodically (Rohatschek and Zulehner 1985), hence for the same particle the direction of the photophoretic force can be ambiguous. However, as the particle moves coincidentally with the direction of light, both types are subsumed to the so-called *longitudinal photophoresis*. Experimental work concerning negative longitudinal photophoresis was done by Lin (1985) and Wurm and Krauss (2008).

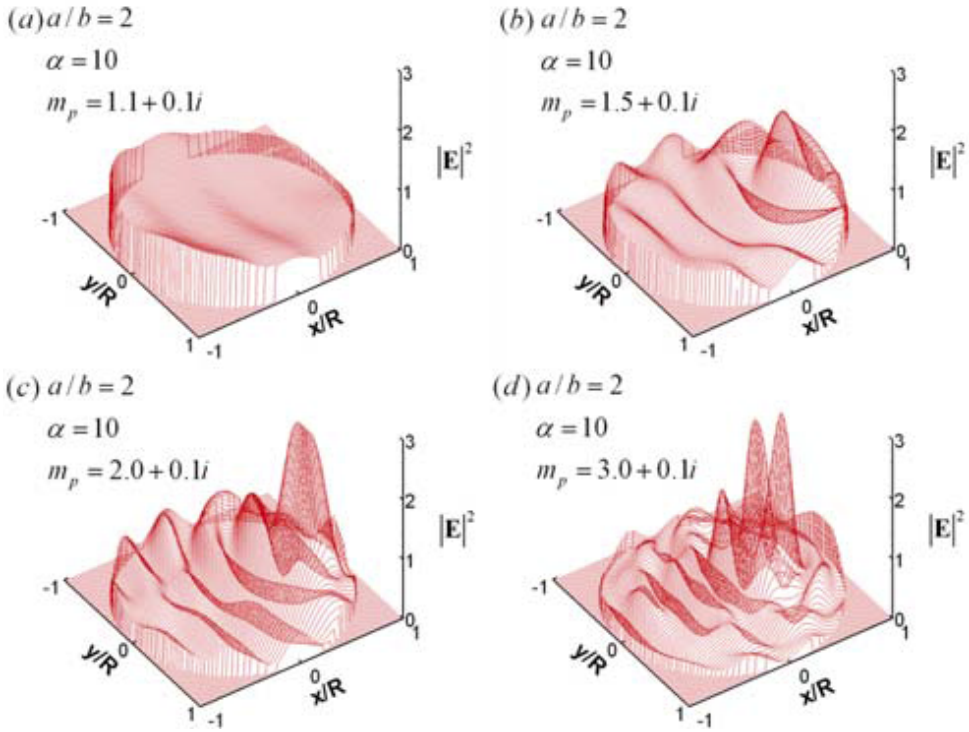

Figure 2.6: Example for the effect of the particle's refractivity on the heat source function q for different complex refraction indices m_p (taken from Li et al. (2010)). The authors use a size parameter $\alpha = 2\pi\frac{a}{\lambda_{\text{light}}}$ (only in this plot α has a different meaning, a, b denote the half-axes of the prolate spheroid). The light is incident towards $\mathbf{e}_x$. As the refractivity rises, the heat source function's highest impact is first at the backside of the particle and later moving towards it's center.

2.9.3 Other types of photophoresis

A free particle exerted to a photophoretic force will start moving, i.e. show translation and rotation (Figure 2.7). Like for longitudinal photophoresis, other occurring types were classified with respect to the particle's trajectories. Longitudinal photophoresis is mostly expected for sphere-like particles with at least small asymmetries. Rather non-spherical particles will show more complex moving patterns. Those can be simple or coiled helices, circles, oscillatory orbits, all oriented with respect to the direction of light. Those types are named *pure photophoresis* (Rohatschek 1984). Longitudinal photophoresis is a special case of pure photophoresis. Other types of photophoresis — unrelated to the direction of irradiation but related to an external field — are *magneto-* and *electro-photophoresis* (Ehrenhaft et al. 1930, 1931 and Ehrenhaft 1940 and Rohatschek and Horvath 2010) as well as *gravito-photophoresis* (Rohatschek 1956a). Rohatschek (1956b) also reported about the complex type of *light-gravito-photophoresis*. The different types are displayed in Figure 2.7. In this work I restrict myself to the effects of pure and longitudinal photophoresis. Therefore I refrain from explaining the mechanisms behind the other effects any further.

Desyatnikov et al. (2009) developed a theoretical approach for optical traps of carbon nanoclusters and calculated the longitudinal and transversal photophoretic force and compared them to experimental data. Shvedov et al. (2012) also reported about polarization-sensitive photophoresis. They point out that the polarization-dependent Fresnel reflection coefficients of a particle's material lead to different strengths of the photophoretic force as they showed by using differently polarized lasers to trap spherical particles.

2.10 Photophoresis on spheres for low Knudsen numbers

Yalamov et al. (1976b) derive an equation for the photophoretic force on large-size volatile aerosols, taking evaporation, diffusion slip and thermal slip into account. The problem is approached by solving hydrodynamic equations at small Reynolds numbers, the convective diffusion equation, and the stationary heat conduction equation (2.2) with constant heat conductivity and a source term q, that is calculated by means of Mie scattering (also see (3.51)) and expressed in terms of the asymmetry factor J_ν. The asymmetry factor will be defined later by (3.105) in sec. 3.3.2. The total force on the sphere is obtained by a pressure balance, similar to (2.39), where all the results from the preceding calculation steps in Yalamov et al. (1976b) enter.

For solid bodies, the force in the continuum regime is a direct result of thermal creep along a surface ∂V of a suspended particle, which occurs in case of a temperature gradient in the gas, which is tangential to ∂V (Reed 1977). This introduces a boundary condition for the fluid-dynamic description, i.e. the tangential (tangent $\mathbf{t}$) mass speed v_m of the gas caused by thermal creep (Brenner 2009)

$$(\mathbb{1} - \mathbf{n} \otimes \mathbf{n}) \cdot (\mathbf{v}_\mathrm{m} - \mathbf{v}) = \kappa\, \eta_\mathrm{kin}\, (\mathbb{1} - \mathbf{n} \otimes \mathbf{n}) \cdot \boldsymbol{\nabla} \log T_\mathrm{gas} \qquad \text{on } \partial V\ . \tag{2.117}$$

Here, $\mathbf{v}_\mathrm{m}$ is the mass velocity (Brenner 2005) in the continuity equation

$$\frac{\partial \rho}{\partial t} + \boldsymbol{\nabla} \cdot \rho \mathbf{v}_\mathrm{m} = 0\ , \tag{2.118}$$

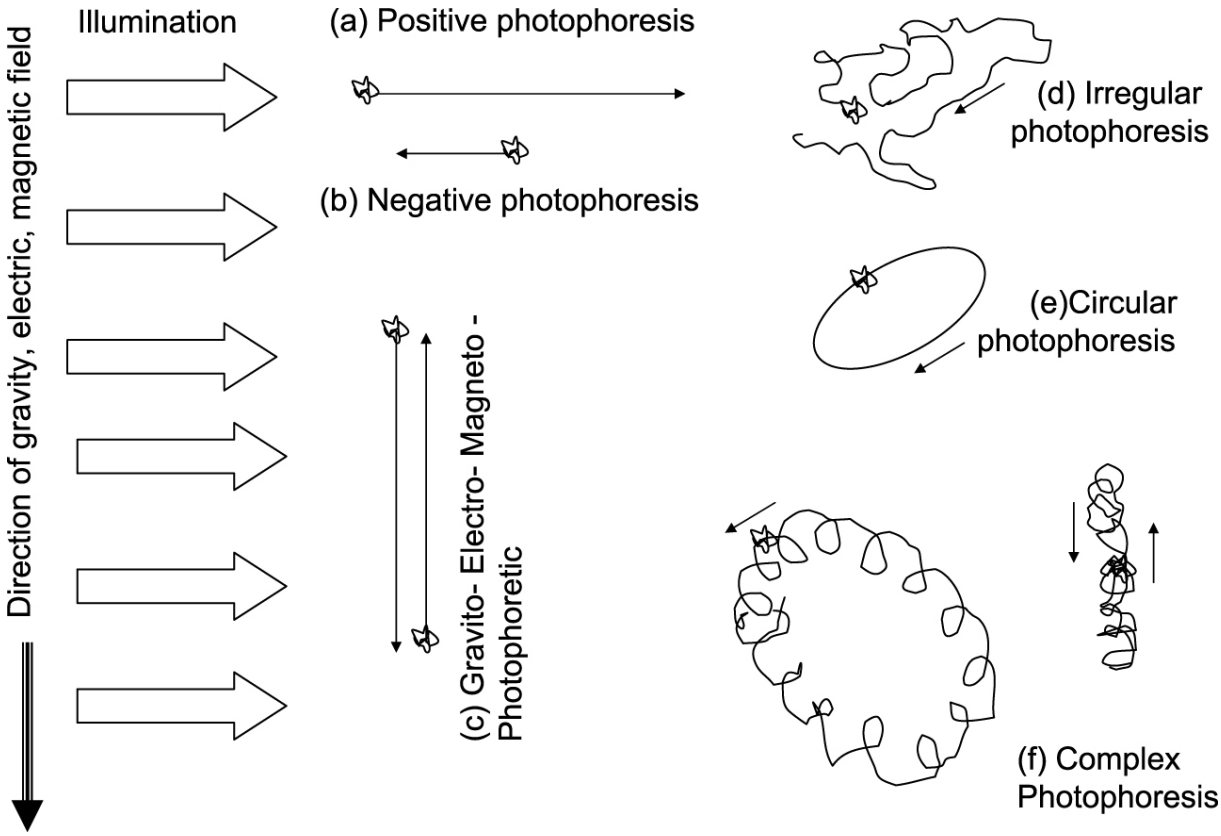

Figure 2.7: Different paths particles can follow when exerted to the photophoretic force (Horvath 2014).

$\mathbf{v}$ is the velocity of the surface ∂V, η_{kin} denotes the kinematic viscosity of the gas, and ρ and $T_{\text{gas}}|_{\partial V}$ the gas mass density and gas temperature at a point on ∂V, respectively. κ is the thermal slip coefficient. $(\mathbb{1} - \mathbf{n} \otimes \mathbf{n})$ is defined on ∂V and projects a vector into the respective tangent plane. Brenner (2009) points out, that various experts on molecular dynamics agree on the correctness of this equation for gases, even though the underlying gas-kinetic molecular theory is not rigorous but only semi-quantitative.

Instead of the vectorial form above, Sharipov (2004) and Reed (1977) use the equation in terms of total values and employ the dynamic viscosity of the gas

$$\eta_{\text{kin}} = \frac{\eta_{\text{dyn}}}{\rho} \tag{2.119}$$

instead, for describing the gas speed as

$$v_{\text{m}} = \kappa \, \frac{\eta_{\text{dyn}}}{\rho} \, \frac{\partial \log T_{\text{gas}}}{\partial \mathbf{t}} \bigg|_{\partial V} \, . \tag{2.120}$$

The original definition with $\kappa = \frac{3}{4}$ goes back to Maxwell (1879). Bakanov (1992) lists a couple of parameters a and b for different models which relate κ and the momentum accommodation coefficient α_{m} by the equation

$$\kappa(\alpha_{\text{m}}) = \frac{3}{4} \left(a + b \, \alpha_{\text{m}} \right) \, , \tag{2.121}$$

where a is close to 1 and b around 0.5, thus the thermal slip coefficient can be expected to obtain values between $0.75 \leq \kappa \leq 1.24$. Rohatschek (1995) assumes a thermal creep coefficient $\kappa = 1.14$ for $\alpha_m = 0.9$ and this value is also used by Loesche et al. (2014) and Hesse (2011). Ivchenko et al. (1993) also suggested a model with more accurate values for κ. One of the latest works is Ivchenko et al. (2007).

Brenner (2006, 2009) also proposed a nonmolecular thermodynamic theory of thermal creep, based on a hydrodynamic theory, that is valid for physiochemically and thermally inert solids suspended in not only gases but also fluids as

$$(\mathbb{1} - \mathbf{n} \otimes \mathbf{n}) \cdot (\mathbf{v}_m - \mathbf{v}) = D\,\gamma_{exp}\,(\mathbb{1} - \mathbf{n} \otimes \mathbf{n}) \cdot \boldsymbol{\nabla} T_{gas} \qquad \text{on } \partial V\ , \tag{2.122}$$

introducing the fluid's self-diffusion coefficient D and the fluid's thermal expansion coefficient (at constant pressure)

$$\gamma_{exp} = -\frac{1}{\rho}\left(\frac{\partial \rho}{\partial T}\right)_p\ . \tag{2.123}$$

In contrast to this equation, (2.117) is only valid for gases and no restrictions on the solids are imposed.

2.10.1 Longitudinal photophoresis in the slip-flow regime

Reed (1977) derives an equation for a *longitudinal* photophoretic force on a sphere with radius r_0 for low Knudsen numbers where thermal creep, frictional gas slippage and temperature jump are accounted for as a boundary condition at the gas-particle interface, providing higher accuracy than Hettner (1926). The illumination is directed along the z-axis. Navier-Stokes calculations with symmetry in ξ (the z-axis is the symmetry axis for the spherical system (ξ, ζ), as sketched in Figure 3.6) include a simplified form of (2.120) as

$$v_m = \kappa\,\frac{\eta_{dyn}}{\rho \overline{T_{gas}|_{\partial V}}}\,\frac{\partial T_{gas}}{\partial \mathbf{t}}\bigg|_{\partial V}\ , \tag{2.124}$$

and yield

$$\boxed{\mathbf{F}_{phot} = -4\pi\,\kappa\,\frac{\eta_{dyn}^2}{\rho\, r_0^2 \overline{T_{gas}|_{\partial V}}}\left(\frac{1}{1 + 3\gamma_m Kn}\right) B_1\,\mathbf{e}_z\ ,} \tag{2.125}$$

where B_1 is the first coefficient in the expansion of the gas/fluid temperature

$$T_{gas}(r, \zeta) = T_\infty + \sum_{\nu=0}^{\infty} B_\nu\, r^{-(\nu+1)}\, P_\nu(\cos\zeta)\ . \tag{2.126}$$

γ_m is a dimensionless factor which is related to the momentum accommodation coefficient α_m, with values around $1.00 \leq \gamma_m \leq 1.35$ and typically taking about 1.25. The drag/resistance force yields

$$\mathbf{F}_{drag} = -6\pi\,\eta_{dyn}\,r_0\,u\left(\frac{1 + 2\gamma_m Kn}{1 + 3\gamma_m Kn}\right)\mathbf{e}_z\ . \tag{2.127}$$

If both forces added up yield zero, the particle moves with speed u. Reed (1977) also calculated the coefficient B_1, with the heat transfer equations for the gas and particles

temperatures being Laplacians. The boundary conditions used are (with the effective irradiation εI and the index 'gas' distinguishing the gas variables from those for the sphere)

$$T_{\text{gas}} \xrightarrow{r\to\infty} T_\infty \tag{2.128a}$$

$$k\frac{\partial T}{\partial \mathbf{n}} = k_{\text{gas}}\frac{\partial T_{\text{gas}}}{\partial \mathbf{n}} + \varepsilon I\,\Theta(\pi/2-\zeta)\,\cos\zeta \qquad \text{at } \partial V \tag{2.128b}$$

$$T_{\text{gas}} - T = \gamma_{\text{t}}\, r_0\, Kn \frac{\partial T_{\text{gas}}}{\partial \mathbf{n}} \qquad \text{at } \partial V \tag{2.128c}$$

The last equation is the temperature jump condition at the gas-particle surface, where the thermal accommodation coefficient α (defined in sec. 2.8.1) defines the dimensionless constant as $\gamma_{\text{t}}(\alpha) \simeq \frac{15}{8}\left(\frac{1-\alpha}{\alpha}\right)$. With this problem definition B_1 yields

$$\boxed{B_1 = \frac{r_0^3\,\varepsilon\, I}{2k}\left(\frac{1}{1+2k_{\text{gas}}/k+2\gamma_{\text{t}}Kn}\right)\,.} \tag{2.129}$$

2.10.2 Longitudinal photophoresis in the continuum regime

Rohatschek (1995) uses Reed's rotationally symmetric solution (2.125) for the continuum regime ($Kn \to 0$) to describe the light absorption with the asymmetry factor J_1 (for definition see (3.105)) and source asymmetry $\mathbf{r}^*_{OQ}$, previously defined in (2.4). He assumes that the sphere's surface and the gas in a thin layer around the surface have the same temperature $T = T_{\text{gas}}|_{\partial V}$, which — together with (2.126) and the expansion of the surface temperature T

$$T(r=r_0,\zeta) = T_\infty + \sum_{\nu=0}^{\infty} A_\nu\, P_\nu(\cos\zeta) \tag{2.130}$$

— leads to the identification $A_\nu = B_\nu\, r_0^{-(\nu+1)}$, and thus

$$A_1 = B_1\, r_0^{-2}\,. \tag{2.131}$$

Subsequently, expressing (2.125) in terms of the surface temperature yields

$$\mathbf{F}_{\text{phot}} = -4\pi\,\kappa\,\frac{\eta_{\text{dyn}}^2}{\rho\, T_{\text{gas}}|_{\partial V}}\,A_1\,\mathbf{e}_z = -4\pi\,\kappa\,\frac{\eta_{\text{dyn}}^2\, R_{\text{gas}}}{p\, M_{\text{gas}}}\,A_1\,\mathbf{e}_z\,. \tag{2.132}$$

This enables to use the approximations for A_1 listed in sec. 3.3. Rohatschek (1995) states, that for good heat conductors, A_1 is pressure-independent and can also be expressed by the source asymmetry and the asymmetry factor, respectively:

$$A_1 = \frac{r_0\, J_1}{k} I \tag{2.133a}$$

$$A_1 = \frac{3}{4\pi\, r_0\, k} A_I\, r^*_{OQ}\, I\,. \tag{2.133b}$$

The derivation of (2.133a) can be found in sec. (3.3.2).

Pluchino (1983) conducted numerical calculations for spherical aerosols at low Knudsen numbers for a Lorenz-Mie source, used with the asymmetry factor J_1. In Rohatschek and

Zulehner (1985) and Zulehner and Rohatschek (1990, 1995) the authors concluded, that nonspherical particles can also be described to some extent by the usage of the source asymmetry. For opaque spheres of radius r_0, it is

$$J_1 = \frac{1}{2} \tag{2.134a}$$

$$A_I = \pi r_0^2 \tag{2.134b}$$

$$r^*_{OQ} = \frac{2}{3}\,, \tag{2.134c}$$

where $\frac{1}{2}$ is the most common used value of J_1, since calculating the source function — especially for non-spherical particles — is not an easy task. The derivation of this value can be found at the end of sec. 3.3.4.2.

An important result of (2.87) is, that the pressure dependence of the photophoretic force is linear in the *fm* regime (if the heat transfer process being responsible for the surface temperature is not pressure-dependent itself). Whereas, for the *co* regime this is not the case anymore, here, the force is essentially inversely proportional to the pressure, which is expressed by (2.132). This is referred to as Westphal's emperical law (Hettner 1928). Thus, it can be expected that for a certain pressure $\hat{p}$ in between the regimes *fm* and *co* the photophoretic force attains a maximum at $\hat{F}$.

2.11 Photophoresis in the transition regime

2.11.1 Interpolating between *fm*- and *co*-photophoresis

An empirical method is employed to describe the photophoretic force in the transition regime due to the complexity of transport processes in this regime. Rohatschek (1995) presented a phenomenological equation satisfying the linear proportionality of the force with the pressure in the *fm* regime and the inverse proportionality in the *co* regime by

$$\boxed{\frac{F}{\hat{F}} = \frac{2+\delta}{\frac{p}{\hat{p}} + \delta + \frac{\hat{p}}{p}}\,,} \tag{2.135}$$

with the free parameter δ to be adjusted along the experimental values (Figure 2.8). Hettner (1928) already suggested the same equation with $\delta = 0$, Rohatschek (1995) favors that, too, justifying it to be the best-fitting version of conducted experiments in the past, including work of other researchers such as Tong (1975) and Arnold and Amani (1980), whereas the experiments of Rosen and Orr (1964) with large carbon agglomerates do not obey above's law. Rohatschek (1985) gave evidence, that for large agglomerates, theories of ΔT-photophoresis cannot be applied because of the superposition of $\Delta\alpha$- and ΔT-photophoresis. One of the experimental results Rohatschek (1995) mentioned implied $\delta = 0.8$. The gas-kinetic calculations made by Chernyak and Beresnev (1993) suggested $\delta \simeq 1$, and for slip-flow theories, e.g. in Reed (1977) it is even $\delta \geq 2$, both fitting about 67% and less than 50%, respectively, of the experimental findings Rohatschek (1995) discussed.

Hettner (1928) suggested an interpolation (Equation (20) in the respective publication), which is

$$\boxed{\frac{1}{F} = \frac{1}{F^{\mathrm{co}}} + \frac{1}{F^{\mathrm{fm}}}\,.} \tag{2.136}$$

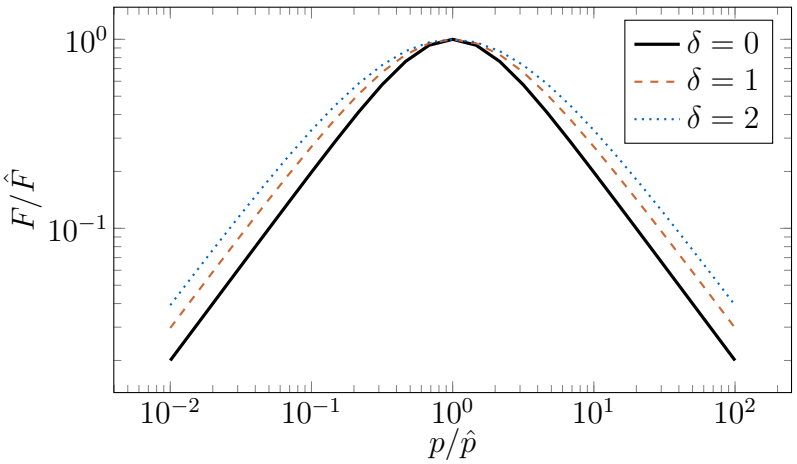

Figure 2.8: Interpolation between *fm* and *co* regimes.

2.11.2 Longitudinal photophoresis in the transition regime

To determine $\hat{F}$ for longitudinal photophoresis, a few more steps have to be made. The force in the *fm* and the *co* regimes is

$$\begin{aligned} F^{\mathrm{fm}} &\overset{(3.32)}{\simeq} \frac{\pi}{3}\,\alpha\,\frac{p}{\sqrt{T^{-}\overline{T^{+}}}}\,r_0^2\,A_1 \quad \text{(derivation in sec. 3.3)} \\ &\simeq 2\,\Xi\,\frac{p}{p^*}\,r_0\,\frac{\alpha}{2}\,A_1 \end{aligned} \tag{2.137a}$$

$$\begin{aligned} F^{\mathrm{co}} &\overset{(2.132)}{=} 4\pi\,\kappa\,\frac{\eta_{\mathrm{dyn}}^2}{\rho\,\overline{T_{\mathrm{gas}}|_{\partial V}}}\,A_1 \\ &= 2\,\Xi\,\frac{p^*}{p}\,r_0\,A_1\,, \end{aligned} \tag{2.137b}$$

where the equation

$$\overline{T_{\mathrm{gas}}|_{\partial V}} = \sqrt{T^{-}\overline{T^{+}}} \tag{2.138}$$

has to be met and the ideal gas equation $p = \frac{\rho}{M} R\,T_{\mathrm{gas}}$ used to express the mean gas speed (2.60a) as

$$\overline{v} = \sqrt{\frac{8p}{\pi\rho}}\,, \tag{2.139}$$

to eventually define the constant Ξ and characteristic pressure p^* along Rohatschek (1995) as

$$\Xi = \frac{\pi}{2}\sqrt{\frac{\pi}{3}\kappa}\,\frac{\overline{v}\,\eta_{\mathrm{dyn}}}{\overline{T_{\mathrm{gas}}|_{\partial V}}} \tag{2.140a}$$

$$p^* = \frac{1}{2}\sqrt{3\pi\kappa}\,\frac{\overline{v}\,\eta_{\mathrm{dyn}}}{r_0} = \frac{3}{\pi}\,\Xi\,\frac{\overline{T_{\mathrm{gas}}|_{\partial V}}}{r_0}\,. \tag{2.140b}$$

Hettner's interpolation equation (2.136) enables — together with the equations just above — to derive

$$\boxed{\begin{aligned} \hat{F} &= \Xi\sqrt{\frac{\alpha}{2}}\, r_0\, A_1 \qquad (2.141a)\\ \hat{p} &= \sqrt{\frac{2}{\alpha}}\, p^* \ . \qquad (2.141b) \end{aligned}}$$

Multiple coefficients A_1 are discussed in sec. 3.3. Also, (2.133b) can be taken, of course.

2.12 Knudsen layer model of pressure dependence for longitudinal ΔT- and $\Delta\alpha$-photophoresis on spheres

Another possible approach suggested by Rohatschek (1995) is to consider the temperature $T_{\mathrm{gas}}|_{\partial V}$ of the thin gas shell (Knudsen layer) around a suspended sphere with radius r_0 to describe F^{fm} and F^{co} instead of the surface temperature T. As $T_{\mathrm{gas}}|_{\partial V}$ covers the whole interaction of the gaseous medium with the particle, ΔT- and $\Delta\alpha$-photophoresis is described simultaneously.

In the *fm* regime, there is no Knudsen layer, hence there is a transient condition the gas temperature has to meet when changing the regime. If the temperature of the Knudsen layer equals the following relation of the temperatures T^+ and T^- in the *fm* regime (Rohatschek 1995)

$$T_{\mathrm{gas}}|_{\partial V} \equiv T_{\mathrm{gas}}(r_0, \zeta) \simeq \sqrt{T^+\, T^-}\ , \qquad (2.142)$$

the integral equation (2.87) for the *fm* photophoresis can be expressed in terms of the Knudsen layer temperature $T_{\mathrm{gas}}|_{\partial V}$ instead of the surface temperature T ($\mathrm{d}A = \sin\zeta\, \mathrm{d}\xi\, \mathrm{d}\zeta$)

$$\mathbf{F}_{\mathrm{phot}} = -\frac{1}{2}\int_{\partial V} \mathrm{d}\mathbf{A}\, p \left(1 + \frac{T_{\mathrm{gas}}(r_0, \zeta)}{T^-}\right)\ . \qquad (2.143)$$

Now, an expansion of $T_{\mathrm{gas}}|_{\partial V}$ into a Legendre series

$$T_{\mathrm{gas}}(r = r_0, \zeta) = T_\infty + \sum_{\nu=0}^{\infty} \tilde{B}_\nu\, P_\nu(\cos\zeta)\ , \qquad (2.144)$$

similar to the one just used before for $T_{\mathrm{gas}}(r, \zeta)$ in (2.126) (see sec. 2.10) — only omitting the $r^{-(\nu+1)}$ in (2.126) — is inserted into the integral above, and the usage of the Legendre polynomials' orthogonality relation (A.11c) yields (2.145a), with an additional factor of 2, compared to the respective equation in the section before.

By analogy with sec. 2.11.2, the two extreme Knudsen number photophoretic forces can be expressed in terms of Ξ and p^* as

$$F^{\mathrm{fm}} = \frac{2\pi}{3}\,\frac{p}{T^-}\,r_0^2\,\tilde{B}_1 \tag{2.145a}$$

$$= 2\,\Xi\,\frac{p}{p^*}\,r_0\,\tilde{B}_1 \tag{2.145b}$$

$$F^{\mathrm{co}} = 4\pi\,\kappa\,\frac{\eta^2}{\rho\,\overline{T_{\mathrm{gas}}|_{\partial V}}}\,\tilde{B}_1$$

$$= 2\,\Xi\,\frac{p^*}{p}\,r_0\,\tilde{B}_1\ . \tag{2.145c}$$

For the case, that $\overline{T_{\mathrm{gas}}|_{\partial V}} = T^-$, it is possible to use (2.135) in order to define the *photophoresis function* (Rohatschek 1995)

$$\Phi(p) = \Xi\,\frac{2}{\frac{p}{p^*} + \frac{p^*}{p}}\,r_0 \tag{2.146a}$$

to interpolate between the regimes, so that the photophoretic force can be described as

$$F(p) = \Phi(p)\,\tilde{B}_1(p)\ . \tag{2.146b}$$

Finally, the expansion coefficient of the Knudsen layer temperature $\tilde{B}_1$ has to be found. In the following two subsection, analytical equations for pure ΔT- and $\Delta\alpha$-photophoresis are given for $\tilde{B}_1$.

2.12.1 Pure ΔT-photophoresis

Comparing (2.137a) and (2.137b) with (2.145b) and (2.145c), respectively, yields the identifications

$$\tilde{B}_1^{\mathrm{fm}} = \frac{\alpha}{2}A_1 \tag{2.147a}$$

$$\tilde{B}_1^{\mathrm{co}} = A_1\ , \tag{2.147b}$$

which enabled Rohatschek (1995) to find an interpolation for $\tilde{B}_1(p)$ as

$$\tilde{B}_1 = \frac{\frac{p}{p^*}\frac{1}{\tilde{B}_1^{\mathrm{co}}} + \frac{p^*}{p}\frac{1}{\tilde{B}_1^{\mathrm{fm}}}}{\frac{p}{p^*} + \frac{p^*}{p}}\ . \tag{2.147c}$$

2.12.2 Pure $\Delta\alpha$-photophoresis

Works on pure $\Delta\alpha$-photophoresis are scarcely found in literature. Rohatschek (1995) used the ansatz (2.146) and presented a function for $\tilde{B}_1(p)$ for pure $\Delta\alpha$-photophoresis (T =const. across the sphere's surface) in the special case of a sphere having two accommodation coefficients, each on one hemisphere, i.e. α_1 and α_2. $\tilde{B}_1$ is the first expansion coefficient of the Knudsen layer temperature as (2.144). The result is (T is still the surface temperature)

$$\tilde{B}_1 = \frac{3}{8}\,\frac{1}{1+\mu\frac{p}{p^*}}\,A_0\,|\alpha_1 - \alpha_2|\ , \tag{2.148a}$$

with the variable μ defined as

$$\mu = \sqrt{\frac{3\kappa}{\pi}} \frac{\frac{c_p}{c_v} + 1}{9\frac{c_p}{c_v} - 5} (\alpha_1 + \alpha_2) \tag{2.148b}$$

and A_0 denoting an expansion coefficient of the surface temperature in (2.130). If the accommodation coefficient does not change across the surface as environmental variables change, the $\Delta\alpha$-photophoresis is body-fixed.

3

SOLUTIONS IN THE *fm* REGIME

In most analytic treatments on ΔT-photophoresis it is only dealt with longitudinal photophoresis on spheres. There, linear approximations of the integral equation (2.87)

$$\mathbf{F}_{\text{phot}} = -\frac{1}{2}\int_{\partial V} \mathrm{d}\mathbf{A}\, p \left(1 + \sqrt{\frac{T^+}{T^-}}\right)$$

with rotational symmetry in the direction of light $T^+(T) = T^+(T(\zeta))$ are used. Rohatschek and Zulehner (1985) suggested a linear analytical model on convex particles, but generally literature for nonspherical particle is scarce. As the experimental works of Prof. Wurm's group are about photophoresis on real chondrules — a NURBS model of one of them is shown in Figure 3.1 —, I found it is worthwhile to try to find the general solution of (2.87) for nonspherical particles to be able to describe pure photophoresis by all three components, and not just the force component in the direction of illumination, as only for a sphere it can be assumed that for most normal cases of directional heating the ensuing photophoretic force is essentially parallel to the direction of irradiation. For non-spherical bodies (e.g. ellipsoids) this is obviously not the case.

Another motivation was triggered by a result in Loesche et al. (2013) (for detailed description see sec. 4.2), that there is a correlation between an expectation value of the photophoretic strength on real chondrules and the radius of the respective volume-equivalent sphere. The aim was to use the general solution (3.20) of the integral equation (2.87) for arbitrary star-convex (see Figure 3.4) particles, such as Figure 3.1, in order to understand this correlation and to check, if this can be mathematically understood. In fact, the general solution could explain the correlation, whilst the behavior of the temperature part was obtained from numerical studies (see sec. 4.2.4.3). Special cases for spheres are considered and discussed in sec. 3.1.2.3 and following pages. In sec. 3.3, linear approximations from literature and a newly found one are discussed and evaluated by their quality.

3.1 Pure *fm*-photophoresis in Hilbert space: general solution of the integral equation (2.87) for star-convex bodies capable of comprising ΔT- and $\Delta\alpha$-photophoresis

A mathematical description of the particle boundary is used, enabling to derive the theoretically exact solution, which is practically a solution of arbitrary order. The knowledge of the geometry is imperative, and possible to attain by, e.g., X-ray tomography. The model can cover ΔT- and $\Delta\alpha$-photophoresis — or any other surface-gas interaction —, provided the particle's surface temperature $T(\mathbf{r})$ and its thermal accommodation coefficient $\alpha(\mathbf{r})$ are known. For all further calculations and derivations, the spherical coordinate system (r, ξ, ζ) shown in Figure 2.1 is used here.

It is expected that the general solution can help understanding the deviation of the force direction from the line of directed illumination for nonspherical particles, as found in experiments.

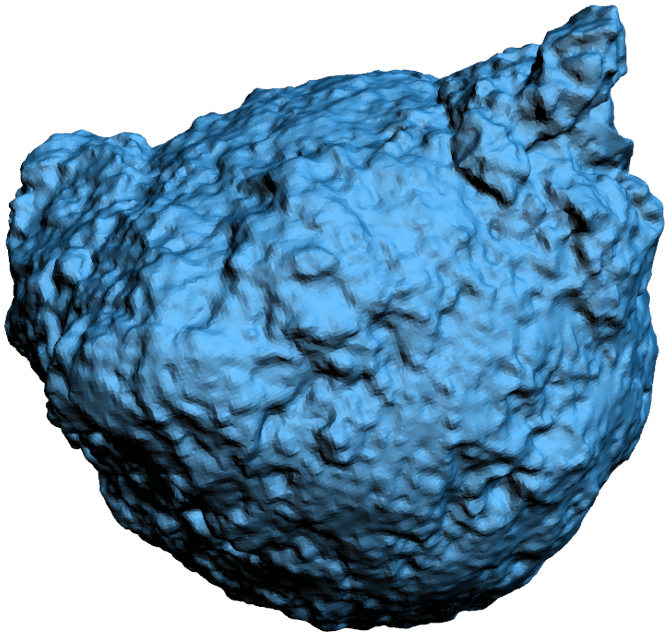

Figure 3.1: Example of a particle having a not-perfect spherical shape (from Loesche et al. (2014)). The domain can be assumed to be quite star-convex. Minor overhangs such as introduced by parts of the outrigger in the right upper corner will introduce a small error, but are not expected to be very common and rather a result of alternation.

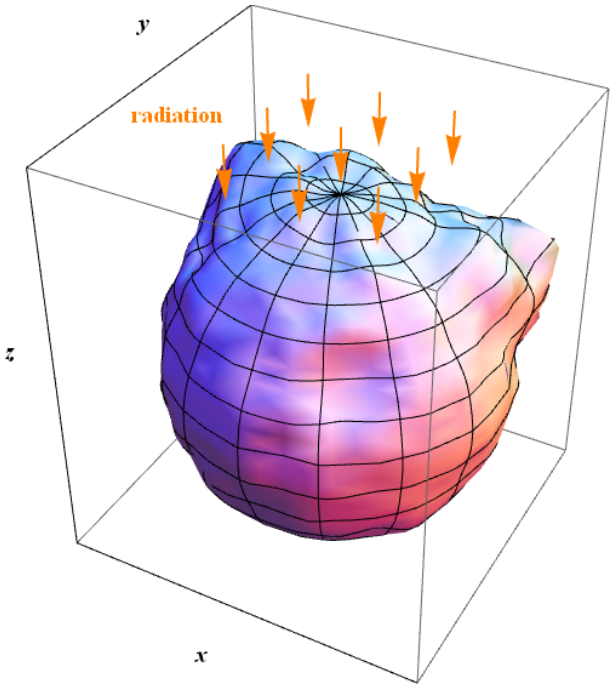

Figure 3.2: Spherical harmonic representation of the particle in Figure 3.1.

3.1.1 Problem description

Only for spheres (with radius r_0), normal vector

$$\mathbf{n}_S(\xi,\zeta) = \begin{pmatrix} \cos\xi\sin\zeta \\ \sin\xi\sin\zeta \\ \cos\zeta \end{pmatrix} \tag{A.1}$$

and parametrization vector (that is the vector function which describes all boundary points by a given parametrization)

$$\mathbf{r}_S : \ (\xi,\zeta) \to (x,y,z) = \mathbf{r} \tag{3.1a}$$

$$\mathbf{r}_S(\xi,\zeta) = r_0 \begin{pmatrix} \cos\xi\sin\zeta \\ \sin\xi\sin\zeta \\ \cos\zeta \end{pmatrix} \tag{3.1b}$$

are always parallel, whilst for an irregular (closed) surface this cannot be expected anymore. Thus, for homogeneous spheres, a rotational-symmetric temperature with respect to the direction of illumination will always result in longitudinal photophoresis.

For those irregular surfaces the normal vector and a parametrization need to be found, eventually enabling to use surface integrals, so that (2.87) can be solved analytically.

3.1.1.1 Definition of tangential space and surface integrals on it

Corresponding to the previous situation, $\partial\Omega = \{\mathbf{\Omega}(\xi,\zeta) \,|\, (\xi,\zeta) \in \Pi\} \subset \mathbb{R}^3$ is the surface of a particle, e.g., a chondrule in Figure 3.1, with the parametrization

$$\mathbf{\Omega} : \ (\xi,\zeta) \to (x,y,z) = \mathbf{r} \tag{3.2}$$

based on the parameter set Π. For high-symmetry particles, an explicit parametrization can be found, however, usually it is not possible. In this general case an atlas of (possibly partially overlapping) maps might be found instead (one map describes a "patch" of the surface with a 'reverse parametrization' $(x, y, z) \to (\xi, \zeta)$, and the integrand has to be partioned in several parts, from which each is addressed by a map, what is called the 'partition of unity' (Oloff 2010)) allowing the usage of line- and surface integrals on manifolds. The term manifold comprises curved lines and surfaces in the three-dimensional Euclidean space (Oloff 2010).

Even though for chondrules there will not be any explicit parametrization, there is still another way to describe the surface with a single parametrization by means of arbitrary approximations, which will be elaborated in sec. 3.1.1.2. At first, before a surface integral can be set up, the surface's tangential space has to be known, spun up by $\boldsymbol{\partial_\xi}$ and $\boldsymbol{\partial_\zeta}$.

$$\boldsymbol{\partial_\xi} := \partial_\xi \boldsymbol{\Omega} \qquad \text{and} \qquad \boldsymbol{\partial_\zeta} := \partial_\zeta \boldsymbol{\Omega} \tag{3.3}$$

are the two tangential vectors of the surface with respect to the parametrization $\boldsymbol{\Omega}(\xi, \zeta)$ (Oloff 2010). In Cartesian coordinates, they have the components $\frac{\partial \Omega_x}{\partial \xi}$, $\frac{\partial \Omega_y}{\partial \xi}$, $\frac{\partial \Omega_z}{\partial \xi}$ and $\frac{\partial \Omega_x}{\partial \zeta}$, $\frac{\partial \Omega_y}{\partial \zeta}$, $\frac{\partial \Omega_z}{\partial \zeta}$, respectively. A sketch of a possible setting is shown in Figure 3.3.

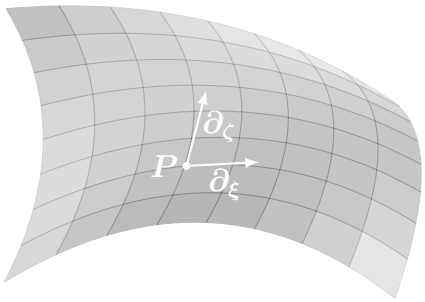

Figure 3.3: Both tangential vectors at point $P = P(\xi_0, \zeta_0)$ of a surface patch.

For a function f on $\partial\Omega$, a surface integral would look like

$$\int_{\partial\Omega} f \, \mathrm{d}\sigma = \iint_{\Pi} f\left(\mathbf{r}(\xi, \zeta)\right) \sqrt{|\det \underline{\mathbf{g}}|} \, \mathrm{d}\xi \, \mathrm{d}\zeta \tag{3.4a}$$

with the metric

$$\underline{\mathbf{g}} = \begin{pmatrix} \boldsymbol{\partial_\xi} \cdot \boldsymbol{\partial_\xi} & \boldsymbol{\partial_\zeta} \cdot \boldsymbol{\partial_\xi} \\ \boldsymbol{\partial_\xi} \cdot \boldsymbol{\partial_\zeta} & \boldsymbol{\partial_\zeta} \cdot \boldsymbol{\partial_\zeta} \end{pmatrix} \tag{3.4b}$$

and the ensuing measure $\sqrt{|\det \underline{\mathbf{g}}|}$.

In $\mathbb{R}^3$, the measure can also be expressed by the cross product of the two tangent vectors as

$$\sqrt{|\det \underline{\mathbf{g}}|} = \|\boldsymbol{\partial_\zeta} \times \boldsymbol{\partial_\xi}\|_2 \tag{3.5}$$

and used in (3.4a) instead, since the total of $\boldsymbol{\partial_\zeta} \times \boldsymbol{\partial_\xi}$ is the area of the respective surface patch at (ξ, ζ). $\|\cdot\|_2$ denotes the Euclidean norm (see (0.1)).

The integral equation (2.87) contains the (outward-pointing) normal vector of the surface $\partial\Omega$, which can be expressed by the cross product of the two tangent vectors[1]

$$\mathbf{n}_{\partial\Omega} = \frac{\boldsymbol{\partial_\zeta} \times \boldsymbol{\partial_\xi}}{\|\boldsymbol{\partial_\zeta} \times \boldsymbol{\partial_\xi}\|_2} \,. \tag{3.6}$$

[1] $\mathbf{a} \times \mathbf{b} \perp \mathbf{a}, \mathbf{b}$.

Now, with the surface integrals at hand, the subsequent form of the photophoretic force on such a particle at temperature $T(\mathbf{\Omega})$ (e.g. upon irradiation) has the form

$$\mathbf{F}_{\text{phot}} \overset{(2.87)}{=} -\frac{1}{2} \iint_{\Pi} p \left(1 + \sqrt{\frac{T^+}{T^-}}\right) \|\boldsymbol{\partial}_{\boldsymbol{\zeta}} \times \boldsymbol{\partial}_{\boldsymbol{\xi}}\|_2 \, \mathbf{n}_{\partial\Omega}(\xi, \zeta) \, \mathrm{d}\xi \, \mathrm{d}\zeta \tag{3.7a}$$

$$\overset{(3.6)}{=} -\frac{1}{2} \iint_{\Pi} p \left(1 + \sqrt{\frac{T^+}{T^-}}\right) \boldsymbol{\partial}_{\boldsymbol{\zeta}} \times \boldsymbol{\partial}_{\boldsymbol{\xi}} \, \mathrm{d}\xi \, \mathrm{d}\zeta \, . \tag{3.7b}$$

T^+ can still be assumed as (2.114) $T^+ = T^- + \alpha\,(T - T^-)$, with $0 < \alpha \leq 1$ being the thermal accommodation coefficient, previously defined in sec. 2.8.1, or any other surface-gas interaction. The usage of the parallelepiped/cross product $\boldsymbol{\partial}_{\boldsymbol{\zeta}} \times \boldsymbol{\partial}_{\boldsymbol{\xi}}$ to express the measure makes sense insofar, that the surface normal (3.6) also has it in the denominator, both canceling in (3.7a) and yielding (3.7b).

It has to be noted that p, T, and α are functions of $\mathbf{r} \in \mathbb{R}^3$ as

$$p = p\,(\mathbf{r})\,, \quad \alpha = \alpha\,(\mathbf{r})\,, \quad T = T\,(\mathbf{r}) \ . \tag{3.8}$$

3.1.1.2 Parametrization of the chondrule surface $\partial\Omega$

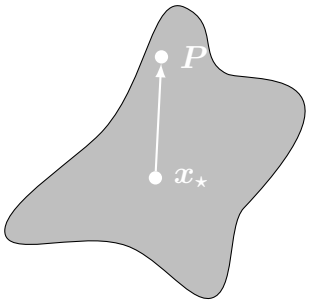

Figure 3.4: A domain is star-convex/star-like concerning a point $x_\star$ if the direct line to all other points of the domain lies within the domain itself, so that $x_\star$ can "see" all other points. $x_\star$ is the so-called star center.

If the particle is required to have a **star-convex domain** (also see Figure 3.4), all angles $[0, 2\pi] \times [0, \pi]$ — starting from the star center $\mathbf{r}_\star$ — can be mapped onto a corresponding surface point $\mathbf{r} \in \partial\Omega$. Thus a distance or 'radius' function

$$\Omega(\xi, \zeta) = \|\mathbf{r} - \mathbf{r}_\star\|_2 \qquad \mathbf{r} \in \partial\Omega, \ (\xi, \zeta) \in \Pi = [0, 2\pi] \times [0, \pi] \tag{3.9a}$$

can be defined. Here, $\mathbf{r}_\star$ can be, e.g., the center of shape or mass, depending on the particle's geometry. Star-convex particles exclude those with voids, tunnels, and overhangs etc. However, this weak constraint on the geometry should be satisfied by most free particles, as any grinding process will most likely 'polish' the surfaces insofar that not any overhanging region will remain after a certain time. Additionally, in space, any liquid that is solidifying will most likely retain its quasi-spherical shape, which particularly can be expected for chondrules. Figure 3.1 seems to be quite star-convex, but for many chondrules extracted from chondrites overhangs and voids can be found which contradict the requirements on the geometry. As chondrules might undergo physical deformation when embedded in a parent body, e.g. caused by shocks or temperature alternation, they do not resemble their pristine shape anymore. Given the chance they will somehow leave the

parent body again (by destruction of the latter one), possible grinding processes or dust deposition will round off the surface again and the particle will meet the aforementioned requirement again for the description by this model.

As the distance function has been defined, the angular mapping from $\mathbf{r}_\star$ to the surface can be described by means of $\mathbf{n}_\mathrm{S}$, and the full parametrization of the chondrule's surface reads

$$\boldsymbol{\Omega} = \mathbf{n}_\mathrm{S}\,\Omega\,. \tag{3.9b}$$

The radius function $\Omega(\xi,\zeta)$ is responsible for deforming the unit sphere, parameterized by $\mathbf{n}_\mathrm{S}(\xi,\zeta)$. For a triaxial ellipsoid, it is possible to get an analytic expression for $\Omega(\xi,\zeta)$ (see (4.12c) and Figure 4.23 in sec. 4.2.4.3). Though, retrieving $\Omega(\xi,\zeta)$ analytically for general star-convex bodies is usually impossible. In any of the two cases, $\Omega(\xi,\zeta)$ can be expanded into a series of orthogonal functions instead, e.g., spherical harmonics $Y_\nu^\mu\,(\xi,\zeta)$, the latter ones are defined on the unit sphere. This eventually allows to solve surface integral easily by collapsing them into sums (later). However, a series of spherical harmonics

$$\Omega = \sum_{\substack{\nu\geq 0\\ -\nu\leq\mu\leq\nu}} \omega_{\nu\mu}^{(1)}\,Y_\nu^\mu \tag{3.9c}$$

eventually allows a full description of the chondrule's surface with only one parametrization. Such an example is shown in Figure 3.2, a degree 25 expansion ($0\leq\nu\leq 25$) of the particle shown in Figure 3.1. In the following, the surface integral (3.7b) has to be set up for the ansatz above.

For the parametrization (3.9b), the partials can be found in (B.1). Their cross product has the form

$$\boldsymbol{\partial_\zeta}\times\boldsymbol{\partial_\xi} = \Omega\begin{pmatrix} \partial_\xi\Omega\sin\xi+\sin\zeta\cos\xi\,(\Omega\sin\zeta-\partial_\zeta\Omega\cos\zeta)\\ \sin\zeta\sin\xi\,(\Omega\sin\zeta-\partial_\zeta\Omega\cos\zeta)-\partial_\xi\Omega\cos\xi\\ \sin\zeta\,(\partial_\zeta\Omega\sin\zeta+\Omega\cos\zeta)\end{pmatrix} \tag{3.10a}$$

and

$$\|\boldsymbol{\partial_\zeta}\times\boldsymbol{\partial_\xi}\|_2 = \Omega\sqrt{(\partial_\xi\Omega)^2+\sin^2\zeta\,\left((\partial_\zeta\Omega)^2+\Omega^2\right)}\,. \tag{3.10b}$$

This can no further be analyzed, hence the cross product is carried out by applying the chain rule in each partials in pairs

$$\boldsymbol{\partial_\zeta}\times\boldsymbol{\partial_\xi} = \underbrace{\mathbf{n}_\mathrm{S}\frac{\partial\Omega}{\partial\zeta}\times\mathbf{n}_\mathrm{S}\frac{\partial\Omega}{\partial\xi}}_{\equiv 0} + \underbrace{\mathbf{n}_\mathrm{S}\frac{\partial\Omega}{\partial\zeta}\times\Omega\frac{\partial\mathbf{n}_\mathrm{S}}{\partial\xi}}_{:=\mathbf{g}^{(\zeta)}} + \underbrace{\Omega\frac{\partial\mathbf{n}_\mathrm{S}}{\partial\zeta}\times\mathbf{n}_\mathrm{S}\frac{\partial\Omega}{\partial\xi}}_{:=\mathbf{g}^{(\xi)}} + \underbrace{\Omega\frac{\partial\mathbf{n}_\mathrm{S}}{\partial\zeta}\times\Omega\frac{\partial\mathbf{n}_\mathrm{S}}{\partial\xi}}_{:=\mathbf{g}^{(0)}} \tag{3.11a}$$

$$= \mathbf{g}^{(\zeta)}+\mathbf{g}^{(\xi)}+\mathbf{g}^{(0)}\,, \tag{3.11b}$$

obtaining a much more flexible representation which is useful for the subsequent considerations. The three addends of the cross product consist of the derivative-free function $\mathbf{g}^{(0)}$, and the two functions $\mathbf{g}^{(\xi)}$ and $\mathbf{g}^{(\zeta)}$, containing derivatives of both the squared radius

function Ω^2 and the unit sphere's normal $\mathbf{n}_\mathrm{S}$ with respect to ξ and ζ, respectively (marked red)

$$\mathbf{g}^{(\zeta)} = \Omega\,\partial_\zeta\Omega\,\sin\zeta \begin{pmatrix} -\cos\xi\cos\zeta \\ -\sin\xi\cos\zeta \\ \sin\zeta \end{pmatrix} = -\frac{1}{2}\sin\zeta\,\partial_\zeta\Omega^2\,\partial_\zeta\mathbf{n}_\mathrm{S}\;, \tag{3.11c}$$

$$\mathbf{g}^{(\xi)} = \Omega\,\partial_\xi\Omega \begin{pmatrix} \sin\xi \\ -\cos\xi \\ 0 \end{pmatrix} = -\frac{1}{2\sin\zeta}\,\partial_\xi\Omega^2\,\partial_\xi\mathbf{n}_\mathrm{S}\;, \tag{3.11d}$$

$$\mathbf{g}^{(0)} = \Omega^2\sin\zeta\,\mathbf{n}_\mathrm{S}\;. \tag{3.11e}$$

The simpler structure of (3.11) — compared to (3.10a) — is striking. Hence, splitting up the cross product into three addends helps evaluating the whole integral.

3.1.1.3 Preliminary consideration

Now the integrand has to be simplified. With w.l.o.g. p =const. in close vicinity to the particle, the ansatz

$$\boxed{\tau^{(n)} := \frac{\sqrt{T^+}}{\Omega^{n-2}}\,, \qquad n = 2, 3, \ldots} \tag{3.12a}$$

and the constant

$$c := -\frac{1}{2}\frac{p}{\sqrt{T^-}}\;. \tag{3.12b}$$

simplify (3.7b) to

$$\boxed{\mathbf{F}_\mathrm{phot} = c\iint \tau^{(2)}\,\boldsymbol{\partial_\zeta}\times\boldsymbol{\partial_\xi}\,\mathrm{d}\xi\,\mathrm{d}\zeta\;,} \tag{3.12c}$$

with $\tau = \tau(\mathbf{r})$. The integer number n is 2 in most cases. For larger values, this is nothing but inserting a $1 = \Omega^{-n}\,\Omega^n$ into the integrand and would result in different expansion coefficients only. However, for later purposes, the obtained solution is needed for $n = 2$ and especially $n = 3$. Thus, $\tau^{(3)}$ is the square root of the scattered gas particles' temperature divided by the radius function $\tau^{(3)} = \frac{\sqrt{T^+}}{\Omega}$. With thermal accommodation (2.114) it is $\tau^{(2)} = \sqrt{T^- + \alpha\,(T - T^-)}$, hence the definition of τ in (3.12a) makes it possible to describe both, ΔT and $\Delta\alpha$-photophoresis at the same time, as the dependencies read $\tau(\mathbf{r}) = \tau\,(T(\mathbf{r}), \alpha(\mathbf{r}))$.

Using (3.11), the integral (3.12c) can be split up into three separate integrals

$$\mathbf{F}_\mathrm{phot} = c\iint \tau^{(2)}\,\left(\mathbf{g}^{(0)} + \mathbf{g}^{(\xi)} + \mathbf{g}^{(\zeta)}\right)\,\mathrm{d}\xi\,\mathrm{d}\zeta \tag{3.13a}$$

$$= \underbrace{c\iint \tau^{(n)}\,\Omega^n\,\mathbf{n}_\mathrm{S}\,\sin\zeta\,\mathrm{d}\xi\,\mathrm{d}\zeta}_{\mathbf{F}_\mathrm{phot}\text{for sphere of radius }\Omega = r = \text{const.}} -$$

$$-\frac{c}{n}\iint \tau^{(n)}\,\partial_\xi\Omega^n\,\partial_\xi\mathbf{n}_\mathrm{S}\,\frac{1}{\sin\zeta}\,\mathrm{d}\xi\,\mathrm{d}\zeta -$$

$$-\frac{c}{n}\iint \tau^{(n)}\,\partial_\zeta\Omega^n\,\partial_\zeta\mathbf{n}_\mathrm{S}\,\sin\zeta\,\mathrm{d}\xi\,\mathrm{d}\zeta\;. \tag{3.13b}$$

Before sketching the solution of each integral in sec. 3.1.2, not only Ω, but also the other two real-valued functions τ and Ω^n on the unit sphere have to be expanded into spherical harmonics (for definition see (A.6a)), which will eventually collapse the three integrals and turn them into sums consisting of weighted expansion coefficients of the respective series. The expansions of τ and the radius functions are

$$\Omega^n = \Omega^{*n} = \sum_{\nu,\,\mu} \omega_{\nu\mu}^{(n)}\, Y_\nu^\mu \qquad \text{with } n = 1, 2, 3, \dots\ , \tag{3.14a}$$

$$\tau^{(n)} = \sum_{\nu,\,\mu} t_{\nu\mu}^{(n)}\, Y_\nu^\mu \qquad \text{with } n = 2, 3, \dots\ . \tag{3.14b}$$

Both, being real-valued and the relation (A.12b) $Y_\nu^{\mu *} = (-1)^\mu\, Y_\nu^{-\mu}$ also make the functions' respective expansions coefficients satisfy the relation (for details see (A.13a))

$$\omega_{\nu\mu}^{(n)*} = (-1)^\mu\, \omega_{\nu,-\mu}^{(n)} \quad \text{and} \qquad t_{\nu\mu}^{(n)*} = (-1)^\mu\, t_{\nu,-\mu}^{(n)}\ . \tag{3.15}$$

Because of this interdependency, for one series of degree $0 \le \nu \le M$ only $\frac{1}{2}\left((M+1)^2 + M + 1\right)$ coefficients instead of $(M+1)^2$ have to be determined.

The spherical harmonics form a Hilbert-space on the unit sphere with the inner product

$$(f\ ,\ g) = \int_0^{2\pi} \int_0^{\pi} f(\zeta, \xi)\, g^*(\zeta, \xi)\, \sin\zeta \,\mathrm{d}\zeta \,\mathrm{d}\xi\ , \tag{0.2}$$

with $\sin\zeta$ being the measure on the unit sphere. Subsequently, products of spherical harmonics and operators (e.g., derivatives) acting on them also have a representation by means of spherical harmonics.

3.1.2 Solution of the surface integral (3.12c)

In this section the integral equation for the photophoretic force in the free-molecule regime will be solved component-wise within the restrictions of the model introduced in sec. 3.1.1.2 and 3.1.1.3. The starting point is (3.13).

To keep this section readable, scalar products are written here instead of integrals (for details see (0.2) and (0.3), respectively). According to (3.13), for each component of $\mathbf{F}_{\text{phot}}$ there are three scalar products to be solved. Therefore existing recurrence relations of associated Legendre polynomials (sec. A.3.6) are extended to spherical harmonics (sec. B.1), which introduce two new coefficients beside $f_{\nu\mu}$, which I denote with $h_{\nu\mu}$ and $d_{\nu\mu}$

$$f_{\nu\mu} = \sqrt{\frac{2\nu+1}{4\pi}\frac{(\nu-\mu)!}{(\nu+\mu)!}} \tag{A.6b}$$

$$h_{\nu\mu} = \sqrt{\frac{\nu^2-\mu^2}{4\nu^2-1}} \tag{A.9a}$$

$$d_{\nu\mu} = \sqrt{\frac{(\nu+\mu-1)(\nu+\mu)}{4\nu^2-1}}\ . \tag{A.9b}$$

3.1.2.1 F_x

In this subsection the solution for the x-component is presented. I will briefly step the reader through the calculations, details are put in the appendix; some steps refer explicitly to equations in the appendix.

Corresponding to (3.13), the x-component, with usage of the series expansion of the squared radius function and the reduced temperature yields:

$$\begin{aligned}
F_x^{(n)} &\equiv \left(\mathbf{F}^{(0)}_{\text{phot}} + \mathbf{F}^{(\xi)}_{\text{phot}} + \mathbf{F}^{(\zeta)}_{\text{phot}}\right)\cdot \mathbf{e}_x \\
&\overset{(3.13)}{=} c\left(\Omega^n\left(-\partial_\zeta P_1^0\right)\cos\xi\,,\,\tau^{(n)}\right) + \frac{c}{n}\left(\partial_\xi\Omega^n\,\frac{\sin\xi}{\left(-\partial_\zeta P_1^0\right)}\,,\,\tau^{(n)}\right) - \frac{c}{n}\left(\partial_\zeta\Omega^n\,P_1^0\cos\xi\,,\,\tau^{(n)}\right) \\
&\overset{\substack{(3.14a),\\(3.14b)}}{=} \frac{c}{2n}\sum_{\nu,\mu,p,q}\omega^{(n)}_{\nu\mu}\,t^{(n)*}_{pq}\left[n\left(-\partial_\zeta P_1^0\,Y_\nu^\mu\,\left(e^{\mathbb{i}\xi}+e^{-\mathbb{i}\xi}\right)\,,\,Y_p^q\right) + \right. \\
&\quad \left. + \left(Y_\nu^\mu\,\frac{\mu}{\left(-\partial_\zeta P_1^0\right)}\,\left(e^{\mathbb{i}\xi}-e^{-\mathbb{i}\xi}\right)\,,\,Y_p^q\right) - \left(P_1^0\,\partial_\zeta Y_\nu^\mu\,\left(e^{\mathbb{i}\xi}+e^{-\mathbb{i}\xi}\right)\,,\,Y_p^q\right)\right] \\
&= \frac{c}{2}\sum_{\nu,\mu,p,q}\omega^{(n)}_{\nu\mu}\,t^{(n)*}_{pq}\,\Phi^{(n)}_{\nu\mu pq}\,.
\end{aligned} \tag{3.16a}$$

As stated in sec. 3.1.1.3, operators acting on spherical harmonics have a representation by means of spherical harmonics, hence the x-component can be represented by a sum of products of the expansion coefficients of $\tau^{(n)}$ and Ω^n with numbers $\Phi^{(n)}_{\nu\mu pq}$. Detailed evaluations of all three addends that $\Phi^{(n)}_{\nu\mu pq}$ consists of can be found in sec. B.2.

In sec. B.2, the calculations yielded, that $\Phi^{(n)}_{\nu\mu pq}$ consists of four Kronecker-deltas ($\delta_{p,\nu\pm1}$ and $\delta_{q,\mu\pm1}$) and four phase integrals $\left(Y^{\mu\pm1}_{\nu\pm1}\,e^{\mp2\mathbb{i}\xi}\,,\,Y_p^q\right)$. To keep everything short, those integrals are now represented by

$$\Lambda^{\mu\pm1,q,\mp2}_{\nu\pm1,p} := \left(Y^{\mu\pm1}_{\nu\pm1}\,e^{\mp2\mathbb{i}\xi}\,,\,Y_p^q\right)\,. \tag{3.16b}$$

With the usage of $\Lambda^{\mu\pm1,q,\mp2}_{\nu\pm1,p}$ the coefficient $\Phi^{(n)}_{\nu\mu pq}$ has the form:

$$\begin{aligned}
\Phi^{(n)}_{\nu\mu pq} \overset{(B.8)}{=}\; & \frac{1}{2n}\delta_{q,\mu-1}\left[(\nu+1+\mu)\left(d_{\nu+1,\mu+1}\,\Lambda^{\mu+1,q,-2}_{\nu+1,p} - d_{\nu,-\mu}\,\Lambda^{\mu+1,q,-2}_{\nu-1,p}\right) + \right. \\
& \left. +(\nu-\mu+1-2n)\,d_{\nu,\mu}\,\delta_{p,\nu-1} + (3\nu+\mu+1+2n)\,d_{\nu+1,1-\mu}\,\delta_{p,\nu+1}\right] - \\
& -\frac{1}{2n}\delta_{q,\mu+1}\left[(\nu+1-\mu)\left(d_{\nu+1,1-\mu}\,\Lambda^{\mu-1,q,2}_{\nu+1,p} - d_{\nu,\mu}\,\Lambda^{\mu-1,q,2}_{\nu-1,p}\right) + \right. \\
& \left. +(\nu+\mu+1-2n)\,d_{\nu,-\mu}\,\delta_{p,\nu-1} + (3\nu-\mu+1+2n)\,d_{\nu+1,\mu+1}\,\delta_{p,\nu+1}\right]\,.
\end{aligned} \tag{3.16c}$$

For the transition $(\mu,q)\to(-\mu,-q)$, the notation for Λ is defined by

$$\Lambda^{-\mu\pm1,-q,\mp2}_{\nu\pm1,p} = \Lambda^{\mu\mp1,q,\pm2}_{\nu\pm1,p}\,. \tag{3.16d}$$

It can be seen, that $\Phi^{(n)}_{\nu\mu pq}$ can be expressed by the difference of the same function alternated in the indices μ and q

$$\Phi^{(n)}_{\nu,\mu,p,q} = \Gamma^{(n)}_{\nu,\mu,p,q} - \Gamma^{(n)}_{\nu,-\mu,p,-q}\,. \tag{3.16e}$$

The representation of $\Phi^{(n)}_{\nu,\mu,p,q}$ in (3.16e) implies it is skew-symmetric with respect to μ and q, which is very important:

$$\Phi^{(n)}_{\nu,\mu,p,q} \overset{(3.16e)}{=} -\Phi^{(n)}_{\nu,-\mu,p,-q} \,. \tag{3.16f}$$

The term with the two $\Lambda^{\mu+1,q,-2}_{\nu\pm1,p}$ has to be analyzed, as in general, each Λ is contributing for not only $p = \nu \pm 1$ but also $p = \nu + 2z + 1$ with $z \in \mathbb{Z}$. But it turns out that for those indices (and μ, q obeying the parameter range law for spherical harmonics) $d_{\nu+1,\mu+1}\,\Lambda^{\mu+1,q,-2}_{\nu+1,p} - d_{\nu,-\mu}\,\Lambda^{\mu+1,q,-2}_{\nu-1,p}$ yield zero unless $p = \nu \pm 1$, as it has been calculated in sec. B.4. Thus the equation can be expressed with $\delta_{p,\nu\pm1}$ and $\delta_{q,\mu\pm1}$ as

$$d_{\nu+1,\mu+1}\,\Lambda^{\mu+1,q,-2}_{\nu+1,p} - d_{\nu,-\mu}\,\Lambda^{\mu+1,q,-2}_{\nu-1,p} = -\delta_{q,\mu-1}\left[d_{\nu+1,1-\mu}\,\delta_{p,\nu+1} - d_{\nu,\mu}\,\delta_{p,\nu-1}\right] \,, \tag{B.12}$$

and $\Gamma^{(n)}_{\nu,\mu,p,q}$ is simply

$$\Gamma^{(n)}_{\nu,\mu,p,q} = \frac{1}{n}\delta_{q,\mu-1}\left[(\nu+n)\; d_{\nu+1,1-\mu}\,\delta_{p,\nu+1} + (\nu+1-n)\; d_{\nu,\mu}\,\delta_{p,\nu-1}\right] \,, \tag{3.16g}$$

with

$$\Gamma^{(n)}_{\nu,0,p,0} = 0 \quad \forall \nu, p \geq 0 \,. \tag{3.16h}$$

With those findings the final form of F_x yields

$$\begin{aligned} F^{(n)}_x \quad &= \quad \frac{c}{2} \sum_{\substack{\nu\geq0\\ \nu\geq\mu\geq0\\ p\geq0\\ p\geq q\geq0}} \left(\omega^{(n)}_{\nu\mu}\, t^{(n)*}_{pq}\, \Phi^{(n)}_{\nu,\mu,p,q} + \omega^{(n)}_{\nu,-\mu}\, t^{(n)*}_{p,-q}\, \Phi^{(n)}_{\nu,-\mu,p,-q}\right) \\ &\overset{\substack{(3.15),\\(3.16f)}}{=} \quad \frac{c}{2} \sum_{\substack{\nu\geq0\\ \nu\geq\mu\geq0\\ p\geq0\\ p\geq q\geq0}} \Phi^{(n)}_{\nu,\mu,p,q} \left(\omega^{(n)}_{\nu,\mu}\, t^{(n)*}_{p,q} - (-1)^{\mu+q}\, \omega^{(n)*}_{\nu,\mu}\, t^{(n)}_{p,q}\right) \\ &\overset{q=\mu\pm1}{=} \quad c \sum_{\substack{\nu\geq0\\ \nu\geq\mu\geq0\\ p\geq0\\ p\geq q\geq0}} \Phi^{(n)}_{\nu,\mu,p,q}\, \Re\left(\omega^{(n)}_{\nu\mu}\, t^{(n)*}_{pq}\right) \,. \end{aligned} \tag{3.17}$$

For a series of the degree $p = \nu$ there are $(2\nu)^2 - 2$ non-zero numbers $\Phi^{(n)}_{pq\nu\mu}$ out of $(\nu+1)^4$ possible values, and therefore up to non-zero addends of F_x of the same number.

3.1.2.2 F_y

The procedure to calculate the y-component only differs by the sign of the phase factors. Like for the x-component a number $\Upsilon^{(n)}_{\nu\mu pq}$ exists that enables to represent $F_y^{(n)}$ as a sum of products of expansion coefficients of $\tau^{(n)}$ and Ω^n together with Υ.

$$\begin{aligned}
F_y^{(n)} &\equiv \left(\mathbf{F}^{(0)}_{\text{phot}} + \mathbf{F}^{(\xi)}_{\text{phot}} + \mathbf{F}^{(\zeta)}_{\text{phot}}\right) \cdot \mathbf{e}_y \\
&\overset{(3.13)}{=} c\left(\Omega^n\left(-\partial_\zeta P_1^0\right)\sin\xi\,,\,\tau^{(n)}\right) - \frac{c}{n}\left(\partial_\xi\Omega^n\,\frac{\cos\xi}{\left(-\partial_\zeta P_1^0\right)}\,,\,\tau^{(n)}\right) - \frac{c}{n}\left(\partial_\zeta\Omega^n\,P_1^0\sin\xi\,,\,\tau^{(n)}\right) \\
&\overset{(3.14a),\,(3.14b)}{=} \mathbb{i}\frac{c}{2n}\sum_{\nu,\mu,p,q}\omega^{(n)}_{\nu\mu}\,t^{(n)*}_{pq}\left[-n\left(-\partial_\zeta P_1^0\,\left(e^{\mathbb{i}\xi}-e^{-\mathbb{i}\xi}\right)\,Y_\nu^\mu\,,\,Y_p^q\right) - \right. \\
&\quad \left. - \left(Y_\nu^\mu\frac{\mu}{\left(-\partial_\zeta P_1^0\right)}\,\left(e^{\mathbb{i}\xi}+e^{-\mathbb{i}\xi}\right)\,,\,Y_p^q\right) + \left(P_1^0\,\partial_\zeta Y_\nu^\mu\,\left(e^{\mathbb{i}\xi}-e^{-\mathbb{i}\xi}\right)\,,\,Y_p^q\right)\right] \\
&= \mathbb{i}\frac{c}{2}\sum_{\nu,\mu,p,q}\omega^{(n)}_{\nu\mu}\,t^{(n)*}_{pq}\,\Upsilon^{(n)}_{\nu\mu pq}\,. \qquad (3.18a)
\end{aligned}$$

The derivation of the addends for $\Upsilon^{(n)}_{\nu\mu pq}$ are listed in sec. B.3.

Like for the x-component, usage of (B.12) enables to solve the scalar products with the phase factor. The final result is:

$$\Upsilon^{(n)}_{\nu,\mu,p,q} \overset{(B.9)}{=} \Gamma^{(n)}_{\nu,\mu,p,q} + \Gamma^{(n)}_{\nu,-\mu,p,-q}\,, \qquad (3.18b)$$

$$\Upsilon^{(n)}_{\nu,\mu,p,q} \overset{(3.18b)}{=} \Upsilon^{(n)}_{\nu,-\mu,p,-q} \qquad (3.18c)$$

and the force component is

$$F_y^{(n)} = -c\sum_{\substack{\nu\geq 0\\ \nu\geq\mu\geq 0\\ p\geq 0\\ p\geq q\geq 0}}\Upsilon^{(n)}_{\nu,\mu,p,q}\,\Im\left(\omega^{(n)}_{\nu\mu}\,t^{(n)*}_{pq}\right)\,. \qquad (3.18d)$$

Again, for a series of the degree $p=\nu$ there are $(2\nu)^2-2$ non-zero $\Upsilon^{(n)}_{pq\nu\mu}$ out of $(\nu+1)^4$ values, therefore up to non-zero addends of F_y of the same number.

3.1.2.3 F_z

For the case the temperature field on the particle's surface arises from directional heating along the z-axis, the z-component of the photophoretic force is most likely higher than the other two components $F_z \gg F_x, F_y$, rendering it the most important one. It is also the only component not depending on ξ, thus it is very easy to derive. The equation shown in this subsection is the most general one and, if certain assumptions are made for the temperature expansion coefficients, it leads to very easy and handy equations. The simplest one is already well-known and in use for many years. It can be found in, for instance, Rohatschek (1995).

The general solution in the z-component is obtained similarly as for the other two components:

$$\begin{aligned} F_z^{(n)} &\equiv \left(\mathbf{F}^{(0)}_{\text{phot}} + \mathbf{F}^{(\zeta)}_{\text{phot}}\right)\cdot \mathbf{e}_z \\ &\overset{(3.13)}{=} c\left(\Omega^2\, P_1^0\,,\, \tau^{(n)}\right) + \frac{c}{n}\left(-\partial_\zeta P_1^0\, \partial_\zeta \Omega^2\,,\, \tau^{(n)}\right) \\ &\overset{\substack{(3.14a),\\(3.14b)}}{=} \frac{c}{n}\sum_{\nu,\mu,p,q} \omega^{(n)}_{\nu\mu}\, t^{(n)*}_{pq}\left(n\left(Y^\mu_\nu\, P_1^0\,,\, Y^q_p\right) + \left(-\partial_\zeta P_1^0\, \partial_\zeta Y^\mu_\nu\,,\, Y^q_p\right)\right) \\ &= c\sum_{\nu,\mu,p,q} \omega^{(n)}_{\nu\mu}\, t^{(n)*}_{pq}\, \Psi^{(n)}_{\nu\mu pq}\,. \end{aligned} \tag{3.19a}$$

Both scalar products inside the sum yield

$$\begin{aligned} \left(Y^\mu_\nu\, P_1^0\,,\, Y^q_p\right) &\overset{(B.2)}{=} \left(h_{\nu+1,\mu}\, Y^\mu_{\nu+1} + h_{\nu\mu}\, Y^\mu_{\nu-1}\,,\, Y^q_p\right) \\ &= \left(h_{\nu+1,\mu}\,\delta_{p,\nu+1} + h_{\nu\mu}\,\delta_{p,\nu-1}\right)\,\delta_{q,\mu}\,, \end{aligned} \tag{3.19b}$$

and

$$\begin{aligned} \left(-\partial_\zeta P_1^0\, \partial_\zeta Y^\mu_\nu\,,\, Y^q_p\right) &\overset{(B.3)}{=} \left(\nu\, h_{\nu+1,\mu}\, Y^\mu_{\nu+1} - (\nu+1)\, h_{\nu\mu}\, Y^\mu_{\nu-1}\,,\, Y^q_p\right) \\ &= \left(\nu\, h_{\nu+1,\mu}\,\delta_{p,\nu+1} - (\nu+1)\, h_{\nu\mu}\,\delta_{p,\nu-1}\right)\,\delta_{q,\mu}\,, \end{aligned} \tag{3.19c}$$

respectively. So for the z-component it is

$$\Psi^{(n)}_{\nu,\mu,p,q} \overset{\substack{(3.19b),\\(3.19c)}}{=} \frac{1}{n}\delta_{q,\mu}\left[(\nu+n)\, h_{\nu+1,\mu}\,\delta_{p,\nu+1} - (\nu+1-n)\, h_{\nu\mu}\,\delta_{p,\nu-1}\right]\,. \tag{3.19d}$$

The symmetry of $h_{\nu,\mu}$

$$h_{\nu,\mu} = h_{\nu,-\mu} \tag{3.19e}$$

is inherited to $\Psi^{(n)}_{\nu,\mu,p,q}$

$$\Psi^{(n)}_{\nu,\mu,p,q} = \Psi^{(n)}_{\nu,-\mu,p,-q}\,. \tag{3.19f}$$

Subsequently, the z-component in its final form is

$$F_z^{(n)} = c\sum_{\substack{\nu\geq 0\\ \nu\geq\mu\geq-\nu\\ p\geq 0\\ p\geq q\geq -p}} \Psi^{(n)}_{\nu,\mu,p,q}\,\omega^{(n)}_{\nu\mu}\, t^{(n)*}_{pq} \tag{3.19g}$$

$$= c\sum_{\substack{\nu\geq 0\\ \nu\geq\mu\geq 0\\ p\geq 0\\ p\geq q\geq 0}} (2-\delta_{\mu,0})\,\Psi^{(n)}_{\nu,\mu,p,q}\,\Re\left(\omega^{(n)}_{\nu\mu}\, t^{(n)*}_{\nu\mu}\right)\,, \tag{3.19h}$$

or simply

$$\boxed{F_z^{(n)} = \frac{c}{n}\sum_{\nu,\mu}\left[(\nu+n)\, h_{\nu+1,\mu}\, t^{(n)*}_{\nu+1,\mu} - (\nu+1-n)\, h_{\nu\mu}\, t^{(n)*}_{\nu+1-n,\mu}\right]\,\omega^{(n)}_{\nu\mu}\,.} \tag{3.19i}$$

Here, for a series of the degree $p=\nu$ there are $2\nu^2-1$ non-zero out of $(\nu+1)^4$ values of $\Psi^{(n)}_{pq\nu\mu}$, therefore up to non-zero addends of F_z of the same number. Also, no mixing terms in μ/q occur (matrix is diagonal concerning μ and p).

3.1.3 General structure of the solution

To conclude all preceding results, the photophoretic force in the free-molecule regime for star-convex particles is:

$$\mathbf{F}_{\text{phot}}^{(n)} = -\frac{1}{2}\frac{p}{\sqrt{T^-}} \sum_{\substack{\nu\geq 0\\ \nu\geq\mu\geq 0\\ p\geq 0\\ p\geq q\geq 0}} \begin{pmatrix} \left(\Gamma_{\nu,\mu,p,q}^{(n)} - \Gamma_{\nu,-\mu,p,-q}^{(n)}\right) \Re\left(\omega_{\nu\mu}^{(n)}\, t_{pq}^{(n)*}\right) \\ -\left(\Gamma_{\nu,\mu,p,q}^{(n)} + \Gamma_{\nu,-\mu,p,-q}^{(n)}\right) \Im\left(\omega_{\nu\mu}^{(n)}\, t_{pq}^{(n)*}\right) \\ (2-\delta_{\mu,0})\, \Psi_{\nu,\mu,p,q}^{(n)} \Re\left(\omega_{\nu\mu}^{(n)}\, t_{pq}^{(n)*}\right) \end{pmatrix}, \tag{3.20a}$$

$$\Gamma_{\nu,\mu,p,q}^{(n)} = \frac{1}{n}\delta_{q,\mu-1}\left[(\nu+n)\; d_{\nu+1,1-\mu}\,\delta_{p,\nu+1} + (\nu+1-n)\; d_{\nu,\mu}\,\delta_{p,\nu-1}\right], \tag{3.16g}$$

$$\Psi_{\nu,\mu,p,q}^{(n)} = \frac{1}{n}\delta_{q,\mu}\left[(\nu+n)\, h_{\nu+1,\mu}\,\delta_{p,\nu+1} - (\nu+1-n)\, h_{\nu\mu}\,\delta_{p,\nu-1}\right]. \tag{3.19d}$$

Both, Γ and Ψ have a very similar structure, but only Γ is always positive, which can be deduced from its addends. Furthermore, it is also $|\Phi_{\nu,\mu,p,q}^{(n)}| = |\Upsilon_{\nu,\mu,p,q}^{(n)}|$, i.e.,

$$|\Gamma_{\nu,\mu,p,q}^{(n)} - \Gamma_{\nu,-\mu,p,-q}^{(n)}| = |\Gamma_{\nu,\mu,p,q}^{(n)} + \Gamma_{\nu,-\mu,p,-q}^{(n)}|\,. \tag{3.20b}$$

In sec. 4.2.4.3, $\mathbf{F}_{\text{phot}}^{(2)}$ and $\mathbf{F}_{\text{phot}}^{(3)}$ are used to calculate the force on a triaxial ellipsoid. Sec. 3.4.2 introduces a linear order approximation of the general solution $\mathbf{F}_{\text{phot}}^{(3)}$.

With this solution, any other surface integral for a function f on star-convex surfaces can be calculated as

$$\int_{\partial\Omega} f\,\mathrm{d}\mathbf{A} = \sum_{\substack{\nu\geq 0\\ \nu\geq\mu\geq 0\\ p\geq 0\\ p\geq q\geq 0}} \begin{pmatrix} \left(\Gamma_{\nu,\mu,p,q}^{(2)} - \Gamma_{\nu,-\mu,p,-q}^{(2)}\right) \Re\left(\omega_{\nu\mu}^{(2)}\, f_{pq}^{*}\right) \\ -\left(\Gamma_{\nu,\mu,p,q}^{(2)} + \Gamma_{\nu,-\mu,p,-q}^{(2)}\right) \Im\left(\omega_{\nu\mu}^{(2)}\, f_{pq}^{*}\right) \\ (2-\delta_{\mu,0})\, \Psi_{\nu,\mu,p,q}^{(2)} \Re\left(\omega_{\nu\mu}^{(2)}\, f_{pq}^{*}\right) \end{pmatrix}. \tag{3.21}$$

3.1.3.1 Volume of a chondrule

The knowledge of the volume defined by the closed surface $\partial\Omega$ usually helps deducing other properties. Here, the volume can be determined by summing up the pairwise products

of the expansion coefficients of the radius functions Ω and Ω^2, respectively, or it can be expressed by the 0-th expansion coefficient for Ω^3:

$$V = \iiint \left|\det \partial_{(\xi,\zeta,r)} \left(r\,\boldsymbol{\Omega}\right)\right| \,\mathrm{d}r\,\mathrm{d}\zeta\,\mathrm{d}\xi \tag{3.22a}$$

$$= \int_0^{2\pi}\int_0^{\pi}\int_0^{1} r^2\,\Omega(\xi,\zeta)^3\,\sin\zeta\,\mathrm{d}r\,\mathrm{d}\zeta\,\mathrm{d}\xi$$

$$= \frac{1}{3}\int_0^{2\pi}\int_0^{\pi} \Omega(\xi,\zeta)^3 \sin\zeta\,\mathrm{d}\zeta\,\mathrm{d}\xi$$

$$= \frac{1}{3}\left(\Omega\,,\,\Omega^2\right) \overset{(3.14a)}{=} \frac{1}{3}\sum_{\nu,\mu}\omega_{\nu\mu}^{(1)}\,\omega_{\nu\mu}^{(2)*} \tag{3.22b}$$

$$= \frac{1}{3}\left(1\,,\,\Omega^3\right) \overset{(3.14a)}{=} \frac{2\sqrt{\pi}}{3}\omega_{0,0}^{(3)}\,. \tag{3.22c}$$

Hence $\omega_{0,0}^{(3)} \propto V$, and it is

$$\omega_{0,0}^{(3)} = \frac{3V}{2\sqrt{\pi}}\,. \tag{3.23}$$

This result will be used in sections 3.4.2 and 4.2.4.3 for describing the force with only the linear term in (3.20) for $n = 3$ ($\mathbf{F}_{\mathrm{phot}}^{(3)}$) to very high precision.

3.1.3.2 Solution for a sphere of radius r_0

In most cases all particles subject to the photophoretic force are treated as spheres. Commonly in literature, the z-component of the photophoretic force on spheres for rotational symmetry around the axis of irradiation is discussed and used. Since rotation and other effects might result into a non-symmetric temperature distribution across the sphere's surface, the application of those models is insufficient. Deducing from the general solution (3.20), the photophoretic force for the special case of a sphere with the radius r_0, but arbitrary temperature $T(\zeta,\xi)$ can be expressed by only two expansion coefficients of τ.

For a sphere, the expansion coefficient $\omega_{0,0}^{(2)}$ is described by

$$\Omega^2 = \omega_{0,0}^{(2)}\,Y_0^0 = r_0^2\,, \tag{3.24}$$

hence (3.20) yield (relation (3.15) is followed)

$$\boxed{\mathbf{F}_{\mathrm{phot}} = \sqrt{\frac{\pi}{3}}\,\frac{p}{\sqrt{T^-}}\,r_0^2 \begin{pmatrix} \sqrt{2}\,\Re\left(t_{1,1}^*\right) \\ \sqrt{2}\,\Im\left(t_{1,1}^*\right) \\ -t_{1,0} \end{pmatrix}\,.} \tag{3.25}$$

Only two out of all coefficients $t_{\nu\mu}$ contribute to $\mathbf{F}_{\mathrm{phot}}$. Because $t_{1,0}$ is real and $t_{1,1}$ complex, only three numbers (two real numbers and one entirely complex number) have to be determined. In the case of a sphere all higher harmonics in the temperature field are irrelevant: only $t_{1,0}$ and $t_{1,1}$ determine the photophoretic force and higher degrees ($\nu > 1$) in the temperature field cannot be "seen" by the sphere.

3.1.3.3 Solution for a sphere of radius r_0 and a rotational-symmetric temperature $T(\zeta)$

In the well-known case of a rotational-symmetric temperature (see Figure 3.6 below) field $T = T(\zeta)$ across the sphere only the z-component of the force contributes and thus it is enough to expand the mantle's reduced temperature τ (see (3.12a)) in ordinary Legendre polynomials

$$\tau(\zeta) = \sum_{\nu} t_\nu \, P_\nu(\cos\zeta) \; . \tag{3.26}$$

On the other hand (3.25) already is the result, when the relation (comparing coefficients of (3.14b) with equation above for $\mu = 0$)

$$f_{\nu,0}\, t_{\nu,0} = t_\nu \tag{3.27}$$

is considered:

$$\boxed{\mathbf{F}_{\text{phot}} = -\frac{2\pi}{3}\frac{p\, r_0^2}{\sqrt{T^-}}\, t_1 \mathbf{e}_z \; .} \tag{3.28}$$

This is a known result in Loesche et al. (2012) and resembles the approximation in Rohatschek (1995), where t_1 is the coefficient of the "linear" term in (3.26). Again, only one component of the temperature field accounts for the photophoretic force; the rest is invisible to the sphere. Hence, if a sphere's surface temperature — resulting from directed illumination — is rotational symmetric, always longitudinal photophoresis prevails.

3.2 How to calculate (longitudinal) photophoretic forces

In the *fm* regime the photophoretic force can be exactly calculated by applying the respective integral equation for the subjacent kinetic model, e.g., (3.7b), on the particle's surface temperature. Most problems hinge on the retrieval of this temperature, it has to be known or the corresponding heat transfer problem has to be solved (heat equation on the respective domain with boundary conditions specifying the problem). For most cases this is tedious, especially when photophoresis shall be discussed on a large number of particles or used for other analytical calculations, hence multiple ways have been explored to bypass the heat transfer problem by simply approximating it. These approximations are then combined with the solution of the integral equation for spheres, yielding approximations widely used (see sec. 3.3). Another way is to express the heat transfer problem in terms of absorption, i.e. by the introduction of the *asymmetry factor* J_ν, connected with the *heat source function* q, describing the effect of the radiation on the particle. Discussions of q are for instance made in Rohatschek and Zulehner (1985). General ways to describe heat source functions for spheres by means of Mie scattering, which exactly describes the electromagnetic field within and near a homogeneous sphere, were presented in, e.g., Yalamov et al. (1976b,a) and Dusel et al. (1979) and Arnold et al. (1984) and Greene et al. (1985) and Mackowski (1989) and Mackowski et al. (1989) and Xu et al. (1999) and even for prolate spheroids in Ou and Keh (2005). Li et al. (2010) also studied the heat source function for prolate spheroids, but employed the T-matrix method for the computation of q, as they cited the method as well-suited for treating electromagnetic scattering by non-spherical objects (see Figure 2.6). The asymmetry factor J_1 was also

derived for atmospheric aerosols in Letfulova et al. (2001), also based on the Lorentz-Mie theory. They studied the absorption efficiency and asymmetry depending on different parameters.

In Figure 3.5 a recapitulation of the possible ways to calculate the photophoretic force is sketched.

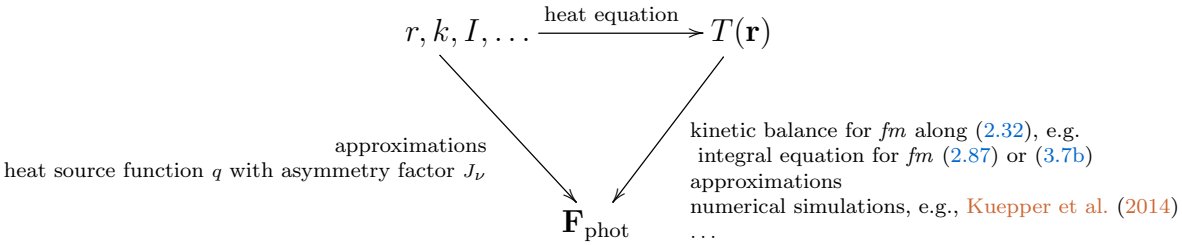

Figure 3.5: Strategies to calculate the photophoretic force.

3.3 Linear approximations for longitudinal *fm*-photophoresis exerted on spheres due to a rotational-symmetric surface temperature

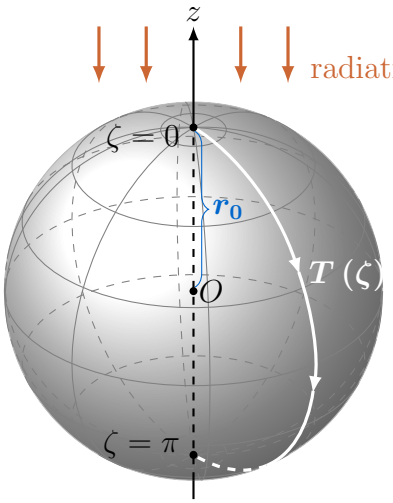

Figure 3.6: Visualization of the basic situation considered. Illumination is directed from one side (parallel to z-axis) and the temperature variation only depends on ζ. The sphere's radius is r_0. Along Loesche and Wurm (2012).

Generally, instead of realistically shaped particles, homogeneous spheres with radius r_0 are assumed in order to derive and apply handy approximations for the calculation of the (longitudinal) photophoretic force in the direction of illumination (w.l.o.g. $-\mathbf{e}_z$), for a known temperature $T(\xi, \zeta)$ across the particle's surface. The temperature T^+ is still considered to be related to the surface temperature by thermal accommodation, described in sec. 2.8

$$T^+ = T^- + \alpha \left(T - T^- \right) \ . \qquad (2.114)$$

For a stationary setup, e.g. in Hidy and Brock (1967) and Tong (1973) and Yalamov et al. (1976a) and Rohatschek (1995) and Loesche and Wurm (2012) and other publications, this sphere has a rotational-symmetric surface temperature $T(\zeta)$ as displayed in Figure 3.6, and the force integral simplifies to

$$\begin{aligned}\mathbf{F}_{\text{phot}} &= -\frac{1}{2}\oint_{\text{sphere}} \mathrm{d}\mathbf{A}\, p\left(1+\sqrt{\frac{T^+}{T^-}}\right)\\ &\overset{\mu:=\cos\zeta}{=} \pi r_0^2\, p\int_{-1}^{1}\mathrm{d}\mu\,\mu\sqrt{\frac{T^+(\mu)}{T^-}}\,\mathbf{e}_z\ .\end{aligned} \tag{3.29}$$

The integral can be collapsed by expanding $T(\zeta)$ into a series of Legendre polynomials P_ν

$$T(r=r_0,\zeta)=\sum_\nu A_\nu\, P_\nu\left(\cos\zeta\right)\ , \tag{3.30}$$

where A_i is the i^{th} expansion coefficient.

Linearization of the square root in (2.87) to its first order around $\overline{T^+}$

$$\sqrt{\frac{T^+}{T^-}}=\frac{\sqrt{\overline{T^+}}}{\sqrt{T^-}}+\frac{1}{2}\frac{T^+-\overline{T^+}}{\sqrt{\overline{T^+}\,T^-}}+\mathcal{O}\left(\left(T^+-\overline{T^+}\right)^2\right)\ , \tag{3.31}$$

and the application of Legendre Polynomial's orthogonality relation (A.11c) yields a function, that is only depending on A_1 (introducing $\approx$):

$$\boxed{\mathbf{F}_{\text{phot}}\approx-\frac{\pi}{3}\,\alpha\,\frac{p}{\sqrt{\overline{T^+}\,T^-}}\,r_0^2\,A_1\,\mathbf{e}_z\ .} \tag{3.32}$$

Different approximations $\mathbf{F}_{\text{phot}}\approx\tilde{F}^{(a)}\,\mathbf{e}_z$ in this section can be expressed by means of this equation, and the coefficient $A_1^{(a)}$ is obtained by comparison. The quality of this linear approximation depends on, if the surface temperature does not vary too much from $\overline{T^+}$. Often this equation is used with $\overline{T^+}\to T^-$, even if the particle is much hotter than the surrounding gas. This is wrong and might lead to overestimation of the force. $\overline{T^+}$ can be obtained, e.g., in case of thermal accommodation (2.114) as

$$\overline{T^+}=T^-+\alpha\left(\overline{T}-T^-\right)\ . \tag{3.33}$$

In this case, $\overline{T}$ can either be obtained by the previous Legendre polynomials expansion

$$\overline{T}\equiv A_0\ , \tag{3.34}$$

or instead — usually due to lack of full surface temperature information — the black-body temperature $\overline{T}=T_{\text{bb}}$, considered as

$$T_{\text{bb}}:=\sqrt[4]{\frac{I}{4\sigma_{\text{SB}}}+\left(T_{\text{gas}}^{\text{rad}}\right)^4}\ . \tag{3.35}$$

As of yet, the coefficient A_1 is still unknown. One way to determine it from restricted knowledge about the particle and its temperature distribution is to measure the temperature extremes along the axis of illumination (Rohatschek 1995)

$$\boxed{A_1^{(1)} \approx \frac{1}{2}\Delta T\,.} \tag{3.36}$$

Here, it is $\Delta T = T_{\max} - T_{\min}$ along the illumination axis. If the temperature differences cannot be measured, A_1 can also be expressed in terms of the setup parameters, like intensity I and thermal conductivities k and k_{gas} of the particle and the gas, respectively. Hidy and Brock (1967) and Yalamov et al. (1976a) and Beresnev et al. (1993) elaborated different linear approximations by employing the kinetic momentum balance for a sphere using different gas velocity distributions to derive the basic integral equation for the photophoretic force (2.87) (except for Yalamov et al. (1976a)). They also calculated a sphere's surface temperature with different boundary conditions, yielding approximations of first order for the photophoretic force.

In this section those approximations are reviewed. They are especially designed for surface temperatures of the sphere close to the temperature of the surrounding gas (equilibrium approximations). Almost every approximation is based on a different gas velocity distributions, thus the surface integral equations resulting from (2.32) can somehow differ from the one in the most frequently used model (2.87). The boundary conditions also differ, thus yielding different surface temperatures. The resulting approximations are therefore only restrictedly comparable, as a heat transfer model is defined by the respective boundary condition. However, the surface integral equations can be employed for different surface expansions if the heat transfer boundary condition do not dependent on the gas velocity distributions itself. In addition to the established ones, two new approximations of unprecedented accuracy are introduced, also valid for non-equilibrium states. The subjacent idea is sketched in Figure 3.6.

3.3.1 Approximation for a sphere without thermal accommodation in Hidy and Brock (1967) and Tong (1973)

Hidy and Brock (1967) present the solution to a heat transfer problem and find an approximate equation of first order for the photophoretic force in the free molecule regime exerted on a sphere with its mean temperature close to those of the surrounding gas. They use the approximation to estimate the time aerosols need to descent from "high levels of the idealized stagnant atmosphere to the lower stratosphere". However, no calculations, but only equations used as starting points and results can be found in this paper. Tong (1973) solves the same analytical heat transfer problem well commented, but he does not explicitly use any velocity distributions for the gas. As supplement, he also conducts Monte Carlo simulations to compare the results with those predicted by the linear approximation found by Hidy and Brock (1967), i.e. (3.48), and introduces a correction factor for their equation. Simulations for the transition regime for Knudsen numbers $0.02 \leq Kn \leq 2$ were also done and discussed.

Hidy and Brock (1967) proceed by solving the homogeneous and stationary heat equation at a constant thermal conductivity k

$$k\Delta T = 0 \tag{3.37}$$

with a Neumann boundary condition that incorporates a boundary heat source corresponding to the directed illumination sketched in Figure 3.6, and a gas-surface heat transfer term. It reads

$$k\frac{\partial T}{\partial \mathbf{n}} = I\,\Theta(\pi/2-\zeta)\,\cos\zeta - \mathbf{n}\cdot\left[\check{\boldsymbol{\varepsilon}}^{+} + \check{\boldsymbol{\varepsilon}}^{-}\right] \qquad \text{at } \partial V\,, \tag{3.38}$$

where the translational energy fluxes $\check{\boldsymbol{\varepsilon}}^{\pm}$, defined in (2.36), were used. Both integrals depend on the velocity distributions for the gas. In their publication, Hidy and Brock (1967) explicitly use two Maxwell-Boltzmann distributions around the mean T^{-} and T^{+}, respectively

$$\sigma^{-}(\mathbf{v}) = n\,\sigma_0^{-}(\mathbf{v}) \overset{(2.58)}{=} n\left(\frac{m}{2\pi k_\mathrm{B} T^{-}}\right)^{3/2} e^{-\frac{mv^2}{2k_\mathrm{B}T^{-}}} \tag{3.39a}$$

$$\sigma^{+}(\mathbf{v}) = n^{+}\,\sigma_0^{+}(\mathbf{v}) \overset{(2.58)}{=} n^{+}\left(\frac{m}{2\pi k_\mathrm{B} T^{+}}\right)^{3/2} e^{-\frac{mv^2}{2k_\mathrm{B}T^{+}}}\,, \tag{3.39b}$$

and continuity of the gas flow at the rigid surface

$$n^{+}\,\overline{v_\mathbf{n}^{+}} = -n\,\overline{v_\mathbf{n}^{-}}\,. \qquad (2.37\text{b})$$

With both distributions, the two translation energy integrals $\check{\boldsymbol{\varepsilon}}^{\pm}$ yield (using $p = n\,k_\mathrm{B}T$)

$$\check{\boldsymbol{\varepsilon}}^{-}\cdot\mathbf{n} \overset{(2.36)}{=} -\frac{1}{2}n\,k_\mathrm{B}\,T^{-}\,\overline{v} = -\frac{1}{2}p\,\overline{v} \tag{3.40a}$$

$$\check{\boldsymbol{\varepsilon}}^{+}\cdot\mathbf{n} \overset{(2.36)}{=} \frac{1}{2}n^{+}\,k_\mathrm{B}\,T^{+}\,\overline{v^{+}}\,, \tag{3.40b}$$

and thus the gas-surface heat transfer term in the boundary condition turns to

$$k\frac{\partial T}{\partial \mathbf{n}}\bigg|_{r=r_0} = I\,\Theta(\pi/2-\zeta)\,\cos\zeta + \frac{1}{2}p\,\overline{v}\left(1-\frac{T^{+}}{T^{-}}\right) \qquad \text{at } \partial V\,. \tag{3.41}$$

Tong (1973) solves the heat equation (3.37) with the following boundary condition

$$k\frac{\partial T}{\partial \mathbf{n}} = I\,\Theta(\pi/2-\zeta)\,\cos\zeta + H_\mathrm{i} - H_\mathrm{r} - \sigma_\mathrm{SB}\,\varepsilon\,T^4 \qquad \text{at } \partial V \tag{3.42a}$$

with the following variable definitions

$$H_\mathrm{i} = \frac{1}{2}p\,\overline{v} \tag{3.42b}$$

$$H_\mathrm{r} = \frac{1}{2}p\,\overline{v}\,\frac{T\big|_{r=r_0}}{T^{-}}\,, \tag{3.42c}$$

and ε denoting the particle's emissivity. Except for the surface radiation term, this is the same boundary condition, that (3.38) yields for two Maxwell-Boltzmann distributions, as used by Hidy and Brock (1967), for

$$T^{+} = T\big|_{r=r_0}\,, \tag{3.43}$$

which is assumed in both papers. Kerker and Cooke (1982) used this boundary condition except the source term for numerical calculations on photophoresis acting on spheres suspended in gas in the *fm* regime using the Lorenz-Mie solution (aerosol study).

Hidy and Brock (1967) use the ansatz for the surface temperature that is symmetric around the z-axis — as heat-up is directed along z-axis —, and that is slightly modified in comparison to the ansatz for a whole sphere (2.21) given in sec. 2.1.2 ($C_\nu = r_0^{-\nu}\, A_\nu$ for $\nu \geq 1$, $C_0 = T^- + A_0$):

$$T(r,\zeta) = T^- + \sum_{\nu=0}^{\infty} A_\nu \left(\frac{r}{r_0}\right)^\nu P_\nu(\cos\zeta)\ . \tag{3.44}$$

They yield the expansion coefficient corresponding to (2.22) as

$$A_\nu = \frac{\pi^{1/2} I}{4\Gamma\left(\frac{3}{2} - \frac{1}{2}\nu\right)\Gamma\left(2 + \frac{1}{2}\nu\right)\frac{2}{2\nu+1}\left(\frac{1}{2} n\, k_\mathrm{B} \overline{v} + \nu\,\frac{k}{r_0}\right)}\ , \tag{3.45}$$

with Γ denoting the gamma function in this equation.

Tong (1973) also visually modifies the ansatz for the heat equation in comparison to (2.21) ($C_\nu = T^-\, r_0^{-\nu}\, \tilde{A}_\nu$) as

$$T(r,\zeta) = T^- \sum_{\nu=0}^{\infty} \tilde{A}_\nu \left(\frac{r}{r_0}\right)^\nu P_\nu(\cos\zeta)\ . \tag{3.46}$$

Without the radiation term $\sigma_\mathrm{SB}\,\varepsilon\, T(r = r_0,\zeta)^4$ the solution of the heat conduction problem is analytically obtainable and given in the publication up to sixth order (in the other case the problem has to be solved numerically). I refrain from citing a series of numbers and will give the closed form solution at the surface instead

$$\tilde{A}_\nu = \frac{1}{2}\frac{1}{T^-}\frac{(2\nu+1)c_\nu\, I + p\,\overline{v}\,\delta_{0,\nu}}{\nu\frac{k}{r_0} + \frac{1}{2}\frac{p\,\overline{v}}{T^-}}\ . \tag{3.47a}$$

The coefficient c_ν is the integral (A.16) of two Legendre polynomials in the half-space $[0,1]$

$$c_\nu = \int_0^1 P_1(x) P_\nu(x)\,\mathrm{d}x = \begin{cases} \frac{1}{3} & \nu = 1 \\ \frac{\Gamma\left(\frac{\nu}{2}+\frac{1}{2}\right)\cos\left(\frac{\nu\pi}{2}\right)}{(1-\nu)(\nu+2)\sqrt{\pi}\,\Gamma\left(\frac{\nu}{2}+1\right)} & \nu \text{ even} \\ 0 & \text{else} \end{cases}\ .$$

The Kronecker delta arises from the Legendre polynomials' orthogonality relation (A.11c), i.e. $P_0(x) = 1$, and thus $\frac{1}{2}\,(P_0\,,\,P_\nu)_{[-1,1]} = \delta_{0,\nu}$. The integral boundaries $[0,1]$ of c_ν result from the Heaviside function Θ, and the identity $P_1(x) = x = \cos\zeta$ from the $\cos\zeta$ in the boundary source term of (3.42a).

In both publications, the resulting surface temperature — rotational-symmetric to the direction of illumination — is employed to calculate the photophoretic force in the free molecule regime by means of the integral equation (2.87), whereas total thermal accommodation is considered (corresponds to $\alpha = 1$). Hidy and Brock (1967) mention, that the kinetic equation (2.39), together with the mass continuity boundary condition (2.37b) for

an impenetrable surface, was their starting point to retrieve (2.87) in case of two Maxwell-Boltzmann distributions describing the two gas fractions. As the surface temperature can be calculated to arbitrary order, the force (2.87) can also be calculated numerically. But Hidy and Brock (1967) and Tong (1973) also give the first order approximation for the case $\frac{T^+}{T^-} \approx 1$, hence they linearize the square root $\sqrt{\frac{T^+}{T^-}}$ in the integral equation (2.87) at T^-, similarly to (3.31). Then, only the linear term $\tilde{A}_1 P_1$ in $T\big|_{r=r_0}$ contributes since the orthogonality relation (A.11c) applies, and the force eventually yields the handy equation ($p = n\, k_\mathrm{B}\, T$)

$$\mathbf{F}_\mathrm{phot} \approx -\frac{\pi}{6}\,\frac{p}{T^-}\,r_0^2\,\frac{I}{\frac{k}{r_0}+\frac{1}{2}\frac{p}{T^-}\overline{v}}\,\mathbf{e}_z\ , \tag{3.48}$$

with $\frac{1}{2}\frac{\overline{v}}{T^-} = \sqrt{\frac{2k_\mathrm{B}}{\pi\, T^-\, m}}$ for thermal equilibrium (Maxwell-Boltzmann distribution).

Additionally, when linearizing the square root at $\overline{T^+}$ — instead of at T^- — the force yields

$$\mathbf{F}_\mathrm{phot} \approx -\frac{\pi}{6}\,\frac{p}{\sqrt{\overline{T^+}T^-}}\,r_0^2\,\frac{I}{\frac{k}{r_0}+\frac{1}{2}\frac{p}{T^-}\overline{v}}\,\mathbf{e}_z\ , \tag{3.49}$$

which resembles the previous force for spheres, whose temperature does not much deviate from the gas they are suspended in and the only difference makes the term $\frac{p}{\sqrt{\overline{T^+}T^-}}$ vs. $\frac{p}{T^-}$. Comparison of (3.49) with (3.32) determines the expansion coefficient $A_1 = T^-\,\tilde{A}_1$ as

$$\boxed{A_1 = \frac{1}{2\alpha}\,\frac{I}{\frac{k}{r_0}+\frac{1}{2}\frac{p}{T^-}\overline{v}}\ .} \tag{3.50}$$

3.3.2 Phorophoresis of (sperical) aerosols in Yalamov et al. (1976a)

One of the most contributing theoretical works on photophoresis in the free molecule regime was done by Yalamov et al. (1976a) (the same for the continuum regime: Yalamov et al. (1976b)). In this publication two modified Maxwell-Boltzmann velocity distribution functions are used to derive the force on a sphere with given temperature. The sphere's surface temperature is obtained by solving the heat equation with a volumetric source term, which is obtained in asymptotic form for weakly and strongly absorbing particles by employing Mie scattering, as the sphere's radius is far below the wavelength of light.

The authors solve the heat equation

$$k\Delta T = \nabla\cdot\mathbf{S}_\mathrm{poynting} = -\frac{4\pi}{\lambda_\mathrm{rad}}\,\tilde{n}_\Re\,\tilde{n}_\Im\,I\,B(r,\cos\zeta) \tag{3.51}$$

where the irradiation intensity is $I = \langle S_\mathrm{poynting}\rangle_t = c_0\,E_0^2/8\pi$ (cgs) and the normalized heat source function

$$B(r,\cos\zeta) := |E(r,\cos\zeta)|^2\,/E_0^2 \tag{3.52}$$

was used ($|E(r,\zeta)|^2$ averaged over the angle ξ, unpolarized light). Two boundary conditions are applied, namely the continuity of the gas flow at the rigid surface (2.37a), which can also be expressed by the simpler equation

$$n^+\,\overline{v_\mathbf{n}^+} = -n\,\overline{v_\mathbf{n}^-}\ , \qquad\qquad (2.37b)$$

and continuity of the heat flux just there (again, the translational energy in (2.36) was used)

$$k\frac{\partial T}{\partial \mathbf{n}}\bigg|_{r=r_0} = -\left[\breve{\boldsymbol{\varepsilon}}^{+}(r_0,\zeta)+\breve{\boldsymbol{\varepsilon}}^{-}(r_0,\zeta)\right]\cdot\mathbf{n}\,. \tag{3.53}$$

The same boundary conditions were applied in Hidy and Brock (1967)/sec. 3.3.1, only replacing the surface source by a volumetric source term in the heat transfer equation above. The dependencies of the integrals on (r_0,ζ) refer to the dependency of the respective distribution function $\sigma^{(i)}(r_0,\zeta,\mathbf{v})$.

Yalamov et al. (1976a) employ a modified Maxwell-Boltzmann velocity distribution for the incident gas particles, i.e. the velocity of the suspended particle $\mathbf{u}$ is taken into account, and a modified version of Maxwell's scattered gas particles with momentum and thermal accommodation coefficients α_m and α as

$$\sigma^{-}(\mathbf{v}) = n\,\sigma_0^{-}(\mathbf{v}+\mathbf{u}) = n\left(\frac{m}{2\pi k_\mathrm{B}T^{-}}\right)^{3/2} e^{-\frac{m(\mathbf{v}+\mathbf{u})^2}{2k_\mathrm{B}T^{-}}} \tag{3.54a}$$

$$\sigma^{+}(\mathbf{v}) = \alpha_\mathrm{m}\,n^{+}\left(\frac{m}{2\pi k_\mathrm{B}T^{+}}\right)^{3/2} e^{-\frac{mv^2}{2k_\mathrm{B}T^{+}}} + (1-\alpha_\mathrm{m})\;\sigma^{-}\left(\mathbf{v}_0^{+}\right)\,, \tag{3.54b}$$

with the partially accommodated gas particles leaving at the temperature

$$T^{+} = T^{-} + \alpha\left(T-T^{-}\right)\,. \qquad (2.114)$$

Additionally, they assume, that $T^{-}=T_\infty$ and $n=n_\infty$. The solution for the surface temperature of the sphere is

$$T(r=r_0,\zeta) = T^{-} + \sum_{\nu=0}^{\infty}\frac{J_\nu\, I\, P_\nu(\cos\zeta)}{\nu\,\frac{k}{r_0}+\alpha_\mathrm{m}\,\alpha\,n\,k_\mathrm{B}\sqrt{\frac{2k_\mathrm{B}T^{-}}{\pi\,m}}} \tag{3.55a}$$

with the mean surface temperature

$$\overline{T}(r=r_0) = T^{-} + \frac{I\,J_0}{\alpha_\mathrm{m}\,\alpha\,n\,k_\mathrm{B}\sqrt{\frac{2k_\mathrm{B}T^{-}}{\pi\,m}}}\,, \tag{3.55b}$$

and the asymmetry factor ($\mu := \cos\zeta$)

$$J_\nu \equiv J_\nu(r_0) \overset{(3.105)}{=} \frac{2\nu+1}{2}\,\tilde{n}_\Re\,\tilde{n}_\Im\,\frac{4\pi}{\lambda_\mathrm{rad}}\int_0^{r_0}\left(\frac{r}{r_0}\right)^{\nu+2}\int_{-1}^{1}B(r,\mu)\,P_\nu(\mu)\,\mathrm{d}\mu\,\mathrm{d}r \tag{3.55c}$$

My own calculations showed, that the highlighted factor k_B in (3.55a) is missing in the original paper, which is probably due to a slip as without this factor the units of the addends in the denominator would not match otherwise.

Eventually, they employ the momentum balance at the particle surface (2.32) to receive the force exerted onto the particle, as it has been done for two Maxwell-Boltzmann velocity distributions in sec. 2.6.2:

$$\begin{aligned}\mathbf{F} &\overset{(2.32)}{=} -\int \mathrm{d}\mathbf{A}\cdot\left[\int_{+}\sigma^{+}(\mathbf{v})\,m\,\mathbf{v}\otimes\mathbf{v}\,\mathrm{d}^3v+\int_{-}\sigma^{-}(\mathbf{v})\,m\,\mathbf{v}\otimes\mathbf{v}\,\mathrm{d}^3v\right]\\ &\overset{\substack{(2.37a),(3.54),\\ u\ll\sqrt{\frac{2k_\mathrm{B}T^-}{m}}}}{=} -\pi r_0^2\,p\left[\alpha_\mathrm{m}\int_{-1}^{1}\sqrt{\frac{T^+}{T^-}}\,\mu\,\mathrm{d}\mu\,\mathbf{e}_z+2m\frac{8+\alpha_\mathrm{m}\,\pi\sqrt{\overline{T^+}/T^-}}{18\pi\,k_\mathrm{B}\,T^-}\mathbf{u}\right]\\ &= \mathbf{F}_\mathrm{phot}+\mathbf{F}_\mathrm{drag}\,.\end{aligned} \tag{3.56}$$

This balance represents a sum of photophoretic force (for $\mathbf{u}=0$)

$$\mathbf{F}_\mathrm{phot}=-\pi r_0^2\,p\,\alpha_\mathrm{m}\int_{-1}^{1}\sqrt{\frac{T^+}{T^-}}\,\mu\,\mathrm{d}\mu\,\mathbf{e}_z \tag{3.57}$$

and drag/resistance force

$$\mathbf{F}_\mathrm{drag}=-\pi\,r_0^2\,p\,m\frac{8+\alpha_\mathrm{m}\,\pi\sqrt{\overline{T^+}/T^-}}{9\pi\,k_\mathrm{B}\,T^-}\mathbf{u}\,. \tag{3.58}$$

Obviously, the drag force arises from $\mathbf{u}\neq 0$ due to velocity distribution of the incident gas particles $\sigma^-(\mathbf{v})=n\,\sigma_0^-(\mathbf{v}+\mathbf{u})$. u is also the speed of the particle when $\mathbf{F}_\mathrm{phot}+\mathbf{F}_\mathrm{drag}=0$. The photophoretic force on a sphere obtained by the general integral equation (2.87) yields the same result as here, if $\alpha_\mathrm{m}=1$, making the solution of Yalamov et al. (1976a) more general than (2.87).

However, by inserting the surface temperature (3.55) into the force integral (3.57) — and describing T^+ by thermal accommodation (2.114) as included in their model —, they yield the approximate photophoretic force acting on a sphere (they linearized the square root at $\overline{T^+}$, $p=n\,k_\mathrm{B}\,T^-$ for an ideal gas)

$$\mathbf{F}_\mathrm{phot}\approx-\frac{\pi}{3}\,\alpha_\mathrm{m}\,\alpha\,\frac{p}{\sqrt{\overline{T^+}\,T^-}}\,r_0^2\,\frac{J_1\,I}{\frac{k}{r_0}+\alpha_\mathrm{m}\,\alpha\,p\sqrt{\frac{2k_\mathrm{B}}{\pi\,T^-\,m}}}\mathbf{e}_z\,. \tag{3.59}$$

Here, comparison with (3.32) gives

$$\boxed{A_1^{(2)}=\frac{\alpha_\mathrm{m}\,J_1\,I}{\frac{k}{r_0}+\alpha_\mathrm{m}\,\alpha\,p\sqrt{\frac{2k_\mathrm{B}}{\pi\,T^-\,m}}}\,,} \tag{3.60}$$

which was already used in the continuum regime in sec. 2.10 with the second addend in the denominator neglected. For $J_1=\frac{1}{2}$ and $\alpha_\mathrm{m}=1$, this A_1 is equal to (3.50), based on the model of Hidy and Brock (1967) in the section before.

The asymmetry factor can be obtained for the case of nearly transparent and opaque particles. Therefore, Yalamov et al. (1976a) derive the normalized heat source function

(3.52). For a weakly absorbing particle (with $\frac{2\pi}{\lambda_{\mathrm{rad}} r_0} \ll 1$), they find ($\tilde{n} = \tilde{n}_{\Re} - \mathrm{i}\,\tilde{n}_{\Im}$ is the complex refractive index, λ_{rad} the wavelength)

$$|E(r,\mu)|^2 = \frac{3E_0^2}{|3+2\tilde{n}^2|^2}\left(3\left|3+2\tilde{n}^2\right|^2 - \frac{4\pi}{\lambda_{\mathrm{rad}}}\tilde{n}_{\Re}\,\tilde{n}_{\Im}\,r\,\mu\left(\left|3+2\tilde{n}^2\right|^2 - 5\right)\right)\,, \tag{3.61}$$

and for a strongly absorbing particle

$$|E(r,\mu)|^2 = \frac{E_0^2}{2\,|\tilde{n}|^2}\mathrm{e}^{-\frac{4\pi}{\lambda_{\mathrm{rad}}}\tilde{n}_{\Im}(r_0-r)}\left(\frac{9}{2} + \frac{25}{36}\left(1-2\mu^2\right)^2 - \frac{9\tilde{n}_{\Re}}{4\,|\tilde{n}|^2}\mu\right)\,. \tag{3.62}$$

3.3.3 Approximation introduced by Beresnev et al. (1993) and Chernyak and Beresnev (1993)

Beresnev et al. (1993) and Chernyak and Beresnev (1993) numerically calculated the photophoretic force for arbitrary Knudsen numbers and give a semi-analytic equation for the force for arbitrary Knudsen numbers based on a kinetic theory, beside the exact force in the *fm* regime. The photophoretic velocity was also determined for spheres with $r_0 > 0.01\,\mu$m, and Brownian motion neglected. They assume a slightly distorted Maxwell-Boltzmann velocity distribution to account for Knudsen numbers beyond the limit of the *fm* regime. Furthermore the results are given for particle temperatures slightly deviating from the gas temperature.

$$\sigma(\mathbf{r},\mathbf{v}) = n_\infty\,\sigma_{0,\infty}(\mathbf{r},\mathbf{v})\,[1+h(\mathbf{r},\mathbf{v})] \overset{(2.58)}{=} n_\infty\left(\frac{m}{2\pi k_{\mathrm{B}} T_\infty}\right)^{3/2}\mathrm{e}^{-\frac{mv^2}{2k_{\mathrm{B}}T_\infty}}\,(1+h(\mathbf{r},\mathbf{v}))\,, \tag{3.63}$$

which is discontinuous at the sphere's surface (Beresnev et al. 1987)

$$\sigma(\mathbf{r},\mathbf{v})|_{r=r_0} = \begin{cases}\sigma^+ & \mathbf{n}\cdot\mathbf{v} > 0\\ \sigma^- & \mathbf{n}\cdot\mathbf{v} < 0\end{cases}\,. \tag{2.31}$$

It is $p = n_\infty k_{\mathrm{B}} T_\infty$. The (dimensionless) perturbation function $h(\mathbf{r},\mathbf{v})$ is required to obey the following (dimensionless) differential equation

$$\mathbf{c}\cdot\boldsymbol{\nabla}_{\mathbf{s}} h(\mathbf{s},\mathbf{c}) = \nu + 2\mathbf{c}\cdot\mathbf{u} + \left(c^2+\frac{3}{2}\right)\tau + \frac{4}{5}(1-Pr)\left(c^2-\frac{5}{2}\right)\mathbf{c}\cdot\mathbf{S} - h(\mathbf{s},\mathbf{c})\,, \tag{3.64}$$

where $\mathbf{c}$ and $\mathbf{s}$ are the dimensionless gas particle velocity and position

$$\mathbf{c} := \left(\frac{m}{2k_{\mathrm{B}}T_\infty}\right)^{1/2}\mathbf{v} \tag{3.65a}$$

$$\mathbf{s} := \frac{2}{3}\frac{p}{Pr\,\eta_{\mathrm{dyn}}}\left(\frac{m}{2k_{\mathrm{B}}T_\infty}\right)^{1/2}\mathbf{r}\,, \tag{3.65b}$$

determined by the Prandtl number

$$Pr = \frac{\eta_{\mathrm{kin}}}{D_{\mathrm{th}}} = \frac{\eta_{\mathrm{dyn}}\,c_p}{k}\,. \tag{3.66}$$

The dynamic viscosity of the gas is assumed as

$$\eta_{\mathrm{dyn}} = \frac{1}{2} m\, n\, \overline{v}\, \lambda\ . \tag{3.67}$$

The mean free path of the gas particles together with the sphere's radius r_0 will lead to the introduction of the Knudsen number Kn in the subsequent considerations.

Since dimensionless variables are used —, instead of $\overline{f}$, here the mean value of a function $f = f(\mathbf{c})$ concerning the dimensionless Maxwell-Boltzmann distribution is abbreviated by

$$\mathcal{M}(f) = \pi^{-3/2} \int \mathrm{e}^{-c^2} f(c)\, \mathrm{d}^3 c\ . \tag{3.68}$$

The dimensionless variables ν (gas number density), $\mathbf{u}$ (macroscopic gas velocity), τ (temperature disturbances) and $\mathbf{S}$ (heat flow) in (3.64) are defined as

$$\nu = \frac{n - n_\infty}{n_\infty} = \mathcal{M}(h) \tag{3.69a}$$

$$\mathbf{u} = \left(\frac{m}{2k_{\mathrm{B}}T_\infty}\right)^{1/2} \mathbf{U} = \mathcal{M}(\mathbf{c}\, h) \tag{3.69b}$$

$$\tau = \frac{T - T_\infty}{T_\infty} = \mathcal{M}(2/3\, c^2\, h - h) \tag{3.69c}$$

$$\mathbf{S} = \left(\frac{m}{2k_{\mathrm{B}}T_\infty}\right)^{1/2} \frac{\mathbf{q}}{p_\infty} = \mathcal{M}(\mathbf{c}\, c^2\, h - 5/2\, \mathbf{c}\, h)\ . \tag{3.69d}$$

The two variables $\mathbf{q}$ and $\mathbf{U}$ denote the heat flow and the macroscopic gas velocity around the suspended particle.

Hermite polynomials H_μ are an orthogonal basis in a Hilbert space for square integrable functions with the measure e^{-x^2}, where the scalar product is defined as

$$(f\ ,\ g)_H = \int_{-\infty}^{\infty} f(x)\, g^*(x)\, \mathrm{e}^{-x^2}\, \mathrm{d}x\ . \tag{3.70}$$

The orthogonality relation is

$$(H_\mu\ ,\ H_\lambda)_H = 2^\mu \mu! \sqrt{\pi}\, \delta_{\mu\lambda}\ . \tag{3.71}$$

Hence, to obtain the unknown perturbation $h(\mathbf{s}, \mathbf{c})$, Beresnev et al. (1993) expanded $\sigma_{0,\infty}(\mathbf{s}, \mathbf{c})\, [1 + h(\mathbf{s}, \mathbf{c})]$ in the subspace + into Hermite polynomials, with the coefficients a_n (indices $\mathbf{n}$ and $\mathbf{n}$ refer to normal and tangential components)

$$\sigma^+(\mathbf{s}, \mathbf{c})\big|_{\partial V} = n_\infty\, \sigma_{0,\infty}(\mathbf{c})\, \left[1 + a_0 + a_{1\mathbf{n}}\, c_r + a_{1\mathbf{t}}\, c_\zeta + a_2(c^2 - 3/2) + \dots\right]\ . \tag{3.72}$$

The four expansion coefficients themselves are expanded in Legendre polynomials, e.g.

$$a_2(\zeta) = \sum_{\mu=0}^{\infty} a_{2,\mu}\, P_\mu(\cos\zeta)\ . \tag{3.73}$$

a_0, $a_{1\mathbf{n}}$, $a_{1\mathbf{t}}$ and a_2 are determined by four kinetic boundary conditions at the sphere's surface: mass conservation (no absorption), flux of tangential (ζ) and normal (r) momentum, and the flux of the translation energy

$$0 = \mathbf{n} \cdot \left[n^+(\mathbf{r},t)\,\overline{\mathbf{v}^+}(\mathbf{r},t) + n^-(\mathbf{r},t)\,\overline{\mathbf{v}^-}(\mathbf{r},t) \right] , \tag{2.37b}$$

$$0 = \mathbf{n} \cdot \left[\breve{\mathfrak{p}}_\zeta^+ + (1-\alpha_{\mathbf{t}})\breve{\mathfrak{p}}_\zeta^- \right] \tag{3.74a}$$

$$0 = \mathbf{n} \cdot \left[\breve{\mathfrak{p}}_r^+ | + \alpha_{\mathbf{n}}\, \breve{\mathfrak{p}}_r^{(0)} + (1-\alpha_{\mathbf{n}})\breve{\mathfrak{p}}_r^- \right] \tag{3.74b}$$

$$0 = \mathbf{n} \cdot \left[\breve{\boldsymbol{\mathcal{E}}}^+ + \alpha\, \breve{\boldsymbol{\mathcal{E}}}^{(0)} + (1-\alpha)\breve{\boldsymbol{\mathcal{E}}}^- \right] , \tag{3.74c}$$

thus three accommodation coefficients (normal and tangential momentum and energy) are used in this model.

Within this model, they derive the surface temperature as a function depending on α, Pr, Kn, k, k_{gas} and the expansion coefficients $a_{2,\mu}$, the latter one yet undetermined. Corresponding to (3.69c), the surface temperature of the sphere is considered a slight deviation from the gas temperature as

$$T(r = r_0, \zeta) \overset{(3.69c)}{=} T_\infty \left[1 + \tau(\zeta)\right] , |\tau| \ll 1 . \tag{3.75}$$

They solve the heat equation with the volumetric heat source function formulated like in sec. 3.3.2

$$k\Delta T = -\frac{4\pi}{\lambda_{\text{rad}}}\, \tilde{n}_{\Re}\, \tilde{n}_{\Im}\, I\, B(r, \cos\zeta) \tag{3.51}$$

with

$$B(r, \cos\zeta) = \left| E(r, \cos\zeta) \right|^2 / E_0^2 . \tag{3.52}$$

The boundary condition comprises of heat flux between particle and gas and thermal emission.

$$k\frac{\partial T}{\partial \mathbf{n}} = -\sigma_{\text{SB}}\, \varepsilon \left(T^4 - T_\infty^4 \right) - \mathbf{n} \cdot \mathbf{q} \qquad \text{at } \partial V , \tag{3.76}$$

where the general solution has the form

$$T(r = r_0, \zeta) = \sum_{\mu=0}^{\infty} \left(c_\mu + b_\mu \frac{r}{r_0} \right) \left(\frac{r}{r_0} \right)^\mu P_\mu(\cos\zeta) . \tag{3.77}$$

The surface temperature function τ was determined as

$$\tau(\zeta) = \sum_{\mu=0}^{\infty} \frac{4Pr\,\tilde{R}\left(\alpha\, a_{2,\mu} + (1-\alpha)\tilde{I}\, J_\mu \right)}{4Pr\,\tilde{R}\,(\alpha + (1-\alpha)\tilde{s}) + 5\sqrt{\pi}\mu(1-\alpha)\frac{k}{k_{\text{gas}}}} P_\mu(\cos\zeta) , \tag{3.78}$$

with $a_{2,\mu}$ from (3.73), the asymmetry factor J_μ from (3.105) and the three abbreviations

$$\tilde{R} = \frac{\sqrt{\pi}}{3Pr\,Kn} \tag{3.79}$$

$$\tilde{I} = I\sqrt{\frac{\pi m}{2k_{\text{B}}T_\infty}}/p \tag{3.80}$$

$$\tilde{s} = 4\varepsilon\sigma_{\text{SB}}T_\infty^4\sqrt{\frac{\pi m}{2k_{\text{B}}T_\infty}}/p . \tag{3.81}$$

Employing the kinetic integral equation (2.39) with the surface temperature, the photophoretic force can be derived. Therefore, ν in (3.69a), $\mathbf{u}$ in (3.69b) and $\mathbf{S}$ in (3.69d) are expanded into Legendre polynomials (associated Legendre polynomials for vectors), just like a_0, $a_{1\mathbf{n}}$, $a_{1\mathbf{t}}$ and a_2 before. Then — as the orthogonality relations for (associated) Legendre polynomials apply — the force is solely determined by first order coefficients. To obtain the expansion coefficients, the differential equation for h (3.64) was at first formally integrated (method of characteristics) with the help of the expansion of σ^+ (3.72), and the ensuing h inserted into the integrals for the dimensionless variables (3.69). The resulting four integrals and the kinetic boundary conditions (3.74) are transformed into another integral form (method of integral moments). Those new eight integral equations were eventually solved by the Bubnov-Garlekin method.

For the limit $Kn \to \infty$, i.e. the *fm* regime, they yield the photophoretic force with three accommodation coefficients

$$\mathbf{F}_{\text{phot}} = -\frac{\pi}{3}\,\varphi_1\,\frac{p}{T_\infty}\,r_0^2\,\frac{J_1\,I}{\frac{k}{r_0} + 4\varepsilon\sigma_{\text{SB}}T_\infty^3 + \varphi_2\,p\,\sqrt{\frac{2k_{\text{B}}}{\pi\,T_\infty\,m}}}\mathbf{e}_z\,, \tag{3.82a}$$

and the two accommodation functions

$$\varphi_1 = \frac{\alpha\,\alpha_{\mathbf{n}}}{1-\pi(9-\alpha)(1-\alpha_{\mathbf{n}})/32} \tag{3.82b}$$

$$\varphi_2 = \frac{\alpha(1-9\pi(1-\alpha_{\mathbf{n}})/32)}{1-\pi(9-\alpha)(1-\alpha_{\mathbf{n}})/32}\,. \tag{3.82c}$$

Comparing the result with (3.32) ($\frac{p}{T_\infty} \to \frac{p}{\sqrt{T^+T_\infty}}$) yields

$$\boxed{A_1^{(3)} = \frac{\frac{\varphi_1}{\alpha}J_1\,I}{\frac{k}{r_0} + \varphi_2\,p\,\sqrt{\frac{2k_{\text{B}}}{\pi\,T_\infty\,m}} + 4\varepsilon\sigma_{\text{SB}}T_\infty^3}\,,} \tag{3.83}$$

For total momentum accommodation $\alpha_{\mathbf{n}} = \alpha_{\mathbf{t}} = 1$, Beresnev et al. (1993) and Chernyak and Beresnev (1993) give a semi-analytic equation for arbitrary Knudsen numbers to describe their numerical calculations better than 3%.

$$\mathbf{F}_{\text{phot}} = -\frac{\pi}{3}\,\alpha\,r_0^2\,J_1\,I\,\sqrt{\frac{\pi m}{2k_{\text{B}}T_\infty}}\,\frac{\psi_1(Kn)}{\alpha + 15\frac{k}{k_{\text{gas}}}Kn(1-\alpha)/4 + \alpha\frac{k}{k_{\text{gas}}}\psi_2(Kn)}\mathbf{e}_z\,, \tag{3.84a}$$

with the two functions $\psi_1(Kn)$ and $\psi_2(Kn)$

$$\psi_1(Kn) = \frac{Kn}{Kn + 5\pi/18}\left(1 + \frac{2\pi^{1/2}Kn}{5Kn^2 + \pi^{1/2}Kn + \pi/4}\right) \tag{3.84b}$$

$$\psi_2(Kn) = \left(\frac{1}{2} + \frac{15}{4}Kn\right)\left(1 - \frac{1.21\pi^{1/2}Kn}{100Kn^2 + \pi/4}\right) \tag{3.84c}$$

This equation is also used in Beresnev et al. (2003c,a,b).

In Beresnev et al. (2012) the same scheme was re-employed to discuss forces on Janus-like spheres.

3.3.4 New I-r-k-based and T-based approximations

This subsection introduces two simple analytic equations to determine photophoretic forces with unprecedented accuracy from the illumination intensity I, thermal conductivity k and temperature differences, respectively. Both approximations apply for rotational-symmetric surface temperatures, ensuing in longitudinal photophoresis.

3.3.4.1 New T-based approximation

The temperature-based approximation is based on the square root of the maximum and minimum temperatures along a spherical particle with rotationally symmetric temperature distribution. In sec. 3.1.3.3 the general solution in case of a sphere with rotational symmetric temperature field was already given by

$$\mathbf{F}_{\text{phot}} = -\frac{2\pi}{3}\frac{p}{\sqrt{T^-}}\, r^2\, t_1 \mathbf{e}_z \ . \tag{3.28}$$

The most frequently used approximations from the previous sections, which all are based on

$$\mathbf{F}_{\text{phot}} \approx -\frac{\pi}{3}\,\alpha\,\frac{p}{T^-}\, r^2\, A_1 \mathbf{e}_z \ , \tag{3.32}$$

i.e. the linearization of the square root at T^-. Both basis-approximations mainly differ in the expansion coefficient used: A_1 is the first coefficient of a Legendre series of T, whereas t_1 is the respective coefficient for τ as defined in (3.12a)

$$\tau := \sqrt{T^+} \qquad \text{, e.g. with (2.114) } \tau = \sqrt{T^- + \alpha\,(T - T^-)}\ .$$

Restating again, in Rohatschek (1995) the square root in (2.87) was linearized, explaining why the approximation used by Rohatschek (1995) only yields an approximate value (denoted by '≈').

As well as the coefficient A_1, its counterpart t_1 is usually unknown. One way to receive both, is a Legendre series fit of the (reduced) temperature. Exemplary calculations showed that in this case it is usually enough to use terms up to degree 25 for exact calculations, but this is not helpful for actual measurements. Instead a good ansatz is just to heuristically consider

$$t_1 :\approx \frac{1}{2}\Delta\tau = \frac{1}{2}\left(\tau\left(T_{\max}\right) - \tau\left(T_{\min}\right)\right) \ , \tag{3.85}$$

which is similar to the existing approximation (3.36)

$$A_1 \approx \frac{1}{2}\Delta T \ .$$

This is a reasonable approximation, since $P_1(x) \equiv x$ and thus t_1 represents something like $\frac{1}{2}\partial_x f|_{x_0}$ in a Taylor expansion of $f(x) = x_0 + \frac{1}{2}\partial_x f|_{x_0}\,(x - x_0) + \dots$), leading to a new handy approximation

$$\boxed{\tilde{F}^{(\tau)} = \frac{\pi}{3}\frac{p}{\sqrt{T^-}}\, r^2 \Delta\tau \ ,} \tag{3.86}$$

with, e.g. for thermal accommodation (2.114)

$$\Delta\tau = \sqrt{\alpha\, T_{\max} + T^-\,(1-\alpha)} - \sqrt{\alpha\, T_{\min} + T^-\,(1-\alpha)}\ .$$

3.3.4.2 New *I*-*r*-*k* approximation

The approximation can be obtained in two ways, only differing in the formulation of the heat transfer problem. In both cases the kinetic model for the *fm* regime is the same, consisting of velocity distributions based on Maxwell-Boltzmann distributions and thermal and momentum accommodation (α and α_m)

$$\sigma^-(\mathbf{v}) = n\,\sigma_0^-(\mathbf{v}) = n\left(\frac{m}{2\pi k_\mathrm{B} T^-}\right)^{3/2} e^{-\frac{mv^2}{2k_\mathrm{B}T^-}} \tag{3.87a}$$

$$\sigma^+(\mathbf{v}) = \alpha_\mathrm{m}\, n^+\left(\frac{m}{2\pi k_\mathrm{B} T^+}\right)^{3/2} e^{-\frac{mv^2}{2k_\mathrm{B}T^+}} + (1-\alpha_\mathrm{m})\;\sigma^-\left(\mathbf{v}_0^+\right) \tag{3.87b}$$

$$T^+ = T^- + \alpha\left(T - T^-\right)\ , \tag{2.114}$$

as well as with the surface-gas boundary condition for the mass continuity

$$n^+\,\overline{v_\mathbf{n}^+} = -n\,\overline{v_\mathbf{n}^-}\ . \tag{2.37b}$$

It is $T^- = T_\infty$ and $n = n_\infty$. With these three equations the basic force equation (2.32) yields the photophoretic force integral as

$$\mathbf{F}_\mathrm{phot} = -\pi r_0^2\, p\,\alpha_\mathrm{m} \int_{-1}^{1} \sqrt{\frac{T^+}{T^-}}\,\mu\,\mathrm{d}\mu\,\mathbf{e}_z\ . \tag{3.88}$$

In both heat transfer problems, the concerning ansatz is chosen insofar, that in both cases the surface temperature can be expressed by the simple Legendre expansion

$$T(r_0,\zeta) = \sum_{\nu=0}^{\infty} \tilde{A}_\nu\, P_\nu(\cos\zeta)\ , \tag{3.89}$$

and the linearization of the square root in (3.88) at $\overline{T^+}$ while using thermal accommodation (2.114) yields (along (3.32), see beginning of sec. 3.3)

$$\mathbf{F}_\mathrm{phot} \overset{(2.114)}{\approx} -\frac{\pi}{3}\,\alpha\,\alpha_\mathrm{m}\frac{p}{\sqrt{T^-\overline{T^+}}}\,r_0^2\,\tilde{A}_1\,\mathbf{e}_z \tag{3.90}$$

$$\overline{T^+} = T^- + \alpha\left(\overline{T} - T^-\right)\ . \tag{3.91}$$

By construction, this equation — where the force is only determined by the first expansion coefficient of the sphere's temperature — can be used for both heat transfer problems.

In the following, the force will be obtained in two ways for the thermal radiation term $\sigma_\mathrm{SB}\varepsilon\,(T^4 - T_\infty^4)$ implemented into the boundary conditions. This is differently done than in Beresnev et al. (1993) and Chernyak and Beresnev (1993), because the untouched structure of this term effectively introduces infinite mixed terms of expansion coefficients from the ansatz function. Therefore, this term is linearized at the black-body temperature (3.35) as

$$\left(T^4 - \left(T_\mathrm{gas}^\mathrm{rad}\right)^4\right) \approx 4T\,T_\mathrm{bb}^3 - \left(T_\mathrm{gas}^\mathrm{rad}\right)^4 - 3T_\mathrm{bb}^4\ . \tag{3.92}$$

This will now be implemented in the boundary conditions.

For the case that the absorption of the incident light is assumed as two-dimensional, the source can be implemented in the boundary condition, like in Hidy and Brock (1967) and Tong (1973)

$$k\frac{\partial T}{\partial \mathbf{n}} = I\,\Theta(\pi/2-\zeta)\,\cos\zeta - \mathbf{n}\cdot\left[\breve{\boldsymbol{\varepsilon}}^{+} + \breve{\boldsymbol{\varepsilon}}^{-}\right] - \sigma_{\mathrm{SB}}\varepsilon\left(4T\,T_{\mathrm{bb}}^{3} - \left(T_{\mathrm{gas}}^{\mathrm{rad}}\right)^{4} - 3T_{\mathrm{bb}}^{4}\right) \qquad \text{at } \partial V\ , \tag{3.93}$$

and the heat equation turns into the Laplace equation

$$k\Delta T = 0\ . \tag{3.37}$$

The ansatz for this heat transfer problem is chosen as

$$T(r,\zeta) = \sum_{\nu=0}^{\infty} \tilde{A}_{\nu}\left(\frac{r}{r_0}\right)^{\nu} P_{\nu}(\cos\zeta)\ . \tag{3.94}$$

Inserted into the boundary condition (3.93), an infinite sum is obtained, whose addends are linear in the Legendre polynomials P_ν. As the P_ν form a basis in the space of the polynomials, those addends with a Legendre polynomial of the same order have to yield zero independently. Generally, those conditions, which have to be independently zero, can be found by integrating the whole equation with any Legendre polynomial in $[-1,1]$. Thus, the ν-th condition is ($h = \alpha_{\mathrm{m}}\,\alpha\,p\,\sqrt{\frac{2k_{\mathrm{B}}}{\pi\,T^{-}\,m}}$)

$$I\,c_\nu + \frac{2\delta_{n,0}\left(hT^{-} + \sigma_{\mathrm{SB}}\varepsilon\left(\left(T_{\mathrm{gas}}^{\mathrm{rad}}\right)^{4} + 3T_{\mathrm{bb}}^{4}\right)\right)}{2\nu+1} - \tilde{A}_\nu\frac{2}{2\nu+1}\left(h + 4\sigma_{\mathrm{SB}}\varepsilon T_{\mathrm{bb}}^{3} + \frac{\nu\,k}{r_0}\right) = 0\ . \tag{3.95}$$

The coefficient c_ν is the integral (A.16) of the two Legendre polynomials $P_1\,P_\nu$ in the half-space $[0,1]$

$$c_\nu \overset{(A.16)}{=} \int_0^1 P_1(x)P_\nu(x)\,\mathrm{d}x = \begin{cases} \frac{1}{3} & \nu = 1 \\ \frac{\Gamma\left(\frac{\nu}{2}+\frac{1}{2}\right)\cos\left(\frac{\nu\pi}{2}\right)}{(1-\nu)(\nu+2)\sqrt{\pi}\,\Gamma\left(\frac{\nu}{2}+1\right)} & \nu \text{ even} \\ 0 & \text{else,} \end{cases}$$

and arises from $\Theta(\pi/2-\zeta)\,\cos\zeta$ in the source addend of the boundary condition. $\tilde{A}_1$ reads

$$\tilde{A}_1 = \frac{1}{2}\frac{I}{\frac{k}{r_0} + \alpha_{\mathrm{m}}\,\alpha\,p\,\sqrt{\frac{2k_{\mathrm{B}}}{\pi\,T^{-}\,m}} + 4\sigma_{\mathrm{SB}}\varepsilon\,T_{\mathrm{bb}}^{3}}\ , \tag{3.96}$$

and the force is

$$\mathbf{F}_{\mathrm{phot}} \approx -\frac{\pi}{6}\,\alpha\,\alpha_{\mathrm{m}}\frac{p}{\sqrt{\left(T^{-}\right)^{2} + \alpha\left(T_{\mathrm{bb}} - T^{-}\right)T^{-}}}\,r_0^2\,\frac{I}{\frac{k}{r_0} + \alpha_{\mathrm{m}}\,\alpha\,p\,\sqrt{\frac{2k_{\mathrm{B}}}{\pi\,T^{-}\,m}} + 4\sigma_{\mathrm{SB}}\varepsilon\,T_{\mathrm{bb}}^{3}}\mathbf{e}_z\ . \tag{3.97}$$

Here, comparison with (3.32) gives

$$\boxed{A_1 = \frac{1}{2}\frac{\alpha_{\mathrm{m}}\,\alpha\,I}{\frac{k}{r_0} + \alpha_{\mathrm{m}}\,\alpha\,p\,\sqrt{\frac{2k_{\mathrm{B}}}{\pi\,T^{-}\,m}} + 4\sigma_{\mathrm{SB}}\varepsilon\,T_{\mathrm{bb}}^{3}}\ .} \tag{3.98}$$

The other, general case is to consider the inhomogeneous heat equation

$$k\Delta T = -I\, q(r, \cos\zeta) \tag{3.99}$$

e.g., with

$$q(r, \cos\zeta) \overset{(3.51)}{=} \frac{4\pi}{\lambda_{\text{rad}}} \tilde{n}_{\Re}\, \tilde{n}_{\Im}\, B(r, \cos\zeta) \tag{3.100}$$

$$B(r, \cos\zeta) = |E(r, \cos\zeta)|^2 / E_0^2 \,, \tag{3.52}$$

where the absorption takes place anywhere in the sphere itself. The boundary condition reduces to

$$k\frac{\partial T}{\partial \mathbf{n}} = -\mathbf{n} \cdot \left[\breve{\boldsymbol{\mathcal{E}}}^{+} + \breve{\boldsymbol{\mathcal{E}}}^{-}\right] - \sigma_{\text{SB}}\varepsilon \left(4T\, T_{\text{bb}}^3 - \left(T_{\text{gas}}^{\text{rad}}\right)^4 - 3T_{\text{bb}}^4\right) \qquad \text{at } \partial V \,. \tag{3.101}$$

The solution for this heat transfer problem is composed of the solution of the homogeneous and the inhomogeneous heat transfer equation

$$T = T_{\text{hom}} + T_{\text{inhom}} \,. \tag{3.102}$$

The ansatz for the homogeneous solution is

$$T_{\text{hom}}(r, \zeta) = \sum_{\nu=0}^{\infty} \left(\tilde{A}_\nu - \tilde{B}_\nu\, J_\nu(r_0)\right) \left(\frac{r}{r_0}\right)^\nu P_\nu(\cos\zeta) \,, \tag{3.103}$$

and the one for the inhomogeneous/particular solution is

$$T_{\text{inhom}}(r, \zeta) = \sum_{\nu=0}^{\infty} \tilde{B}_\nu\, J_\nu(r)\, P_\nu(\cos\zeta) \,. \tag{3.104}$$

The homogeneous solution is nearly the same as before, only modified with term $-\tilde{B}_\nu\, J_\nu(r_0)$, which arises from the motivation to describe the surface temperature by

$$T(r_0, \zeta) = \sum_{\nu=0}^{\infty} \tilde{A}_\nu P_\nu(\cos\zeta) \quad (3.89)$$

(see beginning of sec. 3.3.), so that the linearized equation for the force (3.90) can be used here, too. The function $J_\nu(r)$ is the asymmetry factor, defined as (Yalamov et al. 1976b) (with $x := \cos\zeta$)

$$q_\nu(r) \overset{(2.22)}{=} \frac{2\nu+1}{2} \left(q(r, x)\,,\, P_\nu\right)_{[-1,1]} \tag{3.105a}$$

$$J_\nu(r) = \frac{1}{r_0}\left[r^{-\nu-1} \int_0^r s^{\nu+2} q_\nu(s)\, \mathrm{d}s + r^\nu \int_r^{r_0} s^{\nu-1} q_\nu(s)\, \mathrm{d}s\right] \tag{3.105b}$$

$$J_\nu \equiv J_\nu(r_0) = \int_0^{r_0} \left(\frac{r}{r_0}\right)^{\nu+2} q_\nu(r)\, \mathrm{d}r \,. \tag{3.105c}$$

$J_\nu(r)$ is a direct result of the variation of parameters, after the heat equation was transformed into an ordinary differential equation by integrating it with $\frac{2n+1}{2}P_\nu(x)$ in $[-1,1]$. Details can be found in Mackowski (1989). $\tilde{B}_\nu$ is determined by the condition $k\Delta T_{\text{inhom}} = -I\,q(r,\cos\zeta)$ as

$$\tilde{B}_\nu = \frac{I\,r_0}{k(2\nu+1)}\,. \tag{3.106}$$

The $\tilde{A}_\nu$ have to be obtained from the boundary condition (3.101) in the same manner as above, i.e. by integrating it with the respective Legendre polynomial P_ν in $[-1,1]$, yielding the ν-th condition ($h = \alpha_\text{m}\,\alpha\,p\,\sqrt{\frac{2k_\text{B}}{\pi\,T^-\,m}}$)

$$\begin{aligned}\frac{2}{k(2\nu+1)^2}\Big(&-r_0^{-1}(\tilde{A}_\nu(2\nu+1)k - I\,r_0\,J_\nu(r_0))\left(r_0\left(h+4\sigma_\text{SB}\varepsilon T_\text{bb}^3\right)+k\nu\right)-\\ &-Ir_0\left(J_\nu(r_0)\left(h+4\sigma_\text{SB}\varepsilon T_\text{bb}^3\right)-\frac{k(\nu+1)J_\nu(r_0)}{r_0}\right)\Big)+\\ &+\frac{2}{2\nu+1}\delta_{\nu,0}\left(hT^- + \sigma_\text{SB}\varepsilon\left(\left(T_\text{gas}^\text{rad}\right)^4+3T_\text{bb}^4\right)\right)=0\,.\end{aligned} \tag{3.107}$$

The expansion coefficients yield ($J_\nu \equiv J_\nu(r_0)$)

$$\tilde{A}_\nu = \frac{I\,J_\nu}{\nu\frac{k}{r_0}+\alpha_\text{m}\,\alpha\,p\,\sqrt{\frac{2k_\text{B}}{\pi\,T^-\,m}}+4\sigma_\text{SB}\varepsilon\,T_\text{bb}^3} \qquad \nu\geq 1 \tag{3.108a}$$

$$\tilde{A}_0 = \frac{\alpha_\text{m}\,\alpha\,p\,\sqrt{\frac{2k_\text{B}\,T^-}{\pi\,m}}+\sigma_\text{SB}\varepsilon\left(3T_\text{bb}^4+\left(T_\text{gas}^\text{rad}\right)^4\right)+I\,J_0}{\alpha_\text{m}\,\alpha\,p\,\sqrt{\frac{2k_\text{B}}{\pi\,T^-\,m}}+4\sigma_\text{SB}\varepsilon\,T_\text{bb}^3}\,. \tag{3.108b}$$

The linearization of the square root at $\overline{T^+}$ lets only $\tilde{A}_1$ contribute, and the force is therefore

$$\boxed{\begin{aligned}\mathbf{F}_\text{phot} &\overset{(3.90)}{\approx} -\frac{\pi}{3}\,\alpha\,\alpha_\text{m}\frac{p}{\sqrt{T^-\overline{T^+}}}\,r_0^2\,\frac{I\,J_1}{\frac{k}{r_0}+h+4\sigma_\text{SB}\varepsilon\,T_\text{bb}^3}\mathbf{e}_z\,.\\ \overline{T^+} &= T^- + \alpha\left(T_\text{bb}-T^-\right)\\ T_\text{bb} &= \sqrt[4]{\frac{I}{4\sigma_\text{SB}}+\left(T_\text{gas}^\text{rad}\right)^4} \qquad (3.35)\\ h &= \alpha_\text{m}\,\alpha\,p\,\sqrt{\frac{2k_\text{B}}{\pi\,T^-\,m}}\end{aligned}} \tag{3.109}$$

Eventually, comparison with (3.32) gives

$$\boxed{A_1^{(4)} = \frac{\alpha_\text{m}\,I\,J_1}{\frac{k}{r_0}+\alpha_\text{m}\,\alpha\,p\,\sqrt{\frac{2k_\text{B}}{\pi\,T^-\,m}}+4\sigma_\text{SB}\varepsilon\,T_\text{bb}^3}\,.} \tag{3.110}$$

For $T_\text{gas}^\text{rad} = T^- = 280\,\text{K}$, $p = 1\,\text{Pa}$ and $I = 20\,\text{kW/m}^2$ it is $p\,\sqrt{\frac{2k_\text{B}}{\pi\,T^-\,m}} = 2.87\,\frac{\text{W}}{\text{m}^2}\text{K}$ and $4\sigma_\text{SB}\varepsilon\,T_\text{bb}^3 = 38.6\,\frac{\text{W}}{\text{m}^2}\text{K}$. Basically, all shown I-r-k approximations scale with r_0^2. For small r_0, k/r_0 dominates the denominator and the scaling is effectively r_0^3. In this environment and for this equation this would mean $k \gtrsim 1\,\text{W/mK}$ and $r \lesssim 1\,\text{mm}$, for instance. For lower thermal conductivities and larger particles, the scaling reduces to r_0^2.

Perfectly absorbing particle: Obtaining J_1 remains a challenge. In sec. 3.2 a couple of papers have been mentioned where J_1 was determined, e.g., for Mie scattering, which would also determine the normalized source function q to $q(r, \cos\zeta) = \frac{4\pi}{\lambda_{\mathrm{rad}}} \tilde{n}_{\Re}\, \tilde{n}_{\Im}\, B(r, \cos\zeta)$. For perfectly absorbing particles in the limit of infinite absorption coefficients, the entire radiation is deposited at the surface, which was previously discussed. Nevertheless, for such a perfectly absorbing sphere this special case can also be expressed by usage of the boundary condition (3.93) as

$$q(r, \cos\zeta) = \delta(r - r_0)\, \Theta(\pi/2 - \zeta)\, \cos\zeta \ . \tag{3.111}$$

As the first Legendre expansion coefficient of q is

$$q_1(r) = \frac{1}{2}\delta(r - r_0) \ , \tag{3.112}$$

and thus the asymmetry factor yields

$$J_1 = \frac{1}{2} \ , \tag{3.113}$$

which is a well-known result. In summary, for $J_1 = \frac{1}{2}$, (3.110) confirms (3.98).

3.3.5 Evaluation of approximations for spheres

To describe transport and sorting processes by photophoresis with the help of the approximations, they have to undergo a validity check in a certain parameter range, which was done in Loesche and Wurm (2012) for

$$\tilde{F}^{(1)}(\Delta T, \alpha) = \frac{\pi}{6}\, \alpha\, \frac{p}{T^-}\, r^2\, \Delta T \tag{3.114a}$$

$$\tilde{F}^{(2)}(I, r, k, \alpha) = \frac{\pi}{6}\, \alpha\, \frac{p}{T^-}\, r^3\, \frac{I}{k} \tag{3.114b}$$

$$\tilde{F}^{(4)}(I, r, k, T_{\mathrm{bb}}, \alpha) = \frac{\pi}{6}\, \alpha\, \frac{p}{T^-}\, \frac{r^2\, I}{\frac{k}{r} + 4\sigma_{\mathrm{SB}}\, T_{\mathrm{bb}}^3} \tag{3.114c}$$

with 880 parameter combinations in r, k and α. I, T^- and $T_{\mathrm{gas}}^{\mathrm{rad}}$ were chosen to be constant at $20\,\mathrm{kW/m^2}$ (directed illumination) and normal temperature to resemble laboratory conditions. It has to be noted, that those three equation are valid for $1/\sqrt{T^-\overline{T^+}} \to 1/T^-$ (see sec. 3.3). In Loesche and Wurm (2012) the temperature of the spheres is much greater than the gas temperature, therefore the condition $\overline{T^+} \to T^-$ for accuracy of those equations is not given anymore. Unfortunately, during the time the publication was in work, other equations describing the photophoretic force exerted on spheres were not known. However, the error introduced this way are anyway suppressed with the correction factors $\chi^{(a)}$ introduced in the same publication (also see beginning of sec. 3.3.6). As outlined at the beginning of sec. 3.3, a better way to improve the quality of the approximations is to use the factor $p/\sqrt{T^-\overline{T^+}}$ for the general case

$$\mathbf{F}_{\mathrm{phot}} \approx -\frac{\pi}{3}\, \alpha\, \frac{p}{\sqrt{(T^-)^2 + \alpha\,(T_{\mathrm{bb}} - T^-)\, T^-}}\, r^2\, A_1\, \mathbf{e}_z \ , \tag{3.32}$$

instead of p/T^-. $T_{\rm bb} := \sqrt[4]{\frac{I}{4\sigma} + \left(T_{\rm gas}^{\rm rad}\right)^4}$ is the black body temperature previously defined in (3.35).

Another parameter sweep for accuracy checks was performed for 9,622,800 different parameter combinations in r, k, α, I, T^- and $T_{\rm gas}^{\rm rad}$ for the three approximations above plus

$$\tilde{F}^{(\tau)} = \frac{\pi}{3}\frac{p}{\sqrt{T^-}}\, r^2 \Delta\tau \tag{3.115a}$$

$$\tilde{F}^{(1a)}(\Delta T, \alpha) = \frac{\pi}{6}\,\alpha\,\frac{p}{\sqrt{(T^-)^2 + \alpha\,(T_{\rm bb} - T^-)\,T^-}}\, r^2\,\Delta T \tag{3.115b}$$

$$\tilde{F}^{(2a)}(I, r, k, \alpha) = \frac{\pi}{6}\,\alpha\,\frac{p}{\sqrt{(T^-)^2 + \alpha\,(T_{\rm bb} - T^-)\,T^-}}\, r^3\,\frac{I}{k} \tag{3.115c}$$

$$\tilde{F}^{(3)}(I, r, k, T_{\rm gas}^{\rm rad}, \alpha) = \frac{\pi}{6}\,\alpha\,\frac{p}{T^-}\,\frac{r^2\,I}{\frac{k}{r} + 4\sigma_{\rm SB}\,(T^-)^3} \tag{3.115d}$$

$$\tilde{F}^{(3a)}(I, r, k, T_{\rm gas}^{\rm rad}, \alpha) = \frac{\pi}{6}\,\alpha\,\frac{p}{\sqrt{(T^-)^2 + \alpha\,(T_{\rm bb} - T^-)\,T^-}}\,\frac{r^2\,I}{\frac{k}{r} + 4\sigma\,(T^-)^3}\,. \tag{3.115e}$$

$$\tilde{F}^{(4a)}(I, r, k, T_{\rm bb}, \alpha) = \frac{\pi}{6}\,\alpha\,\frac{p}{\sqrt{(T^-)^2 + \alpha\,(T_{\rm bb} - T^-)\,T^-}}\,\frac{r^2\,I}{\frac{k}{r} + 4\sigma\,T_{\rm bb}^3}\,. \tag{3.115f}$$

(3.115d) is the original equation obtained by Beresnev et al. (1993) and Chernyak and Beresnev (1993), and (3.115e) is the modified one $p/T^- \to p/\sqrt{T^-\overline{T^+}}$. The surface temperatures were obtained from COMSOL (v4.1 and v4.3b) along the scenario shown in Figure 3.6. COMSOL is a finite element method based software suite that enables to solve (custom) partial differential equation systems, including weak boundary conditions to calculate better more accurate fluxes, but it also includes several ready-to-use modules, for instance a model with surface-to-surface radiation ($\propto T^4$).

The governing equation used for determining a sphere's surface temperatures is the sourceless stationary heat equation (2.2) with constant heat conductivity (Laplace equation)

$$k\Delta T = 0\,. \tag{3.37}$$

A Neumann boundary condition along (3.93), describing the full absorption of the incident light and thermal emission to a heat bath at $T_{\rm gas}^{\rm rad}$ was used in all calculations with COMSOL, including Loesche and Wurm (2012) and Loesche et al. (2013, 2014)

$$k\frac{\partial T}{\partial \mathbf{n}}\bigg|_{r=r_0} = I\,\Theta(-\mathbf{e}_I\cdot\mathbf{n})\,\mathbf{e}_I\cdot\mathbf{n} - \sigma_{\rm SB}\left(T^4 - \left(T_{\rm gas}^{\rm rad}\right)^4\right)\,, \tag{3.116}$$

where the direct gas-particle heat transfer $-\mathbf{n}\cdot\left[\check{\boldsymbol{\mathcal{E}}}^+ + \check{\boldsymbol{\mathcal{E}}}^-\right] = -h(T - T^-)$ was not considered as it is effectively contributing for higher pressures, which would necessarily require a smaller radius of the described spheres to remain in the *fm* regime, such as aerosols. Additionally, this work focused on protoplanetary disks with low pressures and mm- and

sub-mm sized particles, therefore this term can be ignored, and the heat transfer coefficient h in all the photophoresis approximations can be omitted, too.

Exemplary temperature distributions $T(\zeta)$ are plotted in Figure 3.7. The exact ensuing photophoretic force was calculated by the respective integral equations for the subjacent kinetic model with thermal accommodation (2.114) only and an emissivity ε of 1. Momentum accommodation included in the new model and those of Yalamov et al. (1976a) and Beresnev et al. (1993) and Chernyak and Beresnev (1993) is not considered and therefore the coefficients α_m, $\alpha_\mathbf{n}$ are set to 1. Hence, all the integrals for a sphere reduce to (3.29) with thermal accommodation (2.114).

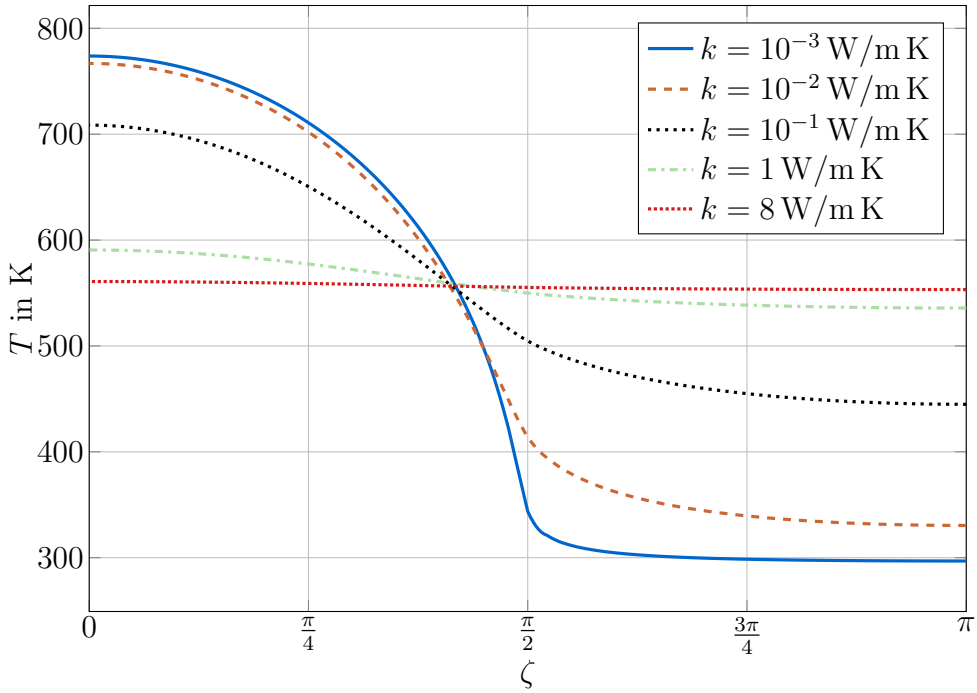

Figure 3.7: Temperature distribution across the surface of a sphere with $r = 0.66\,\mathrm{mm}$ at different thermal conductivities, along the model setup in Figure 3.6. Data from (Loesche and Wurm 2012).

For the given parameter range (see Table 3.1), Figures 3.8, 3.9, and 3.10, and Table 3.2 show clearly the advantage of the factor $p/\sqrt{T^-\overline{T^+}}$ (all equations with labels (ia)) for surface temperatures exceeding the value of the surrounding gas $T > T^-$. Those approximations with the factor p/T^- have a strong spread and can deviate strongly from the real value. The unprecedented accuracy of the two new approximation equations $\tilde{F}^{(4a)}$ and $\tilde{F}^{(\tau)}$ is indicated by the strong peaks at $F/\tilde{F}^{(i)} = 1$ with almost $4.25 \cdot 10^6$ counts at a bin size of 0.005 (0.5%), thus for about half of the 9,622,800 parameter tupels in the parameter range in Table 3.1 $\tilde{F}^{(4a)}$ and $\tilde{F}^{(\tau)}$ give the exact value. Only the ΔT-based equation $\tilde{F}^{(1a)}$ with the factor $p/\sqrt{T^-\overline{T^+}}$ comes close to this, and no further modification of the expansion coefficient A_1 would be necessary. All three relative error histograms are also quite narrow in comparison to the approximations $\tilde{F}^{(1)}$, $\tilde{F}^{(2)}$, $\tilde{F}^{(2a)}$, $\tilde{F}^{(3)}$, $\tilde{F}^{(3a)}$ whose relative error histograms peak at much lower values and overestimate the true photophoretic force. The statistical properties of all four histograms are listed in Table

Table 3.1: Parameter range used (9,622,800 combinations).

parameter	values
r	{0.00011, 0.00022, 0.00033, 0.00044, 0.00055, 0.00066, 0.00077, 0.00088, 0.00099, 0.0011, 0.00132, 0.00154, 0.00176, 0.00198, 0.0022, 0.00242, 0.00264, 0.00286, 0.00308, 0.0033, 0.00352, 0.00374, 0.00396, 0.00418, 0.0044, 0.00462, 0.00484, 0.00506, 0.00528, 0.0055, 0.00572, 0.00594, 0.00616, 0.00638, 0.0066, 0.00682, 0.00704, 0.00726, 0.00748, 0.0077, 0.00792, 0.00814, 0.00836, 0.00858, 0.0088, 0.00902, 0.00924, 0.00946, 0.00968, 0.0099, 0.01012, 0.01034, 0.01056, 0.01078, 0.011} m
k	{0.001, 0.002, 0.003, 0.004, 0.005, 0.006, 0.007, 0.008, 0.009, 0.01, 0.02, 0.03, 0.04, 0.05, 0.06, 0.07, 0.08, 0.09, 0.1, 0.15, 0.2, 0.3, 0.4, 0.5, 0.6, 0.7, 0.8, 0.9, 1, 2, 3, 4, 5, 6, 7, 8} W/(K m)
α	0.1 . . . 1 in 0.1
I	$\{0.5, 1, 1.364, 5, 10, 20, 40\}$ kW/m^2
T^-	$\{10, 50, 100, 150, 200, 250, 293.15, 300, 350\}$ K
$T_{\text{gas}}^{\text{rad}}$	$\{0, 50, 100, 150, 200, 250, 293.15, 300, 350\}$ K

3.2. It has to be noted, that in the given parameter range $F/\tilde{F}^{(\tau)}$ has the smallest standard deviation, closely followed by $F/\tilde{F}^{(1a)}$ and $F/\tilde{F}^{(4a)}$.

From Figure 3.9 it is evident, that approximation $\tilde{F}^{(2)}$, given by (3.114b) has the lowest quality in the given parameter range. This is especially critical, since it expresses the photophoretic force in terms of particle radius r, thermal conductivity k and irradiation intensity I and is hence excessively used in analytic calculations and estimations, e.g. like in Krauss and Wurm (2005) and Wurm and Krauss (2006) and Wurm et al. (2010) to discuss potential transport and sorting processes in the solar nebula.

An improvement to $\tilde{F}^{(2)}$ is $\tilde{F}^{(3)}$ found by Beresnev et al. (1993), which itself is exceeded in quality by the new equation $\tilde{F}^{(4)}$. Both are modified versions of $\tilde{F}^{(2)}$ and account for thermal radiation. The relative error histogram of $\tilde{F}^{(4)}$ is nearly the same as for $\tilde{F}^{(1)}$ in the parameter range analyzed. $\tilde{F}^{(2a)}$ slightly peaks at 1, but is still widely smeared out, rendering this equation quite unreliable for analytical treatments. That means, the factor $p/\sqrt{T^-\overline{T^+}}$ together with the radiation term T_{bb} from $\tilde{F}^{(4)}$ is responsible for the very high quality of $\tilde{F}^{(4a)}$. $\tilde{F}^{(4a)}$ is subsequently the I-r-k-dependent approximation with the highest quality at this point. $\tilde{F}^{(3)}$ and $\tilde{F}^{(3a)}$ are only not notably performing better than their counterparts $\tilde{F}^{(2)}$ and $\tilde{F}^{(2a)}$. The reason is the heat transfer boundary condition Beresnev et al. (1993) used, whereas the kinetic basis remains the most detailed on amongst all the *fm*-approximations discussed in this work.

The findings above render the approximations $\tilde{F}^{(1)}$, $\tilde{F}^{(2)}$, $\tilde{F}^{(2a)}$, $\tilde{F}^{(3)}$ and $\tilde{F}^{(3a)}$ quite unreliable for further use.In principle, their accuracy can be improved with the help of a correction factor $\chi^{(i)}$, which on one hand is valid for a certain parameter range and on the other hand keeps the manageability of the analytic approximations above. This was also done before for fixed $T^-, T_{\text{gas}}^{\text{rad}}$ and I for the approximations (3.114) in Loesche and Wurm (2012) and is briefly shown in the following section.

Concerning the 9,622,800 different parameter combinations of $r, k, I, \alpha, T^-, T_{\text{gas}}^{\text{rad}}$, that were used for the evaluation of the approximations (3.115), no correction could be found to improve their quality. $\tilde{F}^{(4a)}$ does perfectly well for $k \geq 1\,\text{W/(m K)}$, but underestimates

the force up to 53% for $k < 1\,\mathrm{W/(m\,K)}$. The maximum overestimation is only 7.5% . Hence, there is still a need for another correction factor depending on all six variables r, k, α, I, T^- and $T_{\mathrm{gas}}^{\mathrm{rad}}$, which is a task for the future. However, at the moment, $\tilde{F}^{(4a)}$ performs best among the equations depending on I and k compared to similar ones used before in recent literature.

Table 3.2: Statistical properties of old and newly introduced approximations for 9,622,800 values. High-quality equations are highlighted in bold letters and figures. Approximations with indexing numbers use the factor p/T^-, those with numbers and the letter 'a' as index use the factor $p/\sqrt{T^-\overline{T^+}}$.

	origin	mean	median	STD	skewness	min	max
$\boldsymbol{F/\tilde{F}^{(\tau)}}$	**sec. 3.3.4.1**	**1.05**	**1.01**	**0.07**	**1.39**	**0.95**	**1.31**
$F/\tilde{F}^{(1)}$	Rohatschek (1995)	0.79	0.87	0.27	-0.79	0.13	1.70
$\boldsymbol{F/\tilde{F}^{(1a)}}$		**1.05**	**1.00**	**0.09**	**1.88**	**0.95**	**1.57**
$F/\tilde{F}^{(2)}$	Rohatschek (1995)	0.47	0.45	0.33	0.16	0.00	1.27
$F/\tilde{F}^{(2a)}$	Yalamov et al. (1976a)	0.61	0.74	0.36	-0.43	0.00	1.00
$F/\tilde{F}^{(3)}$	Beresnev et al. (1993)	0.54	0.56	0.31	-0.05	0.00	1.27
$F/\tilde{F}^{(3a)}$		0.71	0.84	0.31	-0.81	0.00	1.00
$F/\tilde{F}^{(4)}$		0.77	0.84	0.26	-0.75	0.13	1.74
$\boldsymbol{F/\tilde{F}^{(4a)}}$	**sec. 3.3.4.2**	**1.02**	**1.00**	**0.09**	**3.62**	**0.93**	**1.88**

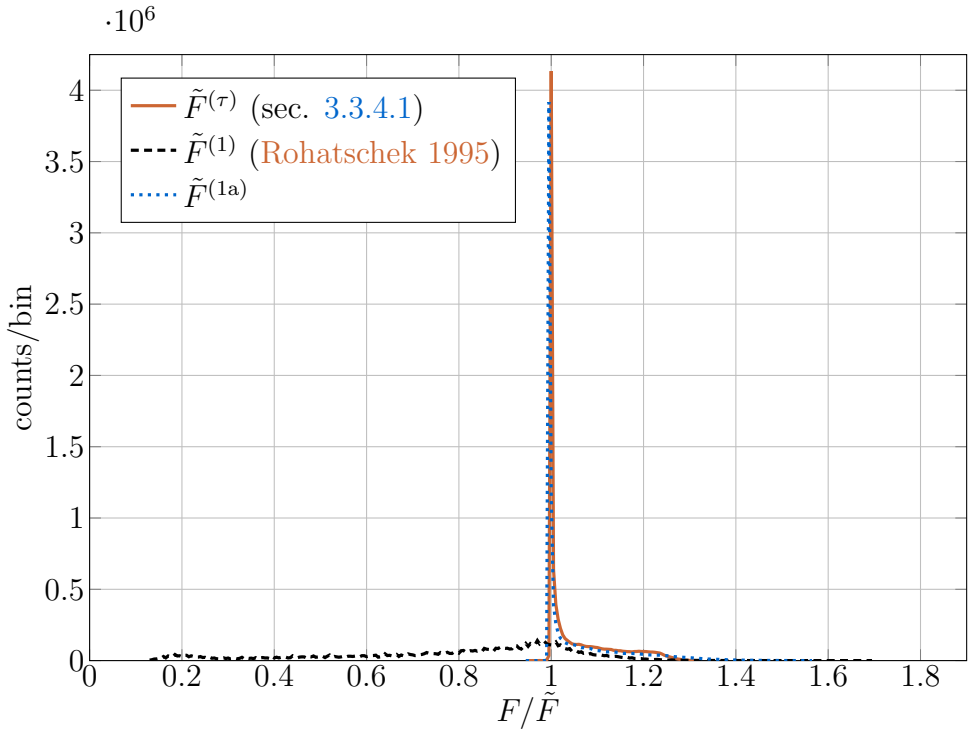

(a) ΔT based approximations: full

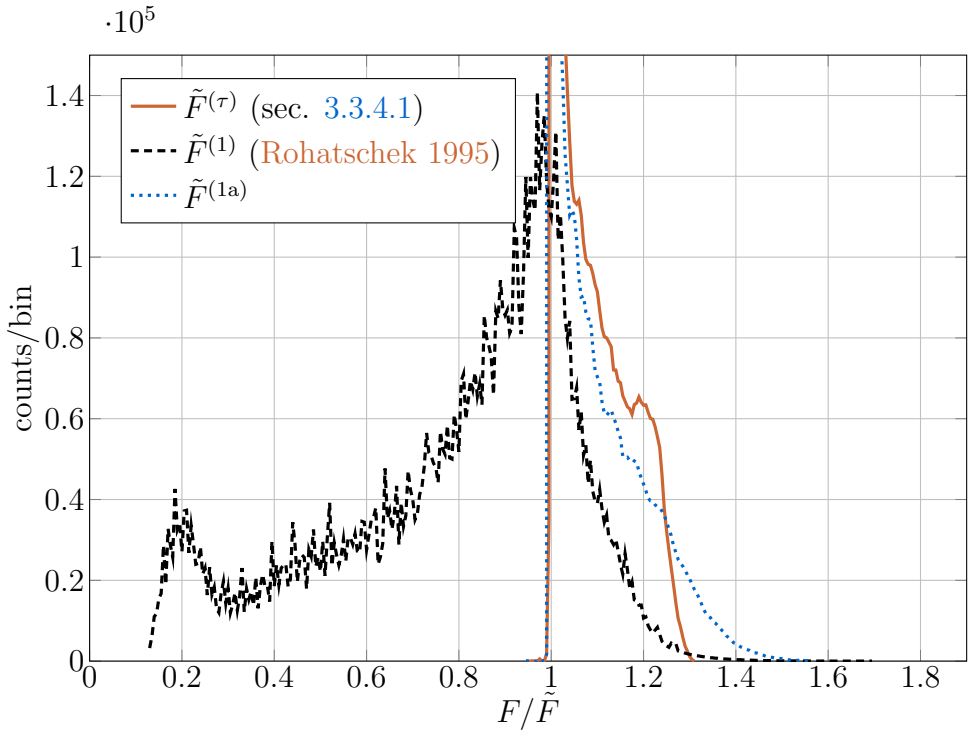

(b) ΔT based approximations: detail

Figure 3.8: Relative error histograms of temperature-based approximations. The bin size remains 0.005 (0.5%). 9,622,800 different parameter combinations were used (Table 3.1). Statistical properties of the relative error for each approximation are shown in Table 3.2.

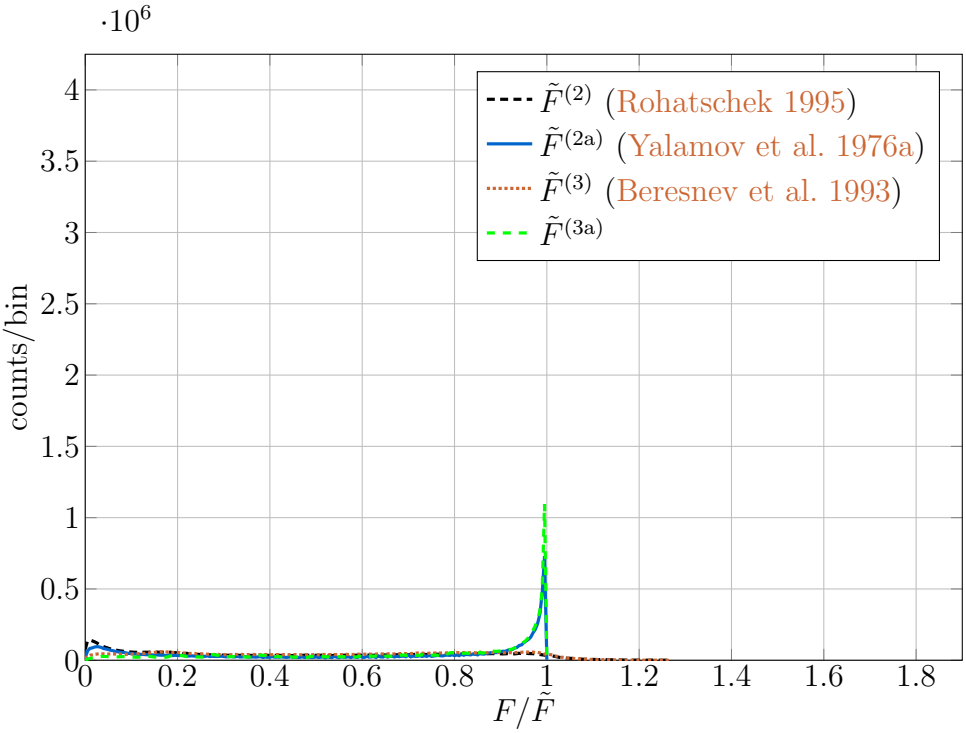

(a) *I-r-k* based approximations: full

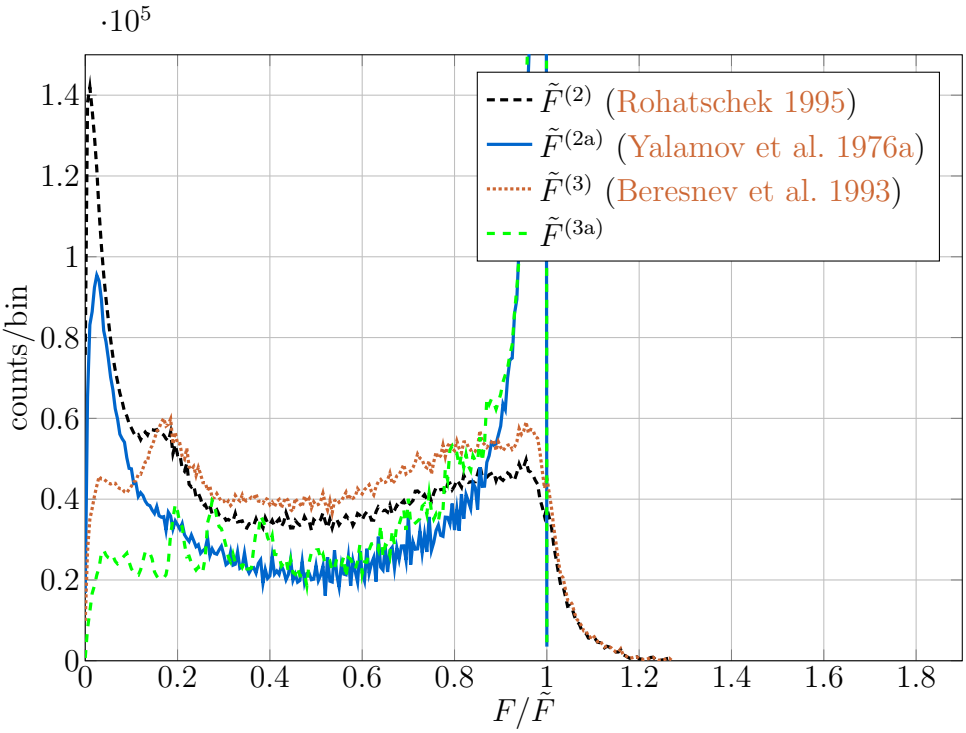

(b) *I-r-k* based approximations: detail

Figure 3.9: Relative error histograms of *I-r-k*-based approximations. The bin size remains 0.005 (0.5%). 9,622,800 different parameter combinations were used (Table 3.1). Statistical properties of the relative error for each approximation are shown in Table 3.2.

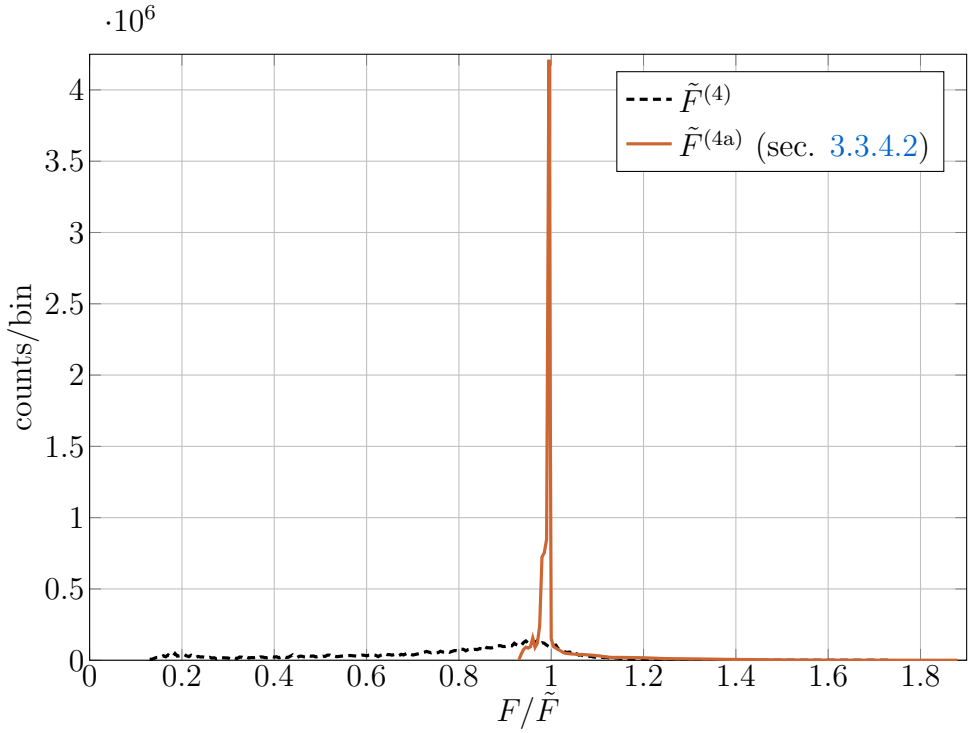

(a) I-r-k-T_{bb} based approximations with thermal radiation: full

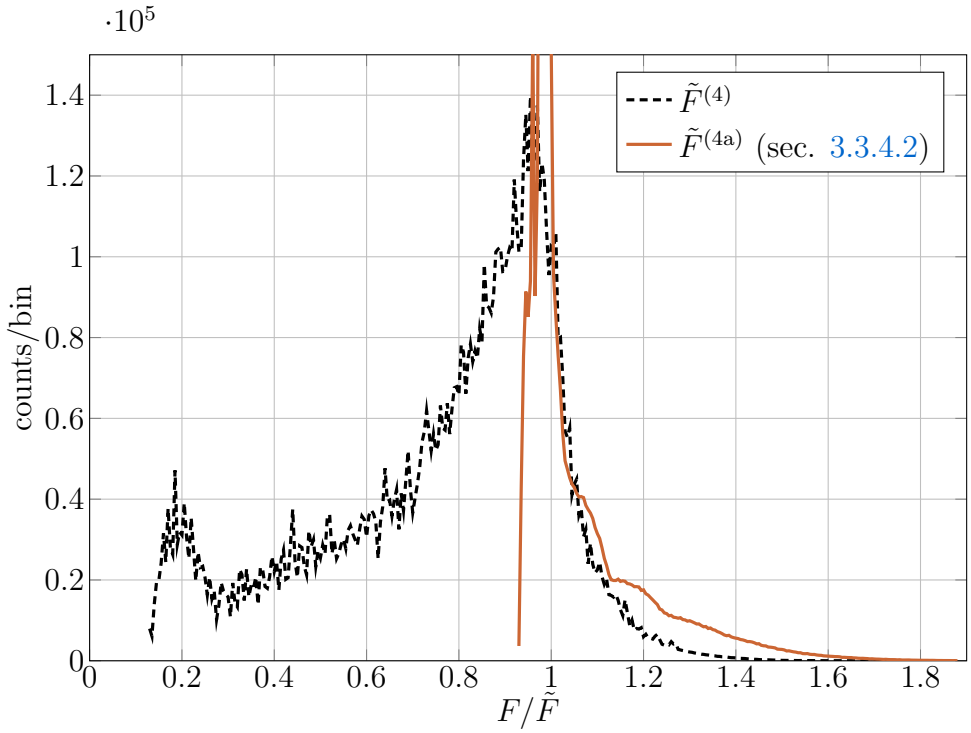

(b) I-r-k-T_{bb} based approximations with thermal radiation: detail

Figure 3.10: Relative error histograms of I-r-k-T_{bb}-based approximations. The bin size remains 0.005 (0.5%). 9,622,800 different parameter combinations were used (Table 3.1). Statistical properties of the relative error for each approximation are shown in Table 3.2.

3.3.6 Modified approximations

In Loesche and Wurm (2012) 3-parameter correction factors for the approximations (3.114) were introduced. They are defined by the ratio of actual value in the *fm*-regime and the result received by the respective approximation:

$$\chi^{(i)} = \frac{F_{\text{phot}}}{\tilde{F}^{(i)}} \,. \tag{3.117}$$

The data to set up the correction factors was used from the aforementioned quality studies on the approximations in Loesche and Wurm (2012) in sec. 3.3.5[2]. The authors found that all three $\chi^{(i)}$ within this range of 880 parameter combinations can be expressed analytically as

$$\chi^{(i)} = \chi_1^{(i)} + \chi_2^{(i)}\, \mathrm{e}^{\chi_3^{(i)} \frac{r}{k}} + \chi_4^{(i)}\, \mathrm{e}^{\chi_5^{(i)} \alpha} \tag{3.118}$$

and correct the respective approximation to better than 2%. At this point, I refrain from reciting the explicit 3-parameter correction factors for the three approximations (3.114) obtained in Loesche and Wurm (2012), as for 6 parameters there were better approximations found (previous section).

For fixed T^-, $T_{\text{gas}}^{\text{rad}}$ and I, a better correction equation the one above could be found recently

$$\chi^{(i)} = \frac{\chi_5^{(i)}}{\chi_4^{(i)} - \mathrm{e}^{-\frac{\chi_2^{(i)}}{\alpha} + -\chi_1^{(i)} \frac{k}{r} - \chi_3^{(i)}}} \,. \tag{3.119}$$

This factor was used for the numerical data analysis with $\tilde{F}^{(4a)}$ in Figure 4.20a and Figure 4.21 for $T^- = T_{\text{gas}}^{\text{rad}} = 293.15\,\text{K}$ and $I = 20\,\text{kW/m}^2$

$$\chi^{(4a)} = \frac{1.14504}{1.15137 - \mathrm{e}^{-\frac{0.05235}{\alpha} - \frac{0.18309k}{r} - 1.42910}} \,. \tag{3.120}$$

The radius range here is $r = 0.11 \ldots 1.1\,\text{mm}$ in steps of 0.11 mm. α was varied between 0 and 1 in steps of 0.1, k varied as shown in Table 3.1. $\chi^{(4a)}$ is effectively non-constant for small thermal conductivities, as the exponent in the denominator indicates. Statistical properties are shown in Table 3.3. The mean error of $F/(\chi^{(4a)}\tilde{F}^{(4a)})$ is effectively 0.

Table 3.3: Statistical properties of $F/\left(\chi^{(4a)}\tilde{F}^{(4a)}\right)$ for 3600 different parameters at $T^- = T_{\text{gas}}^{\text{rad}} = 293.15\,\text{K}$, $I = 20\,\text{kW/m}^2$ and $r \leq 1.1\,\text{mm}$, otherwise along Table 3.1.

	mean	median	STD	min	max
$F/\left(\chi^{(4a)}\tilde{F}^{(4a)}\right)$	0.0000	-0.0031	0.0066	-0.0243	0.0151

[2]Sphere radii were varied between 0.1 and 1.1 mm. The thermal conductivities for core and mantle were varied between 0.01 and 8 W/m K. α was varied between 0.1 and 1. The light flux illuminating the particle was fixed to $20\,\text{kW/m}^2$, both gas temperatures had the value 293 K.

3.4 Linear approximations for pure *fm*-photophoresis

3.4.1 Pure *fm*-photophoresis exerted on convex bodies in Rohatschek and Zulehner (1985)

In this section, the results of Rohatschek and Zulehner (1985) are briefly sketched. The theory the authors developed applies for convex particles. Convex bodies are those, where arbitrary pairs of points have their connecting line fully embedded in the body itself. Hence, this property is stronger than the property of being star-convex/star-like, where only for one point $x_\star$ the connecting line to all other points is required to lay inside of the body.

The authors assume, that the internal heat transfer dominates compared to the external heat transfer by molecular transport through gas particles, which itself they assume to be the dominant external heat transfer process, thus energy loss through radiation is neglected. They start from the stationary heat transfer equation

$$k\Delta T = -q \tag{2.2}$$

with a boundary condition for gas particle energy transport

$$k\frac{\partial T}{\partial \mathbf{n}} = -h(T - T_{\text{gas}}) \,, \tag{3.121}$$

where the heat transfer coefficient is defined as

$$h = h_0\, \alpha\, \frac{p}{T_{\text{gas}}}\, \overline{v} \,, \tag{3.122}$$

with $h_0 = \frac{1}{2}$ for monatomic gases, and $h_0 = \frac{3}{4}$ for diatomic gases ($-h(T - T_{\text{gas}}) \overset{T^- = T_{\text{gas}}}{=} -\mathbf{n}\cdot\left[\breve{\boldsymbol{\mathcal{E}}}^+ + \breve{\boldsymbol{\mathcal{E}}}^-\right]$ for a Maxwell-Boltzmann distribution for monatomic gases with thermal accommodation (2.114), sec. 3.3.1). k denotes the thermal conductivity of the particle. For the internal heat transfer dominating the external one ($h\,l \ll k$, l is the characteristic length of the suspended body), they eventually expand the (dimensionless version of the) difference $T - T_{\text{gas}}$ in a power series of the ratio $\frac{h\,l}{k} \ll 1$, with coefficients a_i, to obtain (in first order)

$$T - T_{\text{gas}} \approx \frac{I}{h} a_0 + \frac{I\,l}{k} a_1 + \dots \,. \tag{3.123}$$

The integral equation for photophoresis (2.116) together with the linearization of the integrand's square root eventually yields

$$\mathbf{F}_{\text{phot}} \approx -\frac{\alpha}{4}\, \frac{p}{\sqrt{T_{\text{gas}}(T_{\text{gas}} + \alpha\, \frac{I}{h}\, a_0)}}\, \frac{I\,l}{k} \int\limits_{\partial V} a_1 \,\mathrm{d}\mathbf{A} \,. \tag{3.124}$$

Replacing the coefficient a_1 with the help of identities obtained by the usage of Gauss' theorem and Green's second identity yields another conspicuous representation of the same equation ($a_0 = A_I/|\partial V|$, $|\partial V|$ meaning the particle's surface area):

$$\mathbf{F}_{\text{phot}} \approx -\frac{\alpha}{4}\, \frac{p}{\sqrt{T_{\text{gas}}(T_{\text{gas}} + \alpha\, \frac{I\,A_I}{h\,|\partial V|})}}\, \frac{I\,A_I}{k} \left(\frac{\int\limits_V q\,\mathbf{r}\,\mathrm{d}V}{\int\limits_V q\,\mathrm{d}V} - \frac{1}{|\partial V|} \int\limits_{\partial V} \mathbf{r}\,\mathrm{d}A \right) \,, \tag{3.125}$$

where the absorption cross section A_I was used, formerly introduced by (2.3). The source asymmetry $\mathbf{r}^*_{OQ}$ (2.4) is written in the numerator inside the brackets.

For the case of a perfectly absorbing opaque particle of convex shape it is

$$\mathbf{F}_{\text{phot}} \approx -\frac{\pi}{6}\alpha \frac{p}{\sqrt{T_{\text{gas}}\left(T_{\text{gas}} + \alpha\frac{I}{4h}\right)}} \frac{I\,l^3}{k}\,\mathbf{e}_z\ . \tag{3.126}$$

This equation resembles the previous approximation (3.114b) that was obtained for an opaque sphere (the characteristic length of a sphere is $l = r_0$)

$$\mathbf{F}_{\text{phot}} \approx -\frac{\pi}{6}\,\alpha\,\frac{p}{\sqrt{T^+\,T^-}}\,r_0^3\,\frac{I}{k}\,\mathbf{e}_z\ .$$

For $\alpha\frac{I}{4h} \ll T_{\text{gas}}$ and $h\,l \ll k$ (3.126) is

$$\mathbf{F}_{\text{phot}} \approx -\frac{\pi}{6}\alpha\frac{p}{T_{\text{gas}}}\frac{I\,l^3}{k}\,\mathbf{e}_z\ , \tag{3.127}$$

in agreement with approximation (3.114b), introduced in the section 3.3.

The usage of a heat source function is insofar helpful, that it is not necessary anymore to solve the respective heat transfer problem in order to obtain the particle's surface temperature. But this only swaps one problem for another one, as retrieving the heat source function $q(\mathbf{r})$ remains a considerable problem, especially for non-spherical particles. As nowadays commercial programs like COMSOL are eligible to solve those heat transfer problems, even for any kind of shape, the usage of the heat source function was not pursued and remains an object of simple reference in this work.

3.4.2 Pure *fm*-photophoresis exerted on star-convex bodies

The general solution (3.20) can be linearized for both, $n = 2$ and $n = 3$, yielding ($\Gamma^{(n)}_{0,0,p,q}$ and $\Psi^{(n)}_{0,0,p,q}$ are constant for different $n = 2, 3, \dots$)

$$\mathbf{F}^{(2)}_{\text{phot}} \approx -\frac{p\,\omega^{(2)}_{0,0}}{\sqrt{6T^-}}\begin{pmatrix} -\Re\,t^{(2)}_{1,1} \\ -\Im\,t^{(2)}_{1,1} \\ \frac{1}{\sqrt{2}}t^{(2)}_{1,0}\end{pmatrix} \tag{3.128}$$

$$\mathbf{F}^{(3)}_{\text{phot}} \simeq -\frac{p\,\omega^{(3)}_{0,0}}{\sqrt{6T^-}}\begin{pmatrix} -\Re\,t^{(3)}_{1,1} \\ -\Im\,t^{(3)}_{1,1} \\ \frac{1}{\sqrt{2}}t^{(3)}_{1,0}\end{pmatrix}\ . \tag{3.129}$$

Especially, $\mathbf{F}^{(3)}_{\text{phot}}$ can be expressed by the volume of the illuminated particle V as

$$\boxed{\mathbf{F}^{(3)}_{\text{phot}} \overset{(3.23)}{\simeq} -\frac{1}{2}\sqrt{\frac{3}{2\pi}}\frac{p\,V}{\sqrt{T^-}}\begin{pmatrix} -\Re\,t^{(3)}_{1,1} \\ -\Im\,t^{(3)}_{1,1} \\ \frac{1}{\sqrt{2}}t^{(3)}_{1,0}\end{pmatrix}\ .} \tag{3.130}$$

The quality of both approximations is evaluated in sec. 4.2.4.3. It will turn out, that (3.130) is an excellent equation to describe the photophoretic force on a directly illuminated ellipsoid of homogeneous composition.

3.5 Photophoretic torques

Rohatschek (1956a, 1984, 1985, 1989) conducted some of the earlier experiments on photophoretic motion, the latest experiments include Loesche et al. (2014) and Kuepper et al. (2014) and van Eymeren and Wurm (2012). While determining the magnitude of the force is one of the easier tasks, it is tricky to predict the rotation of suspended particles due to torques

$$\mathbf{M}_{\text{phot}} = \int_{\partial V} \mathbf{r} \times \mathrm{d}\mathbf{F}_{\text{phot}} = -\frac{1}{2} \int_{\partial V} \mathbf{r} \times \mathrm{d}\mathbf{A}\, p \left(1 + \sqrt{\frac{T^+}{T^-}} \right) , \tag{3.131}$$

since this depends on the particle's geometry, accommodation $\alpha(\mathbf{r})$ and surface temperature distribution $T(\mathbf{r})$. Translation and rotation of a particle suspended in a gas are causing resistance/drag forces and torques if the particle's movement happens to be relative to the gas, which also have to be taken into account. This was done by Epstein (1924) for spheres in the *fm* regime and later by Rohatschek and Zulehner (1987) for convex bodies (namely as constituents of powders/aerosols) in the same regime. They discussed the influence of geometry and momentum accommodation coefficient α_{m} for a perfect heat conductor. Brenner (1963, 1964, 1966) and Happel and Brenner (1983) derived the drag forces and torques for the *co* regime.

Yalamov et al. (1976b) obtained the photophoretic force together with the drag force in the *co* regime (see sec. 2.10), the same was done in Yalamov et al. (1976a) for the *fm* regime (also see sec. 3.3.2)

Rohatschek and Zulehner (1985) derived the photophoretic force in first order for convex particles by usage of the source term, as sketched in sec. 3.4.1. The source term and the asymmetry factor, respectively, enable to calculate the force without solving the heat transfer equation (boundary condition is implicitly embedded into the respective theory). The concept was used to discuss three extremes, namely a "particle with uniform source function, a perfectly opaque particle, and a perfectly transparent particle with an absorbing core". The same concept was extended to torques and discussed in Zulehner and Rohatschek (1990, 1995). Zulehner and Rohatschek (1990) also tested the method on a raindrop-shaped object as an example of a convex body. I refrain from presenting details on how the torques were derived in first order.

4

COMPUTER AND DROP TOWER EXPERIMENTS ON CHONDRULES

4.1 Dust mantled spheres

The motivation for the work in Loesche and Wurm (2012) is the fine grained rim that often surrounds chondrules (Metzler et al. 1991). Also, the sizes of chondrules in different meteorites deviate from each other (Hughes 1978 and Scott et al. 1996 and Kuebler et al. 1999), i.e. they are size-sorted. Its origin is still subject of debates. A possible scenario is that the rims might originate in the dusty solar nebula as bare chondrules move through it and accumulate the dust, which is eventually compressed to the observed rims (Metzler et al. 1992 and Morfill et al. 1998 and Ormel et al. 2008 and Bland et al. 2011 and Carballido 2011). Blum and Wurm (2008) showed through experiments on dust-aggregate collision and growth that this concept is plausible and chondrules are very likely to enshroud themselves with a mantle of small grains in a dust-rich environment. Accretion of dust mantles and its evolution has been studied by Beitz et al. (2011).

That chodrules are size sorted can arise from a number of different scenarios discussed in literature (Loesche and Wurm 2012). For instance, different places of origin might have produced different size distributions of chondrules. Also, Liffman (2005) suggested mechanisms, which drove the size sorting of chondrules. Cuzzi et al. (1996) argued, that particles of different size couple differently to the gas they are suspended in. However, Loesche and Wurm (2012) just assumed the rims to set off as highly porous dust encasing of chondrules, originating in the solar nebula. They further assumed, that a light source, such as the early sun, can result in photophoretic propulsion of chondrules. The question they answered is, if dust-coated chondrules are eligible for size-sorting driven by photophoresis.

As a starting point, Loesche and Wurm (2012) calculated the photophoretic force acting on illuminated core mantle spheres (see Figure 4.1) in a heat transfer model (stationary, thermal radiation) with thermal accommodation and evaluated the quality of the three approximations (3.114) (see sec. 3.3.5 for detailed information). This introduces four new variables

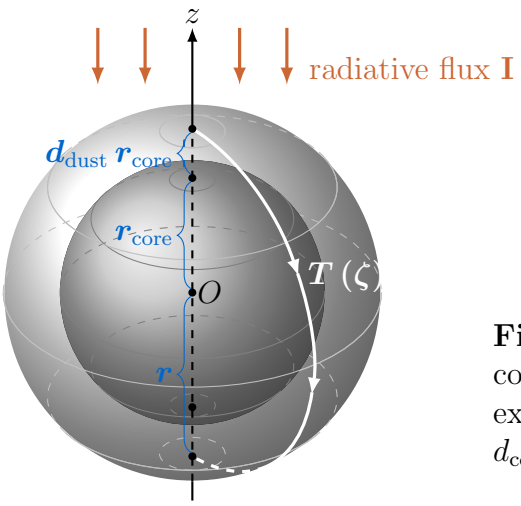

Figure 4.1: Model of a chondrule with a rim. The core radius is denoted with r_{core}, the shell thickness is expressed in relative size of the core radius as $d_{\mathrm{core}} = \frac{r - r_{\mathrm{core}}}{r_{\mathrm{core}}}$.

the radius of the core	r_{core}
the thickness of the shell defined by the dimensionless variable	$d_{\mathrm{dust}} = \frac{r - r_{\mathrm{core}}}{r_{\mathrm{core}}}$
the thermal conductivity of the core	$k_{\mathrm{core}} = \mathrm{const.}$
the thermal conductivity of the dust shell	$k_{\mathrm{dust}} = \mathrm{const.}$

The rigid core consists of silicates and traces of metals and has a thermal conductivity of the magnitude $1\,\mathrm{W/(m\,K)}$ (Opeil et al. 2010), whereas for the highly porous dust mantle Loesche and Wurm (2012) varied k_{dust} between 0.01 and $0.5\,\mathrm{W/(m\,K)}$ (Presley and Christensen 1997a,b and Krause et al. 2011).

$$F^{(4)} = \chi^{(4)}\,\tilde{F}^{(4)} \tag{4.1}$$

was used for further analysis on dust-mantled spheres by employing a correction factor $\chi^{(4)}$, along the definition (3.118) in sec. 3.3.6 for fixed I, T^- and $T^{\mathrm{rad}}_{\mathrm{gas}}$. The calculations of the force for dust-mantled spheres were carried out in the parameter range displayed in Table 4.1.

Table 4.1: Parameter range for the study of the force exerted on dust-mantled spheres (Loesche and Wurm 2012). Irradiation and gas temperatures are constant at $20\,\mathrm{kW/m^2}$ and 293 K, respectively.

parameter	range
r_{core}	0.1 . . . 1.0 mm
d_{dust}	0.1 . . . 1.0 in fractions of r_{core}, also see Figure 4.1
k_{core}	0.1 . . . 4.0 W/(m K)
k_{dust}	0.01 . . . 0.5 W/(m K)
α	0.1 . . . 1.0

Obviously, the thermal conductivity of a bulk sphere is determining the photophoretic strength. For a coated sphere it was unclear so far, how two different thermal conductivities k_{core} and k_{dust} and two size parameters influence the force as well as how to use approximations, which were originally defined for homogeneous spheres.

Loesche and Wurm (2012) pointed out, that heat transfer calculations for different parameter configurations

$$\lambda_\mathrm{m} = \{k_\mathrm{core}, k_\mathrm{dust}, r_\mathrm{core}, d_\mathrm{dust}\} \cup \lambda^{(0)} \tag{4.2a}$$

$$\lambda^{(0)} = \left\{r, I, \alpha, T^-, T^\mathrm{rad}_\mathrm{gas}, \dots\right\} \tag{4.2b}$$

can result in the same photophoretic strength, because for two different surface temperatures T_1 and T_2 resulting from the configurations λ_1 and λ_2, the integral (2.116) can be equal

$$\pi\, p\, r^2 \int_0^\pi \sqrt{1 + \alpha\left(\frac{T_1}{T^-} - 1\right)}\, \mathrm{d}\zeta = \pi\, p\, r^2 \int_0^\pi \sqrt{1 + \alpha\left(\frac{T_2}{T^-} - 1\right)}\, \mathrm{d}\zeta\ . \tag{4.3}$$

Implying, two configurations λ_1 and λ_2 are equivalent (in the sense of the photophoretic force), if

$$\lambda_1 \sim \lambda_2 \ :\Leftrightarrow\ F_\mathrm{phot}\left(\lambda_1\right) = F_\mathrm{phot}\left(\lambda_2\right)\ . \tag{4.4}$$

4.1.1 Defining the effective thermal conductivity $\varkappa$

It is possible to assign an effective thermal conductivity $\varkappa$ by employing the equivalence relation $\sim$ for a set of pairwise different configurations λ_m which share the same base configuration $\lambda^{(0)}$. For this set of λ_m an equivalence class

$$\lambda^{(0)}_{\mathrm{m}/\sim} = \left\{\lambda_\mathrm{m} \,\middle|\, \lambda_\mathrm{m} \sim \lambda^{(\mathrm{r})}_\mathrm{m}\right\} \tag{4.5}$$

with the representative $\lambda^{(\mathrm{r})}_\mathrm{m}$ is considered. One equivalence class identifies all configurations for core mantle spheres which experience the same photophoretic force with each other. Since only the four parameters $\{k_\mathrm{core}, k_\mathrm{dust}, r_\mathrm{core}, d_\mathrm{dust}\}$ are allowed to vary, an equivalence class $\lambda^{(0)}_{\mathrm{m}/\sim}$ defines the effective thermal conductivity for equal base configurations $\lambda^{(0)}$ [1]. For a better use, another representative than $\lambda^{(0)}$ can be chosen, having the form $\{k, k, \dots\}$, i.e. a homogeneous sphere with the thermal conductivity k. In this case, the equivalence class can just be written as $k_{/\sim}$. Such a homogeneous sphere at the thermal conductivity k should always exist (k is the only parameter in a set of λ_m, which would be allowed to vary), because of the following reasons:

1. for the heat transfer boundary conditions (3.101) and directed illumination, the maximum surface temperature is restricted, namely by the addends in the denominator beside the thermal conductivity k and the numerator in (3.108) $\rightarrow$ the highest comes for $k = 0$,

2. any other inhomogeneous sphere under exactly the same conditions will have lower temperatures, because the same inhomogenenous sphere with a sufficiently thin layer at $k = 0$ will experience the same surface temperature as the bulk sphere at $k = 0$,

3. for $k = 0$, the surface temperature inhomogeneity as a result of the directed illumination will result in the highest photophoretic force, other forces for effectively $k > 0$ will be smaller,

[1] From the definition of the effective thermal conductivity it is clear, that it is generally not an effective thermal conductivity in the sense of the heat transfer equation.

4. the photophoretic force integral equation with thermal accommodation (2.116) for the surface of a sphere is a surjective nonlinear functional with the definition $\mathbf{F}_{\text{phot}}(T)$: continuous functions $\mathrm{C}([0, 2\pi] \times [0, \pi], \mathbb{R}) \to \mathbb{R}$, thus there is at least one more temperature distribution, i.e. for a homogeneous sphere, that results in the same total force, which will be less than the force a sphere at $k = 0$ experiences due to above reasons.

Instead of $k_{/\sim}$, Loesche and Wurm (2012) just wrote $\varkappa$, which will be continued in the following.

Practically, the assignment of the effective thermal conductivity $\varkappa$ is carried out by solving (4.1) numerically, since it is $F_{\text{phot}} \simeq F^{(4)}(\lambda)$ by construction of this corrected approximation. Furthermore, in $F^{(4)}(\lambda)$, the thermal conductivity k directly enters as it is $\tilde{F}^{(4)} = \tilde{F}^{(4)}(k, r, I, \alpha, T^{-}, T^{\text{rad}}_{\text{gas}})$. That multiple configurations can result in the same $\varkappa$ is displayed by white lines in Figure 4.3. With other good I-r-k approximations, the respective value for k can also be well approximated.

For a mantled sphere, $\varkappa$ is also isotropic. If extended to spheres of total inhomogeneity, $\varkappa$ is correspondingly anisotropic. The assignment of an effective thermal conductivity can even be extended to star-convex particles like chondrules as shown in Figure 3.1. This needed a relation how to identify the radius of a sphere and the parametrization function $\Omega(\xi, \zeta)$ of a star-convex particle at first, since it was unclear what 'radius' such a 'potato' has. But this is all discussed in sec. 4.2.

4.1.2 Dependence of $\varkappa$ on core and shell configuration

Loesche and Wurm (2012) discussed the dependence of the effective thermal conductivity $\varkappa$ on the different configurations of the mantled sphere in detail. They found out, that $\varkappa$ depends only for low k_{dust} on the total size r, exemplarily shown in Figure 4.2a for $\alpha = 1$, $k_{\text{core}} = 1\,\mathrm{W/m\,K}$, and $k_{\text{dust}} = 0.01\,\mathrm{W/m\,K}$. Conversely, the dependence on core mantle size ratio d_{dust} is very strong. The low conductivity mantle shields the core from heat very effectively, but even for $d_{\text{dust}} = 0.5$ the effective thermal conductivity is still double as much as those of the rim in this configuration. For the limit of a vanishing dust mantle, it is always $\varkappa = k_{\text{core}}$ (by construction). Thus, the most influencing property on $\varkappa$ is the thermal conductivity of the rim — if it has a reasonable value attributed to dust —, as seen in Figure 4.2b and 4.3. This also illustrates that the core thermal conductivity has a rather minor impact except for thin shells.

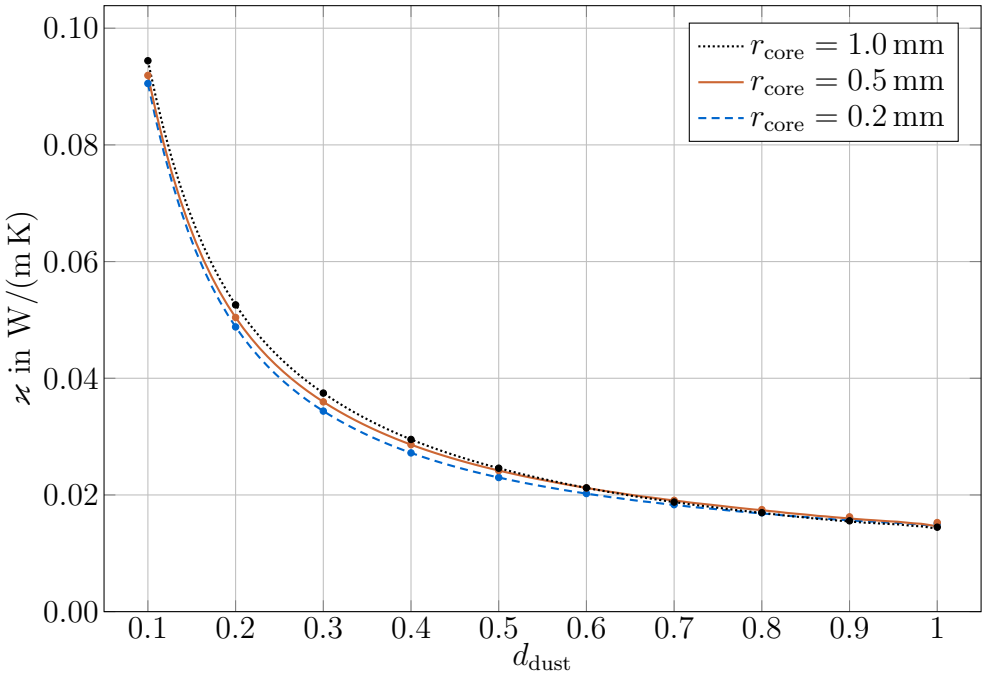

(a) $\varkappa$ over d_{dust} for three different core radii and $\alpha = 1$, $k_{\text{core}} = 1\,\text{W/m K}$, $k_{\text{dust}} = 0.01\,\text{W/m K}$. The order of the plot legend corresponds to the order of each individual line plot.

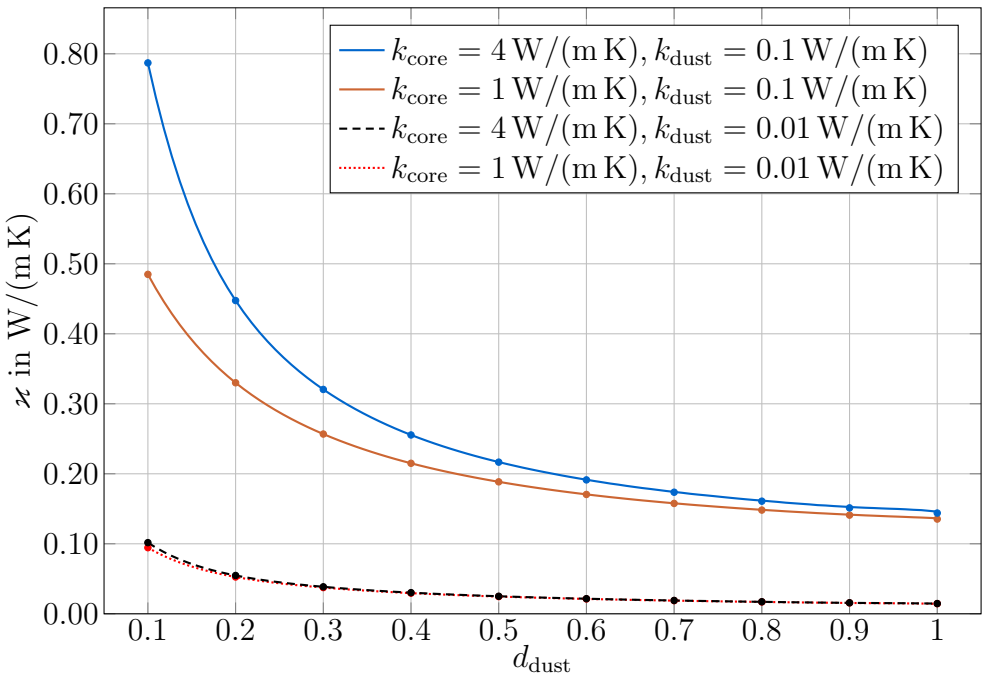

(b) $\varkappa$ over d_{dust} for two different r_{core} and k_{core} at $r_{\text{core}} = 1\,\text{mm}$ and $\alpha = 1$. The order of the plot legend corresponds to the order of each individual line plot.

Figure 4.2: Effective thermal conductivity $\varkappa$ as a function of dust mantle to core size ratio d_{dust} and its thermal conductivity k_{dust}. Data from Loesche and Wurm (2012).

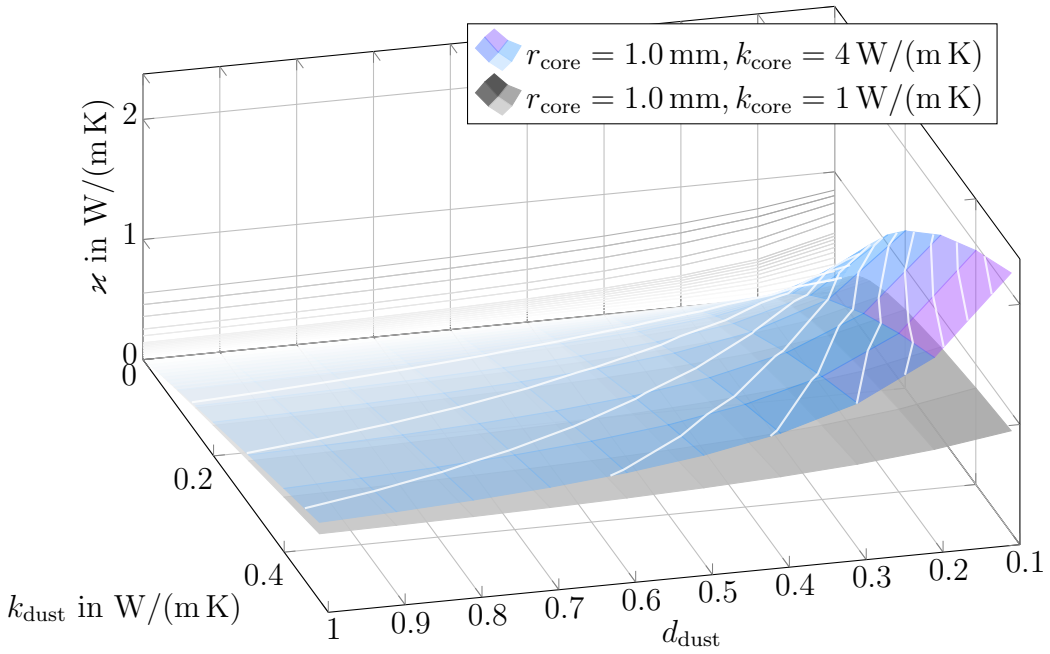

Figure 4.3: Effective thermal conductivity $\varkappa$ as a function of dust mantle to core size ratio d_{dust} and its thermal conductivity k_{dust}. Data from Loesche and Wurm (2012).

4.2 Realistic chondrules

For homogeneous spheres or onion shell particles as used in Loesche and Wurm (2012), the photophoretic force is always longitudinal (sec. 2.9.2 and 3.1). Conversely, nonsphericity or inhomogeneity could cause the direction and strength of photophoresis to be different with orientation of the particle in a given illumination field, as shown and evaluated in Loesche et al. (2013). They used (2.116) to determine the photophoretic force in direction and magnitude exerted on chondrules in COMSOL in situ, with a heat transfer model as described in sec. 3.3.5 for light intensities at $I = 20\,\text{kW/m}^2$ and a gas temperature of 293 K. The motivation was the uncertainty, a priori, if variations of the force in direction and magnitude with different orientations are small. Opeil et al. (2010, 2012) measured average thermal conductivities for meteorites, but they are not helpful in quantifying the orientation-depended deviations of the force which one can expect. Therefore, Loesche et al. (2013) used X-ray tomography scans of chondrules to model them in COMSOL calculations by keeping their surface structure and estimated compositional structure.

For (inhomogeneous) spherical particles, an effective thermal conductivity $\varkappa$ can be defined (sec. 4.1.1). With the help of it (here for onion shell particles), approximations like (3.115) can be employed to calculate the photophoretic force without solving the heat equation with the same boundary conditions that the approximations were derived with. If the sphere is of inhomogeneous composition, then $\varkappa$ is orientation dependent with respect to the illumination field. However, if particles are not only inhomogeneous but also nonspherical, a characteristic size has to be found in order to keep the approximations in use and to extend $\varkappa$ to nonspherical particles as well.

Loesche et al. (2013) did this for 19 chondrules from the Bjurböle chondrite (L/LL4-chondrite type). As variations in the force can be caused by inhomogeneity and/or nonsphericity, both were also separately discussed by studying chemically homogeneous

chondrule-shaped particles and best-fit spheres (see Figure 4.4) with inhomogeneous composition along the respective results from tomography. Loesche et al. (2013) proceeded in the following steps

1. numerically evaluate the force on
   (a) chondrules along X-ray studies
   (b) spheres of chondrule compostion
   (c) chondrule-shaped, but homogeneous particles at different thermal conductivities
2. discuss deviations in direction and magnitude
3. find a radius-analogue (characteristic size) as the I-r-k-approximations (e.g. (3.114) and (3.115)) are yet only defined for spheres with a radius r
4. extend the definition of the effective thermal conductivity $\varkappa$ to nonspherical particles

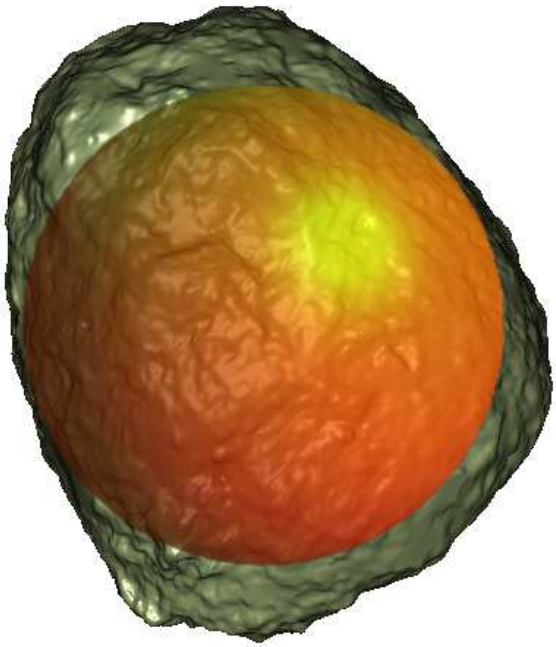

Figure 4.4: Chondrule CAD model and a sphere inscribed, centered at the center of shape. Taken from Loesche et al. (2013).

4.2.1 Tomography

For the numerical studies in Loesche et al. (2013), a sample of 19 chondrules from the Bjurböle chondrite (L/LL4-chondrite type) was used, as the heat transfer calculations required the domain defined by the chondrule's outer surface $\partial\Omega$ and their composition, to deduce the thermal conductivity at each point inside the chondrule. For high resolution and contrast, they used monochromatic synchroton X-ray microtomography (μCT) at 30 keV and a resolution of 5.26 μm/voxel, followed by digital data extraction (Friedrich et al. 2008 and Sasso et al. 2009). The source used is the 13-BMD synchroton beamline located at the Advanced Photon Source of Argonne National Laboratory. The experimental setup is described in Ebel and Rivers (2007). They collectively analyzed the chondrules in poly-honeycomb-like receptables, where each chondrule was placed in its individual cell. Thus, for all chondrules tomography took place under indentical conditions. BLOB3D (Ketcham 2005) allows of digital separation of compounds, and also segmentation in case of bulk material with chondrule inclusions. Similarly, Mathematica can be used to digitally separate the compounds for known gray value thresholds. A sample tomographic slice is depicted in Figure 4.5 (chondrule 1), its gray value histogram is shown in Figure 4.6. The chondrule-background threshold can be set to a value close to the first minimum, marked by the vertical line. The other four compounds are hidden in the histogram due to overlaps. The metals show a strong peak at high gray values. In principle, a decomposition of the chondrule's gray value histogram in sub-distributions is possible to get good thresholds (van den Heuvel 2006).

4.2.2 CAD models of chondrules

The tomographic scans return a series of slices for each chondrule. Every slice is put together and a special written algorithm (originally using Wolfram Mathematica) extracts all boundary points separating the noisy background from the chondrule material whereby empty inclusions are neglected, too. The resulting boundary point cloud is then semi-automatically triangulated and orientated. Following, the set of triangles is converted into a geometric object containing parameterized surfaces (NURBS). A more detailed description of the process is given in sec. 4.2.2.1.

To approximate the material composite of a chondrule, the tomography's grayscale values, delivering mass density information, were mapped to certain minerals, based on mineralogical studies on chondrules. The investigated chondrules are composed of Fe, Ni-metal, FeS (Troilite), olivines and pyroxenes, voids and a matrix of a fine-grained devitrified, plagioclase-normative mesostasis (Figure 4.7). In a stationary setting, thermal conductivities $k(\mathbf{r})$ resembling these materials were used at each voxel (Table 4.2). Generally, k is also a function of the temperature T; for meteoritic material at $T > 200\,\mathrm{K}$, Opeil et al. (2012) finds a $1/T$ dependence. Porosity also influences the thermal conductivity. In the chondrule set used in Loesche et al. (2013), they identified microcracks on the single voxel level, which occasionally even span wide nets within chondrules (Figure 4.8). To account for the influence of radiative heat transfer within the empty spaces inside the chondrules, a thermal conductivity of $k = 0.01\,\mathrm{W/m\,K}$ was assigned to theses voxels. Assumingly, porosity in the mesostasis is dominating thermal conductivity and therefore this material was attributed a low thermal conductivity of $k = 0.1\,\mathrm{W/m\,K}$. Mostly, the fine-grained mesostasis appears darker in the μCT images than the coarser-grained

Table 4.2: Chondrule Brightness Substitution and Material Properties. Typical Bjurböle olivine and pyroxene have a density of about 3.5 and 3.4 $\frac{g}{cm^3}$, respectively. Considering a plagioclase normative mesostasis having about 50% plagioclase (An10-15) and 50% mafic silicates a density of about 3.0 $\frac{g}{cm^3}$ can be estimated. However, for the stationary problem c_p and ρ have not been used. Taken from Loesche et al. (2013).

Material	**Gray Shade**	**Estimated Gray Value Range** ($[0, 1]$)	$\boldsymbol{k}$ in $\frac{W}{m \cdot K}$	$\boldsymbol{c_p}$ *in* $\frac{J}{kg \cdot K}$	$\boldsymbol{\rho}$ *in* $\frac{g}{cm^3}$
Fe,Ni-metal	white	> 0.7	80.4 [3]	*447* [1]	*7.96* [2]
FeS (Iron(II)-sulfide, troilite)	light gray	0.35-0.7	4 (mean) [7]	*588.5 (mean)* [5]	*4.61 (normal temp.)* [6]
olivine & pyroxene	gray	0.17-0.35	4.6 (mean) [7]	*620 (mean)* [4]	*3.45*
fine-grained devitrified, plagioclase-normative mesostasis	dark gray	0.1-0.17	0.1 (estimate)	*530 (estimate)*	*3.0*
void	black	< 0.1	0.01 (estimate)	*1*	*0.1*

[1] Halliday et al. (2009);
[2] Tipler et al. (2009a);
[3] Tipler et al. (2009b);
[4] Robie and Hemingway (1984);
[5] http://webbook.nist.gov/cgi/inchi/InChI%3D1S/Fe.S, Link: Condensed phase thermochemistry data
[6] http://webmineral.com/data/Troilite.shtml
[7] Clauser and Hünges (1995).

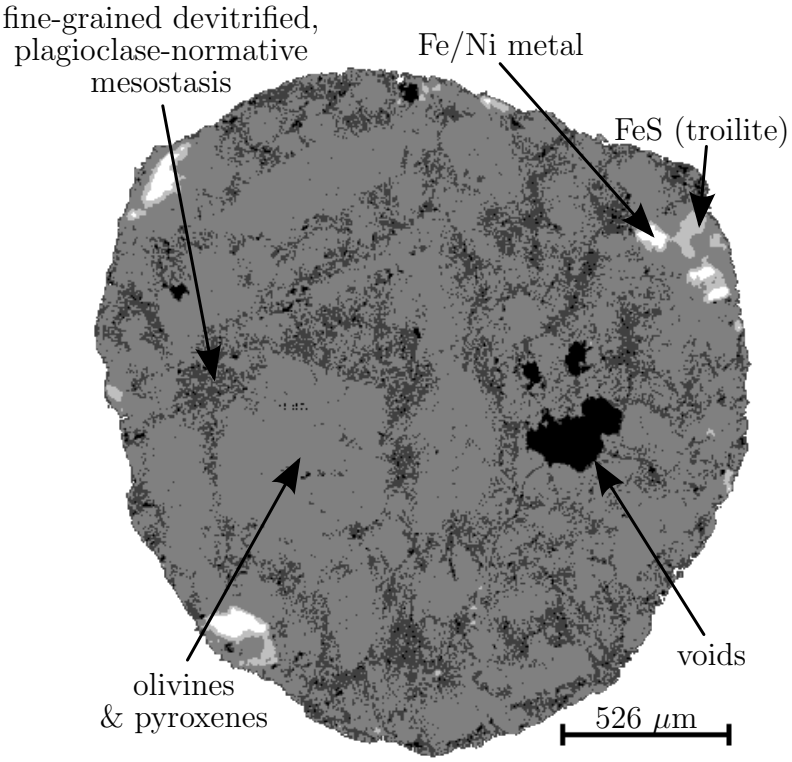

Figure 4.5: X-ray tomography of a Bjurböle chondrule (contrast enhanced along thresholds given by Table 4.2). Heavy atomic weight materials are bright, resolution is 5.26 μm/voxel. Taken from Loesche et al. (2013).

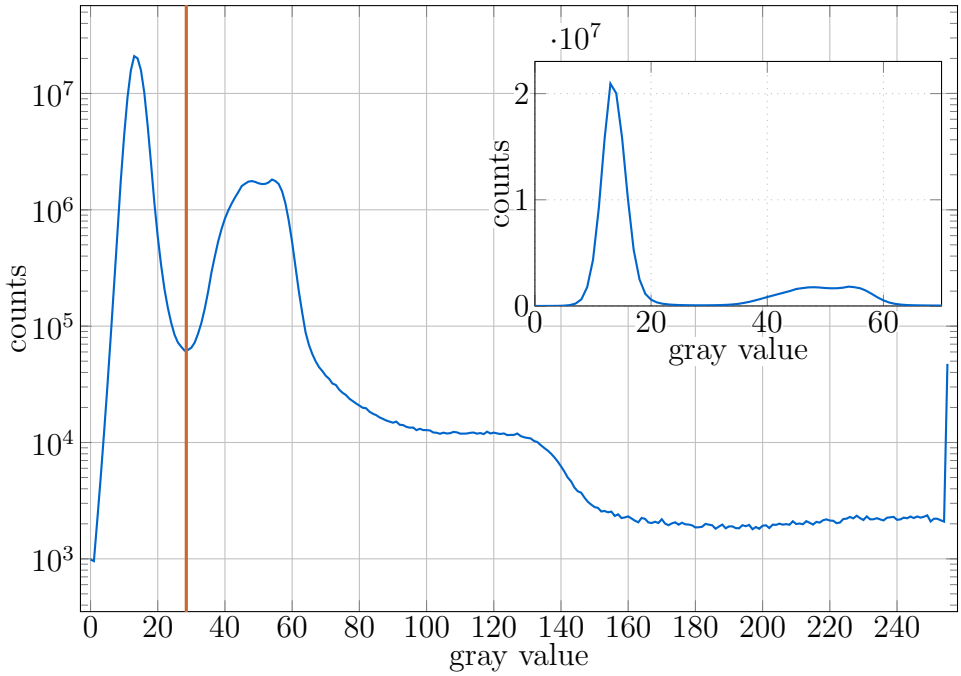

Figure 4.6: Gray value histogram of chondrule 1 (Table 4.4). The vertical line in the main (semi-logarithmic) plot marks the possible threshold to distinguish chondrule and background.

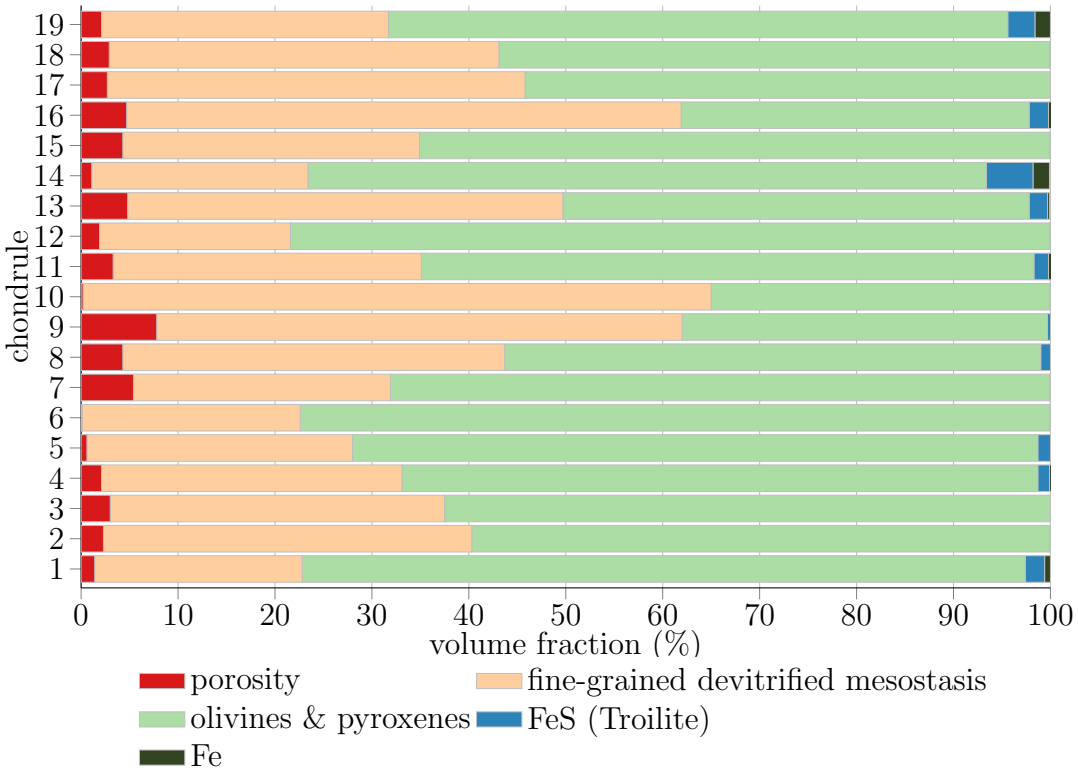

Figure 4.7: Modal composition of 18 Bjurböle chondrules. Data from Loesche et al. (2013).

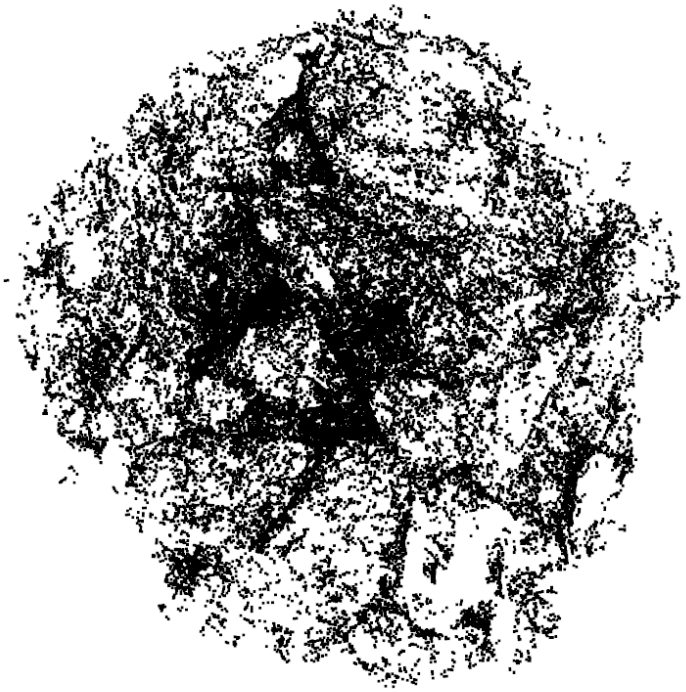

Figure 4.8: Microcrack nets inside of a chondrule (projection). Dots do not fit scale.

olivines and pyroxenes do (Figure 4.5), but it still contains variable abundances of olivines and pyroxenes which cannot be correctly measured at this resolution.

Since (for every individual material) the thermal conductivity is a function of temperature, the photophoretic force is subsequently also changing with the temperature. This association and the influence on transport and sorting is not subject of this work and can be studied in future research. Additionally, other unresolved microcracks add further thermal resistance to the inside of the model. Also, the exact mineralogy cannot be known by X-ray tomography, hence the attributed thermal conductivities can also change. All that manifests itself in modified numbers as results, but the quality of the findings will hold. Thus, Loesche et al. (2013) only give relative outcomes in the context of application in the solar nebula. The description of the chondrule surface, however, will remain correct in any case, and the understanding of the nonspherical surface' impact on the photophoretic behavior will allow of a better description of nonspherical chondrules with the same tools, i.e. the approximations, as before.

4.2.2.1 Chondrule surface extraction from X-ray tomography stacks

The gray shades image stack resulting from a tomography delivers all information needed for a successful creation of a three-dimensional model to perform numerical analysis on. The first step is to detect all points belonging to the object's outer boundary. The chondrule extraction processes uses a managed stack quasi-recursive code, which was necessary to deal with the very high number of up to 1.5×10^8 voxels. A rough description of the relevant algorithms shall be presented here.

The image stack shows many image slices cutting the object along one axis. Due to irregularities and resulting difficulties, it is important to combine all slices form one data object, represented by a three-dimensional matrix filled with numbers corresponding to each voxel's 8-bit gray shades ($[0, 1]$ or $[0, 255]$). For further analysis, the partitioning of this interval into sub-intervals representing the distinct compounds is necessary, especially the setting of a threshold delimiting the chondrule matter from the surroundings (e.g. air/gas/vacuum) and voids. The mapping of gray shades intervals to a group of minerals can be looked up in Table 4.2. An exemplary gray value histogram is shown in Figure 4.6.

Beside characterizing the material, the matrix' numbers can also be subdivided into four groups:

- chondrule material
- voids
- outside/background
- artefacts in the background .

The algorithm can separate all four data entities from each other. To get a chondrule mask, the voids and the chondrule material form a fifth data object. This is very important, because otherwise it is not clear how to define and extract the chondrule's outer boundary voxels from the image stack. The edges have to be sharp, e.g. the edges of horizontally aligned parts are required to be lines with a width of one voxel; only in case of a point cloud

with clearly defined and sharp edges and no other points in the data object (representing artefacts and voids), it is possible to triangulate all boundary points correctly in order to shape a closed surface from orientated triangles for further processing. All other cases return a rather spiky geometrical object which cannot be used.

4.2.2.2 From edge point clouds to parameterized surfaces

Part one — detection of chondrule's outer edge from the outside The edge extraction will be exemplarily discussed for Figure 4.9. The whole process basically consists of a filling/marker algorithm which detects cohesive structures, and an edge detection algorithm. Before the marker starts, the tomogram stack of a chondrule is binarized with the threshold suggested by the histogram, or close to the suggested value (see. Figure 4.6). The resulting slices can be seen in Figure 4.10, where Figure 4.10a was prepared with a 3d median filter to reduce noise, Figure 4.10b is the binarized pristine tomogram slice. For smoother surfaces, noise reduction is suggested. The 3d marker algorithm finds the cohesive chondrule material in Figure 4.11a (marked gray). The remaining white voxels are not connected to the chondrule, and are therefore turned black, making them part of the background voxels (Figure 4.11b). Now, the 3d marker searches for the background voxels outside of the chondrule (blue in Figure 4.12a). The remaining black voxels are the voids within the chondrule. The can be stored and analyzed, a projection of all voids was already shown in Figure 4.8. To obtain a 3d mask for the chondrule, the voids are turned into chondrule color (orange in Figure 4.12b). Since all voids, defects and artefacts in the image stack are wiped out and the two volumes defined by the chondrule known, the chondrule's boundary voxels are extracted. The responsible algorithm detecting the edges is shown in the appendix A.5.2. It returns thin edges needed for the triangularization with Geomagic Studio and subsequent parametrization for the use with COMSOL.

Originally, an iterative Mathematica code was developed to fill/mark the voxels. It is fractal in three levels and does well in detecting convex areas. Later, a C# algorithm was developed to replace it. It is based on the commonly used three-dimensional stack-managed 6-connected Floodfill algorithm. 6-connected means, diagonal neighbors are not 'seen', i.e. the cubic voxel has 6 neighbors as it has 6 surface parts. This algorithm finds connected structures, but uses a managed stack, i.e. a list, in order to prevent stack overflow. The 'color' conversions were carried out in the same way as above to identify or exclude structures. The essential code can be found in the appendix A.5.1.

Part two — triangulation and parametrization After the point cloud containing the chondrule's edge points is successfully obtained, it is necessary to connect all points to outwards-orientated triangles (triangulation). Even though there are some commercial programs available at the market capable of handling a massive number of points (I used Geomagic Studio 12 [2]), the processing of those point clouds is semi-automatic and needs user control. One of the chondrules modeled with Geomagic Studio was already shown in sec. 3.1, i.e. Figure 3.1. The geometrical object only consisting of triangles is not suitable for numerical calculations with COMSOL as it is not parameterized; COMSOL can only import simple geometries and parameterize them itself. Parametrizations or maps (see sec. 3.1) describing the surface and thus defining the enclosed domain are needed. Though

[2] FEMET GmbH placed an extended trial version at my disposal.

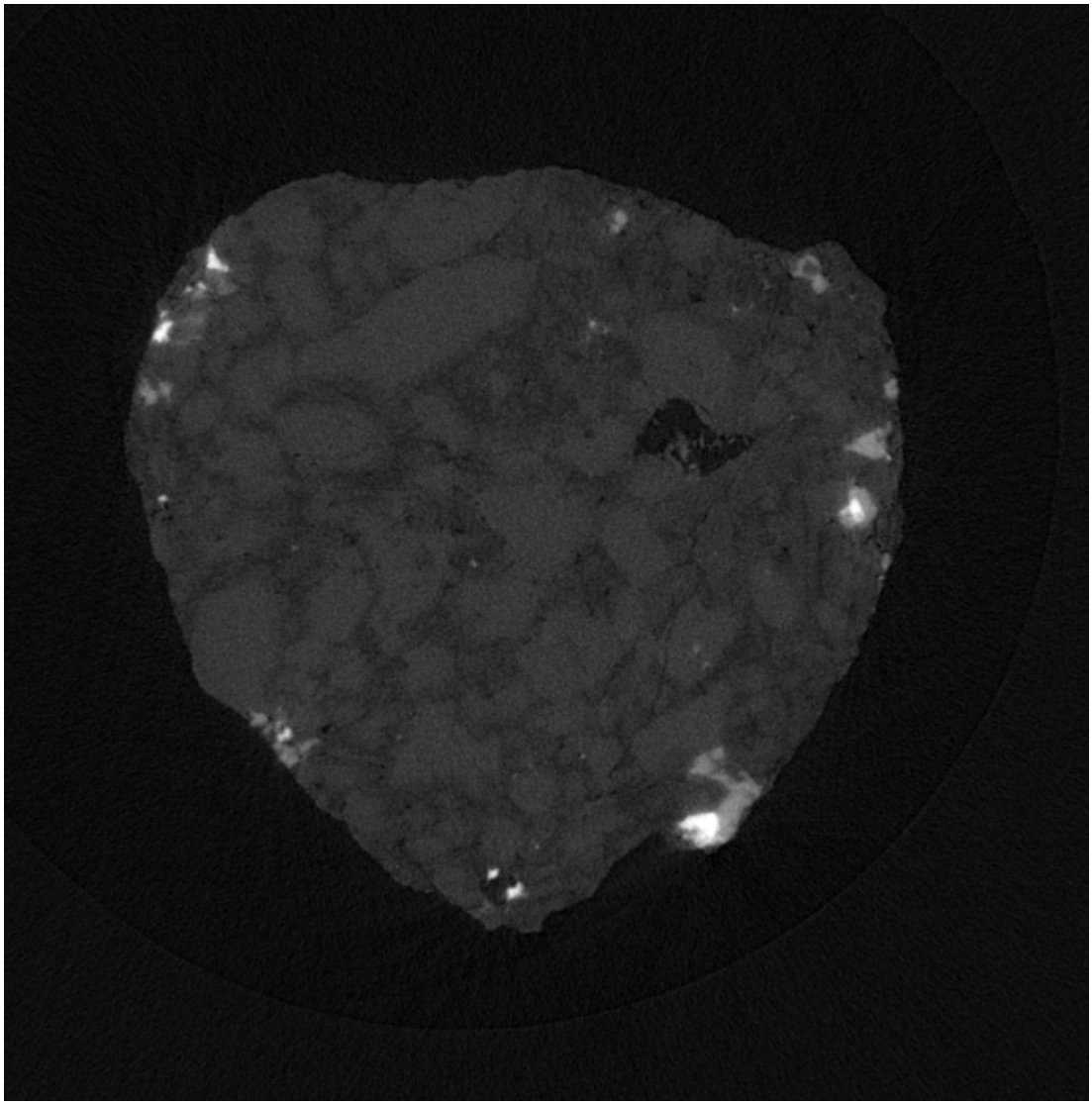

Figure 4.9: The alorithm will briefly be discussed on the basis of this tomography slice of chondrule 1.

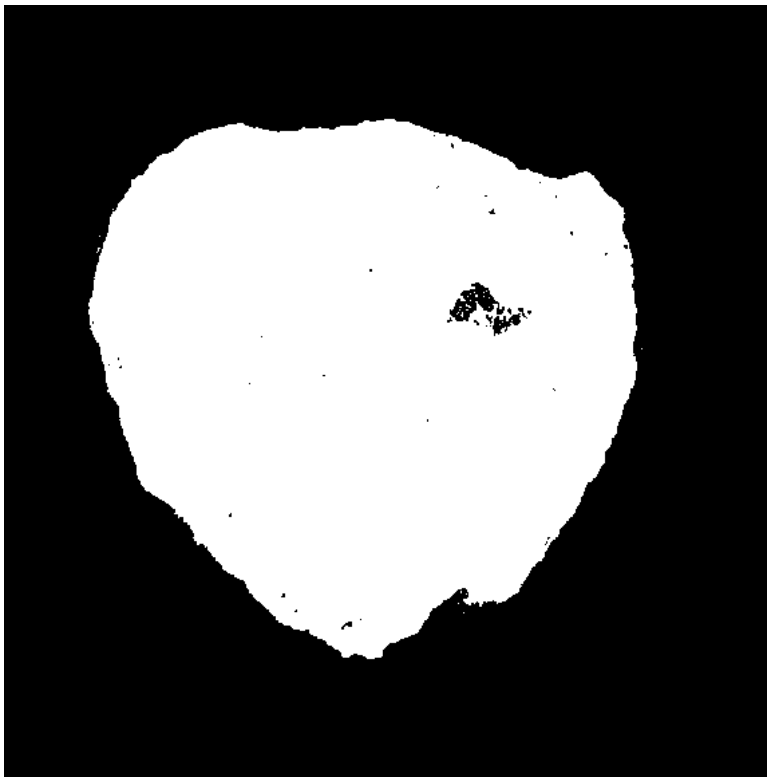

(a) The tomography is smoothened by a 3d median filter to reduce noise (here with pixel radius 1). Subsequent binarization yields a raw data object of the chondrule.

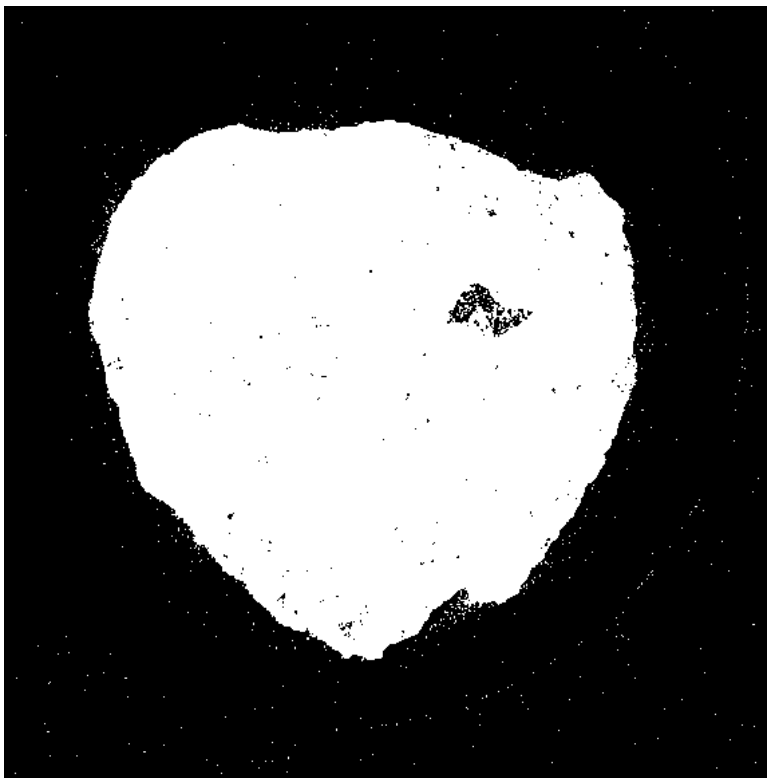

(b) The unsmoothened tomography is binarized.

Figure 4.10: Binarization at the lowest threshold returns locked voxels (black) and candidate voxels (white).

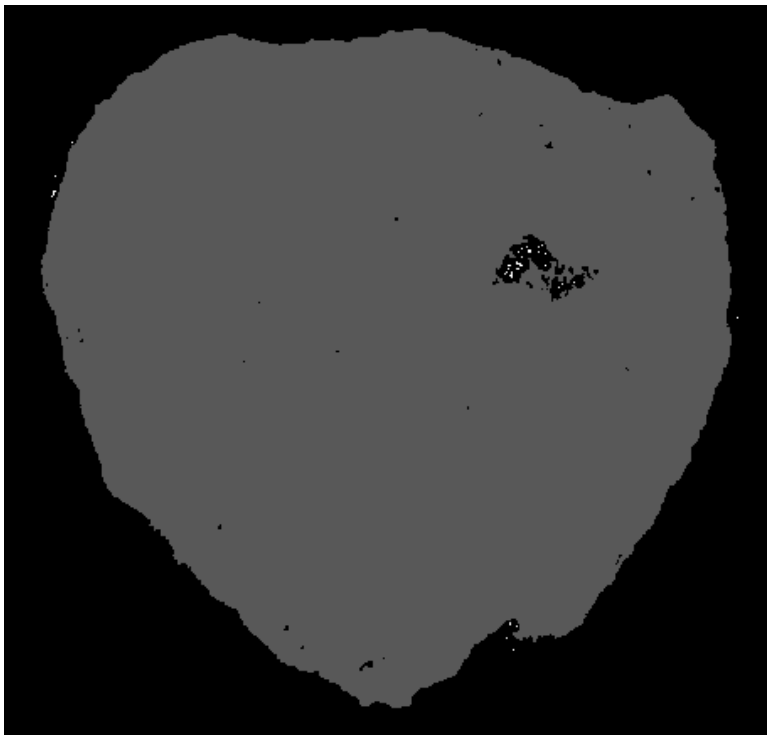

(a) The inside is filled up with a third color to mark voxels identified as part of the chondrule. White voxels are not connected (3d) to the chondrule.

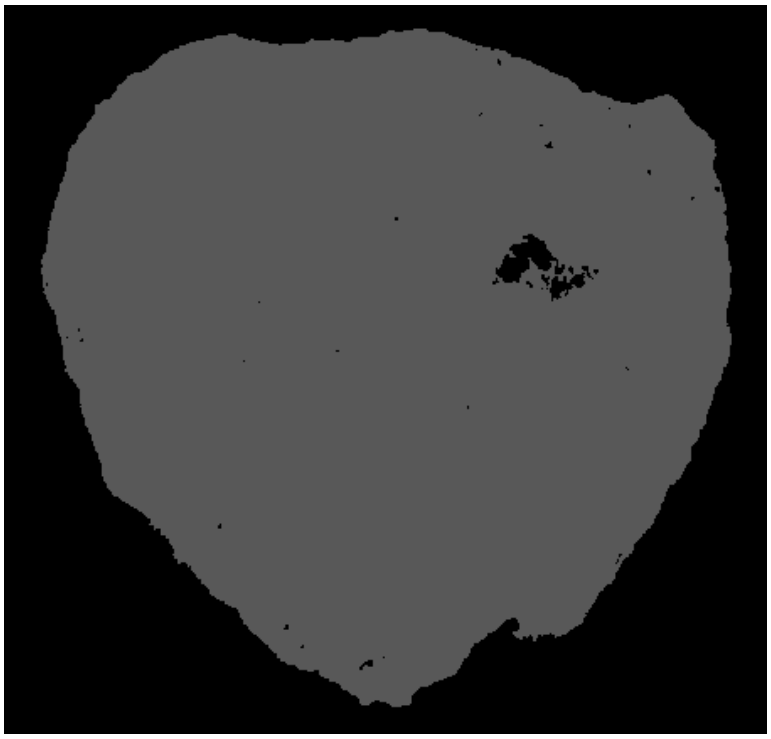

(b) White voxels turned into black to identify them as background.

Figure 4.11: Scanning the inside, starting from the geometrical center of the data object.

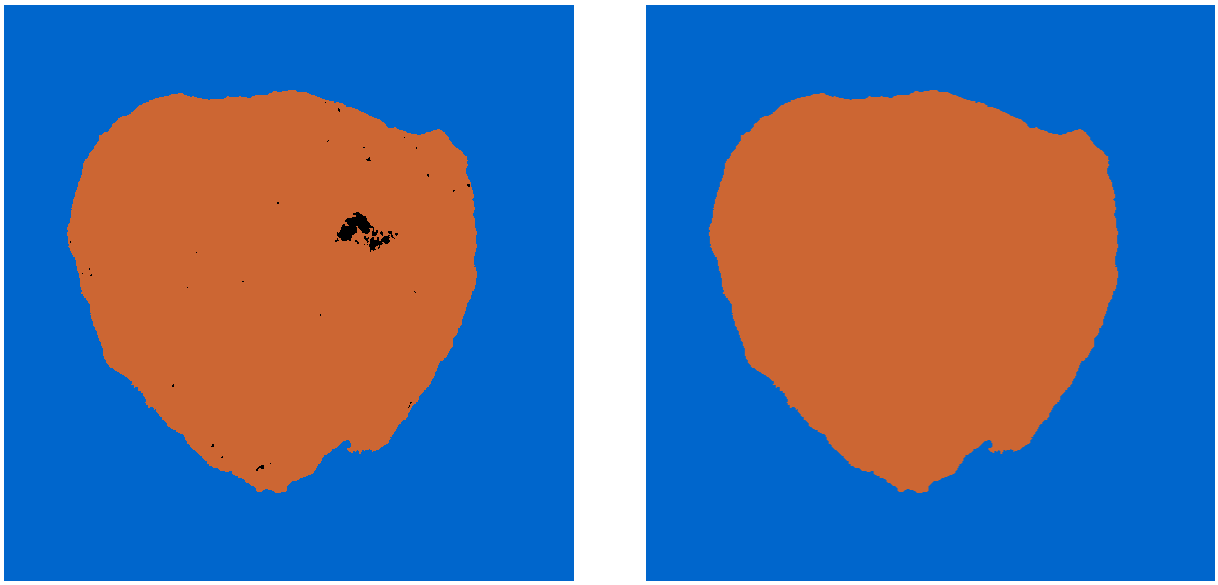

(a) The outside is scanned and marked (blue). Black voxels are found within the chondrule. Those are the voids.

(b) Voids and chondrule material are identified to form a mask (orange).

Figure 4.12: Scanning the outside, starting from an arbitrary voxel at the data object's bound.

it is mostly impossible to describe a body's surface with only one parametrization, but a solid's surface can be composed of several surface patches, all together forming the cohesive surface of a body. All this can easily be understood with the help of Figure 4.14, showing an actual chondrule surface defined by patches. This NURBS model was used in COMSOL calculations, and the results of all chondrule studies with COMSOL are discussed in sec. 4.2.4 and following.

4.2.3 Numericals

Loesche et al. (2013) numerically solved the steady state heat transfer problem with COMSOL for $k = k(\mathbf{r})$

$$\boldsymbol{\nabla} \cdot k \boldsymbol{\nabla} T = 0 \tag{2.2}$$

with the previously used Neumann boundary condition

$$k \frac{\partial T}{\partial \mathbf{n}}\bigg|_{r=r_0} = I\,\Theta(-\mathbf{e}_I \cdot \mathbf{n})\,\mathbf{e}_I \cdot \mathbf{n} - \sigma_{\mathrm{SB}}(T^4 - \left(T_{\mathrm{gas}}^{\mathrm{rad}}\right)^4) \tag{3.116}$$

for an illumination at $I = 20\,\mathrm{kW/m^2}$ and both gas temperatures at 293 K. For this setting, a corrected $\tilde{F}^{(4)}$ was used along the definition in sec. 3.3.6

$$\begin{aligned} F &= F\left(r, k, \alpha, I, T^-, T_{\mathrm{gas}}^{\mathrm{rad}}\right) \\ &= \left(0.7231 - 0.1741\mathrm{e}^{-2.180\frac{r}{k}\mathrm{W/(m^2\,K)}} + 0.4316\mathrm{e}^{-0.9251\alpha}\right) \cdot \\ &\quad \cdot \alpha\,\frac{\pi}{6}\,\frac{p}{T^-}\,I\,r^2\left[\frac{k}{r} + 4\sigma\,T_{\mathrm{bb}}^3\right]^{-1} . \end{aligned} \tag{4.6}$$

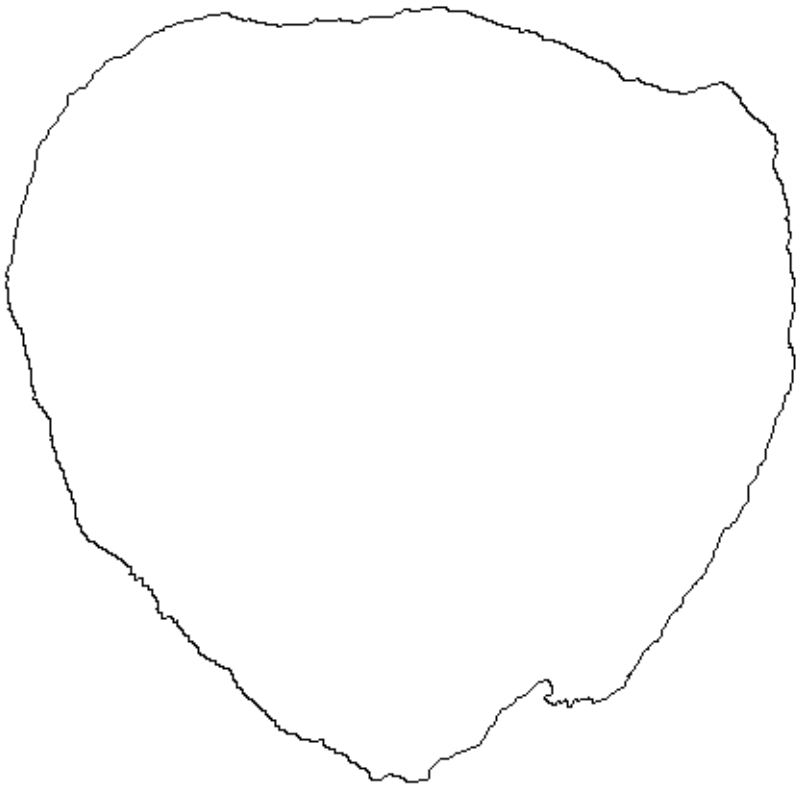

Figure 4.13: The edges of the mask after detection.

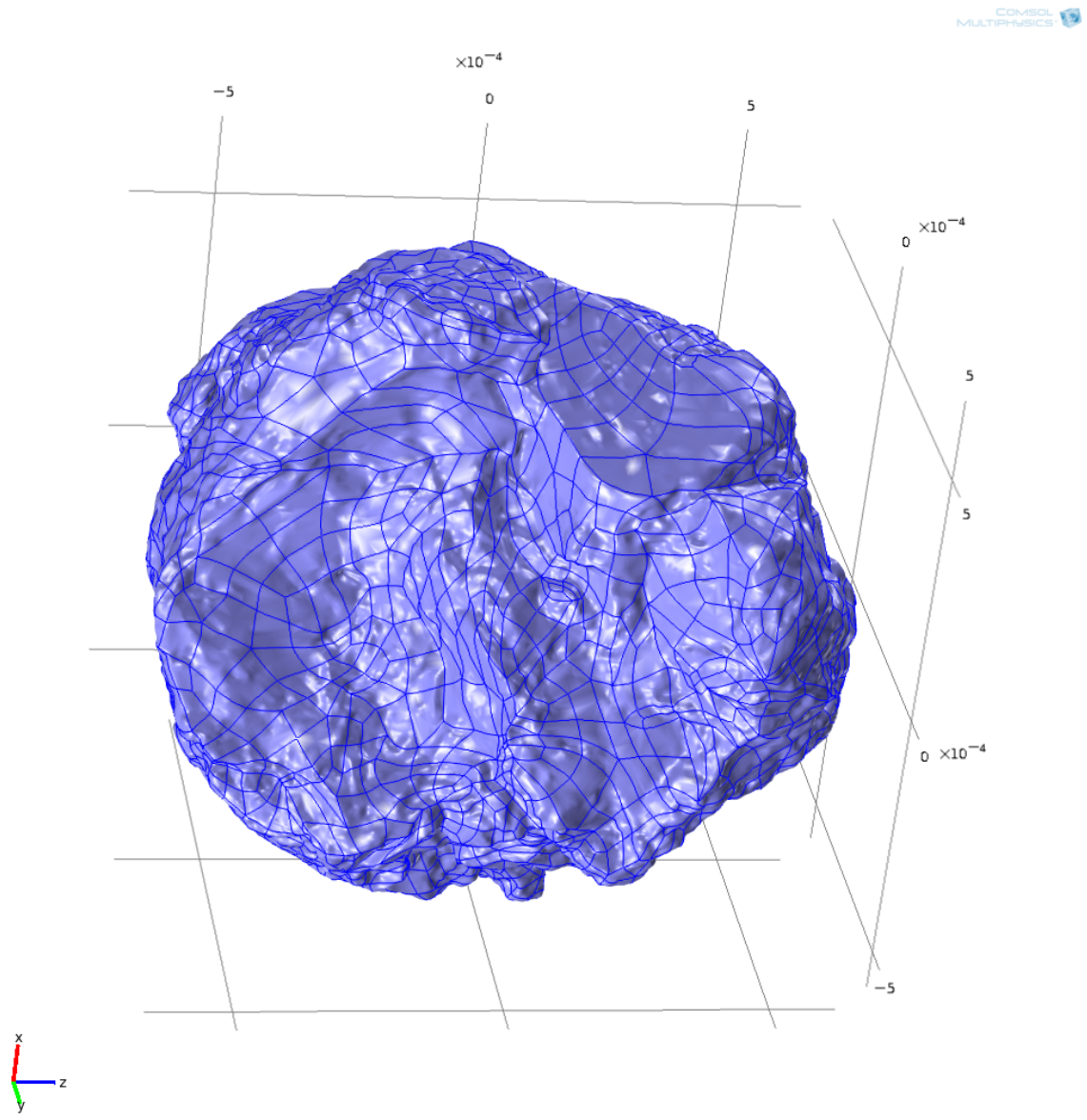

Figure 4.14: NURBS-model showing the surface patches (each patch's bound marked in dark blue). Taken from

Loesche et al. (2013) used tetrahedral meshes, the edges being the finite elements. Averaged for all chondrules, the mean size of a mesh cell was 23 μm, which is comparable to the tomography resolution of 5.26 μm/voxel. Hence, the coarse-grained material is appropriately resolved, but refinements of the mesh can alter the structure and abundance of the fine-grained material. COMSOL has nine predefined settings for different resolutions, based on five parameters: maximum element size (dimension of length), minimum element size (dimension of length), maximum element growth rate, resolution of curvature, resolution of narrow regions. For differently shaped domains, represented by bodies (e.g. spheres, blocks, etc.) in the geometry section of COMSOL, the parameter values for the different resolution settings change. However, in the context of (star-)convex bodies they are a function of the body's volume. The results obtained with numerical calculations on spheres are usually not notably changing for resolutions between medium to highest setting. Due to the irregular shape of chondrules and their inhomogeneity, the behavior at different mesh resolutions has to be tested. Loesche et al. (2013) confirmed convergence of their results with higher resolution (Figure 4.15). The force at the two highest resolutions varies on the order of 2%, which Loesche et al. (2013) attributed to the mentioned change in the resolved composition.

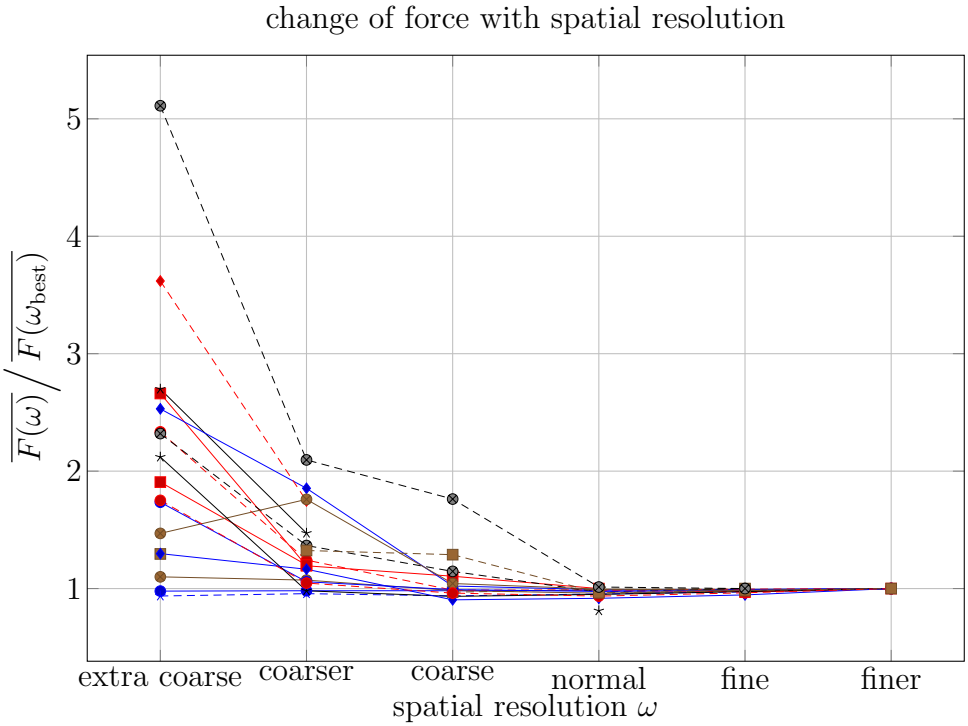

Figure 4.15: Mean photophoretic strength calculated at varying resolutions in multiple numerical studies, each represented by a line. Values were normalized to the value calculated with the best possible resolution. Convergence can be seen for higher resolutions. Data from Loesche et al. (2013).

The intensity of the light source and the gas temperature in the numerical calculations in Loesche et al. (2013) were chosen to rather match experimental conditions, e.g. those in Loesche et al. (2014). For directed illumination at $I = 20\,\mathrm{kW/m^2}$ and gas temperatures of 293 K, a sphere of 0.5 mm radius and a thermal conductivity of 0.5 W/m K would

experience a temperature difference across the surface of 37 K. In the model of Hayashi et al. (1985), a light flux of $I = 20\,\mathrm{kW/m^2}$ would correspond to a radial distance to the sun of 0.26 AU. The asteroid belt, though, is at 3 AU, which would correspond to a an intensity of $I = 152\,\mathrm{W/m^2}$. The gas temperature was chosen to match room temperature, but in protoplanetary disk, temperatures vary very strongly. As mentioned before, the goal is to give a qualitative description of photophoresis on nonspherical shaped particles, such as chondrules with star-like domain.

4.2.4 Photophoretic Forces

For all three sorts of particles described before, the photophoretic force was calculated by usage of (2.116). In the free molecule regime, it is $F_\mathrm{phot} \propto p$, thus, Loesche et al. (2013) discussed the ratio F_phot/p rather than F_phot. The angle enclosed by photophoretic force and direction of illumination $\mathbf{e}_I$ is denoted by

$$\Phi = \sphericalangle\left(\mathbf{F}_\mathrm{phot}, \mathbf{e}_I\right) \ . \tag{4.7}$$

4.2.4.1 Chondrules

Above, a dependence of the photophoretic force exerting of actual chondrules from the orientation with respect to the light field was expected. To account for that, the force for $N = 100$ different orientations was determined in the COMSOL model (the chondrule was space-fixed, the light source rotated, instead). The vectors of the incident light are steadily placed around a sphere. In a spherical coordinate system with the coordinates (φ, ϑ) denoting the direction of light, this was achieved by approximating the problem by specially chosen points $(\varphi(N,\nu), \vartheta(N,\nu))$ on a spiral, that is wrapped around the unit sphere (along Rakhmanov et al. (1994)). For a chosen number of points N, the index ν ($1 \leq \nu \leq N$, ν are natural numbers) is mapped to each individual point on the unit sphere by

$$\varphi(N,\nu) = 2\lfloor N^{0.485} \rfloor \arccos\left(\frac{1+N-2\nu}{1-N}\right) \tag{4.8a}$$

$$\vartheta(N,\nu) = \arccos\left(\frac{1+N-2\nu}{1-N}\right) \ . \tag{4.8b}$$

The 100 points used in Loesche et al. (2013) are shown in Figure 4.16.

With inhomogeneity and nonsphericity, the photophoretic force varies in direction and magnitude. Figure 4.17a shows the averaged angular deviation $\overline{\Phi}$ per chondrule, i.e. the angle between light and ensuing photophoretic force for the aforementioned 100 orientations. Averaging $\overline{\Phi}$ for all chondrules yields the $\overline{\Phi}_\mathrm{mean} = 3.0° \pm 1.5°$. Such a sideward motion was also measured in drop tower experiments carried out by Loesche et al. (2014). Variations with respect to the mean force per chondrules are plotted in Figure 4.17b. The overall average deviation from the mean value is $(\delta F/\overline{F})_\mathrm{mean} = 4.17\%$.

4.2.4.2 Best-fit spheres

As outlined before, the influence of irregular shape and inhomogeneous composition on the photophoretic behavior can be investigated by separating both effects in two different

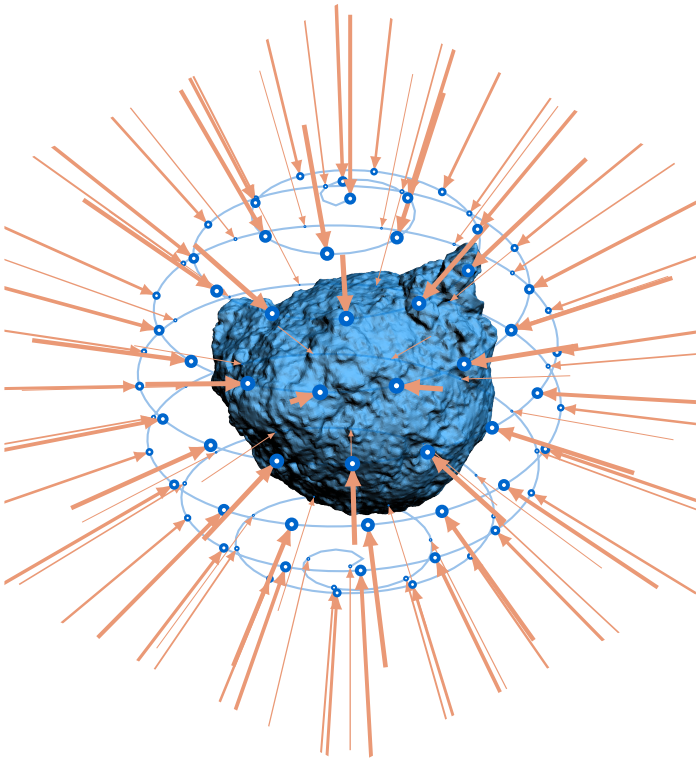

Figure 4.16: Evenly distributed points on a sphere, approximated by picking points on a spiral on the surface. Along Loesche et al. (2013).

models. To discuss the influence of inhomogeneity, Loesche et al. (2013) studied the photophoretic properties of spheres of chondrule composition (Figure 4.4). In the case that the best-fit sphere cuts voids, they are manually filled with olivine and pyroxenes to restore the sphericity of the particle. For those particles, (Loesche et al. 2013) found a total average angular deviation of $\overline{\Phi}_{\text{mean}} = 1.81° \pm 1.59°$. The overall average deviation from the force to its mean value is $(\delta F/\overline{F})_{\text{mean}} = 3.25\%$. Both values are on the same order as for the actual chondrules (sec. 4.2.4.1). For individual particles, Figure 4.18a and Figure 4.18b compare both, angular deviations and variations in the photophoretic force.

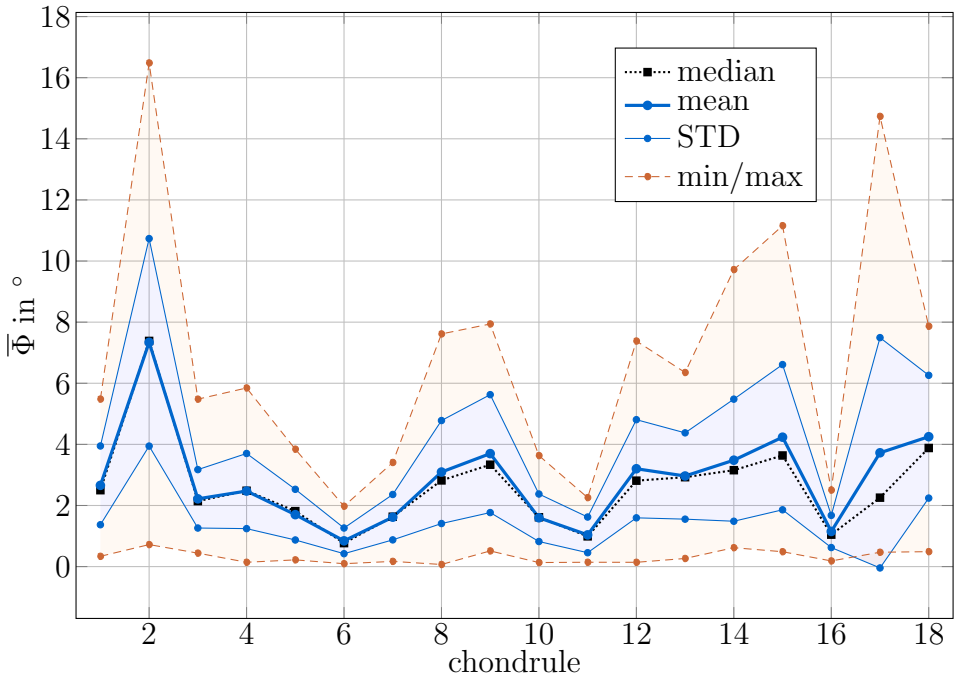

(a) Angular deviation $\overline{\Phi}$ per chondrule.

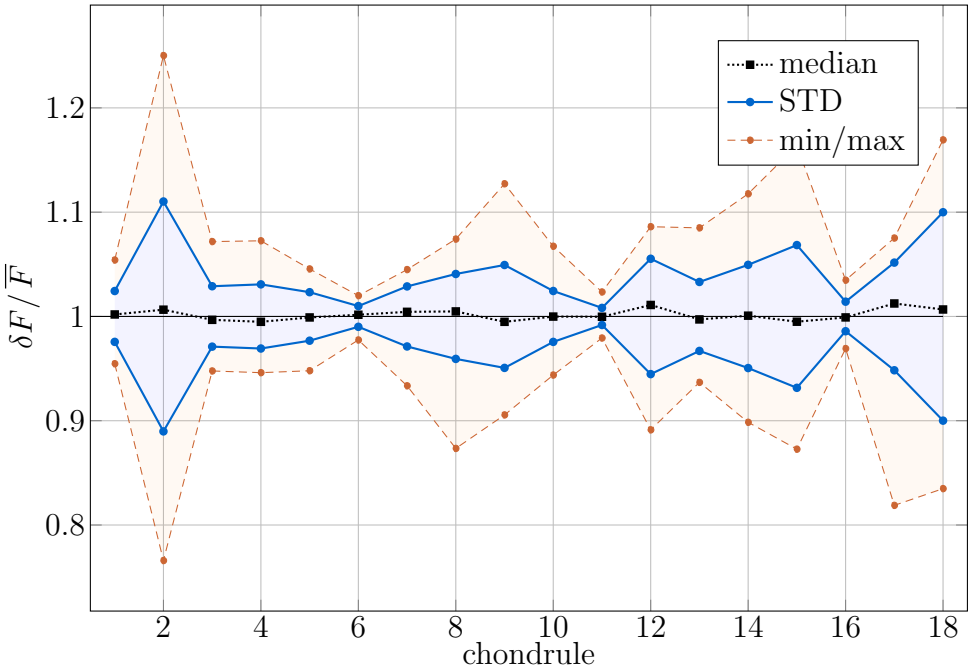

(b) Relative force deviations $\delta F/\overline{F}$ per chondrule.

Figure 4.17: Chondrules at 100 different orientations with respect to the light. Displayed are standard deviations and minimum/maximum values. The angular distribution of the incident light along different orientations is shown in Figure 4.16. Data from Loesche et al. (2013).

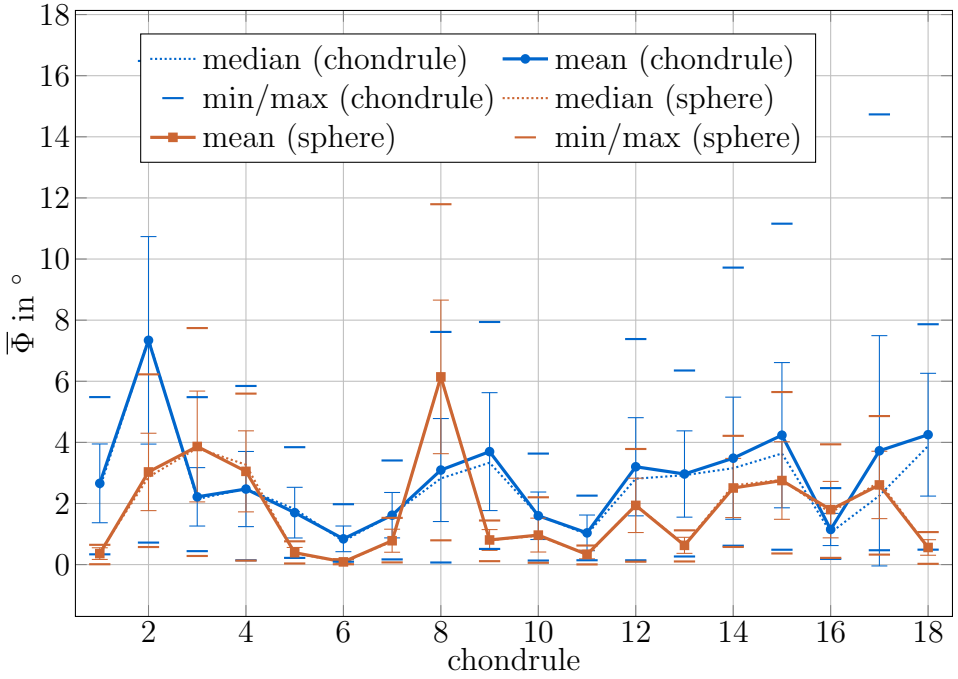

(a) Angular deviation $\overline{\Phi}$ for full and spherical chondrules.

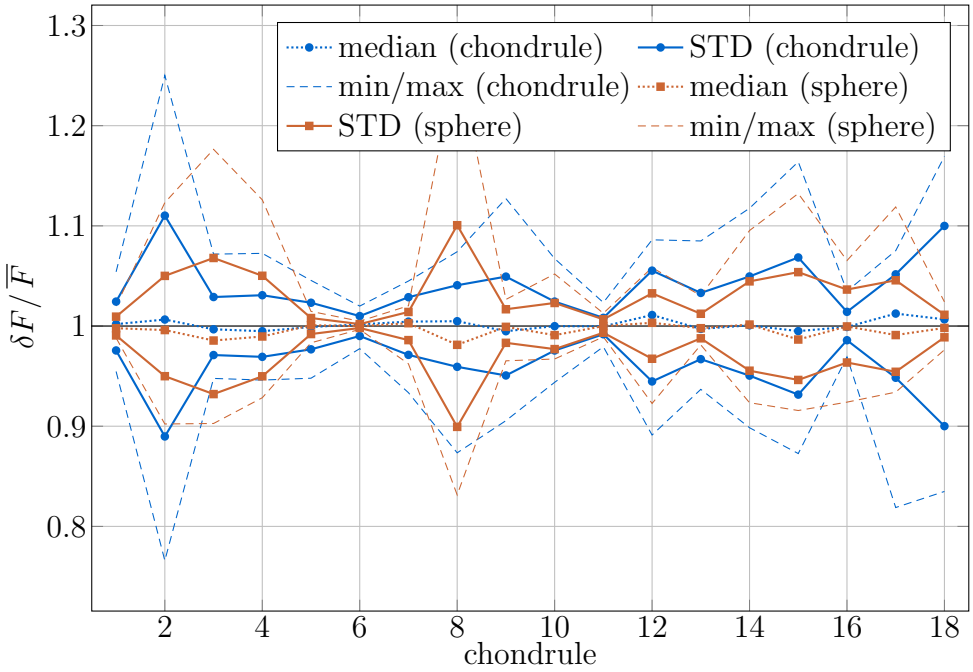

(b) Relative force deviations $\delta F/\overline{F}$ for full and spherical chondrules.

Figure 4.18: Best-fit spheres compared to chondrules at 100 different orientations with respect to the light. Displayed are standard deviations and minimum/maximum values. The angular distribution of the incident light along different orientations is shown in Figure 4.16. Data from Loesche et al. (2013).

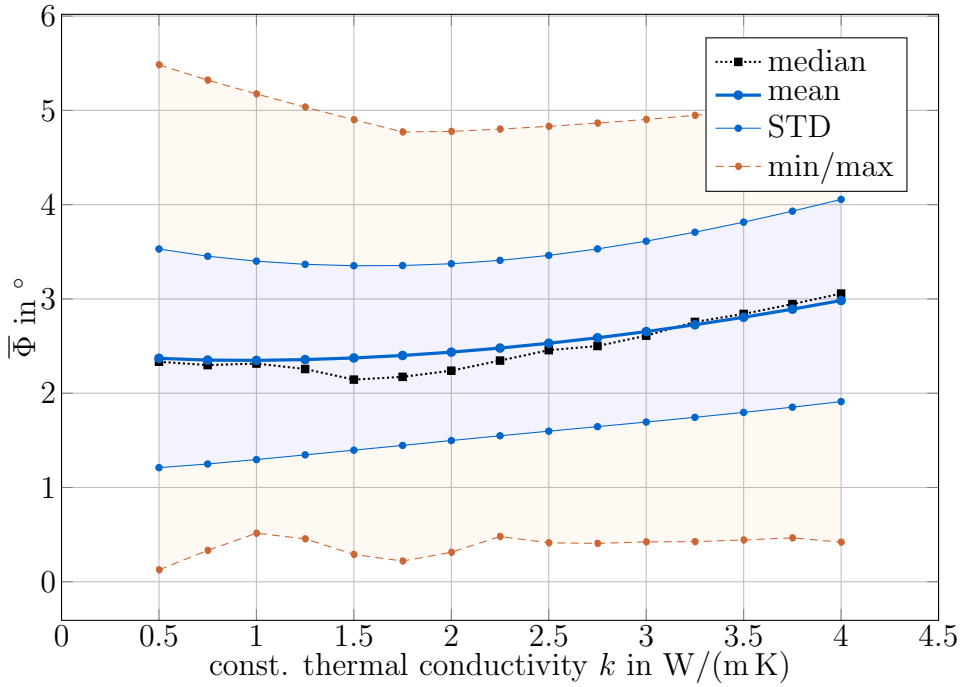

Figure 4.19: Mean angular deviation $\overline{\Phi}$ for homogeneous chondrule-shaped particle at different thermal conductivities. Data from Loesche et al. (2013).

4.2.4.3 Homogeneous chondrule-shaped particles at multiple thermal conductivities

The study of the photophoretic properties of homogeneous particles of chondrule shape shed new light on photophoresis of star-convex particles. Figure 4.19 shows the mean angle Φ for one exemplary particle at different thermal conductivities. The average for this particle over all k is $\overline{\Phi}_{\text{mean}} = 2.54° \pm 1.00°$. Exemplarily, Figure 4.20b shows an increasing variation of the photophoretic force around its mean value as the thermal conductivity of the chondrule-shaped particles increases. More interestingly, Figure 4.20a shows the force to pressure ratio for different thermal conductivities, averaged over the 100 different orientations per k for an exemplary chondrule shaped particle. The graph can surprisingly be described by the corrected approximation $\chi^{(4a)}(r_s, k)\, \tilde{F}^{(4a)}(r_s, k)$, whereas Loesche et al. (2013) used (4.6) — which were originally developed for homogeneous spheres — for the given light intensity and gas temperature, when the radius of a volume equivalent sphere r_s is used.

The same correlation $\chi^{(4a)}(r_s)\, \tilde{F}^{(4a)}(r_s) = \overline{F}$ was verified for the remaining chondrules when homogenized. The quality of the description of $\overline{F}$ for the three different radii with $\chi^{(4a)}\, \tilde{F}^{(4a)}$ is shown in Figure 4.22. The statistics of the three data lines are listed in Table 4.3. It is assumed, that the radius of a volume equivalent sphere is the characteristic size needed as one of the two descriptors to explain the photophoretic force exerting on chondrules (see beginning of sec. 4.2). To test the hypothesis, that the average photophoretic force — averaged concerning the 100 different angles of incident light — can be expressed by any corrected I-r-k-approximation (e.g., the corrected approximation $\chi^{(4)}(r_s)\, \tilde{F}^{(4)}(r_s)$ (4.6)), Loesche et al. (2013) considered an ellipsoid as another particle shape. Even for half-axes (1,2,3) mm the orientation-averaged photophoretic force for this

ellipsoid can very well be expressed by any corrected I-r-k-approximation for the radius of the volume-equivalent sphere enters as $r_\mathrm{s} = 1.82\,\mathrm{mm}$, as Figure 4.21 shows well, whereas the surface-averaged radius $\overline{r} = 1.97\,\mathrm{mm}$ does not describe the numerical data (averaged from the center of shape). The mean radius of the ellipsoid with parameterization $\boldsymbol{\rho}$ was calculated by

$$\boldsymbol{\rho}(\zeta,\xi,r) = r \begin{pmatrix} 1\,\cos\xi\,\sin\zeta \\ 2\,\sin\xi\,\sin\zeta \\ 3\,\cos\zeta \end{pmatrix} \tag{4.9a}$$

$$V = \int_0^{2\pi}\int_0^{\pi}\int_0^{1} \left|\det \partial_{(\xi,\zeta,r)}\boldsymbol{\rho}\right| \,\mathrm{d}r\,\mathrm{d}\zeta\,\mathrm{d}\xi \;\Rightarrow\; r_\mathrm{s} = \sqrt[3]{\frac{3V}{4\pi}} \tag{4.9b}$$

$$|\partial V| = \int_0^{2\pi}\int_0^{\pi} \|\boldsymbol{\partial}_\zeta \times \boldsymbol{\partial}_\xi\|_2 \,\mathrm{d}\zeta\,\mathrm{d}\xi \tag{4.9c}$$

$$\overline{r} = \frac{1}{|\partial V|}\int_0^{2\pi}\int_0^{\pi} \rho(\zeta,\xi,1)\,\|\boldsymbol{\partial}_\zeta \times \boldsymbol{\partial}_\xi\|_2 \,\mathrm{d}\zeta\,\mathrm{d}\xi\,. \tag{4.9d}$$

As most chondrules are relatively spherical, $\overline{r}$ does only slightly worse than r_s. A strong deviation is evident for the ellipsoid, which is the most non-spherical particle in the subjacent numerical analysis. Here, the good performance of $\overline{F}(r_\mathrm{s}) = \chi^{(4a)}(r_\mathrm{s})\,\tilde{F}^{(4a)}(r_\mathrm{s})$ can be seen. However, the description with r_s shows only an average error of 1.29% to reproduce the data points, which is very close to the fitted values of r. The error is within the error interval of $\chi^{(4a)}\tilde{F}^{(4a)}$ (Table 3.3) for the radius interval $[0.11\,\mathrm{mm}, 1.1\,\mathrm{mm}]$. However, other numerical effects such as geometry alternation by meshing or the setting up of the NURBS surfaces for the COMSOL calculations can cause this small error error. However, no analytical proof of this behavior is given in this work, but the general solution (3.20) for star-convex particles is suggested to be the starting point.

Table 4.3: Overall deviation of calculated data with different radii from the numerical data to describe $\overline{F}/p$ on irregularly shaped particles (averaged over 100 different orientations). Individual deviations for chondrules shown in Figure 4.22.

	mean of mean deviations	median of mean devaitions	STD of mean devaitions
r_s	1.29%	1.37%	1.29%
$\overline{r}$	2.99%	2.66%	6.22%
r_fit	-1.07%	-0.72%	0.97%

Example: Triaxial ellipsoid. The general parametrization $\tilde{\boldsymbol{\Omega}}$ for a triaxial ellipsoid is

$$\tilde{\boldsymbol{\Omega}}(\varphi,\vartheta) = \begin{pmatrix} a\,\cos\varphi\,\sin\vartheta \\ b\,\sin\varphi\,\sin\vartheta \\ c\,\cos\vartheta \end{pmatrix}\,. \tag{4.10}$$

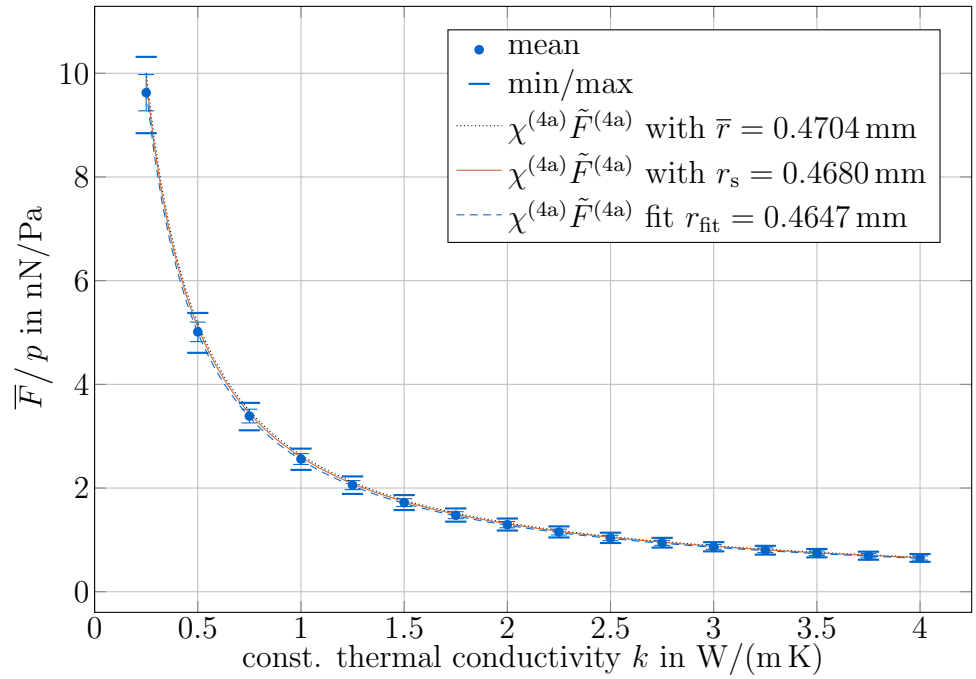

(a) $\overline{F/p}$ for a chondrule-shaped particle at different thermal conductivities k. Overplotted are graphs obtained with $\chi^{(4a)}\tilde{F}^{(4a)}$ with fitted radius, mean radius and volume-equivalent sphere radius. Error bars are standard deviation. $T^- = T^{rad}_{gas} = 293.15\,\mathrm{K}$, $\alpha = 1$ and $I = 20\,\mathrm{kW/m^2}$. Correction factor $\chi^{(4a)}$ from (3.120).

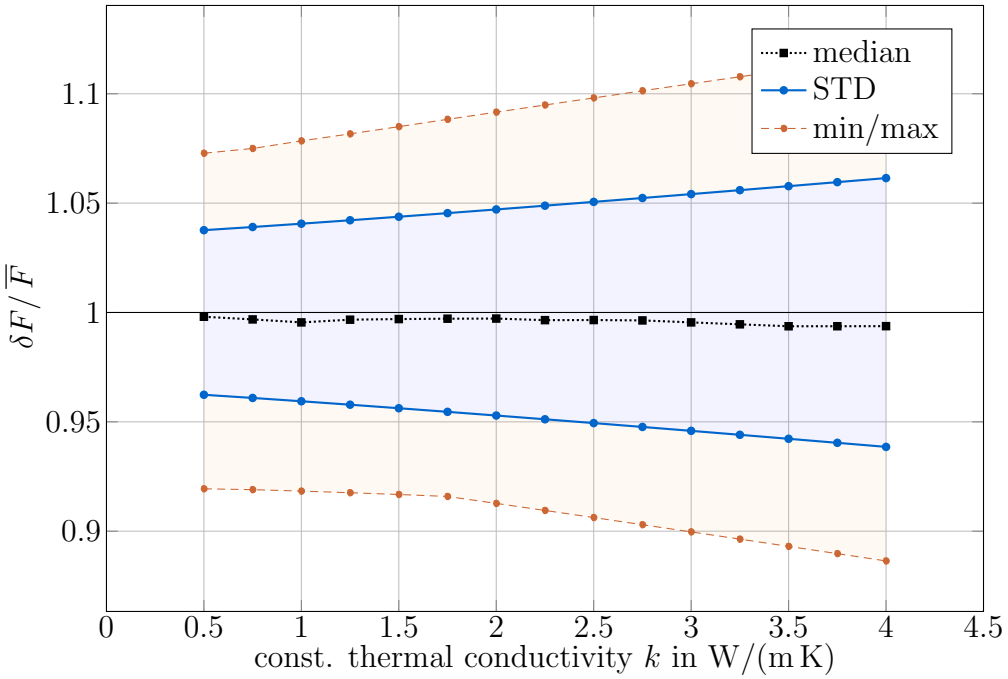

(b) Mean relative force deviations $(\delta F/\overline{F})_{mean}$ for a chondrule-shaped particle at different thermal conductivities.

Figure 4.20: Photohoretic behavior of a chondrule-shaped particles at 100 different orientations with respect to the light. Displayed are standard deviations and minimum/maximum values. The angular distribution of the incident light along different orientations is shown in Figure 4.16. Data from Loesche et al. (2013).

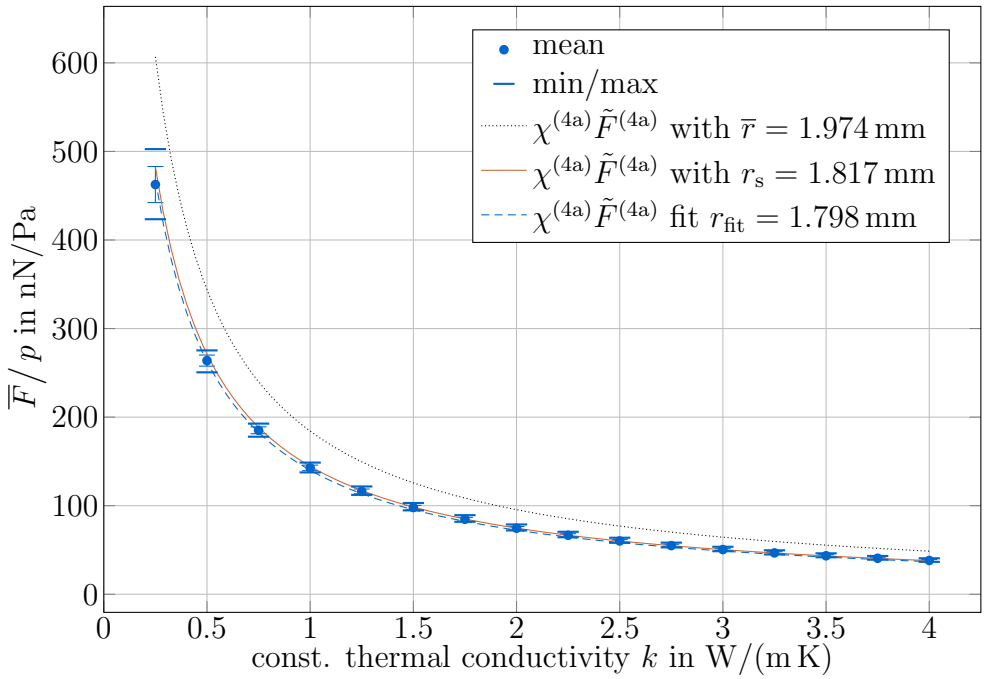

Figure 4.21: $\overline{F/p}$ for an ellipsoid with half-axes (1,2,3) mm for different thermal conductivities k. Overplotted are graphs obtained with $\chi^{(4a)}\tilde{F}^{(4a)}$ with fitted radius, mean radius and volume-equivalent sphere radius. Error bars are standard deviation. $T^- = T^{\mathrm{rad}}_{\mathrm{gas}} = 293.15\,\mathrm{K}$, $\alpha = 1$ and $I = 20\,\mathrm{kW/m^2}$. Data from Loesche et al. (2013). Correction factor $\chi^{(4a)}$ from (3.120).

Along the parametrization

$$\mathbf{\Omega}(\xi,\zeta) = \Omega(\xi,\zeta)\,\mathbf{n}_{\mathrm{S}}(\xi,\zeta)\,, \tag{3.9b}$$

the radius function can be analytically obtained as

$$\Omega(\xi,\zeta) = a^2\,\cos^2\varphi(\xi)\,\sin^2\vartheta(\xi,\zeta) + b^2\,\sin^2\varphi(\xi)\,\sin^2\vartheta(\xi,\zeta) + c^2\,\cos^2\vartheta(\xi,\zeta) \tag{4.11}$$

with the coordinates φ and ϑ being functions of the spherical coordinates ξ and ζ

$$\varphi(\xi) = \mathrm{atan2}(a\,\sin\xi,\, b\,\cos\xi) \tag{4.12a}$$

$$\vartheta(\xi,\zeta) = \mathrm{atan2}\left(c\,\sin\zeta,\, \cos\zeta\sqrt{a^2\,\cos^2\varphi(\xi) + b^2\,\sin^2\varphi(\xi)}\right) \tag{4.12b}$$

$$\Rightarrow \Omega(\xi,\zeta) = \frac{a\,b\,c}{\sqrt{c^2\,\sin^2\zeta\left(a^2\,\sin^2\xi + b^2\,\cos^2\xi\right) + a^2\,b^2\,\cos^2\zeta}}\,. \tag{4.12c}$$

The function $\mathrm{atan2(y,x)} : \mathbb{R}\times\mathbb{R} \to [0, 2\pi]$ denotes the quadrant-sensitive arctangent function. The resulting plots of the ellipsoid can be seen in Figure 4.23, where the white lines are the coordinate lines, described by the coordinate vectors. Figure 4.23a shows the ellipsoid in the new parametrization (3.9b) with (4.12c), Figure 4.23b is the ellipsoid in the simple parametrization (4.10). The need for a mapping between the different coordinate system is shown in Figure 4.23c, where the new parametrization is used in the

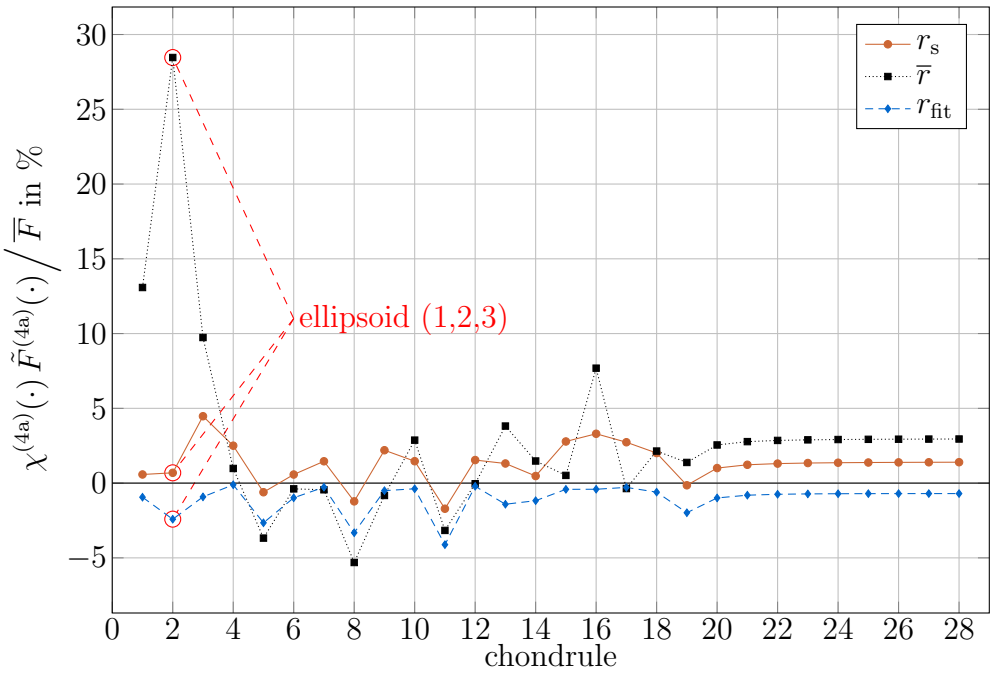

Figure 4.22: Individual deviation of calculated data for different radii from the numerical data for $\overline{F}/p$ on irregularly shaped particles (averaged over 100 different orientations). Overall statistics in Table 4.3. The last ten data runs are for the same chondrule at $\alpha = 0.1, 0.2, \ldots, 1$, otherwise $\alpha = 1$. The ellipsoid is the second data point. Obviously, r_s describes the mean photophoretic force the best. Correction factor $\chi^{(4a)}$ from (3.120).

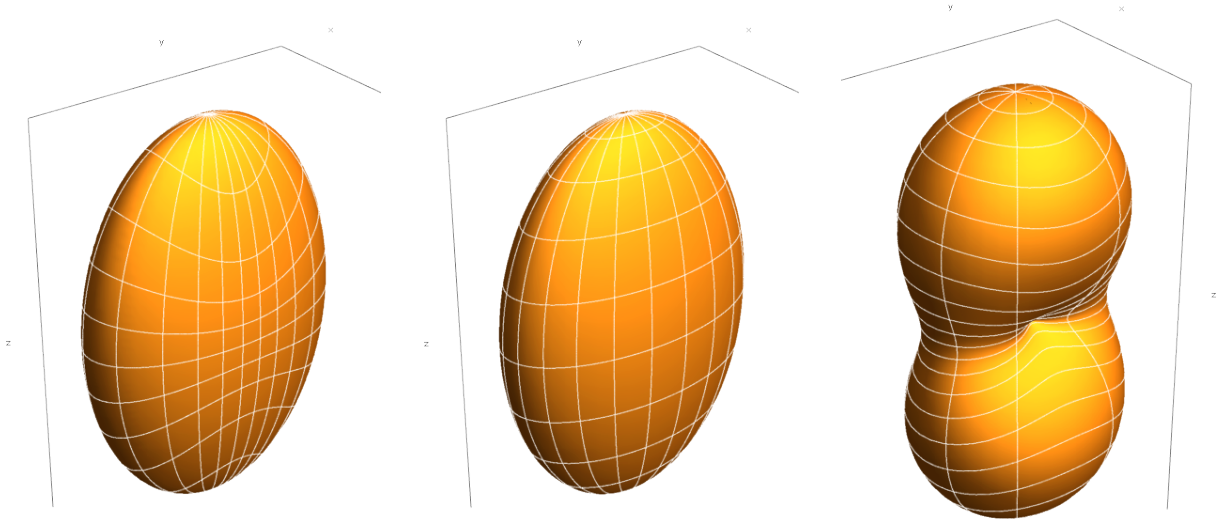

(a) In spherical coordinates (ξ, ζ) with the parametrization $\Omega(\varphi(\xi), \vartheta(\xi, \zeta))\,\mathbf{n}_S(\xi, \zeta)$.

(b) In the coordinates (φ, ϑ) with the parametrization (4.10).

(c) In the parametrization $\Omega(\varphi, \vartheta)\,\mathbf{n}_S(\varphi, \vartheta)$, where (φ, ϑ) are directly varied (wrong).

Figure 4.23: Triaxial ellipsoids.

old coordinate system, yielding something else but the triaxial ellipsoid. The expansion of $\Omega(\xi,\zeta)^n$, $n=1,2,3$ in spherical harmonics along (3.14) can be achieved by numerically evaluating

$$\omega_{\nu\mu}^{(n)} = (\Omega^n\,,\,Y_\nu^\mu)\ . \tag{4.13}$$

The volume of the ellipsoid is calculated in three different ways. In both parametrizations, the volume is

$$V = \int_0^\pi\int_0^{2\pi}\int_0^1 \left|\det\partial_{(\varphi,\vartheta,r)}\left(r\,\tilde{\mathbf{\Omega}}\right)\right|\,\mathrm{d}r\,\mathrm{d}\varphi\,\mathrm{d}\vartheta = \int_0^\pi\int_0^{2\pi}\int_0^1 a\,b\,c\,r^2\,\sin\vartheta\,\mathrm{d}r\,\mathrm{d}\varphi\,\mathrm{d}\vartheta = \frac{4\pi}{3}a\,b\,c \tag{4.14a}$$

$$= \int_0^\pi\int_0^{2\pi}\int_0^1 \left|\det\partial_{(\xi,\zeta,r)}\left(r\,\mathbf{\Omega}\right)\right|\,\mathrm{d}r\,\mathrm{d}\xi\,\mathrm{d}\zeta = \int_0^\pi\int_0^{2\pi}\int_0^1 \Omega(\xi,\zeta)^3\,r^2\,\sin\vartheta\,\mathrm{d}r\,\mathrm{d}\xi\,\mathrm{d}\zeta \tag{4.14b}$$

$$\overset{(3.22b)}{=} \frac{1}{3}\sum_{\nu,\mu}\omega_{\nu\mu}^{(1)}\,\omega_{\nu\mu}^{(2)*} \tag{4.14c}$$

$$\overset{(3.22c)}{=} \frac{2\sqrt{\pi}}{3}\omega_{0,0}^{(3)} \tag{4.14d}$$

Now, the general solution (3.20) is employed to calculate the photophoretic on an ellipsoid with the half-axes (1,2,3) mm at 100 different angles of illumination as sketched in Figure 4.16 in sec. 4.2.4.3. The parameters are set to $I = 20\,\mathrm{kW/m^2}$, $T^- = T_{\mathrm{gas}}^{\mathrm{rad}} = 293.15\,\mathrm{K}$, $k = 0.25\,\mathrm{W/m\,K}$ and $\alpha = 1$. The surface temperatures are calculated with COMSOL and subsequently exported into a spreadsheet file ($x-y-z-T_1-T_2-\dots$). From the x, y, z coordinates, the respective spherical angles ξ and ζ are sampled with the help of Mathematica, which then finds a spherical harmonic expansion for $\tau^{(n)} \overset{\alpha=1}{=} \frac{\sqrt{T}}{\Omega^{n-2}}$ for $n = 2,3,4,\dots$ in the coordinates (ξ,ζ) along (3.14b). With $\omega_{\nu\mu}^{(n)}$ and $t_{pq}^{(n)}$ obtained to 14-th degree for $n = 2$, 3, 4, the average force yields (averaged over the 100 total values obtained with the general solution (3.20))

$$\overline{F^{(n)}} = 463\,\mathrm{nN/Pa}\ . \tag{4.15}$$

Compared to the in situ obtained values in COMSOL, the photophortic force, its standard deviation, minimum and maximum are met to better than $2\cdot10^{-3}\%$. The force depending on the thermal conductivity k is shown in Figure 4.21. In other words, all the 100 different values for the force give the same result as the in situ COMSOL calculations for the force. The convergence of $F_{\mathrm{phot}}^{(n)}$ for $n = 2,3,4$ is shown in Figure 4.24 for different maximum orders $\nu_{\max}$. Especially for $n = 3$, the convergence is really fast, already 98.5% of the real value for $\nu_{\max} = 0$. From COMSOL or lab experiments, it is possible to get the temperature distribution across the surface. However, obtaining an analytical expression for $\tau^{(n)}$ is probably impossible. For only the temperature distribution, the heat transfer equation in the new coordinate system would have to be solved. Just for demonstration, the Laplace operator for the coordinate system

$$\boldsymbol{r}(r,\xi,\zeta) = r\,\Omega(\xi,\zeta)\,\mathbf{n}_{\mathrm{S}}(\xi,\zeta) \tag{4.16}$$

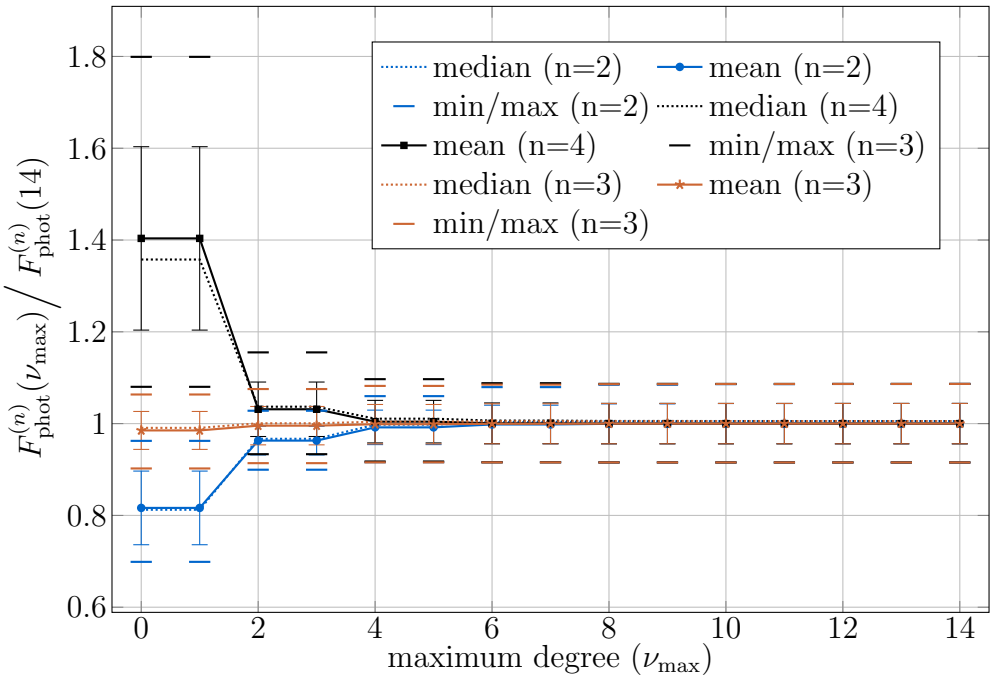

Figure 4.24: Convergence of $F^{(2)}$, $F^{(3)}$ and $F^{(4)}$ for different $\nu_{\max}$. $F^{(3)}$ is almost exact for $\nu_{\max} = 0$, i.e. (3.130).

with the non-orthogonal curvilinear coordinate vectors $\boldsymbol{\partial}_r$, $\boldsymbol{\partial}_\xi$, $\boldsymbol{\partial}_\zeta$ is

$$\Delta T(r,\xi,\zeta) = \frac{1}{h_r\, h_\xi\, h_\zeta}\left[\partial_r\left(\frac{h_\xi h_\zeta}{h_r}T\right) + \partial_\xi\left(\frac{h_r h_\zeta}{h_\xi}T\right) + \partial_\zeta\left(\frac{h_r h_\xi}{h_\zeta}T\right)\right] \tag{4.17a}$$

$$h_r = \|\boldsymbol{\partial}_r\|_2 \qquad h_\xi = \|\boldsymbol{\partial}_\xi\|_2 \qquad h_\zeta = \|\boldsymbol{\partial}_\zeta\|_2 \ . \tag{4.17b}$$

However, it is possible to use the approximation

$$\mathbf{F}^{(3)}_{\text{phot}} \simeq -\frac{1}{2}\sqrt{\frac{3}{2\pi}}\frac{p\,V}{\sqrt{T^-}}\begin{pmatrix} -\Re\, t^{(3)}_{1,1} \\ -\Im\, t^{(3)}_{1,1} \\ \frac{1}{\sqrt{2}}\, t^{(3)}_{1,0} \end{pmatrix} , \tag{3.130}$$

too, assuming, that the behavior for $\mathbf{F}^{(3)}_{\text{phot}}(\nu_{\max})$ is always as shown in Figure 4.24, which is quite likely the case for directed illumination, because the fact that for spheres the respective linear part t_1 also contributes the most, suggests that. Here, this could only be verified for the ellipsoid, the temperature data for the chondrules has not been stored since every solution needs about 50-150 GB.

However, for the further argumentation it is assumed, that the force acting on the chondrules (they are less non-spherical than the ellipsoid) can also be quite well described with $\mathbf{F}^{(3)}_{\text{phot}}(0)$. As for $\nu \geq 0$, $-\nu \leq \mu \leq \nu$ the expansion coefficients $\omega^{(n)}_{\nu\mu}$ are linearly independent, and it is $\omega^{(3)}_{0,0} = \frac{3}{2\sqrt{\pi}}V$, it can be inferred that the force is linear in the volume of the particle (for about 98% only though; on the other hand the two $t_{1,x}$ also somehow change with the volume since they have the dimension $\sqrt{\mathrm{K}}/\mathrm{m}$). Furthermore, for all the investigated homogeneous chondrule-shaped particles, the mean force (averaged over all 100 irradiation directions) is a function of the volume-equivalent sphere's radius

to also about 98% $r_\mathrm{s} = \frac{1}{\pi^{1/6}} \left(\frac{\omega_{0,0}^{(3)}}{2} \right)^{1/3}$ (Figure 4.20a, Figure 4.21, Figure 4.22 and Table 4.3). So, for the irradiation coming from the direction (φ, ϑ) it must be

$$\frac{1}{4\pi} \int_0^{2\pi} \int_0^{\pi} \left\| \begin{pmatrix} -\Re\, t_{1,1}^{(3)}(\varphi,\vartheta) \\ -\Im\, t_{1,1}^{(3)}(\varphi,\vartheta) \\ \frac{1}{\sqrt{2}} t_{1,0}^{(3)}(\varphi,\vartheta) \end{pmatrix} \right\|_2 \sin\vartheta \,\mathrm{d}\vartheta \,\mathrm{d}\varphi = \sqrt{\frac{2\pi}{3T^+}} \frac{\alpha\, \alpha_\mathrm{m}\, I\, J_1}{k + r_0\, h + 4 r_0 \sigma_\mathrm{SB} \varepsilon\, T_\mathrm{bb}^3} \,. \quad (4.18)$$

Of course, (4.18) is only an empirical identification, and the origin of r_s is unclear. Probably, for certain assumptions, the Laplace operator (4.17) in this coordinate system can be simplified and analyzed, so that aboves empirical rule can analytically somehow be confirmed.

4.2.5 Photophoretic properties of chondrules

Investigation on the photophoretic force acting on realistic chondrules, their best-fit spheres and homogeneous, chondrule-shaped particles show, that the force varies in direction and strength within a few percent each. The numerical experiments showed a rather small variation, compared to the drop tower experiments in Loesche et al. (2014). The explanation for the discrepancy is given in sec. 4.3.

As outlined at the beginning of this sec. 4.2, a radius equivalent, i.e. a characteristic size, and extension of the effective thermal conductivity $\varkappa$ to nonspherical particles is needed. The characteristic size, as Loesche et al. (2013) found out and explained just above, is the radius of a particle volume equivalent sphere r_s. The effective thermal conductivity $\varkappa$ can subsequently obtained by solving (4.6) or $\chi^{(4a)} \tilde{F}^{(4a)}$ for a given force for k, which then is the sought-after effective thermal conductivity $\varkappa$. Figure 4.25a shows the values of $\varkappa$ plotted over the volume fraction of the two dominating phases, which differ strongly in their individual thermal conductivity. A strong correlation can be seen. For better analysis, Figure 4.25b has the olivine/pyroxene axis reversed. As both phases dominate the investigated chondrules, the solid line in the same plot describes the resulting two-phase system, eligible to be described by a third-order polynomial as

$$\varkappa = -1.87 \times 10^{-7} x^3 + 2.94 \times 10^{-4} x^2 - 7.22 \times 10^{-2} x + 4.54 \,, \quad (4.19)$$

with x denoting the mesostasis fraction in the corresponding two-phase system.

Recapitulating the findings, the averaged photophoretic force acting on a real chondrule can be described with I-k-approximations, like (4.6) or (3.115f), depending on $(r_\mathrm{s}, \varkappa)$, where $\varkappa$ is determined by the ratio of the two primary phases. Following, for other chondrules which essentially are dominated by two phases, the same procedure allows to calculate the average photophoretic on this particle $\overline{F}$ (like an expectation value), if the fraction of the two primary phases and the volume of the particle is known. The results for the whole chondrule set is given in Table 4.4.

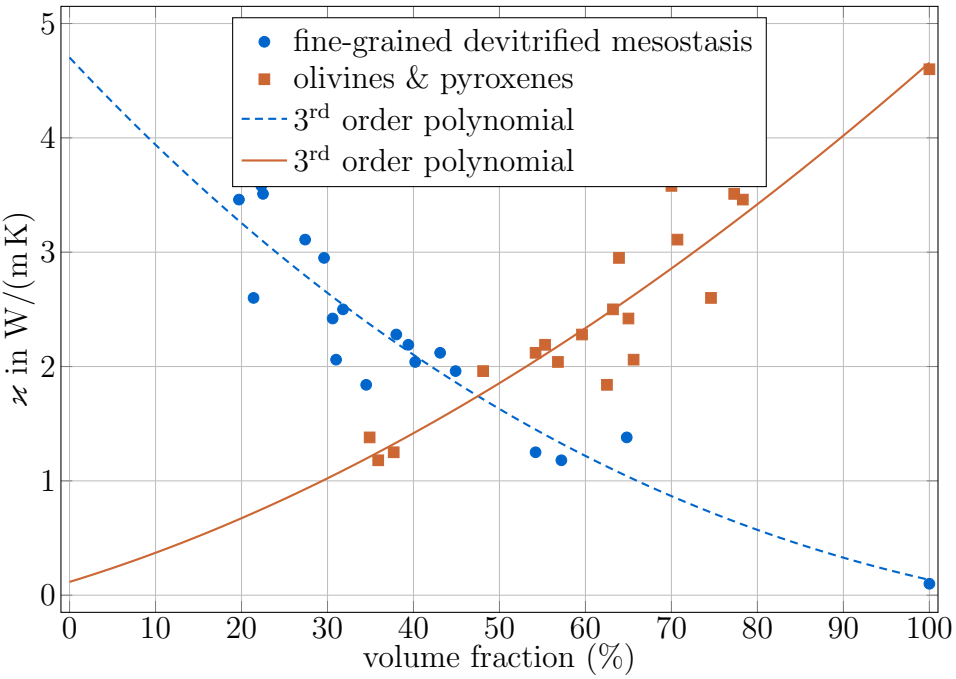

(a) Effective thermal conductivity $\varkappa$ plotted over volume fraction of fine-grained devitrified mesostasis and olivines/pyroxenes, respectively. Overplotted with third-order polynomial graphs.

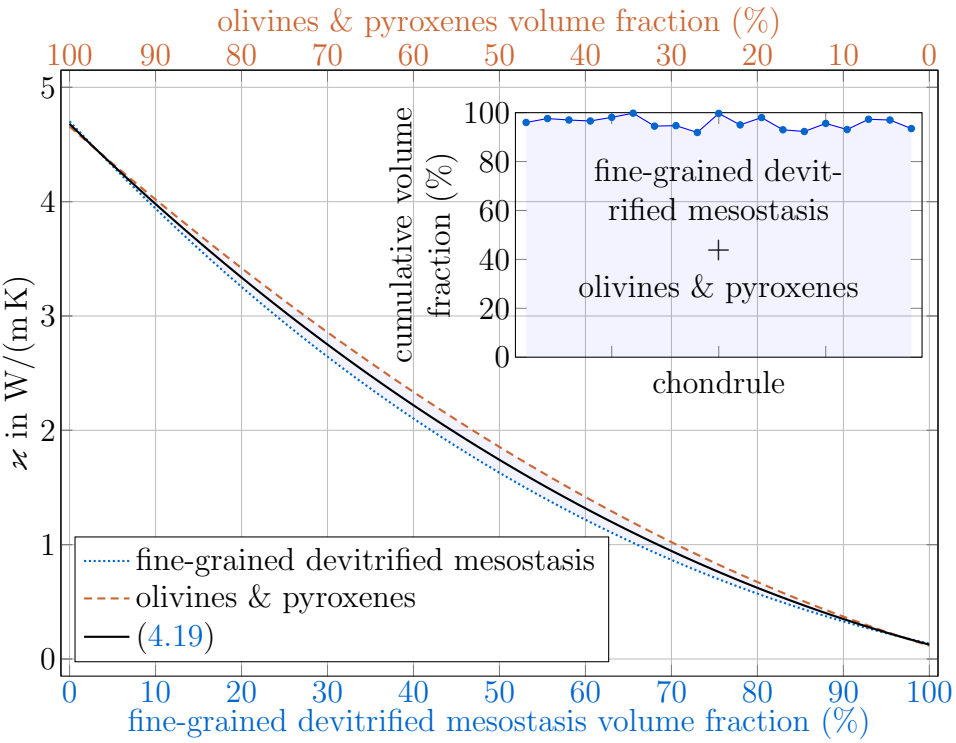

(b) Rearranged version of Figure 4.25a, where the olivines and pyroxenes axis was inverted. Inset shows the volume share of both phases. The solid line in the middle is the subsequent suggestion for a two-phase system description.

Figure 4.25: Definition of the effective thermal conductivity $\varkappa$ for actual chondrules. Data from Loesche et al. (2013).

Table 4.4: Chondrule properties. From Loesche et al. (2013).

		Compounds (%)					Radii (mm) Ref. Point: Center of Shape			Eff. Thermal Conductivity $\varkappa\left(\frac{\mathrm{W}}{\mathrm{m\cdot K}}\right)$	
Sample	Total Volume (mm^3)	Porosity	Fine-Grained Devitrified Mesostasis	Olivines and Pyroxenes	FeS (Troilite)	Fe-, Ni-metal	r_{max}	r_s	r_{min}	**Mean**	STD Interval
1	5.065	1.4	21.4	74.6	2.0	0.6	1.36	**1.065**	0.82	**2.60**	2.54 – 2.67
2	0.020	2.3	38.0	59.6	0.0	0.0	0.24	**0.167**	0.09	**2.28**	2.06 – 2.57
3	0.096	3.0	34.5	62.5	0.0	0.0	0.36	**0.284**	0.20	**1.84**	1.79 – 1.90
4	0.398	2.1	31.0	65.6	1.2	0.2	0.56	**0.456**	0.34	**2.06**	2.00 – 2.13
5	0.369	0.6	27.4	70.7	1.3	0.0	0.53	**0.445**	0.38	**3.11**	3.04 – 3.19
6	0.227	0.1	22.5	77.3	0.0	0.0	0.43	**0.379**	0.28	**3.51**	3.47 – 3.54
7	0.189	4.3	39.4	55.3	1.0	0.1	0.41	**0.356**	0.25	**2.19**	2.13 – 2.26
8	0.122	7.8	54.2	37.7	0.3	0.0	0.39	**0.308**	0.17	**1.25**	1.20 – 1.30
9	0.186	0.2	64.8	34.9	0.0	0.0	0.51	**0.354**	0.24	**1.38**	1.32 – 1.46
10	0.226	3.3	31.8	63.2	1.5	0.4	0.53	**0.378**	0.27	**2.50**	2.44 – 2.56
11	0.186	1.9	19.7	78.3	0.1	0.0	0.41	**0.354**	0.27	**3.46**	3.44 – 3.49
12	0.766	4.8	44.9	48.1	1.9	0.2	0.73	**0.568**	0.32	**1.96**	1.86 – 2.08
13	0.535	1.1	22.3	70.0	4.8	1.7	0.62	**0.504**	0.39	**3.58**	3.46 – 3.70
14	0.063	4.3	30.6	65.0	0.0	0.0	0.33	**0.246**	0.18	**2.42**	2.30 – 2.54
15	0.036	4.7	57.2	35.9	2.0	0.4	0.29	**0.205**	0.14	**1.18**	1.11 – 1.27
16	0.068	2.7	43.1	54.2	0.1	0.0	0.29	**0.253**	0.17	**2.12**	2.09 – 2.15
17	0.182	2.9	40.2	56.8	0.1	0.0	0.45	**0.351**	0.22	**2.04**	1.94 – 2.15
18	0.429	2.1	29.6	63.9	2.8	1.6	0.66	**0.468**	0.33	**2.95**	2.68 – 3.28

4.3 Drop tower experiments

In the paper Loesche et al. (2014) they report on experiments carried out at the drop tower of the Center of Applied Space Technology and Microgravity at the University of Bremen. Hesse et al. (2011) measured the photophoretic force on chondrules from the L/LL4 Bjurböle chondrite, including those discussed in Loesche et al. (2013), i.e. sec. 4.2. To supplement those experiments, the numerical model in sec. 4.2.3 was modified (time-dependency) for use on rotating spheres.

Loesche et al. (2014) carried out the drop tower experiments in catapult mode, where the drop of the experiment is preceded by an upwards launch, essentially doubling the microgravity time compared to a drop to about 9 s. The experimental setup is shown in Figure 4.26a. The illumination comes from top (not shown) with a laser intensity of $I = 41.3 \pm 4.5\,\mathrm{kW/m^2}$. During the launch of the experimental apparatus of Loesche et al. (2014), the setup is strongly accelerated and subject to tensions, and the chondrules are kept in small cavities in a sample mount behind two sliders. Only 200 ms after the onset of the microgravity phase, the two sliders spring outwards to release the chondrules into the middle of the glass housing. After release, chondrules only move slowly, because initial motion caused by the launch was largely damped by collisions within the cavities. Generally, the release speed of the chondrules are arbitrary and typically less than 2 cm/s. The authors cannot rigorously quantify rotation, but they estimate the rotation frequency to be $f < 10\,\mathrm{Hz}$.

The glass housing and the sample mount with the two sliders are placed in a vacuum chamber (not shown in Figure 4.26a) at pressures of $9 - 50\,\mathrm{Pa}$, which is in the transisition regime for chondrules. In this pressure range photophoresis on chondrules is strong enough to ensue in readily detectable accelerations. The particle trajectories (exemplarily shown in Figure 4.26b) are recorded by the two cameras as shown in Figure 4.26a. The vertical

z component is recorded by two cameras, thus Loesche et al. (2014) took the mean value, the other two components, i.e. the x and the y component are subsequently separately recorded. The time step Δt is directly given by the cameras' frame rate, enabling to determine velocity and acceleration of the observed chondrules. Assuming a quasi-constant acceleration, the trajectories are piecewisely fitted by parabolas ($s = \frac{1}{2} a\, t^2 + v_0\, t + s_0$). Figure 4.26b shows trajectories as an overlay of multiple frames that were recorded with the front camera. For accurately determined photophoretic forces F, the chondrules' masses were determined to better than $\pm 1\%$.

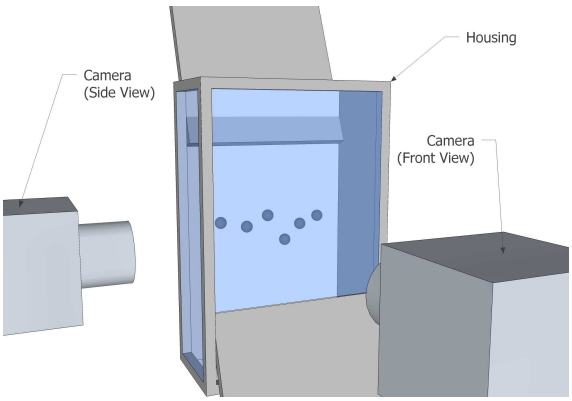

(a) Experimental setup. Two cameras record the projected chondrule trajectories as seen in Figure 4.26b. The chondrules, illuminated from top by a laser, are released by two sliders within a small glass housing.

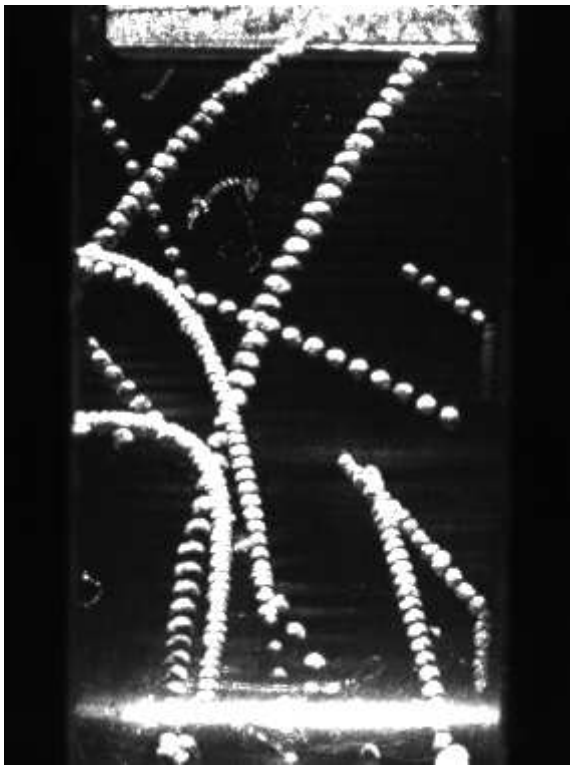

(b) Exemplary chondrule trajectories recorded with the front camera (overlay of several frames).

Figure 4.26: Drop tower experiments with chondrules. From Loesche et al. (2014).

4.3.1 Experiment versus steady state model

As the drop tower experiments were carried out in the transition regime, but the work from Loesche et al. (2013) discussed in sec. 4.2 applies for the free molecular flow, Loesche et al. (2014) employed the semi-empirical theory for the transition regime, already discussed in sec. 2.11, to account for the pressure dependence of the force (Figure 2.8), i.e. to set up a comparison criteria for the photophoretic forces in both pressure regimes. This criteria is

the maximum possible photophoretic force $\hat{F} = F(\hat{p})$ for the respective pressure $\hat{p}$. They used (2.135) for $\delta = 0$ as

$$\hat{F} = \frac{F}{2}\left(\frac{p}{\hat{p}} + \frac{\hat{p}}{p}\right) \tag{4.20a}$$

$$\hat{p} = \sqrt{\frac{3\pi\,\kappa}{2\alpha}}\,\frac{\overline{v}\,\eta_{\mathrm{dyn}}}{r_{\mathrm{s}}}\,, \tag{4.20b}$$

to deduce $\hat{F}$ for each chondrule. For details see sec. 2.11. They use a thermal creep coefficient of $\kappa = 1.14$ and a thermal accommodation coefficient of $\alpha = 0.7$. For the chondrules, that are not listed in Table 4.4, neither tomography data exists nor a numerical study. Subsequently, their characteristic size had to be determined otherwise, i.e. employing a two-dimensional image analysis. They used images taken from several orientations and determined the cross section. The characteristic size will be approximated by the radius of a sphere with the same mean cross section.

$\hat{F}$ was determined for forces F obtained from the trajectories (transition regime) and for those that were calculated by means of (4.6) (*fm* regime), used earlier in sec. 4.2. For the latter one, the intensity I measured in the experiments and the chondrule data in Table 4.4 were used ($r_{\mathbf{s}}$, $\varkappa$). Both values of $\hat{F}$ for all chondrules, including multiple experiments, are shown in Figure 4.27. The values of $\hat{F}$ that were determined by means of (4.6) are associated with a systematic uncertainty, e.g. as the thermal conductivities of the minerals can differ, as outlined previously. Especially the thermal conductivity of the mesostasis is rather uncertain, hence, the calculated photophoretic force can systematically be too high or too low. Another unknown factor is the light absorption by the chondrules. Loesche et al. (2014) roughly guessed the possible offset to a factor of two or three for a given chondrule and argue, that the possible quantitative change, however, will not affect the investigation of qualitative matter.

The steps for the calculated $\hat{F}$ mark chondrules, that were measured several times (Figure 4.27), whereas the corresponding experimentally determined value varies strongly, clearly seen in Figure 4.27b. Even if considering the aforementioned offset, the experimental values are not in agreement with the steady state theory from Loesche et al. (2013) discussed in sec. 4.2, as on average, the experimental values are a factor of three smaller than the steady state model suggests, and there is up to a factor of 10 scatter in ratios (Figure 4.27b), which cannot be explained with the steady state model.

The overall average scattering angle Φ as defined in sec. 4.2 is $\overline{\Phi}_{\mathrm{mean}} = 3.0° \pm 1.5°$ for the steady state model, and the maximum value measured was less than 20°. Contradictingly, the experimental data $\langle\Phi\rangle_t$ (averaged over the time interval where the trajectory could be fitted) clearly shows scattering angles of much higher values, as depicted in Figure 4.28. Most of the angles seem to be smaller than 50°. The steady state theory and the experiments differ insofar, that in the experiments (1) chondrules do rotate, and (2) there is a time evolution in heating up the chondrules. This will be discussed in the following pages.

4.3.2 Computational study of rotating spheres

To investigate, how rotation and heating can explain the difference between the experiments and the previous steady state COMSOL (v4.3b) study, Loesche et al. (2014) also

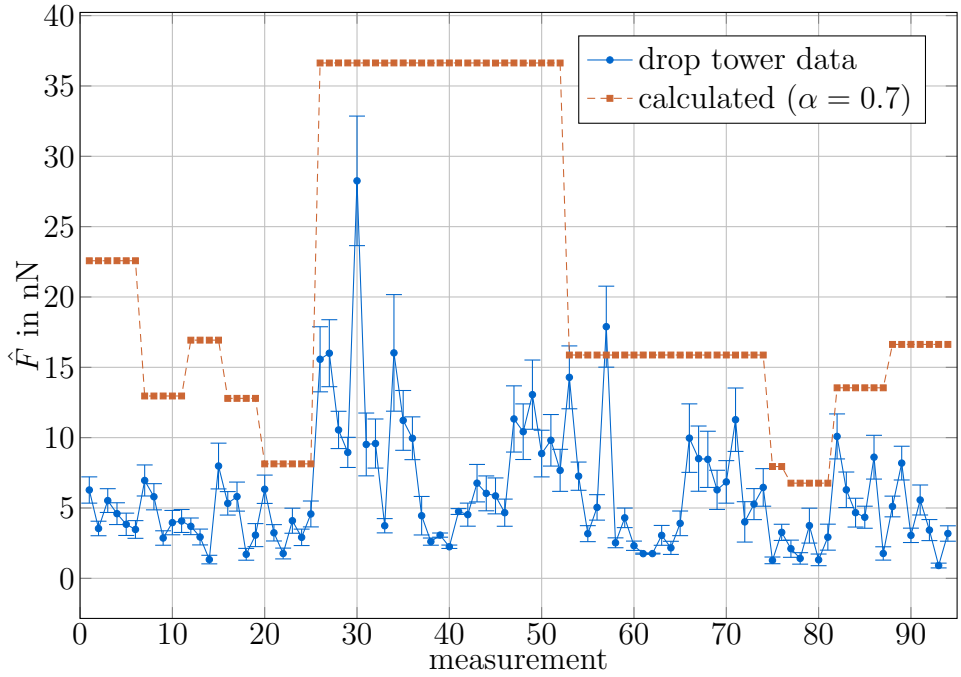

(a) $\hat{F}$ calculated (orange) and measured (blue) for different chondrules. Piecewise constant values imply multiple measurements of the same chondrule.

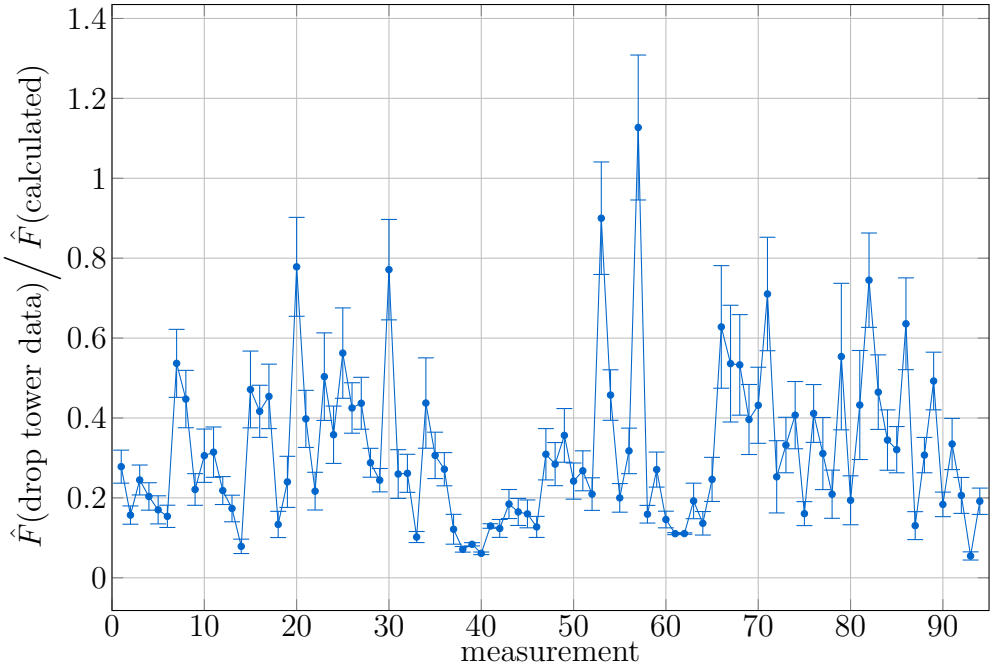

(b) Ratio of both $\hat{F}$ that are determined by the experimental setting and the calculated one.

Figure 4.27: $\hat{F}$ experimentally determined versus the calculated one. Data from Loesche et al. (2014).

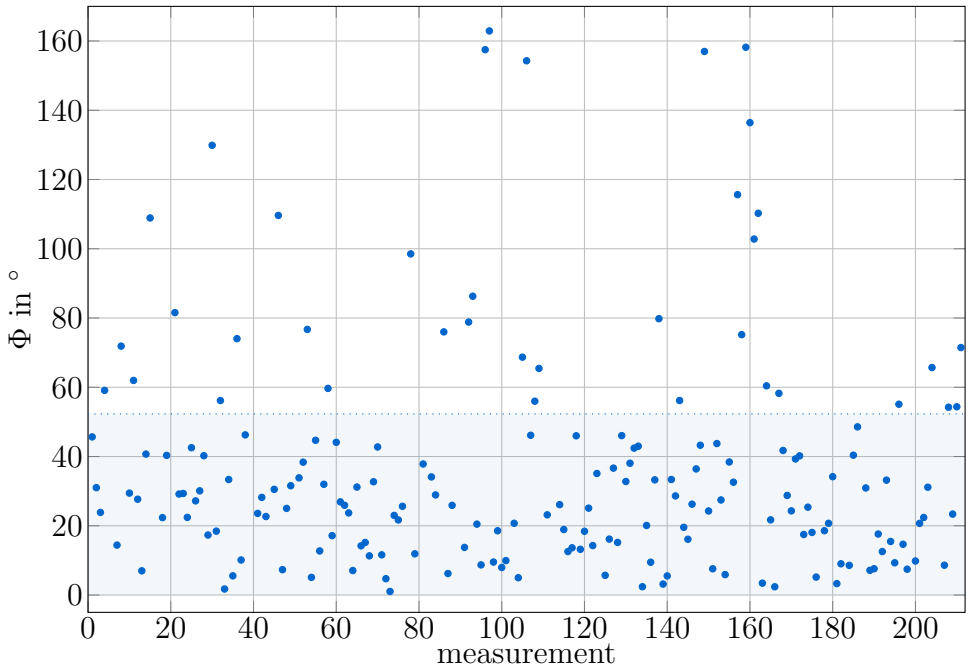

Figure 4.28: Scattering angles Φ from experimental data. For a quasi-stationary rotating sphere around one well-defined axis, numerical modeling predicts maximum angles of 52°. From Loesche et al. (2014).

carried out numerical calculations on rotating spheres. They solved the time-dependent heat equation (2.1) ($q = 0$)

$$\boldsymbol{\nabla} \cdot k \boldsymbol{\nabla} T = \rho\, c\, \partial_t T \tag{4.21}$$

with the same boundary conditions as in Loesche et al. (2013), i.e. sec. 4.2.3. The emissivity is still 1, the ambient temperature was set to $T_{\mathrm{gas}} = 301\,\mathrm{K}$, and the (reduced, i.e. totally absorbed) light flux $I = 20\,\mathrm{kW/m^2}$.

4.3.2.1 Heat up, no rotation

In a COMSOL model Loesche et al. (2014) calculated the temporal evolution of the photophoretic force during heat up for the following particle configurations:

- k: $10^{-3} \ldots 4\,\mathrm{W/m\,K}$
- r: $10^{-4} \ldots 10^{-2}\,\mathrm{m}$.

They discussed the typical course of the photophoretic force for good and poor conductors as seen in Figure 4.29. Two timescales can be noted for $k \geq 0.01\,\mathrm{W/m\,K}$, i.e. a relatively fast rise to a maximum value F_{max} and a relatively slow decline towards the respective steady state value that was obtained in the previous model. The time when the maximum value is reached inversely correlates with the thermal conductivity. The course ofter reaching the maximum value for $k \geq 0.01\,\mathrm{W/m\,K}$ can be described by an exponential decay with the factor $1 - \mathrm{e}^{f - t/\tau_{\mathrm{h}}}$ with a time constant τ_{h}.

For bare chondrules ($\approx 1\,\mathrm{W/m\,K}$), the warming time is about $1 - 3\,\mathrm{s}$ (Figure 4.29b). Measuring the photophoretic force on chondrules for similar times or less after being

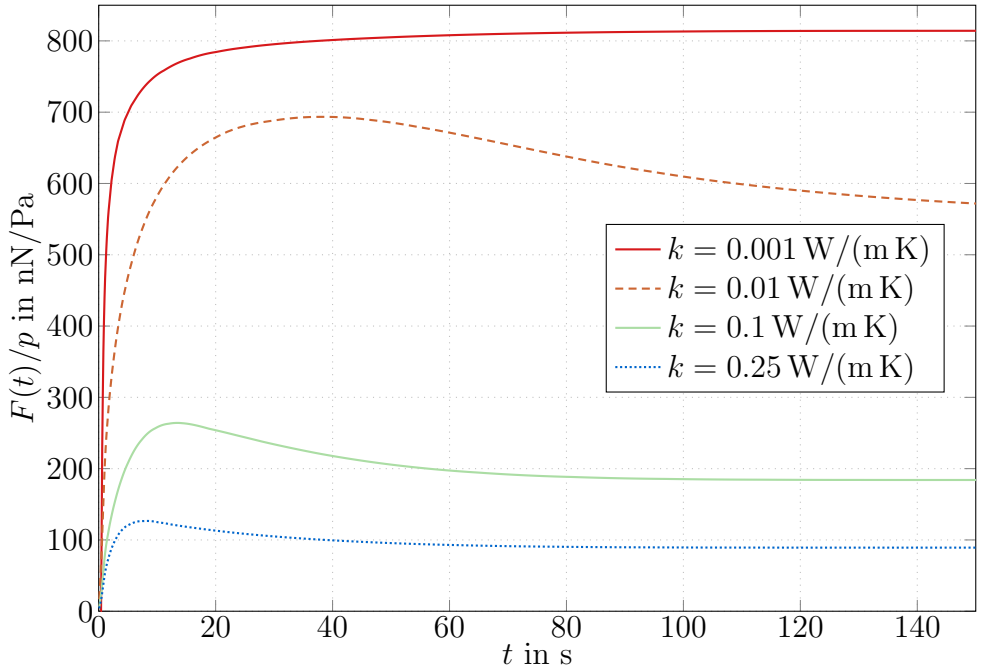

(a) Poor conductors.

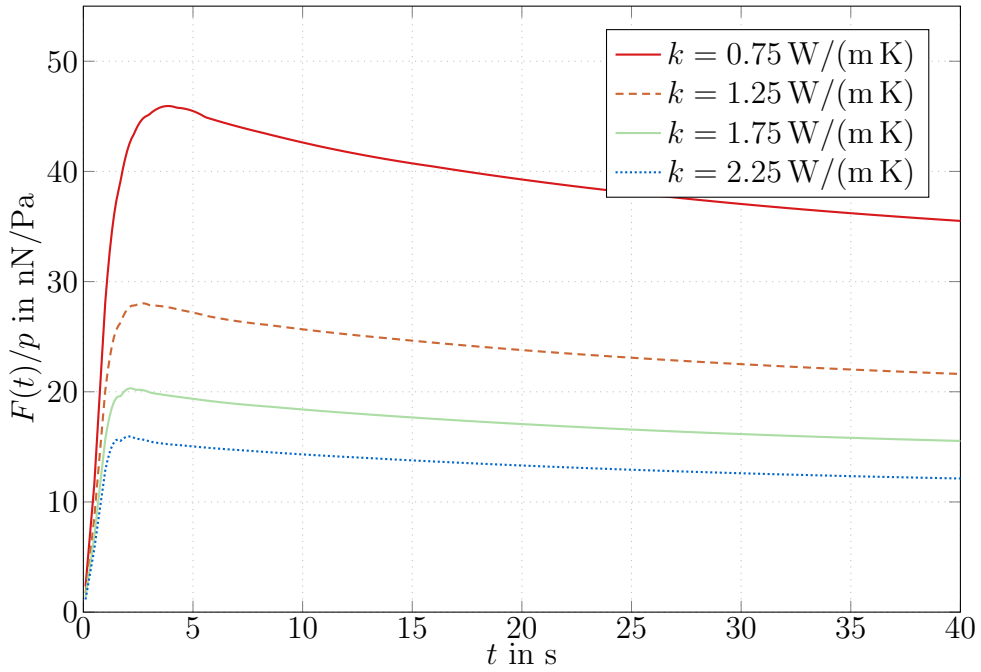

(b) Good conductors.

Figure 4.29: Exemplary graphs for $F(t)/p$ at $\alpha = 1$ and $r = 1\,\mathrm{mm}$. Thermal conductivities k in $\mathrm{W/m\,K}$. Data from Loesche et al. (2014).

illuminated by a light source quite likely results in smaller forces than the equilibrium force in sec. 4.2. If the chondrule was preheated (e.g., within the sample holder or previous illumination from another direction), large forces should be measured. Bouncing from a wall, subsequent reorientation and a measurement for short times can even lead to negative z components (i.e., negative photophoresis). In total, large variations of the force should especially occur, if photophorestic forces were determined from (sub-)trajectories that lasted only a short time. This is consistent with the experimental results (Figure 4.30 and Figure 4.31).

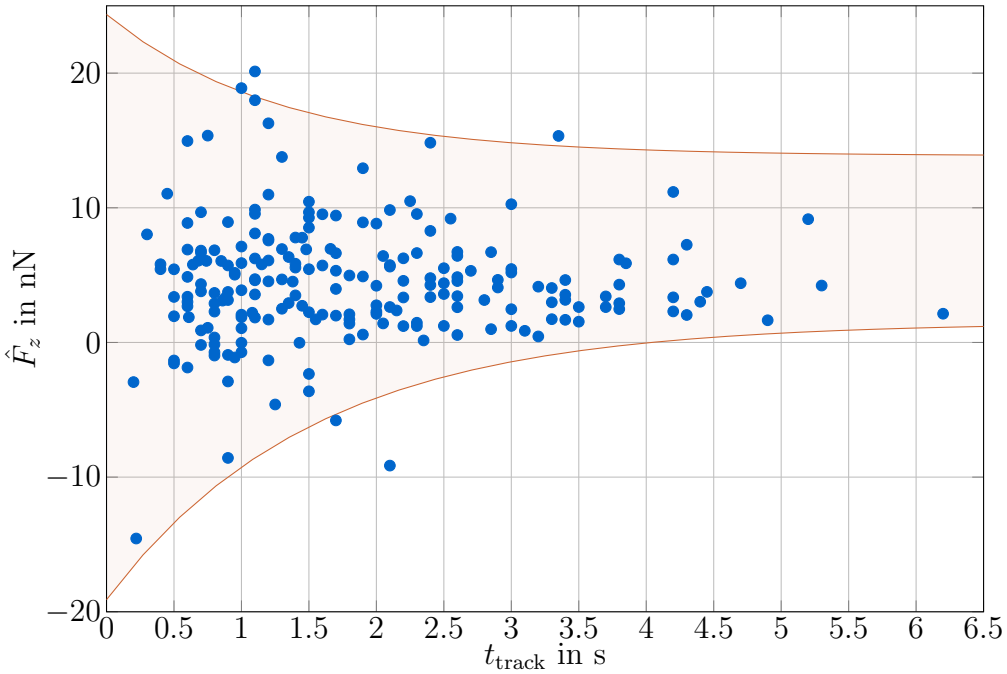

Figure 4.30: z component of $\hat{\mathbf{F}}$ over duration of a trajectory with the solid lines emphasizing the tendency. Data from Loesche et al. (2014).

4.3.2.2 Rotation

Another supplement for the experiments in Loesche et al. (2014) are COMSOL studies on rotating spheres. Early studies were already shown in Loesche et al. (2011). The angle between rotation axis and illumination field also influences the magnitude of the photophoretic force, but the highest contribution of rotation can be expected for the rotation around an axis that is perpendicular to the illumination field. The rotation frequencies used for the study vary from 0 to 12 Hz in steps of 1 Hz. The particle rotation has two consequences on the photophoretic force, i.e. reducing the magnitude of the force, and changing the direction of the force, as the warmer part of the surface trails into the shadow. The resulting angle enclosed between $\mathbf{F}_{\text{phot}}(t)$ and $\mathbf{e}_I(t)$ (body-fixed coordinate system, hence light source rotates) is now time-dependent $\Phi(t) = \sphericalangle(\mathbf{F}_{\text{phot}}(t), \mathbf{e}_I(t))$, as exemplarily shown in Figure 4.32a. The time evolution of the force magnitude (Figure 4.32b) shows a similar course for the heat up scenario discussed before. Due to computational limits, only one sphere of $r = 0.568\,\text{mm}$ at the thermal conductivity of $k = 1.96\,\text{W/K}$ — corresponding to sample 12 in Table 4.4 — was studied. Again, a rapid increase of the

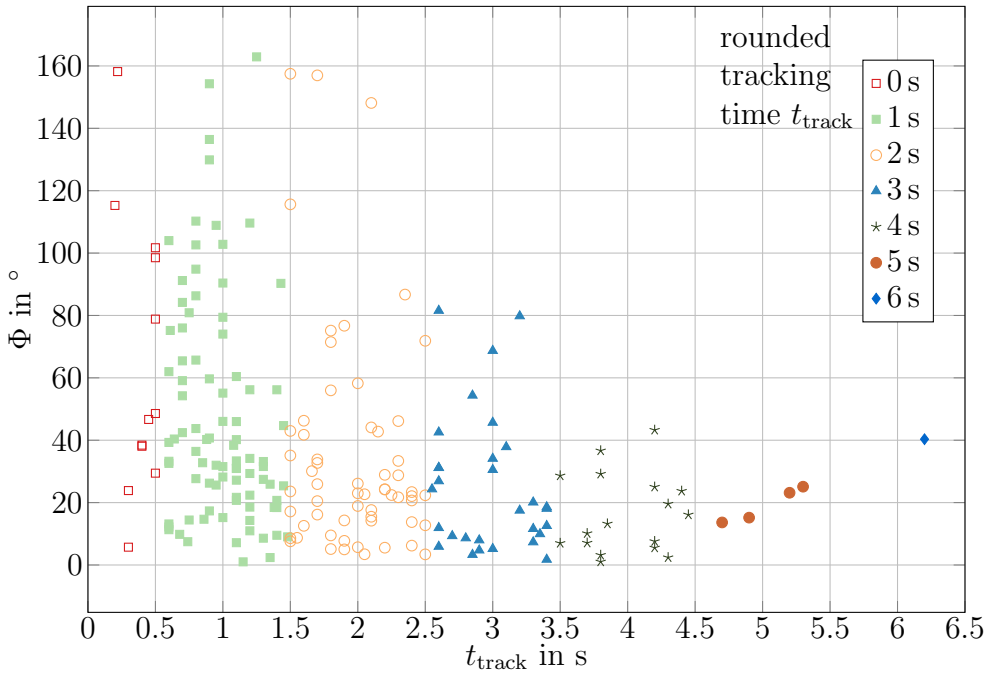

Figure 4.31: Scattering angle Φ for different tracking times t_{track}. Data from Loesche et al. (2014).

photophoretic force to a maximum can be seen, and a slow decrease to about 70% of the maximum value, that can also be described by the factor $1 - \mathrm{e}^{f - t/\tau_{\mathrm{h}}}$. In Figure 4.32b, the time constant is $\tau_{\mathrm{h}} \approx 10\,\mathrm{s}$. Beside introducing a time-dependent scattering angle $\Phi(t)$, the principle mechanisms of heating and cooling are not changed by rotation.

Figure 4.33a shows the course of the maximum photophoretic force $F_{\mathrm{max}} = \max_t F(t)$ for different rotation frequencies f. The absolute values of the force decrease as the rotation frequency increases and will eventually converge as $F_{\mathrm{max}} \xrightarrow{f\to\infty} 0$. In the studied frequency range, the total force varies by a factor of three to four. Overall, it was shown, that rotation can strongly reduce the magnitude of the photophoretic force. Rotation can therefore explain the strong variations seen in the experiments, even for chondrules with the longest tracking times $t_{\mathrm{track}} > 3\,\mathrm{s}$. Also, the scattering angle Φ increases with the frequency, but converges to a value of about $\Phi_\infty \simeq 52°$ for $f \gtrsim 8\,\mathrm{Hz}$, as seen in Figure 4.33b. It is possible that the value itself can change slightly for different radii or thermal conductivities of the rotating sphere. However, it explains the strong clustering of the experimental scattering angles in Figure 4.28 at values below $\simeq 52°$. Still, this model cannot explain the angles larger than those 52° in the experimental data. In the experiments, the chondrules have an intial speed and collide with the walls of the glass housing. As mentioned in sec. 4.3.2.1, preheated chondrules allowed to readjust after they were released or a collision can result in negative photophoresis until the temperature gradient is reequilibrated. Hence, those overlarge angles should occur for a few heat-up timescales of below 3 s, what is consistent with the experimental data, shown in Figure 4.31, which connects the scattering angles with the respective duration of the fitted (sub-)trajectories (tracking time t_{track}).

In the modelings, the rotation frequency correlates with the photophoretic force and the scattering angle Φ, respectively. From this correlation, a curve can be plotted, that re-

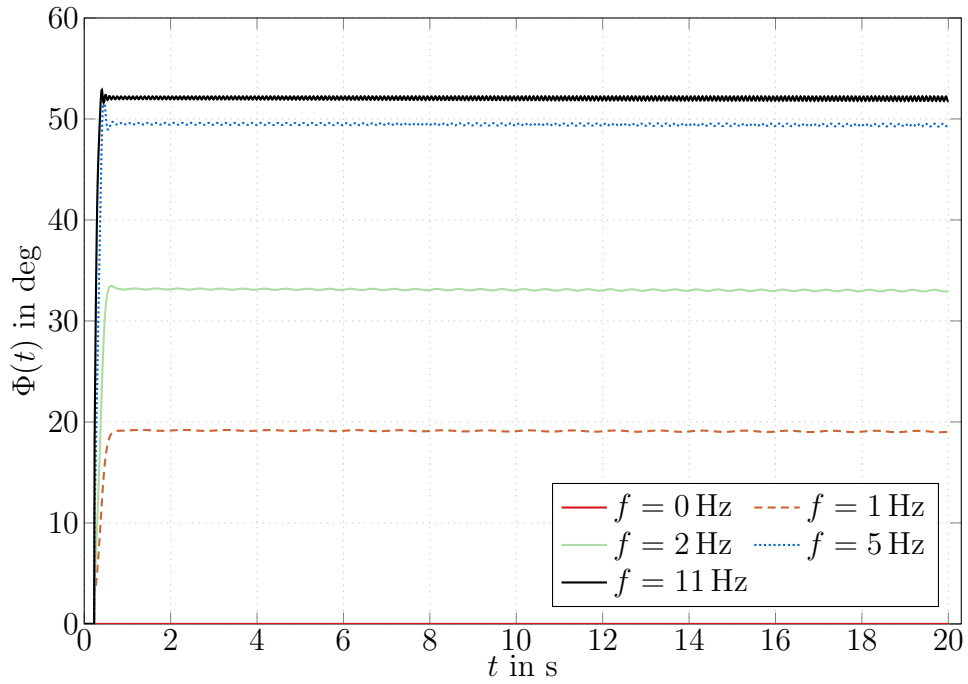

(a) Scattering angle $\Phi(t)$.

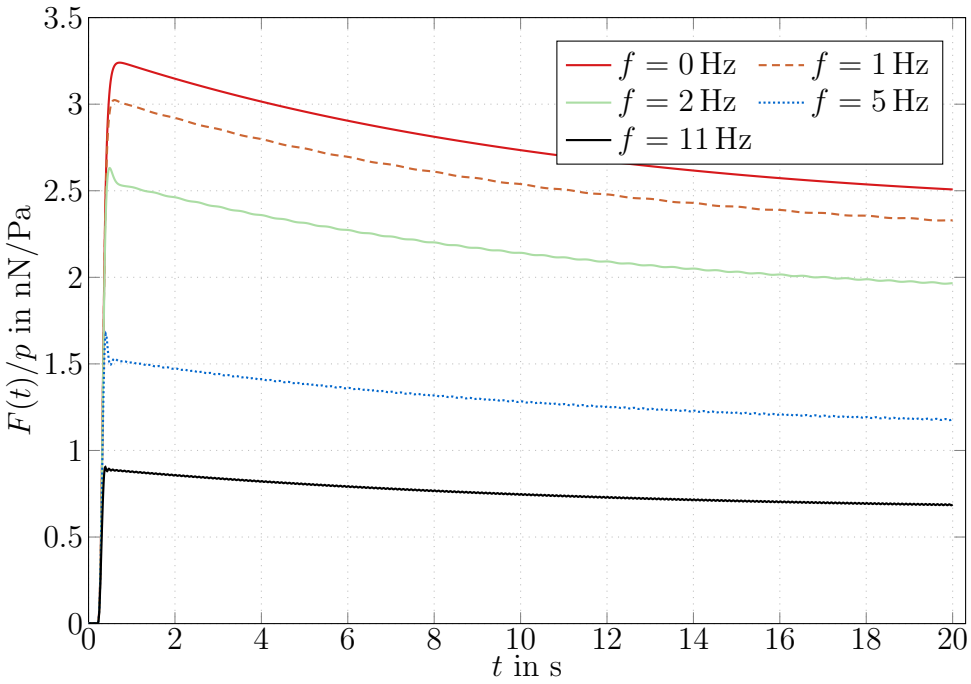

(b) Photophoretic force $F(t)/p$.

Figure 4.32: Time-evolution of scattering angle $\Phi(t)$ and force to pressure ratio $F(t)/p$ for a rotating sphere. Illumination axis $\mathbf{e}_I$ and rotation axis $\mathbf{e}_f$ are perpendicular to each other. Oscillations are of numerical origin. Data from Loesche et al. (2014).

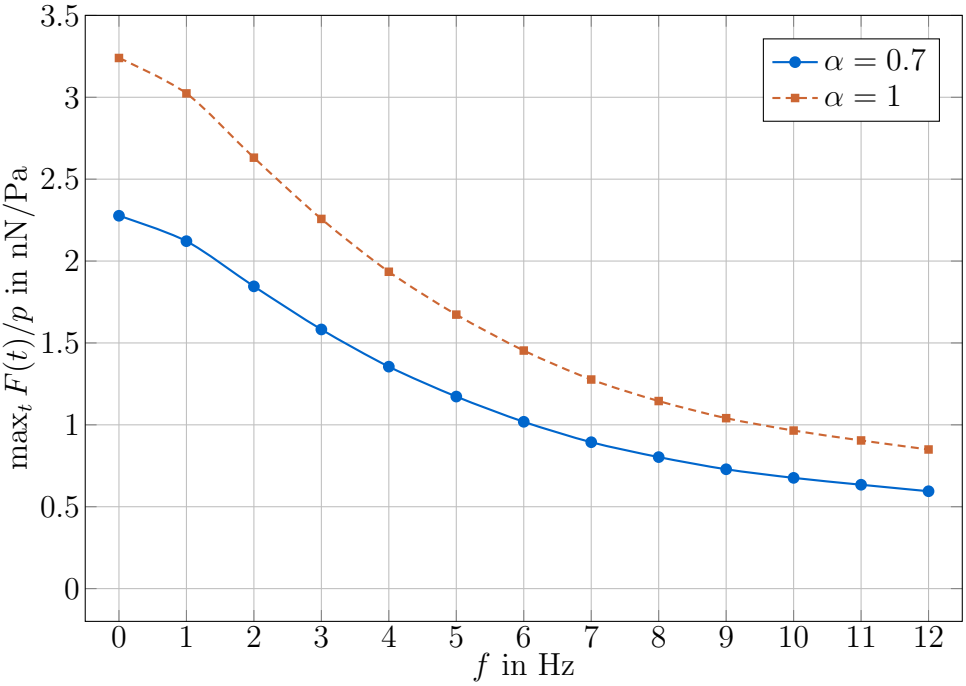

(a) $F_{\max}$ for different rotation frequencies.

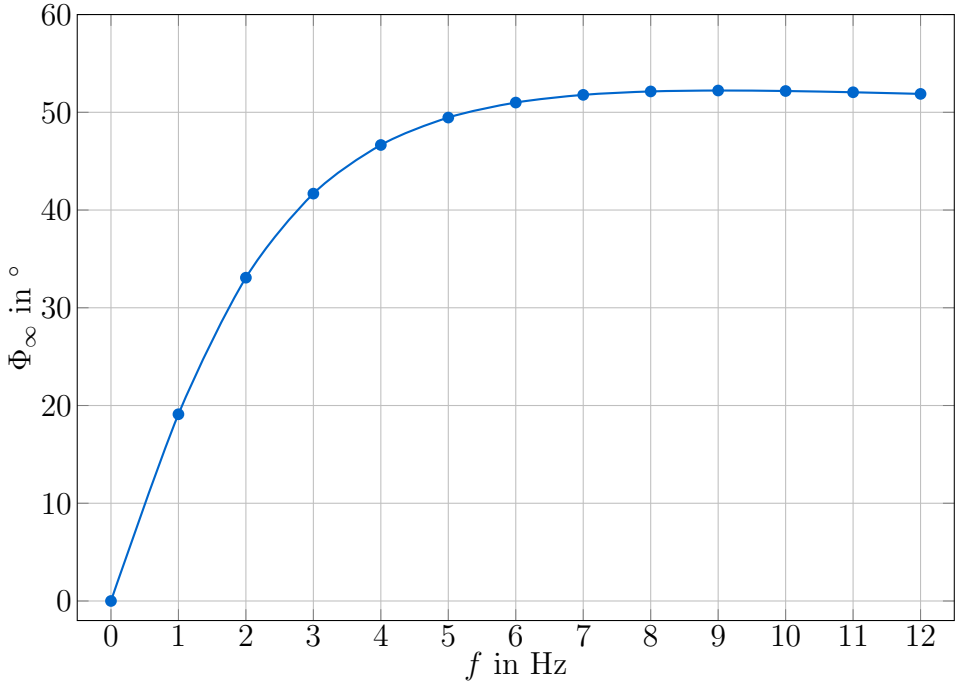

(b) Scattering angle Φ_∞ for $t \to \infty$.

Figure 4.33: Maximum values of force and scattering angle. Data from Loesche et al. (2014).

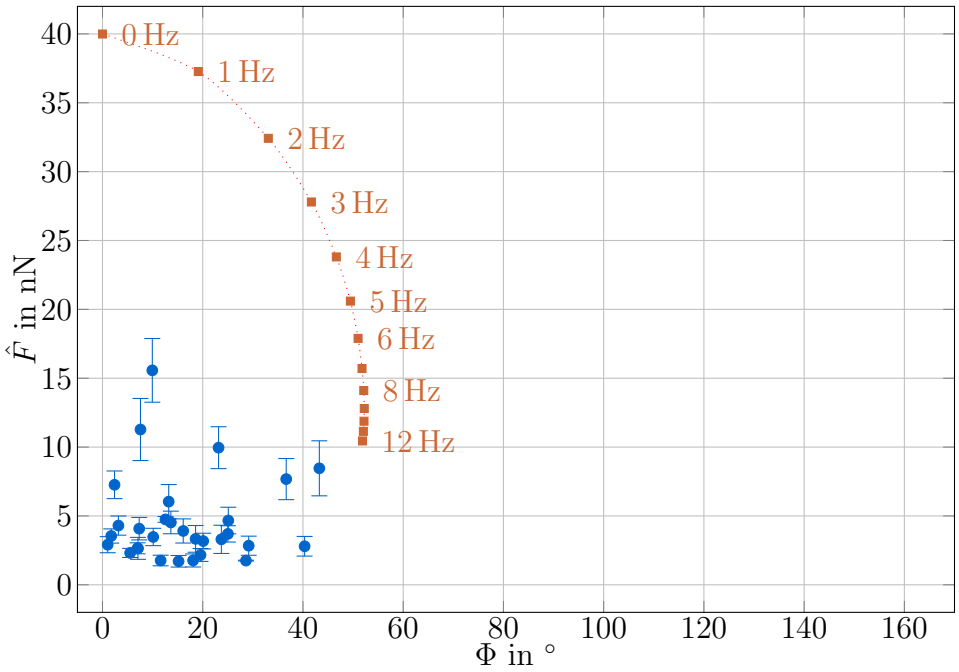

Figure 4.34: $\hat{F}$ in theory (orange squares) and those from the experimental data (blue bulls) for tracking times $t_{\text{track}} > 2.3\,\text{s}$ over scattering angles Φ. Data from Loesche et al. (2014).

lates the equilibrium angle Φ_∞ to the corresponding force (orange squares in Figure 4.34). Plotting $\hat{F}$ for the experimental data over the respective scattering angle Φ for tracking times larger than 2.3 s shows a cluster constraint by $\Phi < 50°$ and $\hat{F} < 20\,\text{nN}$ (blue bulls in Figure 4.34), which is also constraint by the theoretical curve. The strong clustering and the gap to the modeled curve can be explained, since in the experiments, the rotation is not fixed to one axis and the torques and precession, induced by the nonsphericity of the chondrules. Wurm et al. (2010) published an indication, that the rotation of a chondrule can change on subsecond timescales. Loesche et al. (2014) also state, that even for the torque-free case, nutation can change the rotation axis systematically. Hence, the photophoretic force decreases due to rotation, but the measured scattering angle is no longer correlated to this decrease and can take values between 0 and the maximum, e.g. 52°.

4.3.2.3 Photophoretic Yarkovsky analog

As for slower rotations, the warm heated part of a particle trails into the shadows side and vice versa, Loesche et al. (2014) argue, this will introduce a sideward component of the photophoretic force, i.e. the force is not longitudinal anymore. This is closely related to the Yarkovsky effect, that is a radiation pressure caused force acting on a rotating body, e.g., an asteroid, changing the orbit around the sun (Rubincam 1995). Chesley et al. (2003) reported about observerations on this effect.

The basic ideas behind those two circumstances are similar, as a rotating asteroid has a cool and a warm side corresponding to the orientation towards the sun. For a rotating asteroid, the warm side trails into the shadowed side, and the surface temperature is no longer symmetric to the direction of illumination, which was already argued for the

rotating chondrules. In the case of the Yarkovsky effect, the warmer surface parts emit more radiation $\propto \sigma T^4$ along the Stefan-Boltzmann law, than the cold parts do, thus — since the photons carry momentum — the astroid has to balance this. The difference of photons and gas particles essentially give the difference in absolute magnitude of both forces (see sec. 5.3.2), but the basic mechanisms are identical.

Photophoresis of a rotating particle suspended in a gas is subsequently closely approximating a Yarkovsky-like effect. The drop tower experiments together with the heat transfer simulations in COMSOL can be regarded as experimental proof of the effect. Future studies of rotating nonsymmetric bodies might also allow model experiments of, for instance, the YORP effect, where rotational momentum due to radiation pressure changes the rotation of a rotating asteroid. As chondrules are indeed nonsymmetric and thus subject to torques — as outlined above —, such changes in the rotation are clearly present in the measured data. But, as the experiments were not optimized to study rotation, e.g. the spatial resolution limits do not allow a quantitative reconstruction. Mostly, the rotating chondrules also nutate or precess, thus the rotation is not axis-fixed.

Some experimental data of Loesche et al. (2014) imply that the direction of rotation is linked to the sideward motion of the rotating chondrule, as illustrated in Figure 4.35. Here, the chondrule moves perpendicular to the direction of illumination as it rotates in a direction fitting to the photophoretic Yarkovsky effect, which is in agreement with the simulations of a rotating sphere.

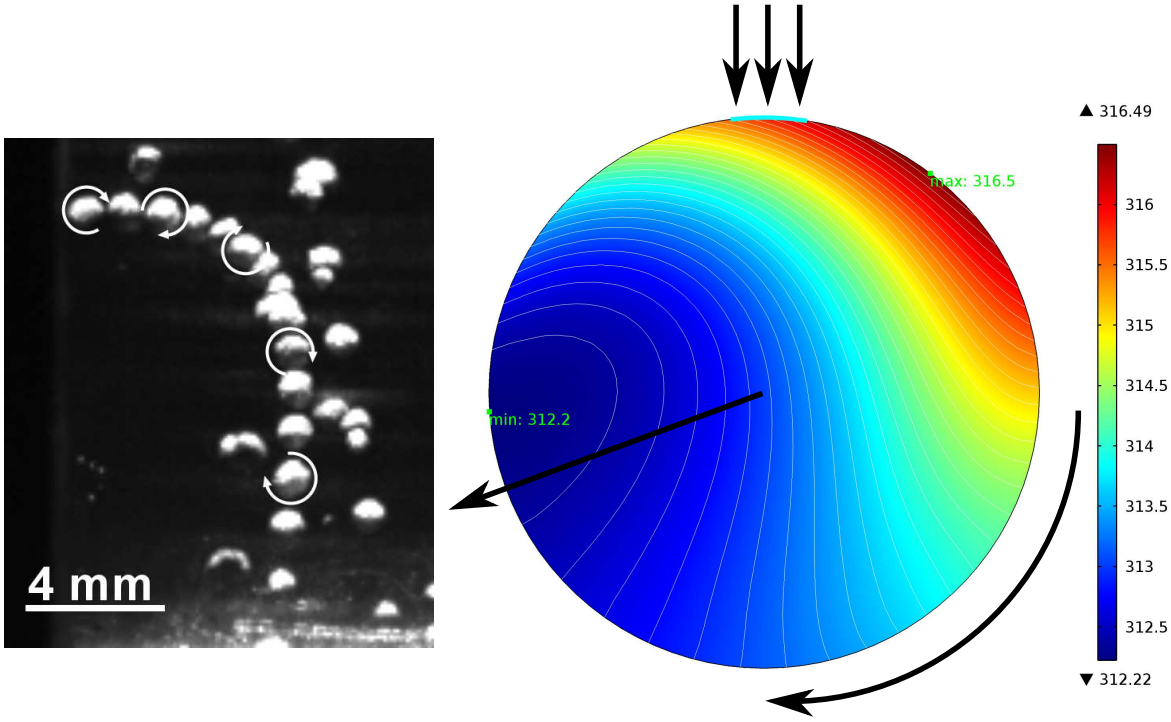

Figure 4.35: Rotation of chondrule superimposed on its trajectory (based on Figure 4.26b, left); Photophoretic force of a rotating sphere superimposed on its temperature field (central plane parallel rotation axis $\mathbf{e}_f$, $\mathbf{e}_I \perp \mathbf{e}_f$). From Loesche et al. (2014).

5

APPLICATION FOR TRANSPORT AND SORTING

In this chapter a brief overview about possible sorting mechanisms — as precise investigations require elaborated disk models — will be given along Loesche and Wurm (2012) and Loesche et al. (2013). Arnold and Lewittes (1982) reported a size dependence of the photophoretic force for micron-sized glycerol spheres for $Kn < 1$. Krauss and Wurm (2005) were the first to apply photophoresis to describe physics of protoplanetary disks, and Wurm and Krauss (2006) first tried to explain photophoretic size sorting and concentration of chondrules due to varying thermal conductivities. The photophoretic strenght on chondrules was first measured by Wurm et al. (2010) to support the thesis of transport and sorting of chondrules by means of photophoresis. Due to the optical thickness in disks the central star cannot provide radiation in the midst of it, which would rule out photophoresis in this region. Wurm et. al. (in preparation) try to explain photophoretic motion induced by temperature fluctuations caused by magnetorotational instability in protoplanetary disks (McNally et al. 2014). If the inner parts of a protoplanetary disk are optically thin, however, photophoresis can be orders of magnitudes larger than the central star's gravity and is, thus, eligible for transport processes (Krauss et al. 2007 and Mousis et al. 2007 and Herrmann and Krivov 2007 and Takeuchi and Krauss 2008 and Wurm and Haack 2009 and Moudens et al. 2011). Such disks have been found in increasing number, so-called transition disks with larger inner clearings (Calvet et al. 2002 and Najita et al. 2007 and Sicilia-Aguilar et al. 2008). In some of them the central star still accretes matter, and hence the inner region is still gaseous (Espaillat et al. 2014). Within such gaps the sorting idea of Wurm and Krauss (2006) can naturally be applied, especially for dust-mantled chondrules, whose lower effective thermal conductivity can (over-) compensate the low gas density and chondrules could concentrate in the asteroid belt region. Creating the inner clearing takes time. This would also fit well with the fact that chondrules are forming their parent bodies only a few million years after the beginning of the solar nebula.

With the help of simple disk models, transport and sorting mechanisms can be sketched and discussed. Wurm and Krauss (2006) used a disk mass density profile $\rho(a)$ which decreases with radial distance to the star a. In this model the gas is being supported against stellar gravity while rotating slower than Keplerian speed in order to have a stable orbit. Small suspended particles, such as chondrules, couple to the gas rapidly,

thus rotate with the same speed as the gas but contrarily not feel the support of the gas' pressure gradient, and subsequently move inward as they are subject to a radial force (Weidenschilling 1977)

$$F_{\mathrm{D}}(a) = n\frac{R_{\mathrm{gas}}\,T_{\mathrm{gas}}\,m_{\mathrm{par}}}{M_{\mathrm{gas}}\,a}\,, \tag{5.1}$$

also called residual gravity (Loesche and Wurm 2012). m_{par} is the mass of the suspended particle, R_{gas} and M_{gas} the gas constant and its molar mass, respectively. T_{gas} is the gas temperature, which has been denoted by T^{-} in the kinetic context. n is the power in the disk's density profile $\rho(a) \propto a^n$, e.g. in the minimum mass solar nebula it is $n = 11/4$, corresponding to Equation 6 in Hayashi et al. (1985) and (1.1), respectively. This includes gas drag insofar, that the gas–particle coupling time is much less than the timescale for gas orbits, eventually reducing this to only a radial problem (Loesche and Wurm 2012).

Figure 5.2 shows size sorting at the inner edge of a transition disk, which might also move over the asteroid belt (Haack and Wurm 2007 and Wurm et al. 2006 and Wurm and Haack 2009). Thus, the focus then is not the spatially extended inner clearing but the actual edge of it that is moving outwards. At the edge, the disk is supposed to be of its original density. The optical depth in the disk decreases further away from the edge, hence the photophoresis driven outward drift prevails as long as inward forces are smaller, caused by effects such as turbulent diffusion. Here, the sorting distances are strongly disk-dependent, but the principle is the same (Loesche and Wurm 2012).

Wurm and Krauss (2006) use approximation (3.114b) to discuss in- and outward drift of spherical chondrules on the basis of the ratio $\tilde{F}^{(2)}/F_{\mathrm{D}}$. Here, the approximation (3.115f) $\tilde{F}^{(4\mathrm{a})}$ is considered instead and the force ratio is plotted in Figure 5.1. In this simplified model, the chondrules with radius of 1 mm concentrate at different radial positions in the minimum mass solar nebula. For instance, spherical chondrules of 1 mm and thermal conductivities of $k = 0.05\,\mathrm{W/m\,K}$ and $k = 0.1\,\mathrm{W/m\,K}$ have a force ratio of 1 at 5.37 AU and 4.35 AU, respectively, i.e. about 1 AU apart from each other. Wurm and Krauss (2006) discussed the separation of particles to different radial positions whose thermal conductivity varies by a factor of, e.g., 2. Scaling linearly, particle separation of about 0.1 AU is possible for particles whose thermal conductivity vary about 10 %.

5.1 Size sorting of dust mantled, spherical chondrules

The dependence of the effective thermal conductivity on three of the four parameters $\varkappa = \varkappa(d_{\mathrm{dust}}, k_{\mathrm{dust}}, k_{\mathrm{core}})$ enables for multiple size sorting scenarios. Wurm et. al. (in preparation) investigate photophoretic motion driven by temperature fluctuations, where direct size sorting can be achieved. Indirect size sorting mechanisms are briefly reviewed below.

The core thermal conductivity has a very low influence on the effective thermal conductivity. Loesche and Wurm (2012) found, that the variations of $\varkappa$ for thin mantles, e.g. $d_{\mathrm{dust}} = 0.2$ at different k_{core} along Table 4.1 are about 10%. For high conductive dust mantles at $0.1\,\mathrm{W/m\,K}$ the influence of the core will be larger, but still less important than the dependency of $\varkappa$ on d_{dust}. Subsequently, this property can be ruled out driving size sorting. In this section, possible sorting mechanisms for dust mantled chondrules are given, worked out in Loesche and Wurm (2012).

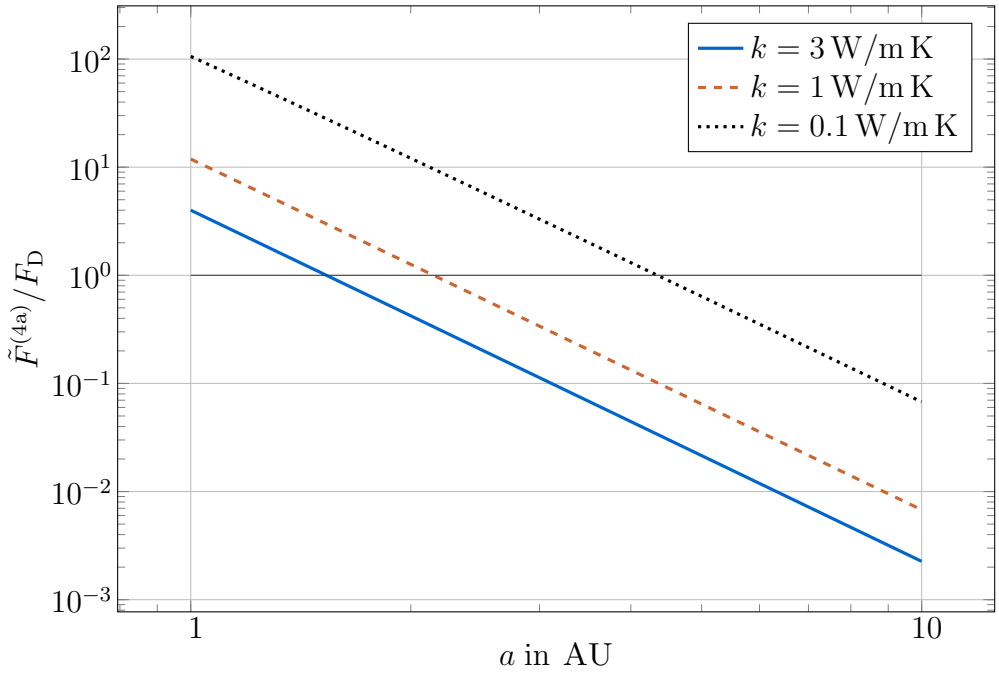

Figure 5.1: Sorting example: Spherical chondrules with a size of 1 mm concentrate at different positions in the solar nebula. The disk model is the minimum mass solar nebula from Hayashi et al. (1985), briefly mentioned in sec. 1.1.

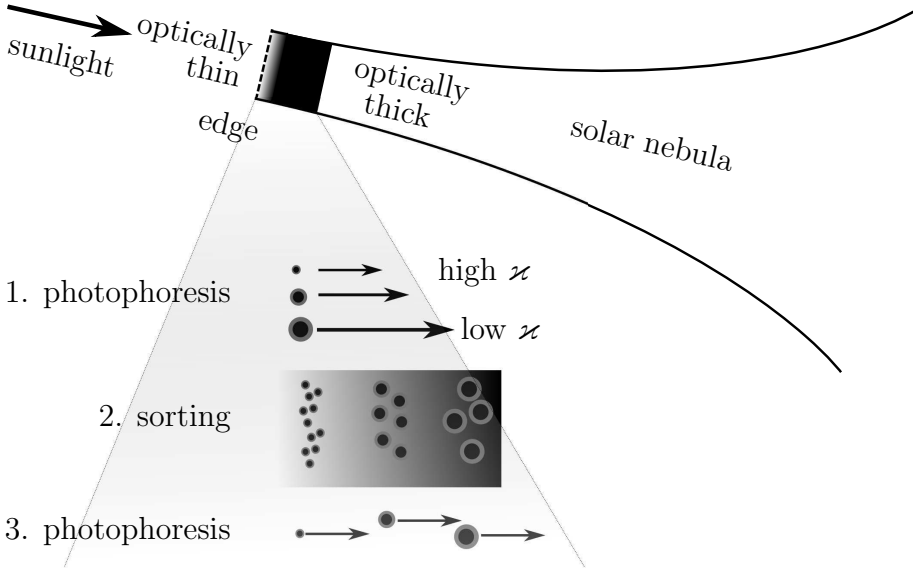

Figure 5.2: Principles of sorting dust mantled chondrules by photophoresis (taken from Loesche and Wurm (2012)).

5.1.1 Sorting by r–k_{dust} correlation

The dust mantle's thermal conductivity is so far unknown and depends on many parameters, such as the porosity. Concentrating on this parameter while assuming all others are constant over a set of chondrules, a sorting mechanism can be worked out. Bland et al. (2011) suggests the mantle porosity to be around 0.7 or more, being in consistency with experimental findings in Teiser et al. (2011). Krause et al. (2011) finds thermal conductivities 0.01 W/m K and below for this porosity for micrometer sized dust. Since typically the collision speed between particles rises with their size, this also has influence on the porosity of the mantle, as Teiser et al. (2011) and Kothe et al. (2011) show. This introduces an inverse total size dependence of the porosity, typically several percent. According to Krause et al. (2011), porosity variations of 0.05 change the thermal conductivity of the dust mantle about a factor of 1.5. For instance, a core of 1 mm size with dust at $k_{\mathrm{dust}} = 0.01\,\mathrm{W/m\,K}$, would change $\varkappa$ by a factor of 1.54 for $d_{\mathrm{dust}} = 1$, and 1.46 for $d_{\mathrm{dust}} = 0.5$. This difference in thermal conductivity can manifest itself in size sorting, i.e. larger particles have a lower $\varkappa$ and thus are found be close to the sun.

5.1.2 Sorting by r_{core}–d_{dust} correlation

In 4.1.2 the quasi-indenpendence of the effective thermal conductivity $\varkappa$ of r_{core} was stated, e.g. seen in Figure 4.2a. Hence, for fixed mantle properties and fixed k_{core}, no size-sorting (r_{core}) of the chondrules would be possible. Carballido (2011) studied the growth of dust mantles swept up by spherical chondrules by means of magnetohydrodynamic simulations of a turbulent solar nebula. The simulations show, that $d_{\mathrm{dust}} = d_{\mathrm{dust}}(r_{\mathrm{core}})$, i.e. different core sizes accrete dust mantles with different thicknesses. Subsequently, it is $\varkappa = \varkappa(d_{\mathrm{dust}}(r_{\mathrm{core}}))$ for fixed thermal conductivities of core and mantle.

For example, in Figure 4.2a the dependence $\varkappa(d_{\mathrm{dust}})$ is plotted at $k_{\mathrm{core}} = 1\,\mathrm{W/m\,K}$ and $k_{\mathrm{dust}} = 0.01\,\mathrm{W/m\,K}$. Estimating from Figure 9 in Carballido (2011), a 0.3 mm core has a mantle of 0.2 mm, i.e. $d_{\mathrm{dust}} \approx 0.6$, but a 1 mm core sized sphere has a mantle of 0.4 mm thickness, i.e. $d_{\mathrm{dust}} = 0.4$. From Figure 4.2a $\varkappa$ for both configurations can be estimated, i.e. $\varkappa = 0.02\,\mathrm{W/m\,K}$ and $\varkappa = 0.03\,\mathrm{W/m\,K}$, respectively. This difference in the effective thermal conductivity is sufficient to separate both particles by photophoretic motion, as seen in (3.115f).

A thinner dust mantle increases the overall average mass density of the coated chondrule and gravitational attraction (Loesche and Wurm 2012), while the photophoretic strength decreases as the thermal conductivity of the core has a higher impact on $\varkappa$.

5.2 Sorting of chondrules in protoplanetary disks

The findings with the steady state model in Loesche et al. (2013), discussed in sec. 4.2 could now be applied in general transport models with photophoresis. Loesche et al. (2013) found a correlation between characteristic particle size r_{s} and effective thermal conductivity $\varkappa$, shown in Figure 5.3. The slight trend, that $\varkappa$ depends on r_{s} allows of a size sorting according to sec. 5.1.2 and Loesche and Wurm (2012) and Wurm and Krauss (2006). However, the experimental results in Loesche et al. (2014), discussed in sec. 4.3 show that rotation, nutation and precession occur. Rotation and heat-up reduce the force

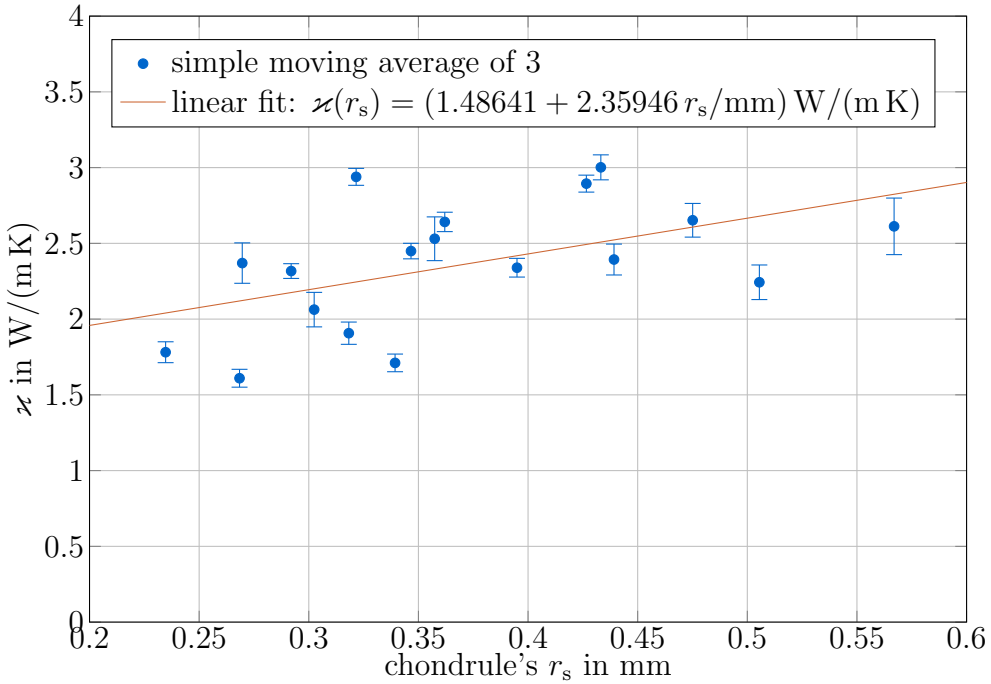

Figure 5.3: Simple moving average of third order of $\varkappa$ for actual chondrules plotted over their respective characteristic radius r_s. Data from Loesche et al. (2013).

as the rotation frequency increases. The differences between the results as well as their origin were already discussed in sec. 4.3.

The implication for the motion of illuminated chondrules in the early solar system is tied to their rotation in a protoplanetary disk. If they rotate randomly, the photophoretic force can still be significant, but the deviations found in Loesche et al. (2014) would prevent them from sorting due to composition and size. Meaning, that any sorting is bound to the question "if" and "how" chondrules/particles actually rotate in protoplanetary disks. There has been much debate about this and the answer has different aspects, discussed in the next section.

5.3 Caveats

5.3.1 Rotation

If applied to the solar nebula, rotation does not play a role, due to the following reasons. Random rotation is damped on the time scale of the gas-particle coupling time, given in the free molecule regime as (Blum et al. 1996)

$$\tau_c = \varepsilon_\tau \frac{m_{par}}{\mathcal{A}_{par}} \frac{1}{\rho\, \overline{v}} \,, \tag{5.2}$$

where the geometrical cross section of the suspended particle $\mathcal{A}_{par}$ has been introduced, together with its mass m_{par}. ρ is still the mass density of the gas, and $\overline{v}$ the mean gas speed. Employing the minimum mass solar nebula again (Hayashi et al. 1985), it is $\tau_c = 10^3\,\mathrm{s}$ for a sphere of 1 mm radius (Loesche and Wurm 2012). Correspondingly,

random rotation decays rapidly — if not excited continuously on similar time scales — and hence does not influence photophoretic motion. Rotation can be generated by, e.g., inter-particle collisions. The time between collisions between mm-sized particles for a 'typical' disk was estimated by Krauss et al. (2007) as

$$\tau_{\mathrm{coll}} = 33 \frac{\rho_{\mathrm{par}}}{\rho} \frac{r}{u} \,, \tag{5.3}$$

with u denoting the relative particle speed, ρ_{par} their mass density, and r their radius. For $u = 1\,\mathrm{m/s}$, it is $\tau_{\mathrm{coll}} \approx 10^4 \tau_{\mathrm{c}} \gg \tau_{\mathrm{c}}$, and therefore triggered rotation by collisions can be neglected. From both findings it can be concluded, that even for strongly varying disk conditions, rotation is damped quickly, and the short times of decreased photophoretic strength do not account on long time scales (Loesche and Wurm 2012). Brownian motion is another source of random rotation. For the thermal energy of a spherical particle converted to rotational energy $\mathcal{E}_{\mathrm{rot}} = \frac{3}{2} k_{\mathrm{B}} T_{\mathrm{gas}}$ (moment of inertia denoted by J_{par}), the radian frequency is

$$\omega = \sqrt{\frac{3 k_{\mathrm{B}} T_{\mathrm{gas}}}{J_{\mathrm{par}}}} = \sqrt{\frac{45 k_{\mathrm{B}} T_{\mathrm{gas}}}{8\pi r^5 \rho_{\mathrm{par}}}} \,. \tag{5.4}$$

A half rotation period takes a time

$$\tau_{\mathrm{rot}} = \sqrt{\frac{8\pi^3 r^5 \rho_{\mathrm{par}}}{45 k_{\mathrm{B}} T_{\mathrm{gas}}}} \,, \tag{5.5}$$

which is on the order of $10^4\,\mathrm{s}$ for 1 mm spheres. On the other hand, the time scale for thermal conduction, given by ($c_{\mathrm{p,par}}$ denoting the particle's isobaric heat capacity)

$$\tau_{\mathrm{cond}} = \frac{r^2}{k} \rho_{\mathrm{par}} c_{\mathrm{p,par}} \,, \tag{5.6}$$

is just on the order of 1 s, following, that Brownian motion cannot interfere the temperature distribution across the particle's surface, and Brownian rotation can be neglected, too (Loesche and Wurm 2012). The photophoretic force can excite a continuous rotation due to torques ((3.131) in sec. 3.5), if exerting on non-spherical particles, such as chondrules. Numerical simulations on this are being conducted in a COMSOL model with the same chondrule CAD models extracted by X-ray tomography (see sec. 4.2.2.1. However, results are not available yet. Detailed experiments on particle rotation were carried out by van Eymeren and Wurm (2012), where particle levitation was produced by means of thermophoresis and photophoresis (Kelling et al. 2011). The experiments showed, that more than 95% of the particles rotate around the (vertical) axis of illumination. Illumination-aligned rotation does not alter photophoretic strength. Given, that only this rotation can occur, rotation in general — as outlined — does not reduce photophoretic strenth. The small differences between the photophoretic force and the direction of light, together with the remaining rotation leads to helical motion around the direction of light which has been shown by Kuepper et al. (2014).

5.3.2 Photophoresis versus radiation pressure

Often radiation pressure is used to serve as transport mechanism instead of photophoresis, the first one based on direct momentum transfer from photons to a particle, not necessarily

suspended in a gas. Klačka and Kocifaj (2002) also considered Poynting-Robertson effect. Radiation pressure is approximately given by

$$F_{\mathrm{rad}} = \frac{\pi}{c} I\, r^2 \,. \tag{5.7}$$

However, for chondrule-sized particles and reasonable gas pressures and densities, photophoresis is much stronger as plotted in Figure 5.4 using the simple model of Hayashi et al. (1985). Another difference between photophoresis and radiation pressure — as commented above — is, that the latter one does also occur in the vacuum, as no interaction with the gas is needed. In this case, rotating particles will not be damped.

5.3.3 Heat exchange with the ambient gas

The heat exchange with the ambient gas is not considered in the heat transfer model in sec. 3.3.5, which is the basis for the whole discussion on the quality of approximations as well as transport and sorting scenarios in the free molecule regime. Stoffels et al. (1996) quantified the heat flux to the gas for large Knudsen numbers as

$$j_{\mathrm{cond}} = \frac{\frac{c_{\mathrm{p}}}{c_{\mathrm{v}}} + 1}{\frac{c_{\mathrm{p}}}{c_{\mathrm{v}}} - 1}\, \alpha \left(\overline{T} - T_{\mathrm{gas}}\right) \frac{p}{4} \sqrt{\frac{k_{\mathrm{B}}}{2\pi\, T_{\mathrm{gas}}\, m}} \,. \tag{5.8}$$

For H_2 gas it is $c_{\mathrm{p}}/c_{\mathrm{v}} \approx 9/7$, and $\overline{T}$ denotes the mean temperature of the spherical chondrule. Employing the minimum mass solar nebula (Hayashi et al. 1985), for a chondrule at radial distance to the sun of 2 AU, it is $I = 341\,\mathrm{W/m^2}$, $p = 0.15\,\mathrm{Pa}$ and $T_{\mathrm{gas}} = 262\,\mathrm{K}$. For temperature differences between chondrule and gas as $\overline{T} - T_{\mathrm{gas}} \leq 10\,\mathrm{K}$, the resulting heat flux into the gas is $j_{\mathrm{cond}} = 35\,\mathrm{W/m^2} \ll I$ (Loesche and Wurm 2012). Subsequently, the exchange heat flux between chondrule and gas is neglectable. For the typical laboratory experiments laser intensities of $I = 20\,\mathrm{kW/m^2}$ are used in an environment of air ($m_{\mathrm{gas}} = 29\,\mathrm{u}$) at $p = 1\,\mathrm{Pa}$ and $T_{\mathrm{gas}} = 293\,\mathrm{K}$. The maximum temperature difference between spherical chondrule and surrounding gas is $\overline{T} - T_{\mathrm{gas}} \leq 400\,\mathrm{K}$, along Figure 3.7. This leads to an heat flux of $j_{\mathrm{cond}} = 315\,\mathrm{W/m^2} \ll I$ (Loesche and Wurm 2012), hence also here the heat flux can be neglected. For chondrules suspended in gas at higher pressures ($p = 10\,\mathrm{Pa} \ldots 100\,\mathrm{Pa}$) the heat flux will contribute to the heat transfer problem, but this is not the free molecule regime anymore, which is in the focus of this work, as it is important for mm-sized particles in protoplanetary disks. Plus, also the used approximations (3.115) for the photophoresis are not valid anymore. However, for transition disks at low pressures, the considerations are still valid, conversely, for disks at higher densities, another treatment of photophoretic transport is necessary, which is beyond the scope of this work.

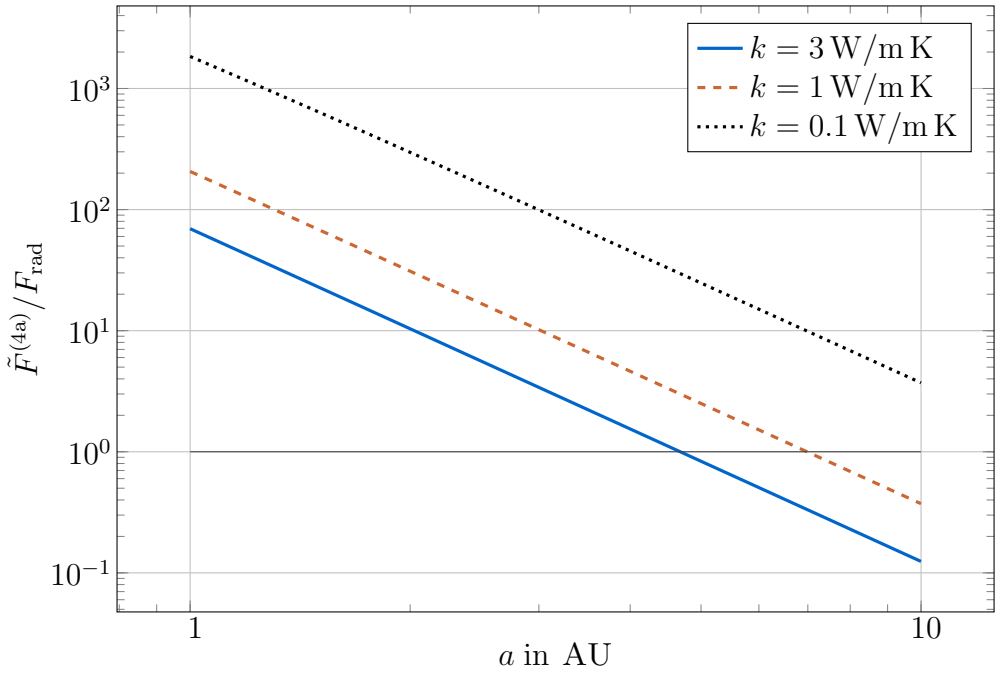

(a) Spheres at 1 mm radius and different thermal conductivities.

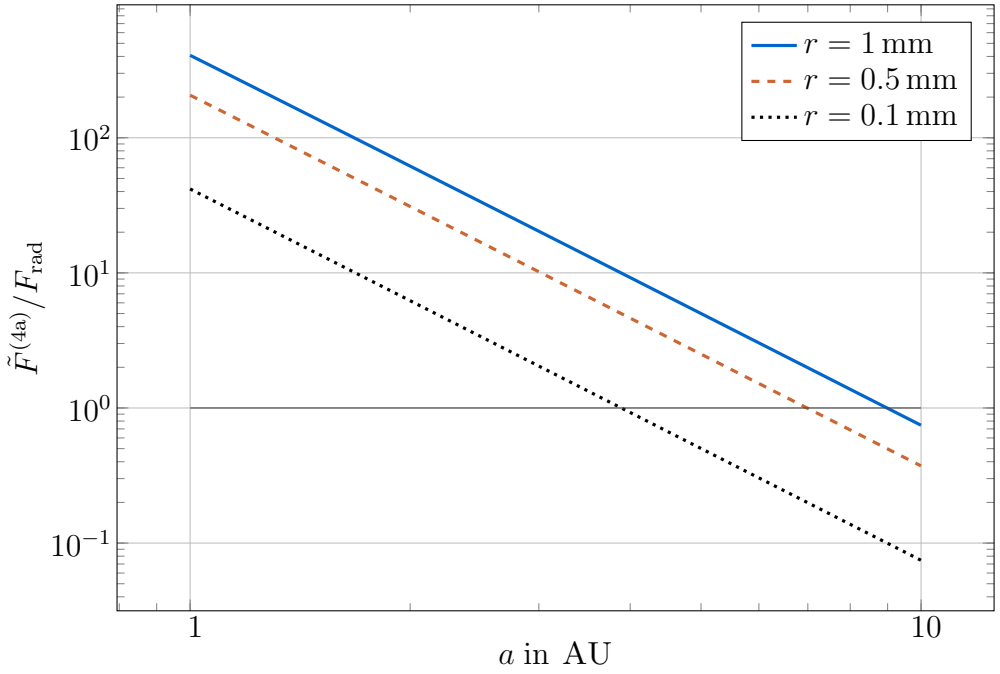

(b) Spheres at $k = 0.5\,\mathrm{W/m\,K}$ and different radii.

Figure 5.4: Radiation pressure (5.7) versus photophoresis in the model of Hayashi et al. (1985).

6

CONCLUSIONS

The pure photophoretic force on a star-convex particle in the free molecule regime is described by the surface integral

$$\mathbf{F}_{\text{phot}} = c \iint \tau \, \boldsymbol{\partial}_{\boldsymbol{\zeta}} \times \boldsymbol{\partial}_{\boldsymbol{\xi}} \, \mathrm{d}\xi \, \mathrm{d}\zeta \;, \tag{3.12c}$$

with a constant c and the integrand τ. The latter one is determined by the subjacent velocity distributions of the gas around the suspended particle. For Maxwell-Boltzmann velocity distributions it is $c = -\frac{1}{2} p/\sqrt{T^-}$, and the integral can be collapsed by means of expanding both $\tau^{(n)} = \sqrt{T^+}/\Omega^{n-2}$ and the radius function of the particle Ω^n $(n = 2, 3, \dots)$ in spherical harmonics with the expansion coefficients $t_{pq}^{(n)}$ and $\omega_{\nu\mu}^{(n)}$:

$$\mathbf{F}_{\text{phot}}^{(n)} = -\frac{1}{2} \frac{p}{\sqrt{T^-}} \sum_{\substack{\nu \geq 0 \\ \nu \geq \mu \geq 0 \\ p \geq 0 \\ p \geq q \geq 0}} \begin{pmatrix} \left(\Gamma_{\nu,\mu,p,q}^{(n)} - \Gamma_{\nu,-\mu,p,-q}^{(n)}\right) \Re\left(\omega_{\nu\mu}^{(n)} \, t_{pq}^{(n)*}\right) \\ -\left(\Gamma_{\nu,\mu,p,q}^{(n)} + \Gamma_{\nu,-\mu,p,-q}^{(n)}\right) \Im\left(\omega_{\nu\mu}^{(n)} \, t_{pq}^{(n)*}\right) \\ (2 - \delta_{\mu,0}) \, \Psi_{\nu,\mu,p,q}^{(n)} \, \Re\left(\omega_{\nu\mu}^{(n)} \, t_{pq}^{(n)*}\right) \end{pmatrix} \tag{3.20a}$$

$$\Gamma_{\nu,\mu,p,q}^{(n)} = \frac{1}{n} \delta_{q,\mu-1} \left[(\nu + n) \; d_{\nu+1,1-\mu} \, \delta_{p,\nu+1} + (\nu + 1 - n) \; d_{\nu,\mu} \, \delta_{p,\nu-1}\right] \tag{3.16g}$$

$$\Psi_{\nu,\mu,p,q}^{(n)} = \frac{1}{n} \delta_{q,\mu} \; \left[(\nu + n) \, h_{\nu+1,\mu} \, \delta_{p,\nu+1} - (\nu + 1 - n) \, h_{\nu\mu} \, \delta_{p,\nu-1}\right] \tag{3.19d}$$

$$h_{\nu\mu} = \sqrt{\frac{\nu^2 - \mu^2}{4\nu^2 - 1}} \tag{A.9a}$$

$$d_{\nu\mu} = \sqrt{\frac{(\nu + \mu - 1)(\nu + \mu)}{4\nu^2 - 1}} \;. \tag{A.9b}$$

This allows a description of the force to arbitrary order. In case of a sphere, the pure force is solely determined by the two expansion coefficients $t_{1,0}$ and $t_{1,1}$

$$\mathbf{F}_{\text{phot}} = \sqrt{\frac{\pi}{3}} \frac{p}{\sqrt{T^-}} r_0^2 \begin{pmatrix} \sqrt{2} \, \Re\left(t_{1,1}^*\right) \\ \sqrt{2} \, \Im\left(t_{1,1}^*\right) \\ -t_{1,0} \end{pmatrix} \;. \tag{3.25}$$

If the integrand is rotational symmetric with respect to the z-axis, the force is longitudinal and very well determined by the approximation

$$\tilde{F}^{(\tau)} = -\frac{\pi}{3} \frac{p}{\sqrt{T^-}} \, r^2 \left(\tau(T_{\max}) - \tau(T_{\min})\right) \tag{3.86}$$

for the case of thermal accommodation (2.114) $\tau = \sqrt{T^- + \alpha\,(T - T^-)}$. Frequently used approximations which include thermal accommodation, momentum accommodation (even up to tangential and normal momentum accommodation) can be improved by replacing the factor $\frac{p}{T}$ by $\frac{p}{\sqrt{\overline{T^+}\,T^-}}$, resulting in a very high accuracy even for $T > T_{\mathrm{gas}}$, i.e. for intensities of about $20\,\mathrm{kW/m^2}$. A new excellent I-r-k approximation for longitudinal photophoresis was also found (accommodation coefficients are: α: thermal, α_{m} momentum; $J_1 = \frac{1}{2}$ for perfectly absorbing spheres):

$$\tilde{F}^{(4\mathrm{a})} = -\frac{\pi}{3}\,\alpha\,\alpha_{\mathrm{m}}\frac{p}{\sqrt{T^-\overline{T^+}}}\,r_0^2\,\frac{I\,J_1}{\frac{k}{r_0} + h + 4\sigma_{\mathrm{SB}}\varepsilon\,T_{\mathrm{bb}}^3} \tag{3.109}$$

$$\overline{T^+} = T^- + \alpha\left(T_{\mathrm{bb}} - T^-\right) \tag{3.33}$$

$$T_{\mathrm{bb}} = \sqrt[4]{\frac{I}{4\sigma} + \left(T_{\mathrm{gas}}^{\mathrm{rad}}\right)^4} \tag{3.35}$$

$$h = \alpha_{\mathrm{m}}\,\alpha\,p\sqrt{\frac{2k_{\mathrm{B}}}{\pi\,T^-\,m}}\,.$$

Approximations for longitudinal photophoresis, depending on I, k and r give the photophoretic force for homogeneous spheres. Loesche and Wurm (2012) extended their definition (for corrected approximations) to onion shell-like spheres by means of the definition of the effective thermal conductivity $\varkappa$, introduced in sec. 4.1.1. This extension and the replacement $k(\mathbf{r}) \to \varkappa$ still gives a photophoretic force. Loesche et al. (2013) explained a definition for (corrected) approximations for nonspherical and inhomogeneous particles. Instead of a radius and thermal conductivity the variables $r \to r_{\mathrm{s}}$, that is the radius of a volume-equivalent sphere and $k(\mathbf{r}) \to \varkappa$ the effective thermal conductivity are used. $\varkappa$, defined in Loesche et al. (2013) for chondrules dominated by two major phases, depends on the assignment of the thermal conductivities for both phases. Additionally, unresolved microcracks would seriously reduce the thermal conductivity and Loesche et al. (2013) set the thermal conductivity of the fine-grained devitrified mesostasis to an estimated value of $0.1\,\mathrm{W/m\,K}$, which could not be measured so far. Hence, (4.19) can look different for other materials or more phases. As this would not change the qualitative findings, the equation for the effective thermal conductivity (4.19) can be seen as a proof of concept. The replacement $r \to r_{\mathrm{s}}$ was discussed in sec. (4.2.4.3) on the basis of the general solution (3.20) of the integral equation for the photophoretic force (2.87) in the case of star-convex particles. However, in this extended definition, the (corrected) approximations give a value for the photophoretic force, that effectively represents the orientation-averaged total of the photophoretic force for nonspherical and inhomogeneous particles. Hence, by employing those approximations on realistic non-spherical particles mean photophoretic strengths are obtained (Table 6.1).

In the conducted study, for realistically modeled chondrules, the overall averaged angle between incident light and ensuing photophoretic force is $\overline{\Phi}_{\mathrm{mean}} = 3.0° \pm 1.5°$, the overall average deviance from the mean force is $(\delta F/\overline{F})_{\mathrm{mean}} = 4.17\%$. This was compared to the variances found in drop tower experiments by Loesche et al. (2014), discussed in sec. 4.3. With the help of the drop tower experiments and numerical studies particle rotation and its influence on the photophoretic strength and the scattering angle with respect to the direction of light could be studied. The numerical studies only included a sphere with one radius and thermal conductivity, corresponding to the photophoretic properties of one

Table 6.1: Interpretation of the approximations applied on spherical and star-convex particles.

$\chi(I, r, k, \dots)\tilde{F}(I, r, k, \dots)$	$\chi(I, r_\mathrm{s}, \varkappa, \dots)\tilde{F}(I, r_\mathrm{s}, \varkappa, \dots)$
direct value for spheres	orientation averaged value (expectation value) for star-convex particles

chondrule examined in the steady state model used in Loesche et al. (2013). However, it was found, that rotation can lower the force strength on timescales of seconds in the drop tower experiments in comparison to steady-state models. Nevertheless, random particle rotation in protoplanetary disks does not occur on long timescales due to gas-grain friction. Only a well-constraint forced rotation can be sustained, leading to helical trajectories along the direction of illumination.

As proof of concept, possible photophoresis-driven size-sorting scenarios were given on the basis of simple disk models, especially for dust-mantled chondrules. Detailed sorting discussions need more realistic disk models and are beyond the scope of this work.

Appendix A

GENERAL

A.1 Spherical coordinates (r, φ, ϑ)

A.1.1 Normal vector

$$\mathbf{n}_\mathrm{S}(\varphi,\vartheta) = \begin{pmatrix} \cos\varphi\sin\vartheta \\ \sin\varphi\sin\vartheta \\ \cos\vartheta \end{pmatrix} \tag{A.1}$$

A.1.2 Unit vectors

$$\mathbf{e}_r(\varphi,\vartheta) = \mathbf{n}_\mathrm{S}(\vartheta,\varphi)\ , \tag{A.2a}$$

$$\mathbf{e}_\vartheta(\varphi,\vartheta) = \frac{\boldsymbol{\partial}_\vartheta}{\|\boldsymbol{\partial}_\vartheta\|_2} = \begin{pmatrix} \cos\varphi\cos\vartheta \\ \sin\varphi\cos\vartheta \\ -\sin\vartheta \end{pmatrix}\ , \tag{A.2b}$$

$$\mathbf{e}_\varphi(\varphi,\vartheta) = \frac{\boldsymbol{\partial}_\varphi}{\|\boldsymbol{\partial}_\varphi\|_2} = \begin{pmatrix} -\sin\varphi \\ \cos\varphi \\ 0 \end{pmatrix} \tag{A.2c}$$

$$\Rightarrow \dot{\mathbf{e}}_r = \dot{\varphi}\,\sin\vartheta\,\mathbf{e}_\varphi + \dot{\vartheta}\,\mathbf{e}_\vartheta \tag{A.3}$$

A.1.3 Representations

$$\mathbf{r} = r\,\mathbf{e}_r \equiv r\,\mathbf{n}_\mathrm{S} \tag{A.4a}$$

$$\mathbf{v} = \dot{r}\,\mathbf{e}_r + r\,\dot{\mathbf{e}}_r \overset{(A.3)}{=} v_r\,\mathbf{e}_r + r\,v_\vartheta\,\mathbf{e}_\vartheta + r\,\sin\vartheta\,v_\varphi\,\mathbf{e}_\varphi \tag{A.4b}$$

$$v_z \overset{(A.4b)}{=} (v_r\,\mathbf{e}_r)_z + (r\,v_\vartheta\,\mathbf{e}_\vartheta)_z = v_r\cos\vartheta - v_\vartheta\,r\,\sin\vartheta \tag{A.4c}$$

$$v^2 = v_r^2 + r^2\,\sin^2\vartheta\,v_\varphi^2 + r^2\,v_\vartheta^2 \tag{A.4d}$$

A.2 Functions

The modified Bessel functions of first kind for integers n are (Abramowitz and Stegun 1964)

$$I_n(z) = \frac{1}{\pi}\int_0^\pi \mathrm{e}^{z\,\cos\vartheta}\,\cos(n\vartheta)\,\mathrm{d}\vartheta\ . \tag{A.5}$$

A.3 Legendre polynomials and spherical harmonics

Unless noted otherwise, all indices are integers.

A.3.1 Definition

For integers ν, μ with $\nu \geq 0$ and $-\nu \leq \mu \leq \nu$ the spherical harmonics Y_ν^μ can be defined as

$$Y_\nu^\mu(\xi,\zeta) = f_{\nu\mu}\, P_\nu^\mu(\cos\zeta)\, e^{\mathrm{i}\mu\xi} \tag{A.6a}$$

$$f_{\nu\mu} = \sqrt{\frac{2\nu+1}{4\pi}\frac{(\nu-\mu)!}{(\nu+\mu)!}}\,. \tag{A.6b}$$

Legendre polynomials P_ν can be obtained from the Rodrigues formula, and a similar formula exists for the associated Lengendre polynomials P_ν^μ (Hahn and Özişik 2012)

$$P_\nu(x) = \frac{1}{2^\nu \nu!}\frac{\mathrm{d}^\nu}{\mathrm{d}x^\nu}\left(x^2-1\right)^\nu \qquad \nu \geq 0 \tag{A.7}$$

$$P_\nu^\mu(x) = (-1)^\mu \left(1-x^2\right)^{\mu/2}\frac{1}{2^\nu\nu!}\frac{\mathrm{d}^\mu}{\mathrm{d}x^\mu}P_\nu(x) \qquad \nu \geq 0,\ -\nu \leq \mu \leq \nu\,. \tag{A.8}$$

A.3.1.1 Personal definition of coefficients for recurrence relations of spherical harmonics in sec. B.1

$$h_{\nu\mu} = \sqrt{\frac{\nu^2-\mu^2}{4\nu^2-1}} \tag{A.9a}$$

$$d_{\nu\mu} = \sqrt{\frac{(\nu+\mu-1)(\nu+\mu)}{4\nu^2-1}} \tag{A.9b}$$

A.3.2 Single derivatives

$$\partial_\xi Y_\nu^\mu(\xi,\zeta) = (\mathrm{i}\,\mu)\, Y_\nu^\mu(\xi,\zeta)\ , \tag{A.10a}$$

$$\partial_\zeta Y_\nu^\mu(\xi,\zeta) = \frac{1}{\sin\zeta}\left((2\nu+1)\underbrace{\sqrt{\frac{(\nu+1)^2-\mu^2}{4(\nu+1)^2-1}}}_{h_{\nu+1,\mu}} Y_{\nu+1}^\mu(\xi,\zeta) - (\nu+1)\cos\zeta\, Y_\nu^\mu(\xi,\zeta)\right) \tag{A.10b}$$

A.3.3 Orthogonality relations (Abramowitz and Stegun 1964)

$$\left(Y_\nu^\mu\,,\, Y_\psi^\lambda\right) = \delta_{\nu\psi}\,\delta_{\mu\lambda} \tag{A.11a}$$

$$\left(Y_\nu^\mu\,,\, Y_\psi^{\lambda *}\right) = \delta_{\nu\psi}\,(-1)^\mu\,\delta_{\mu\lambda} \tag{A.11b}$$

$$\left(P_\nu\,,\, P_\psi\right)_{[-1,1]} = \frac{2}{1+2\nu}\,\delta_{\psi\nu} \tag{A.11c}$$

$$\left(P_\nu^\mu\,,\, P_\psi^\mu\right)_{[-1,1]} = \frac{1}{2\pi\, f_{\nu\mu}^2}\delta_{\nu\psi} \quad ,\mu \geq 0 \tag{A.11d}$$

$$\left(P_\nu^\mu\,,\, P_\nu^\lambda\frac{1}{1-x^2}\right)_{[-1,1]} = \frac{(\nu+\mu)!}{\mu\,(\nu-\mu)!}\delta_{\mu\lambda} \quad ,\mu,\lambda > 0 \tag{A.11e}$$

$$\left(\mathrm{e}^{\mathrm{i}\mu\xi}\,,\, \mathrm{e}^{\mathrm{i}\lambda\xi}\right)_{[0,2\pi]} = \delta_{\nu\lambda} \quad \mu,\ \lambda \in \mathbb{R} \tag{A.11f}$$

A.3.4 Special relations

For the work on sec. 3.1 it was necessary to work out the following relations.

A.3.4.1 Coefficients and indices

$$P_\nu^{-\mu} = (-1)^\mu \frac{(\nu-\mu)!}{(\nu+\mu)!} P_\nu^\mu \tag{A.12a}$$

$$Y_\nu^{\mu *} = (-1)^\mu \, Y_\nu^{-\mu} \tag{A.12b}$$

For real-valued functions f, expanded in spherical harmonics, the respective coefficients satisfy a special relation:

$$\begin{aligned} f = f^* &= \sum_{\nu,\mu} c_{\nu\mu} \, Y_\nu^\mu \\ &\overset{(A.12b)}{=} \sum_{\substack{\nu,\mu \\ \mu>0}} \left(c_{\nu,\mu} \, Y_\nu^\mu + (-1)^\mu \, c_{\nu,-\mu} \, Y_\nu^{\mu *} \right) + \sum_\nu c_{\nu,0} \, Y_\nu^0 \\ &= \sum_{\substack{\nu,\mu \\ \mu>0}} \left(c_{\nu,\mu}^* \, Y_\nu^{\mu *} + (-1)^\mu \, c_{\nu,-\mu}^* \, Y_\nu^\mu \right) + \sum_\nu c_{\nu,0} \, Y_\nu^0 \end{aligned}$$

and thus

$$c_{\nu,\mu}^* = (-1)^\mu \, c_{\nu,-\mu} \tag{A.13a}$$

by comparison of coefficients.

A.3.4.2 $d_{\nu\mu}$ and $f_{\nu\mu}$

$$d_{\nu,-\mu} \, f_{\nu-1,\mu+1} \equiv d_{\nu+1,\mu+1} \, f_{\nu+1,\mu+1} \quad \nu \geq 0 \wedge -\nu \leq \mu \leq \nu \tag{A.14a}$$

$$d_{\nu,-\mu} \, f_{\nu-1,|\mu+1|} \equiv d_{\nu+1,\mu+1} \, f_{\nu+1,|\mu+1|} \quad \nu \geq 0 \wedge \nu \geq \mu \geq -1 \tag{A.14b}$$

$$d_{\nu,\mu} \, f_{\nu-1,|\mu-1|} \equiv d_{\nu+1,-\mu+1} \, f_{\nu+1,|\mu-1|} \quad \nu \geq 0 \wedge -\nu \leq \mu \leq 1 \tag{A.14c}$$

A.3.4.3 Index-identities for integrals of spherical harmonics

For positive *and* negative upper indexes it is (see (A.6a) and (A.12b)):

$$\begin{aligned} &\forall \nu, p \geq 0 \\ -\nu \leq \mu \leq \nu,\ -p \leq q \leq p& \\ \left(Y_\nu^\mu \, , \, Y_\psi^\lambda \right) &\overset{\substack{(A.6a) \\ (A.11f)}}{=} \delta_{\mu\lambda} \, f_{\nu\mu} \, f_{\psi\lambda} \left(P_\nu^\mu \, , \, P_\psi^\lambda \right)_{[-1,1]} \\ &= \delta_{\mu\lambda} \, (-1)^{\Theta(-\mu)\,\mu + \Theta(-\lambda)\,\lambda} \, f_{\nu,|\mu|} \, f_{\psi,|\lambda|} \left(P_\nu^{|\mu|} \, , \, P_\psi^{|\lambda|} \right)_{[-1,1]} \end{aligned} \tag{A.15}$$

A.3.5 Integrals of two (associated) Legendre polynomials

A.3.5.1 $(P_\sigma\,,P_\nu)_{[0,1]}$

$\Gamma(x)$ denotes the Gamma function. For the integral of two ordinary Legendre polynomials on the half-space $[0,1]$ it is

$$(P_\sigma\,,P_\nu)_{[0,1]} = \int_0^1 P_\sigma(x)\,P_\nu(x)\,\mathrm{d}x \tag{A.16a}$$
$$= \begin{cases} 0 & \nu \neq \sigma \;\wedge\; \nu+\sigma \text{ even} \\ \frac{1}{1+2\nu}\,\delta_{\sigma\nu} & \nu=\sigma \text{ [1]} \\ \frac{A(\nu,\sigma)\cos\left(\frac{\pi\nu}{2}\right)\sin\left(\frac{\pi\sigma}{2}\right)-A(\nu,\sigma)^{-1}\sin\left(\frac{\pi\nu}{2}\right)\cos\left(\frac{\pi\sigma}{2}\right)}{\frac{1}{2}\pi(\sigma-\nu)(\nu+\sigma+1)} & \text{else [2],} \end{cases}$$

with

$$A(\nu,\sigma) := \frac{\Gamma\left(\frac{\nu}{2}+\frac{1}{2}\right)\Gamma\left(\frac{\sigma}{2}+1\right)}{\Gamma\left(\frac{\nu}{2}+1\right)\Gamma\left(\frac{\sigma}{2}+\frac{1}{2}\right)}\,. \tag{A.16b}$$

[1] Abramowitz and Stegun (1964)
[2] Gradshteyn and Ryzhik (2007)

A.3.5.2 $\left(P_\nu^\mu\,,P_\psi^\lambda\right)_{[-1,1]}$ (Mavromatis and Alassar 1999)

An Integral of two Associated Legendre Polynomials can be written as (Saalschützian)

$$\left(P_\nu^\mu\,,P_\psi^\lambda\right)_{[-1,1]} = \frac{(-1)^\lambda\,\pi}{2^{2|\lambda-\mu|+1}\,\Gamma\left(\frac{1}{2}+\frac{|\lambda-\mu|}{2}\right)\Gamma\left(\frac{3}{2}+\frac{|\lambda-\mu|}{2}\right)}\sqrt{\frac{(\nu+\mu)!(\psi+\lambda)!}{(\nu-\mu)!(\psi-\lambda)!}}\cdot \tag{A.17a}$$
$$\cdot\sum_j W\left(j,\nu,\mu,\psi,\lambda\right)\cdot\left(1+(-1)^{j+|\lambda-\mu|}\right)\sqrt{\frac{(j+|\lambda-\mu|)!}{(j-|\lambda-\mu|)!}}\;{}_3F_2\left[\begin{matrix}\frac{|\lambda-\mu|+j+1}{2},\frac{|\lambda-\mu|-j}{2},\frac{|\lambda-\mu|}{2}+1\\ |\lambda-\mu|+1,\frac{|\lambda-\mu|+3}{2}\end{matrix}\right]$$

for $j+\mu+\lambda$ even $\wedge$ $|\nu-\psi|\leq j\leq\nu+\psi$, with

$$W\left(j,\nu,\mu,\psi,\lambda\right) = (-1)^{\lambda-\mu}(2j+1)\begin{pmatrix}\nu & \psi & j\\ 0 & 0 & 0\end{pmatrix}\begin{pmatrix}\nu & \psi & j\\ -\mu & \lambda & \mu-\lambda\end{pmatrix}, \tag{A.17b}$$
$$|\nu-\psi|\leq j\leq\nu+\psi\,,$$
$$j+\mu+\lambda \text{ even}\,,$$

and

$$\begin{pmatrix}j_1 & j_2 & j_3\\ m_1 & m_2 & m_3\end{pmatrix}$$

being the Wigner 3-j symbols. Here, the generalized hypergeometric function yields

$${}_3F_2\left[\begin{matrix}\frac{|\lambda-\mu|+j+1}{2},\frac{|\lambda-\mu|-j}{2},\frac{|\lambda-\mu|+2}{2}\\ |\lambda-\mu|+1,\frac{|\lambda-\mu|+3}{2}\end{matrix}\right] = \frac{\Gamma\left(\frac{1}{2}\right)\Gamma\left(\frac{j}{2}\right)\Gamma\left(|\lambda-\mu|+1\right)\Gamma\left(-\frac{j+2}{2}\right)}{\Gamma\left(\frac{|\lambda-\mu|-j+2}{2}\right)\Gamma\left(\frac{|\lambda-\mu|}{2}\right)\Gamma\left(\frac{|\lambda-\mu|+j+2}{2}\right)\Gamma\left(\frac{-|\lambda-\mu|-1}{2}\right)}\,. \tag{A.17c}$$

A.3.5.3 Special cases

$$\begin{aligned}&\forall \nu \geq \mu \geq 0,\\ &\forall \nu \geq \lambda \geq 0:\end{aligned}$$
$$\left(P_\nu^\mu\,,\,P_\nu^\lambda\right)_{[-1,1]} = \begin{cases}(-1)^{\frac{\mu-\lambda}{2}}\frac{2}{2\nu+1}\frac{\nu+\min(\lambda,\mu)!}{\nu-\max(\lambda,\mu)!} & \mu+\lambda \text{ even}\\ 0 & \text{else}\end{cases}, \tag{A.18}$$

$$\begin{aligned}&\forall \nu \geq \mu \geq 0,\\ &\forall \psi \geq 0:\end{aligned}$$
$$\left(P_\nu^\mu\,,\,P_\psi^{\mu+2}\right)_{[-1,1]} = \begin{cases}4\frac{(\nu+\mu)!}{(\nu-\mu)!}(\mu+1) & \nu+\psi \text{ even} \wedge \psi > \nu \wedge \psi \geq \mu+2\\ -\frac{2}{2\nu+1}\frac{(\nu+\mu)!}{(\nu-(\mu+2))!} & \psi = \nu\\ 0 & \text{else}\end{cases}. \tag{A.19}$$

For negative indices (A.12a) has to be applied, or simply (A.15), if possible.

A.3.6 Recurrence relations of associated Legendre polynomials

A.3.6.1 Gradshteyn and Ryzhik (2007)

$$(1-x^2)\frac{\mathrm{d}}{\mathrm{d}x}P_\nu^\mu(x) = (\nu+\mu)\,P_{\nu-1}^\mu(x) - \nu\,x\,P_\nu^\mu(x) \tag{A.20a}$$
$$= (\nu+1)\,x\,P_\nu^\mu(x) - (\nu+1-\mu)\,P_{\nu+1}^\mu(x) \tag{A.20b}$$
$$= \sqrt{1-x^2}P_\nu^{\mu+1}(x) + \mu\,x\,P_\nu^\mu(x) \tag{A.20c}$$
$$= -(\nu+\mu)(\nu-\mu+1)\sqrt{1-x^2}\,P_\nu^{\mu-1}(x) - \mu\,x\,P_\nu^\mu(x) \tag{A.20d}$$
$$(2\nu+1)\,x\,P_\nu^\mu(x) = (\nu-\mu+1)\,P_{\nu+1}^\mu(x) + (\nu+\mu)P_{\nu-1}^\mu(x) \tag{A.20e}$$
$$2\mu\,x\,P_\nu^\mu(x) = -\sqrt{1-x^2}\left[P_\nu^{\mu+1}(x) + (\nu+\mu)(\nu-\mu+1)P_\nu^{\mu-1}(x)\right] \tag{A.20f}$$
$$\sqrt{1-x^2}\,P_\nu^\mu(x) = \frac{1}{2\nu+1}\left[(\nu-\mu+1)(\nu-\mu+2)P_{\nu+1}^{\mu-1}(x) - (\nu+\mu-1)(\nu+\mu)P_{\nu-1}^{\mu-1}(x)\right] \tag{A.20g}$$
$$\sqrt{1-x^2}\,P_\nu^\mu(x) = \frac{1}{2\nu+1}\left[P_{\nu-1}^{\mu+1}(x) - P_{\nu+1}^{\mu+1}(x)\right] \tag{A.20h}$$
$$\sqrt{1-x^2}\,P_\nu^{\mu+1}(x) = (\nu-\mu)\,x\,P_\nu^\mu(x) - (\nu+\mu)P_{\nu-1}^\mu(x) \tag{A.20i}$$
$$\sqrt{1-x^2}\,P_\nu^{\mu+1}(x) = (\nu-\mu+1)P_{\nu+1}^\mu(x) - (\nu+\mu+1)\,x\,P_\nu^\mu(x) \tag{A.20j}$$
$$\sqrt{1-x^2}\,P_\nu^\mu(x) = \frac{1}{\nu-\mu}\left[P_{\nu-1}^{\mu+1}(x) - x\,P_\nu^{\mu+1}(x)\right] \tag{A.20k}$$
$$\sqrt{1-x^2}\,P_\nu^\mu(x) = \frac{1}{\nu+\mu+1}\left[x\,P_\nu^{\mu+1}(x) - P_{\nu+1}^{\mu+1}(x)\right] \tag{A.20l}$$

A.3.6.2 Abramowitz and Stegun (1964)

$$\sqrt{z^2-1}\,P_\nu^{\mu+1}(z) = (\nu-\mu)\,z\,P_\nu^\mu(z) - (\nu+\mu)\,P_{\nu-1}^\mu(z) \tag{A.20m}$$

$$(z^2-1)\,\frac{\mathrm{d}}{\mathrm{d}z}P_\nu^\mu(z) = (\nu+\mu)(\nu-\mu+1)\sqrt{z^2-1}\,P_\nu^{\mu-1}(z) - \mu\,z\,P_\nu^\mu(z) \tag{A.20n}$$

$$(\nu-\mu+1)\,P_{\nu+1}^\mu(z) = (2\nu+1)\,z\,P_\nu^\mu(z) - (\nu+\mu)\,P_{\nu-1}^\mu(z) \tag{A.20o}$$

$$(z^2-1)\,\frac{\mathrm{d}}{\mathrm{d}z}P_\nu^\mu(z) = \nu\,z\,P_\nu^\mu(z) - (\nu+\mu)\,P_{\nu-1}^\mu(z) \tag{A.20p}$$

$$P_{\nu+1}^\mu(z) = P_{\nu-1}^\mu(z) + (2\nu+1)\,\sqrt{z^2-1}\,P_\nu^{\mu-1}(z) \tag{A.20q}$$

A.3.6.3 Personal derivations

(A.20a) + (A.20b):

$$(1-x^2)\,\frac{\mathrm{d}}{\mathrm{d}x}P_\nu^\mu(x) = \frac{1}{2\nu+1}\left[(\nu+1)(\nu+\mu)P_{\nu-1}^\mu(x) - \nu(\nu+1-\mu)P_{\nu+1}^\mu(x)\right] \tag{A.20r}$$

(A.20c) + (A.20d):

$$\sqrt{1-x^2}\,P_\nu^{\mu\prime}(x) = \frac{1}{2}\left[(\nu+\mu)(\nu-\mu+1)P_\nu^{\mu-1}(x) - P_\nu^{\mu+1}(x)\right] \tag{A.20s}$$

$$2\mu\,P_\nu^\mu(x) = -\sqrt{1-x^2}\left[P_{\nu-1}^{\mu+1}(x) + (\nu+\mu-1)(\nu+\mu)P_{\nu-1}^{\mu-1}(x)\right] \tag{A.20t}$$

$$2\mu\,P_\nu^\mu(x) = -\sqrt{1-x^2}\left[P_{\nu+1}^{\mu+1}(x) + (\nu-\mu+1)(\nu-\mu+2)P_{\nu+1}^{\mu-1}(x)\right] \tag{A.20u}$$

A.4 Boltzmann's H-Theorem

The function $H(t)$ is defined as [1]

$$H(t) = \int \mathrm{d}^3v_1\,\sigma(\mathbf{v}_1,t)\,\ln\sigma(\mathbf{v}_1,t)\,. \tag{A.21}$$

Its derivation after time is

$$\frac{\mathrm{d}H}{\mathrm{d}t} \overset{\int\dot\sigma\,\mathrm{d}^3v=1}{=} \int \mathrm{d}^3v_1\,\frac{\partial\sigma(\mathbf{v}_1,t)}{\partial t}\ln\sigma(\mathbf{v}_1,t)\,, \tag{A.22}$$

and with collision balance (2.66) inserted $\dfrac{\mathrm{d}H}{\mathrm{d}t}$ yields

$$\begin{aligned}\frac{\mathrm{d}H}{\mathrm{d}t} \overset{(2.66)}{=} &-\int \mathrm{d}^3v_1\int \mathrm{d}^3v_2\int \mathrm{d}^3v_1'\int \mathrm{d}^3v_2'\,c(\mathbf{v}_1\to\mathbf{v}_1',\mathbf{v}_2\to\mathbf{v}_2')\times\\ &\times\left[\sigma(\mathbf{v}_1,t)\,\sigma(\mathbf{v}_2,t) - \sigma(\mathbf{v}_1',t)\,\sigma(\mathbf{v}_2',t)\right]\ln\sigma(\mathbf{v}_1,t)\,.\end{aligned} \tag{A.23}$$

Adding (A.23) up for swapped velocities as indexed yields

$$\begin{aligned}4\frac{\mathrm{d}H}{\mathrm{d}t} &= \frac{\mathrm{d}H}{\mathrm{d}t} + \frac{\mathrm{d}H}{\mathrm{d}t}_{v_1\leftrightarrow v_2,v_1'\leftrightarrow v_2'} + \frac{\mathrm{d}H}{\mathrm{d}t}_{v_1\leftrightarrow v_1',v_2\leftrightarrow v_2'} + \frac{\mathrm{d}H}{\mathrm{d}t}_{v_1\leftrightarrow v_2',v_2\leftrightarrow v_1'} =\\ &\overset{(A.23)}{\overset{(2.64)}{=}} -\int \mathrm{d}^3v_1\int \mathrm{d}^3v_2\int \mathrm{d}^3v_1'\int \mathrm{d}^3v_2'\,c(\mathbf{v}_1\to\mathbf{v}_1',\mathbf{v}_2\to\mathbf{v}_2')\times\\ &\times\left[\sigma(\mathbf{v}_1,t)\,\sigma(\mathbf{v}_2,t) - \sigma(\mathbf{v}_1',t)\,\sigma(\mathbf{v}_2',t)\right]\ln\frac{\sigma(\mathbf{v}_1,t)\sigma(\mathbf{v}_2,t)}{\sigma(\mathbf{v}_1',t)\sigma(\mathbf{v}_2',t)}\,,\end{aligned} \tag{A.24}$$

[1] It can be considered $-H \propto S$ (entropy).

and thus

$$\sigma(\mathbf{v}_1,t)\,\sigma(\mathbf{v}_2,t) \neq \sigma(\mathbf{v}_1',t)\,\sigma(\mathbf{v}_2',t) \qquad \Longrightarrow \qquad \frac{\mathrm{d}H}{\mathrm{d}t} < 0\,. \tag{A.25}$$

The condition

$$\sigma(\mathbf{v}_1,t)\,\sigma(\mathbf{v}_2,t) - \sigma(\mathbf{v}_1',t)\,\sigma(\mathbf{v}_2',t) = 0\,, \tag{2.72}$$

is not only sufficient (sec. 2.4.2) for the equilibrium velocity distribution but also necessary, as the H-theorem states.

The Newton motion equations apply for a kinetic system composed of $N \to \infty$ gas particles, and if $\{\mathbf{r}_i(t)|i = 1,\ldots,N\}$ solve them, so probably does $\{\mathbf{r}_i(-t)\}$, as the equations of motion are mostly invariant with respect to time reversal (this is not true for, e.g., velocity-dependent forces such as friction forces). Subsequently, it is impossible to decide whether $t < t'$ or $t' < t$ for two snapshots $\{\mathbf{r}_i(t)\}$ and $\{\mathbf{r}_i(t')\}$. Conversely, as it is $\partial_t H < 0$, it can very well be decided if $t < t'$ or $t' < t$. The contradiction arises from the fact that the system is statistically analyzed — introduced by the collision kernel $c(\mathbf{v}_1 \to \mathbf{v}_1', \mathbf{v}_2 \to \mathbf{v}_2')$ — and only an averaged behavior is predictable. As a full knowledge about the kinetic system is impossible to achieve, an information loss was introduced with H being a measure for it.

A.5 Edge detection of chondrules from tomograms

A.5.1 Floodfill algorithm

```
/// <summary>
/// 3D iterative flood fill with 6 neighbors
/// replaces all connected pixels with one color by another color
/// </summary>
/// <param name="x">x coordinate; width-based)</param>
/// <param name="y">y coordinate; height-based</param>
/// <param name="z">y coordinate; height-based</param>
/// <param name="colorOld">all connected pixels with this color will be replaced</param>
/// <param name="colorNew">the color to set connected pixels to</param>
public byte fill6Iterative(Point3D coordinate, byte colorOld, byte colorNew)
{
    //if (this.pixel[coordinate[0], coordinate[1], coordinate[2]] != colorOld)
      //  return 1;

    try
    {
        this.stack.Push(coordinate);

        while (this.stack.IsNotEmpty)
        {
            coordinate = stack.Pop();

            if ((this.pixel[coordinate.X, coordinate.Y, coordinate.Z] >= _valueThresholdLow) && (this.pixel[coordinate.X, coordinate.Y, coordinate.Z] <= _valueThresholdHigh) && (this.pixel[coordinate.X, coordinate.Y, coordinate.Z] != _valueShape))
            {
                this.pixel[coordinate.X, coordinate.Y, coordinate.Z] = colorNew;
                this.stack.Push(Point3D.Add(coordinate, new Point3D(0, 1, 0))); // unten
                this.stack.Push(Point3D.Add(coordinate, new Point3D(-1, 0, 0))); // links
                this.stack.Push(Point3D.Add(coordinate, new Point3D(0, -1, 0))); // oben
                this.stack.Push(Point3D.Add(coordinate, new Point3D(1, 0, 0))); // rechts
                this.stack.Push(Point3D.Add(coordinate, new Point3D(0, 0, -1))); // oben
                this.stack.Push(Point3D.Add(coordinate, new Point3D(0, 0, 1))); // rechts
            }
        }

        this.stack.Flush();

        return 0;
    }
        catch (Exception e)
    {
        MessageBox.Show("An error occured while trying to detect connected areas." + Environment.NewLine + Environment.NewLine + e.Message, "ERROR", MessageBoxButtons.OK, MessageBoxIcon.Error);
        return 2;
    }
}
```

A.5.2 Edge extraction algorithm

```
private bool NeighbourIsFree(int x, int y, int z)
{
    if (this.DetectHorizontalEdges)
    {
        if ((x - 1 >= 0) && (pixel[x - 1, y, z] != ValueShape)) { return true; }
        if ((x + 1 < this._dim1) && (pixel[x + 1, y, z] != ValueShape)) { return true; ↩
            }
    }
    if (this.DetectVerticalEdges)
    {
        if ((y - 1 >= 0) && (pixel[x, y - 1, z] != ValueShape)) { return true; }
        if ((y + 1 < this._dim2) && (pixel[x, y + 1, z] != ValueShape)) { return true; ↩
            }
    }
    if (this.ThreeDimensional)
    {
        if ((z - 1 >= 0) && (pixel[x, y, z - 1] != ValueShape)) { return true; }
        if ((z + 1 < this._dim3) && (pixel[x, y, z + 1] != ValueShape)) { return true; ↩
            }
    }
    return false;
}

/// <summary>
/// detects item boundaries
/// </summary>
public void DetectEdges(byte itemColor)
{
    edgePoints = new List<Point3D>();

    try
    {
        for (int i = 0; i < _dim1; i++)
            for (int j = 0; j < _dim2; j++)
                for (int k = 0; k < _dim3; k++)
                    if (pixel[i, j, k] == this.ValueShape)
                    {
                        if (this.NeighbourIsFree(i, j, k))
                        {
                            edgePoints.Add(new Point3D(i, j, k));
                        }
                    }

        this.EdgesDetected = true;
    }
    catch (Exception e)
    {
        MessageBox.Show("error getting edges." + Environment.NewLine + Environment.↩
            NewLine + e.Message, "ERROR", MessageBoxButtons.OK, MessageBoxIcon.Error);
    }
    finally
    {
    }
}
```

Appendix B

DETAILS FOR CHAPTER 3.1

The coordinate vector fields for the parametrization $\boldsymbol{\Omega}$ (3.9b) are

$$\boldsymbol{\partial_\xi} = \begin{pmatrix} \Omega_\xi \cos\xi \sin\zeta - \Omega \sin\xi \sin\zeta \\ \Omega_\xi \sin\xi \sin\zeta + \Omega \cos\xi \sin\zeta \\ \Omega_\xi \cos\zeta \end{pmatrix} , \tag{B.1a}$$

$$\boldsymbol{\partial_\zeta} = \begin{pmatrix} \Omega_\zeta \cos\xi \sin\zeta + \Omega \cos\xi \cos\zeta \\ \Omega_\zeta \sin\xi \sin\zeta + \Omega \sin\xi \cos\zeta \\ \Omega_\zeta \cos\zeta - \Omega \sin\zeta \end{pmatrix} . \tag{B.1b}$$

B.1 Recurrence relations of spherical harmonics

The following recurrence relations of spherical harmonics were derived to calculate scalar products of functions developed in spherical harmonics.

With (A.20e) and coefficient $h_{\nu\mu}$ (see (A.9a)) it is (P_1^0 is short for $P_1^0(\cos\zeta)$)

$$P_1^0\, Y_\nu^\mu = \frac{f_{\nu\mu}}{2\nu+1}\left[\frac{\nu+1-\mu}{f_{\nu+1,\mu}}\, Y_{\nu+1}^\mu + \frac{\nu+\mu}{f_{\nu-1,\mu}}\, Y_{\nu-1}^\mu\right] = h_{\nu+1,\mu}\, Y_{\nu+1}^\mu + h_{\nu\mu}\, Y_{\nu-1}^\mu . \tag{B.2}$$

With (A.20r) it is

$$-\,\partial_\zeta P_1^0\, \partial_\zeta Y_\nu^\mu = \nu\, h_{\nu+1,\mu}\, Y_{\nu+1}^\mu - (\nu+1)\, h_{\nu\mu}\, Y_{\nu-1}^\mu . \tag{B.3}$$

With (A.20h) and (A.20g) and coefficient $d_{\nu\mu}$ (see (A.9b)) it is

$$\begin{aligned} (-\partial_\zeta P_1^0)\, Y_\nu^\mu\, e^{\mathbb{i}\xi} &= \frac{f_{\nu\mu}}{2\nu+1}\left[\frac{1}{f_{\nu-1,\mu+1}} Y_{\nu-1}^{\mu+1} - \frac{1}{f_{\nu+1,\mu+1}} Y_{\nu+1}^{\mu+1}\right] \\ &= d_{\nu,-\mu}\, Y_{\nu-1}^{\mu+1} - d_{\nu+1,\mu+1}\, Y_{\nu+1}^{\mu+1} \end{aligned} \tag{B.4a}$$

and

$$\begin{aligned} (-\partial_\zeta P_1^0)\, Y_\nu^\mu\, e^{-\mathbb{i}\xi} &= \frac{f_{\nu\mu}}{2\nu+1}\left[\frac{(\nu-\mu+1)(\nu-\mu+2)}{f_{\nu+1,\mu-1}} Y_{\nu+1}^{\mu-1} - \frac{(\nu+\mu-1)(\nu+\mu)}{f_{\nu-1,\mu-1}} Y_{\nu-1}^{\mu-1}\right] \\ &= d_{\nu+1,-\mu+1}\, Y_{\nu+1}^{\mu-1} - d_{\nu,\mu}\, Y_{\nu-1}^{\mu-1} . \end{aligned} \tag{B.4b}$$

With (A.20s) it is

$$\partial_\zeta Y_\nu^\mu\, e^{-\mathrm{i}\xi} = \frac{f_{\nu\mu}}{2}\left[\frac{1}{f_{\nu,\mu+1}} Y_\nu^{\mu+1}\, e^{-2\mathrm{i}\xi} - \frac{(\nu+\mu)(\nu-\mu+1)}{f_{\nu,\mu-1}} Y_\nu^{\mu-1}\right] \tag{B.5a}$$

and

$$\partial_\zeta Y_\nu^\mu\, e^{\mathrm{i}\xi} = \frac{f_{\nu\mu}}{2}\left[\frac{1}{f_{\nu,\mu+1}} Y_\nu^{\mu+1} - \frac{(\nu+\mu)(\nu-\mu+1)}{f_{\nu,\mu-1}} Y_\nu^{\mu-1}\, e^{2\mathrm{i}\xi}\right] . \tag{B.5b}$$

Hence, with (B.2), (B.5a) and (B.5b) it is

$$\begin{aligned} P_1^0\, \partial_\zeta Y_\nu^\mu \left(e^{\mathrm{i}\xi} - e^{-\mathrm{i}\xi}\right) &= \frac{1}{2}\sqrt{(\nu+\mu)(\nu+1-\mu)}\left(1 - e^{2\mathrm{i}\varphi}\right)\left[h_{\nu,\mu-1}\, Y_{\nu-1}^{\mu-1} + h_{\nu+1,\mu-1}\, Y_{\nu+1}^{\mu-1}\right] + \\ &+ \frac{1}{2}\sqrt{(\nu-\mu)(\nu+1+\mu)}\left(1 - e^{-2\mathrm{i}\varphi}\right)\left[h_{\nu,\mu+1}\, Y_{\nu-1}^{\mu+1} + h_{\nu+1,\mu+1}\, Y_{\nu+1}^{\mu+1}\right] \end{aligned} \tag{B.6a}$$

$$\begin{aligned} &= \frac{1}{2}\left(1 - e^{2\mathrm{i}\varphi}\right)\left[(\nu+\mu)\, d_{\nu+1,-\mu+1}\, Y_{\nu+1}^{\mu-1} + (\nu+1-\mu)\, d_{\nu,\mu}\, Y_{\nu-1}^{\mu-1}\right] + \\ &+ \frac{1}{2}\left(1 - e^{-2\mathrm{i}\varphi}\right)\left[(\nu+1+\mu)\, d_{\nu,-\mu}\, Y_{\nu-1}^{\mu+1} + (\nu-\mu)\, d_{\nu+1,\mu+1}\, Y_{\nu+1}^{\mu+1}\right] \end{aligned} \tag{B.6b}$$

and

$$\begin{aligned} P_1^0\, \partial_\zeta Y_\nu^\mu \left(e^{\mathrm{i}\xi} + e^{-\mathrm{i}\xi}\right) &= \frac{1}{2}\sqrt{(\nu-\mu)(\nu+1+\mu)}\left(1 + e^{-2\mathrm{i}\varphi}\right)\left[h_{\nu,\mu+1}\, Y_{\nu-1}^{\mu+1} + h_{\nu+1,\mu+1}\, Y_{\nu+1}^{\mu+1}\right] - \\ &- \frac{1}{2}\sqrt{(\nu+\mu)(\nu+1-\mu)}\left(1 + e^{2\mathrm{i}\varphi}\right)\left[h_{\nu,\mu-1}\, Y_{\nu-1}^{\mu-1} + h_{\nu+1,\mu-1}\, Y_{\nu+1}^{\mu-1}\right] \end{aligned} \tag{B.6c}$$

$$\begin{aligned} &= \frac{1}{2}\left(1 + e^{-2\mathrm{i}\varphi}\right)\left[(\nu+1+\mu)\, d_{\nu,-\mu}\, Y_{\nu-1}^{\mu+1} + (\nu-\mu)\, d_{\nu+1,\mu+1}\, Y_{\nu+1}^{\mu+1}\right] - \\ &- \frac{1}{2}\left(1 + e^{2\mathrm{i}\varphi}\right)\left[(\nu+\mu)\, d_{\nu+1,-\mu+1}\, Y_{\nu+1}^{\mu-1} + (\nu+1-\mu)\, d_{\nu,\mu}\, Y_{\nu-1}^{\mu-1}\right] . \end{aligned} \tag{B.6d}$$

With (A.20t) and (A.20u) it is

$$\begin{aligned} \frac{\mu}{(-\partial_\zeta P_1^0)} Y_\nu^\mu\, e^{-\mathrm{i}\xi} &= \frac{-f_{\nu\mu}}{2}\left[\frac{1}{f_{\nu-1,\mu+1}} Y_{\nu-1}^{\mu+1}\, e^{-2\mathrm{i}\xi} + \frac{(\nu+\mu-1)(\nu+\mu)}{f_{\nu-1,\mu-1}} Y_{\nu-1}^{\mu-1}\right] \\ &= -\frac{2\nu+1}{2}\left[d_{\nu,-\mu} Y_{\nu-1}^{\mu+1}\, e^{-2\mathrm{i}\xi} + d_{\nu,\mu} Y_{\nu-1}^{\mu-1}\right] \end{aligned} \tag{B.7a}$$

$$\begin{aligned} \frac{\mu}{(-\partial_\zeta P_1^0)} Y_\nu^\mu\, e^{\mathrm{i}\xi} &= \frac{-f_{\nu\mu}}{2}\left[\frac{1}{f_{\nu-1,\mu+1}} Y_{\nu-1}^{\mu+1} + \frac{(\nu+\mu-1)(\nu+\mu)}{f_{\nu-1,\mu-1}} Y_{\nu-1}^{\mu-1}\, e^{2\mathrm{i}\xi}\right] \\ &= -\frac{2\nu+1}{2}\left[d_{\nu,-\mu} Y_{\nu-1}^{\mu+1} + d_{\nu,\mu} Y_{\nu-1}^{\mu-1}\, e^{2\mathrm{i}\xi}\right] \end{aligned} \tag{B.7b}$$

or alternatively

$$\begin{aligned} \frac{\mu}{(-\partial_\zeta P_1^0)} Y_\nu^\mu\, e^{-\mathrm{i}\xi} &= \frac{-f_{\nu\mu}}{2}\left[\frac{1}{f_{\nu+1,\mu+1}} Y_{\nu+1}^{\mu+1}\, e^{-2\mathrm{i}\xi} + \frac{(\nu-\mu+1)(\nu-\mu+2)}{f_{\nu+1,\mu-1}} Y_{\nu+1}^{\mu-1}\right] \\ &= -\frac{2\nu+1}{2}\left[d_{\nu+1,\mu+1} Y_{\nu+1}^{\mu+1}\, e^{-2\mathrm{i}\xi} + d_{\nu+1,-\mu+1} Y_{\nu+1}^{\mu-1}\right] \end{aligned} \tag{B.7c}$$

$$\begin{aligned} \frac{\mu}{(-\partial_\zeta P_1^0)} Y_\nu^\mu\, e^{\mathrm{i}\xi} &= \frac{-f_{\nu\mu}}{2}\left[\frac{1}{f_{\nu+1,\mu+1}} Y_{\nu+1}^{\mu+1} + \frac{(\nu-\mu+1)(\nu-\mu+2)}{f_{\nu+1,\mu-1}} Y_{\nu+1}^{\mu-1}\, e^{2\mathrm{i}\xi}\right] \\ &= -\frac{2\nu+1}{2}\left[d_{\nu+1,\mu+1}\, Y_{\nu+1}^{\mu+1} + d_{\nu+1,-\mu+1}\, Y_{\nu+1}^{\mu-1}\, e^{2\mathrm{i}\xi}\right] . \end{aligned} \tag{B.7d}$$

B.2 Scalar products for F_x in section 3.1.2.1

The underlined scalar products are not directly solved. Instead their pairwise difference for the same phases are evaluated in sec. B.4, yielding terms depending on the four ds and $\delta_{q,\mu\pm1}$, $\delta_{p,\nu\pm1}$.

$$\left(-\partial_\zeta P_1^0\, Y_\nu^\mu \left(e^{\mathrm{i}\xi}+e^{-\mathrm{i}\xi}\right),\, Y_p^q\right) = \tag{B.8a}$$

$$\overset{\text{(B.4a), (B.4b)}}{=} \left(d_{\nu,-\mu}\, Y_{\nu-1}^{\mu+1} - d_{\nu+1,\mu+1}\, Y_{\nu+1}^{\mu+1} + d_{\nu+1,-\mu+1}\, Y_{\nu+1}^{\mu-1} - d_{\nu,\mu}\, Y_{\nu-1}^{\mu-1},\, Y_p^q\right)$$

$$= d_{\nu,-\mu}\,\delta_{\nu-1,p}\,\delta_{\mu+1,q} - d_{\nu+1,\mu+1}\,\delta_{\nu+1,p}\,\delta_{\mu+1,q} + d_{\nu+1,-\mu+1}\,\delta_{\nu+1,p}\,\delta_{\mu-1,q} - d_{\nu,\mu}\,\delta_{\nu-1,p}\,\delta_{\mu-1,q}$$

$$\left(Y_\nu^\mu \frac{\mu}{(-\partial_\zeta P_1^0)}\left(e^{\mathrm{i}\xi}-e^{-\mathrm{i}\xi}\right),\, Y_p^q\right) = \tag{B.8b}$$

$$\overset{\text{(B.7c), (B.7d)}}{=} \frac{2\nu+1}{2}\left[d_{\nu+1,\mu+1}\left(Y_{\nu+1}^{\mu+1}\left(e^{-2\mathrm{i}\xi}-1\right),\, Y_p^q\right) + d_{\nu+1,-\mu+1}\left(Y_{\nu+1}^{\mu-1}\left(1-e^{2\mathrm{i}\xi}\right),\, Y_p^q\right)\right]$$

$$= \frac{2\nu+1}{2}\left[d_{\nu+1,\mu+1}\left(\underline{\left(Y_{\nu+1}^{\mu+1}\, e^{-2\mathrm{i}\xi},\, Y_p^q\right)} - \delta_{p,\nu+1}\,\delta_{q,\mu+1}\right) + \right.$$

$$\left. + d_{\nu+1,-\mu+1}\left(\delta_{p,\nu+1}\,\delta_{q,\mu-1} - \underline{\left(Y_{\nu+1}^{\mu-1}\, e^{2\mathrm{i}\xi},\, Y_p^q\right)}\right)\right]$$

$$-\left(P_1^0\,\partial_\zeta Y_\nu^\mu \left(e^{\mathrm{i}\xi}+e^{-\mathrm{i}\xi}\right),\, Y_p^q\right) = \tag{B.8c}$$

$$\overset{\text{(B.6d)}}{=} \frac{1}{2}\left(\left[(\nu+\mu)\, d_{\nu+1,-\mu+1}\, Y_{\nu+1}^{\mu-1} + (\nu+1-\mu)\, d_{\nu,\mu}\, Y_{\nu-1}^{\mu-1}\right]\left(e^{2\mathrm{i}\varphi}+1\right),\, Y_p^q\right) -$$

$$-\frac{1}{2}\left(\left[(\nu+1+\mu)\, d_{\nu,-\mu}\, Y_{\nu-1}^{\mu+1} + (\nu-\mu)\, d_{\nu+1,\mu+1}\, Y_{\nu+1}^{\mu+1}\right]\left(e^{-2\mathrm{i}\varphi}+1\right),\, Y_p^q\right)$$

$$= \frac{1}{2}\left[(\nu+\mu)\, d_{\nu+1,-\mu+1}\left(\underline{\left(Y_{\nu+1}^{\mu-1}\, e^{2\mathrm{i}\varphi},\, Y_p^q\right)} + \delta_{p,\nu+1}\,\delta_{q,\mu-1}\right) + \right.$$

$$+(\nu+1-\mu)\, d_{\nu,\mu}\left(\underline{\left(Y_{\nu-1}^{\mu-1}\, e^{2\mathrm{i}\varphi},\, Y_p^q\right)} + \delta_{p,\nu-1}\,\delta_{q,\mu-1}\right) -$$

$$-(\nu+1+\mu)\, d_{\nu,-\mu}\left(\underline{\left(Y_{\nu-1}^{\mu+1}\, e^{-2\mathrm{i}\varphi},\, Y_p^q\right)} + \delta_{p,\nu-1}\,\delta_{q,\mu+1}\right) -$$

$$\left. - (\nu-\mu)\, d_{\nu+1,\mu+1}\left(\underline{\left(Y_{\nu+1}^{\mu+1}\, e^{-2\mathrm{i}\varphi},\, Y_p^q\right)} + \delta_{p,\nu+1}\,\delta_{q,\mu+1}\right)\right]$$

B.3 Scalar products for F_y in section 3.1.2.2

$$-\left(-\partial_\zeta P_1^0 \left(e^{\mathrm{i}\xi}-e^{-\mathrm{i}\xi}\right) Y_\nu^\mu\,,\, Y_p^q\right) = \tag{B.9a}$$

(B.4a), (B.4b)
$$= \left(d_{\nu+1,\mu+1}\, Y_{\nu+1}^{\mu+1} - d_{\nu,-\mu}\, Y_{\nu-1}^{\mu+1} + d_{\nu+1,-\mu+1}\, Y_{\nu+1}^{\mu-1} - d_{\nu,\mu}\, Y_{\nu-1}^{\mu-1}\,,\, Y_p^q\right)$$
$$= d_{\nu+1,\mu+1}\,\delta_{\nu+1,p}\,\delta_{\mu+1,q} - d_{\nu,-\mu}\,\delta_{\nu-1,p}\,\delta_{\mu+1,q} + d_{\nu+1,-\mu+1}\,\delta_{\nu+1,p}\,\delta_{\mu-1,q} - d_{\nu,\mu}\,\delta_{\nu-1,p}\,\delta_{\mu-1,q}$$

$$-\left(Y_\nu^\mu \frac{\mu}{(-\partial_\zeta P_1^0)} \left(e^{\mathrm{i}\xi}+e^{-\mathrm{i}\xi}\right)\,,\, Y_p^q\right) = \tag{B.9b}$$

(B.7c), (B.7d)
$$= \frac{2\nu+1}{2}\left[d_{\nu+1,\mu+1}\left(Y_{\nu+1}^{\mu+1}\left(1+e^{-2\mathrm{i}\xi}\right)\,,\, Y_p^q\right) + d_{\nu+1,-\mu+1}\left(Y_{\nu+1}^{\mu-1}\left(1+e^{2\mathrm{i}\xi}\right)\,,\, Y_p^q\right)\right]$$
$$= \frac{2\nu+1}{2}\left[d_{\nu+1,\mu+1}\,\delta_{p,\nu+1}\,\delta_{q,\mu+1} + d_{\nu+1,\mu+1}\underline{\left(Y_{\nu+1}^{\mu+1}\,e^{-2\mathrm{i}\xi}\,,\, Y_p^q\right)} + \right.$$
$$\left. + d_{\nu+1,-\mu+1}\,\delta_{p,\nu+1}\,\delta_{q,\mu-1} + d_{\nu+1,-\mu+1}\underline{\left(Y_{\nu+1}^{\mu-1}\,e^{2\mathrm{i}\xi}\,,\, Y_p^q\right)}\right]$$

$$\left(P_1^0\,\partial_\zeta Y_\nu^\mu \left(e^{\mathrm{i}\xi}-e^{-\mathrm{i}\xi}\right)\,,\, Y_p^q\right) = \tag{B.9c}$$

(B.6b)
$$= \frac{1}{2}\left(\left[(\nu+\mu)\,d_{\nu+1,-\mu+1}\,Y_{\nu+1}^{\mu-1} + (\nu+1-\mu)\,d_{\nu,\mu}\,Y_{\nu-1}^{\mu-1}\right]\left(1-e^{2\mathrm{i}\varphi}\right)\,,\, Y_p^q\right) +$$
$$+\frac{1}{2}\left(\left[(\nu+1+\mu)\,d_{\nu,-\mu}\,Y_{\nu-1}^{\mu+1} + (\nu-\mu)\,d_{\nu+1,\mu+1}\,Y_{\nu+1}^{\mu+1}\right]\left(1-e^{-2\mathrm{i}\varphi}\right)\,,\, Y_p^q\right)$$
$$= \frac{1}{2}\left[(\nu+\mu)\,d_{\nu+1,-\mu+1}\left(\delta_{p,\nu+1}\,\delta_{q,\mu-1} - \underline{\left(Y_{\nu+1}^{\mu-1}e^{2\mathrm{i}\varphi}\,,\, Y_p^q\right)}\right) + \right.$$
$$+(\nu+1-\mu)\,d_{\nu,\mu}\left(\delta_{p,\nu-1}\,\delta_{q,\mu-1} - \underline{\left(Y_{\nu-1}^{\mu-1}e^{2\mathrm{i}\varphi}\,,\, Y_p^q\right)}\right) +$$
$$+(\nu-\mu)\,d_{\nu+1,\mu+1}\left(\delta_{p,\nu+1}\,\delta_{q,\mu+1} - \underline{\left(Y_{\nu+1}^{\mu+1}e^{-2\mathrm{i}\varphi}\,,\, Y_p^q\right)}\right) +$$
$$\left. + (\nu+1+\mu)\,d_{\nu,-\mu}\left(\delta_{p,\nu-1}\,\delta_{q,\mu+1} - \underline{\left(Y_{\nu-1}^{\mu+1}e^{-2\mathrm{i}\varphi}\,,\, Y_p^q\right)}\right)\right]\,.$$

B.4 Representation of $d_{\nu+1,\mu+1} Y_{\nu+1}^{\mu+1}\, e^{-2\mathrm{i}\xi} - d_{\nu,-\mu} Y_{\nu-1}^{\mu+1}\, e^{-2\mathrm{i}\xi}$, used in sections 3.1.2.1 and 3.1.2.2

The difference of two weighted scalar products shall be calculated

$$d_{\nu+1,\mu+1}\, \Lambda_{\nu+1,p}^{\mu+1,q,-2} - d_{\nu,-\mu}\, \Lambda_{\nu-1,p}^{\mu+1,q,-2} \equiv d_{\nu+1,\mu+1} \left(Y_{\nu+1}^{\mu+1}\, e^{-2\mathrm{i}\xi}\,,\, Y_p^q \right) - d_{\nu,-\mu} \left(Y_{\nu-1}^{\mu+1}\, e^{-2\mathrm{i}\xi}\,,\, Y_p^q \right) .$$

Because of the identity

$$d_{\nu,-\mu}\, f_{\nu-1,\mu+1} \equiv d_{\nu+1,\mu+1}\, f_{\nu+1,\mu+1} \quad \nu \geq 0 \wedge -\nu \leq \mu \leq \nu \qquad \text{(A.14a)}$$

the above equation can be expressed in Legendre polynomials multiplied with the same factor

$$\left(d_{\nu+1,\mu+1} Y_{\nu+1}^{\mu+1} - d_{\nu,-\mu} Y_{\nu-1}^{\mu+1}\,,\, Y_p^q\, e^{2\mathrm{i}\xi} \right) \overset{\substack{\text{(A.6a)}\\ \text{(A.11f)}\\ \text{(A.14a)}}}{=} 2\pi\, d_{\nu,-\mu}\, f_{\nu-1,\mu+1}\, f_{p,\mu-1}\, \delta_{q,\mu-1} \left(P_{\nu+1}^{\mu+1} - P_{\nu-1}^{\mu+1}\,,\, P_p^{\mu-1} \right)_{[-1,1]} . \qquad \text{(B.10)}$$

The scalar product is solved by the same index transformation, at first on the left, then on the right side of the scalar product. Eventually the associated Legendre polynomials orthogonality relation for the same upper index is applied.

$$\left(P_{\nu+1}^{\mu+1} - P_{\nu-1}^{\mu+1}\,,\, P_p^{\mu-1} \right)_{[-1,1]} \overset{\text{(A.20h)}}{=} -(2\nu+1) \left(\sqrt{1-x^2}\, P_\nu^\mu\,,\, P_p^{\mu-1} \right)_{[-1,1]} \qquad \text{(B.11a)}$$

$$\overset{\text{(A.20h)}}{=} -\frac{2\nu+1}{2p+1} \left(P_\nu^\mu\,,\, P_{p-1}^\mu - P_{p+1}^\mu \right)_{[-1,1]} \qquad \text{(B.11b)}$$

$$\overset{\text{(A.11d)}}{=} \frac{2\nu+1}{2p+1} \frac{1}{2\pi\, f_{\nu\mu}^2} \left[\delta_{\nu,p+1} - \delta_{\nu,p-1} \right] \qquad \text{(B.11c)}$$

With this result, the two weighted scalar products can be easily written as

$$d_{\nu+1,\mu+1} \left(Y_{\nu+1}^{\mu+1}\, e^{-2\mathrm{i}\xi}\,,\, Y_p^q \right) - d_{\nu,-\mu} \left(Y_{\nu-1}^{\mu+1}\, e^{-2\mathrm{i}\xi}\,,\, Y_p^q \right) \overset{\text{(B.11c)}}{=} \delta_{q,\mu-1} \begin{cases} -d_{\nu+1,1-\mu} & p = \nu+1 \\ d_{\nu,\mu} & p = \nu-1 \\ 0 & \text{else} \end{cases} . \qquad \text{(B.12)}$$

Bibliography

Abramowitz, M. and Stegun, I. A., editors (1964). *Handbook of Mathematical Functions with Formulas, Graphs, and Mathematical Tables*. Dover, New York, ninth dover printing, tenth gpo printing edition.

Amelin, Y., Krot, A., Hutcheon, I., and Ulyanov, A. (2002). Lead isotopic ages of chondrules and calcium-aluminum-rich inclusions. *Science*, **297**(5587):1678–1683.

Arnold, S. and Amani, Y. (1980). Broadband photophoretic spectroscopy. *Optics Letters*, **5**:242–244.

Arnold, S., Leung, K. M., and Pluchino, A. B. (1984). Influence of surface-mode-enhanced local fields on photophoresis. *Phys. Rev. A*, **29**:654–660.

Arnold, S. and Lewittes, M. (1982). Size dependence of the photophoretic force. *Journal of Applied Physics*, **53**:5314–5319.

Bakanov, S. P. (1992). Thermophoresis in gases at small Knudsen numbers. *Soviet Physics Uspekhi*, **35**(9):783–792.

Beitz, E., Güttler, C., Blum, J., Meisner, T., Teiser, J., and Wurm, G. (2011). Low-velocity Collisions of Centimeter-sized Dust Aggregates. *ApJ*, **736**:34.

Beresnev, S., Chernyak, V., and Fomyagin, G. (1993). Photophoresis of a spherical particle in a rarefied gas. *Physics of Fluids*, **5**:2043–2052.

Beresnev, S., Vasiljeva, M., and Suetin, D. (2012). Predictions and detection of the "accommodation" forces on Janus particles subjected to directed radiation in a rarefied gas. *Vacuum*, **86**:1663–1668.

Beresnev, S. A., Chernyak, V. G., and Suetin, P. E. (1987). Motion of a spherical particle in a rarefied gas. Part 1. A liquid particle in its saturated vapour. *Journal of Fluid Mechanics*, **176**:295–310.

Beresnev, S. A., Kochneva, L. B., and Suetin, P. E. (2003a). Photophoresis Of Aerosols In The Earth Atmosphere. *Thermophyiscs and Aeromechanics*, **10**(2):287–301.

Beresnev, S. A., Kochneva, L. B., Suetin, P. E., Zakharov, V. I., and Gribanov, K. G. (2003b). Photophoresis of atmospheric aerosols in the Earth's thermal radiation field. *atmospheric and oceanic optics c/c of optika atmosfery I okeana*, **16**(5/6):431–438.

Beresnev, S. A., Kovalev, F. D., Kochneva, L. B., Runkov, V. A., Suetin, P. E., and Cheremisin, A. A. (2003c). On the possibility of particle's photophoretic levitation in the stratosphere. *atmospheric and oceanic optics c/c of optika atmosfery I okeana*, **16**(1):44–48.

Bischoff, A., Palme, H., Ash, R. D., Clayton, R. N., Schultz, L., Herpers, U., Stoffler, D., Grady, M. M., Pillinger, C. T., Spettel, B., Weber, H., Grund, T., Endress, M., and Weber, D. (1993a). Paired Renazzo-type (CR) carbonaceous chondrites from the Sahara. *Geochim. Cosmochim. Acta*, **57**:1587–1603.

Bischoff, A., Palme, H., Schultz, L., Weber, D., Weber, H. W., and Spettel, B. (1993b). ACFER 182 and paired samples, an iron-rich carbonaceous chondrite - Similarities with ALH85085 and relationship to CR chondrites. *Geochim. Cosmochim. Acta*, **57**:2631–2648.

Bland, P. A., Howard, L. E., Prior, D. J., Wheeler, J., Hough, R. M., and Dyl, K. A. (2011). Earliest rock fabric formed in the solar system preserved in a chondrule rim. *Nature Geoscience*, **4**:244–247.

Blum, J. and Wurm, G. (2008). The Growth Mechanisms of Macroscopic Bodies in Protoplanetary Disks. *ARA&A*, **46**:21–56.

Blum, J., Wurm, G., Kempf, S., and Henning, T. (1996). The Brownian Motion of Dust Particles in the Solar Nebula: an Experimental Approach to the Problem of Preplanetary Dust Aggregation. *Icarus*, **124**:441–451.

Bockelée-Morvan, D., Gautier, D., Hersant, F., Huré, J.-M., and Robert, F. (2002). Turbulent radial mixing in the solar nebula as the source of crystalline silicates in comets. *A&A*, **384**:1107–1118.

Borman, V. D., Krylov, S. I., and Prosianov, A. V. (1988). The theory of nonequilibrium phenomena at the gas-solid interface. *Zhurnal Eksperimentalnoi i Teoreticheskoi Fiziki*, **94**:271–289.

Brenner, H. (1963). The Stokes resistance of an arbitrary particle. *Chemical Engineering Science*, **18**(1):1–25.

Brenner, H. (1964). The Stokes resistance of an arbitrary particle II: An extension. *Chemical Engineering Science*, **19**(9):599–629.

Brenner, H. (1966). The Stokes resistance of an arbitrary particle V: Symbolic operator representation of intrinsic resistance. *Chemical Engineering Science*, **21**(1):97–109.

Brenner, H. (2005). Nonisothermal Brownian motion: Thermophoresis as the macroscopic manifestation of thermally biased molecular motion. *Phys. Rev. E*, **72**(6):061201.

Brenner, H. (2006). Elementary kinematical model of thermal diffusion in liquids and gases. *Phys. Rev. E*, **74**(3):036306.

Brenner, H. (2009). A nonmolecular derivation of Maxwell's thermal-creep boundary condition in gases and liquids via application of the LeChatelier-Braun principle to Maxwell's thermal stress. *Physics of Fluids*, **21**(5):053602.

Brownlee, D., Tsou, P., Aléon, J., Alexander, C. M. O. ., Araki, T., Bajt, S., Baratta, G. A., Bastien, R., Bland, P., Bleuet, P., and coauthors (2006). Comet 81P/Wild 2 Under a Microscope. *Science*, **314**:1711–1716.

Calvet, N., D'Alessio, P., Hartmann, L., Wilner, D., Walsh, A., and Sitko, M. (2002). Evidence for a developing gap in a 10 myr old protoplanetary disk. *ApJ*, **568**:1008–1016.

Carballido, A. (2011). Accretion of dust by chondrules in a mhd-turbulent solar nebula. *Icarus*, **211**:876–884.

Cercignani, C. (1988). *The Boltzmann Equation and Its Applications*, volume 67 of *Applied Mathematical Sciences*. Springer (New York).

Cercignani, C. and Lampis, M. (1971). Kinetic models for gas-surface interactions. *Transport Theory and Statistical Physics*, **1**(2):101–114.

Chang, Y. C. and Keh, H. J. (2012). Effects of thermal stress slip on thermophoresis and photophoresis. *Journal of Aerosol Science*, **50**(0):1–10.

Cheremisin, A. A. and Kushnarenko, A. V. (2013). Photophoretic interaction of aerosol particles and its effect on coagulation in rarefied gas medium. *Journal of Aerosol Science*, **62**(0):26–39.

Cheremisin, A. A., Shnipov, I. S., Horvath, H., and Rohatschek, H. (2011). The global picture of aerosol layers formation in the stratosphere and in the mesosphere under the influence of gravito-photophoretic and magneto-photophoretic forces. *Journal of Geophysical Research (Atmospheres)*, **116**:19204.

Cheremisin, A. A., Vassilyev, Y. V., and Horvath, H. (2005). Gravito-photophoresis and aerosol stratification in the atmosphere. *Journal of aerosol science*, **36**(11):1277–1299.

Chernyak, V. G. and Beresnev, S. A. (1993). Photophoresis of aerosol particles. *Journal of Aerosol Science*, **24**(7):857–866.

Chesley, S. R., Ostro, S. J., Vokrouhlický, D., Čapek, D., Giorgini, J. D., Nolan, M. C., Margot, J.-L., Hine, A. A., Benner, L. A. M., and Chamberlin, A. B. (2003). Direct Detection of the Yarkovsky Effect by Radar Ranging to Asteroid 6489 Golevka. *Science*, **302**:1739–1742.

Ciesla, F. J. (2007). Outward Transport of High-Temperature Materials Around the Midplane of the Solar Nebula. *Science*, **318**:613–615.

Clauser, C. and Hünges, E. (1995). *Thermal conductivity of rocks and minerals*, volume 3 of *AGU Reference Shelf*, pages 105–126. American Geophysical Union, Washington, D.C.

Cuzzi, J. N., Davis, S. S., and Dobrovolskis, A. R. (2003). Blowing in the wind. II. Creation and redistribution of refractory inclusions in a turbulent protoplanetary nebula. *Icarus*, **166**:385–402.

Cuzzi, J. N., Dobrovolskis, A. R., and Hogan, R. C. (1996). Turbulence, chondrules, and planetesimals. In Hewins, R. H., Jones, R. H., and Scott, E. R. D., editors, *Chondrules and the Protoplanetary Disk*, pages 35–43. Cambridge University Press, Cambridge, U.K.

D'Alessio, P., Hartmann, L., Calvet, N., Franco-Hernández, R., Forrest, W. J., Sargent, B., Furlan, E., Uchida, K., Green, J. D., Watson, D. M., Chen, C. H., Kemper, F., Sloan, G. C., and Najita, J. (2005). The Truncated Disk of CoKu Tau/4. *ApJ*, **621**:461–472.

Daun, K. J., Smallwood, G. J., and Liu, F. (2008). Investigation of Thermal Accommodation Coefficients in Time-Resolved Laser-Induced Incandescence. *J. Heat Transfer*, **130**(12):121201.

Daun, K. J., Smallwood, G. J., and Liu, F. (2009). Molecular dynamics simulations of translational thermal accommodation coefficients for time-resolved LII. *Applied Physics B*, **94**(1):39–49.

de Beule, C., Kelling, T., Wurm, G., Teiser, J., and Jankowski, T. (2013). From Planetesimals to Dust: Low-gravity Experiments on Recycling Solids at the Inner Edges of Protoplanetary Disks. *ApJ*, **763**:11.

Desyatnikov, A. S., Shvedov, V. G., Rode, A. V., Krolikowski, W., and Kivshar, Y. S. (2009). Photophoretic manipulation of absorbing aerosol particles with vortex beams: theory versus experiment. *Optics Express*, **17**:8201.

Dittrich, K., Klahr, H., and Johansen, A. (2013). Gravoturbulent Planetesimal Formation: The Positive Effect of Long-lived Zonal Flows. *ApJ*, **763**:117.

Dusel, P. W., Kerker, M., and Cooke, D. D. (1979). Distribution of absorption centers within irradiated spheres. *Journal of the Optical Society of America (1917-1983)*, **69**:55.

Ebel, D. S. and Rivers, M. L. (2007). Meteorite 3-D synchrotron microtomography: Methods and applications. *Meteoritics and Planetary Science*, **42**:1627–1646.

Ehrenhaft, F. (1940). Photophoresis of Small Particles in a Magnetic Field. *Physical Review*, **57**:659–659.

Ehrenhaft, F., Reiss, M., and Wasser, E. (1930). Magnetophotophorese und Elektrophotophorese. *Zeitschrift für Physik*, **60**(11-12):754–758.

Ehrenhaft, F., Reiss, M., and Wasser, E. (1931). Zur Deutung der Elektrophotophorese und Magnetophotophorese. *Zeitschrift für Physik*, **67**(7-8):519–522.

Epstein, M. (1967). A model of the wall boundary condition in kinetic theory. *AIAA Journal*, **5**:1797–1800.

Epstein, P. S. (1924). On the Resistance Experienced by Spheres in their Motion through Gases. *Physical Review*, **23**:710–733.

Espaillat, C., Muzerolle, J., Najita, J., Andrews, S., Zhu, Z., Calvet, N., Kraus, S., Hashimoto, J., Kraus, A., and D'Alessio, P. (2014). An Observational Perspective of Transitional Disks. In Beuther, H., Klessen, R. S., Dullemond, C. P., and Henning, T., editors, *Protostars and Planets VI*, pages 497–520. University of Arizona Press, Tucson, AZ.

Fresnel, A. (1825). Notiz über die Repulsion, welche erhitzte Körper in merklichen Abständen auf einander ausüben. *Annalen der Physik*, **80**:355–363.

Friedrich, J. M., Wignarajah, D. P., Chaudhary, S., Rivers, M. L., Nehru, C. E., and Ebel, D. S. (2008). Three-dimensional petrography of metal phases in equilibrated L chondrites — Effects of shock loading and dynamic compaction. *Earth and Planetary Science Letters*, **275**:172–180.

Goodman, F. O. (1968). Classical perturbation theory of the thermal accommodation coefficient in n dimensions. *Surface Science*, **11**(2):283–316.

Goodman, F. O. (1974). Thermal accommodation. *Progress In Surface Science*, **5**:261–375.

Goodman, F. O. (1980). Thermal accommodation coefficients. *The Journal of Physical Chemistry*, **84**(12):1431–1445.

Goodman, F. O. and Wachman, H. Y. (1967). Formula for Thermal Accommodation Coefficients. *J. Chem. Phys.*, **46**(6):2376–2386.

Goodman, F. O. and Wachman, H. Y. (1976). *Dynamics of Gas-Surface Scattering*. Academic Press (New York, San Francisco, London).

Gorban, A. N. and Yablonsky, G. S. (2011). Extended Detailed Balance for Systems with Irreversible Reactions. *Chemical Engineering Science*, **66**(21):5388–5399.

Gradshteyn, I. S. and Ryzhik, I. M. (2007). *Table of Integrals, Series, and Products*. Academic Press, 7 edition.

Greene, W. M., Spjut, R. E., Bar-Ziv, E., Sarofim, A. F., and Longwell, J. P. (1985). Photophoresis of irradiated spheres: absorption centers. *Journal of the Optical Society of America B Optical Physics*, **2**:998–1004.

Haack, H. and Wurm, G. (2007). Life on the edge - formation of cais and chondrules at the inner edge of the dust disk. volume 42, page 5157.

Hahn, D. W. and Özişik, M. N. (2012). *Heat conduction*. John Wiley & Sons, Inc., 3 edition.

Halliday, D., Resnick, R., Koch, S., Walker, J., Schleitzer, A., Filk, T., Flegel, I., Greß, J., and Bär, M. (2009). *Halliday Physik*. Number Bd. 1. Wiley VCH Verlag GmbH.

Happel, J. and Brenner, H. (1983). *Low Reynolds number hydrodynamics: with special applications to particulate media*, volume 1. Springer.

Hayashi, C., Nakazawa, K., and Nakagawa, Y. (1985). Formation of the solar system. In Black, D. C. and Matthews, M. S., editors, *Protostars and Planets II*, pages 1100–1153. University of Arizona Press, Tucson, AZ.

Herrmann, F. and Krivov, A. V. (2007). Effects of photophoresis on the evolution of transitional circumstellar disks. *A&A*, **476**:829–839.

Hesse, A. (2011). Mikrogravitations- und laborexperimente zur bestimmung photophoretischer kräfte auf extraterrestrische materialien. Master's thesis, Universität Duisburg-Essen.

Hesse, A., Teiser, J., and Wurm, G. (2011). Photophoretic forces on chondrules in drop tower experiments. *Journal of Physics Conference Series*, **327**(1):012044.

Hettner, G. (1926). Zur Theorie der Photophorese. *Zeitschrift für Physik*, **37**(3):179–192.

Hettner, G. (1928). Neuere experimentelle und theoretische Untersuchungen über die Radiometerkräfte. *Ergebnisse der exakten Naturwissenschaften*, **7**:209–237.

Hewins, R. H. (1996). Chondrules and the protoplanetary disk: an overview. In Hewins, R. H., Jones, R. H., and Scott, E. R. D., editors, *Chondrules and the Protoplanetary Disk*, pages 3–9.

Hewins, R. H., Jones, R. H., and Scott, E. R. D., editors (2011). Cambridge University Press, Cambridge, U.K.

Hezel, D. and Palme, H. (2010). The chemical relationship between chondrules and matrix and the chondrule matrix complementarity. *Earth and Planetary Science Letters*, **294**(1):85–93.

Hidy, G. M. and Brock, J. R. (1967). Photophoresis and the Descent of Particles into the Lower Stratosphere. *J. Geophys. Res.*, **72**(2):455–460.

Hidy, G. M. and Brock, J. R., editors (1970). *The Dynamics of Aerocolloidal Systems*, volume 1 of *International Reviews in Aerosol Physics and Chemistry*. Pergamon Press, Oxford, first edition.

Hinchen, J. J. and Foley, W. M. (1965). Scattering of Molecular Beams by Metallic Surfaces. In de Leeuw, J. H., editor, *Rarefied Gas Dynamics*, volume 2, page 505.

Hinchen, J. J. and Shepherd, E. F. (1967). Molecular Beam Scattering From Surfaces of Various Metals. In Brundin, C. L., editor, *Rarefied Gas Dynamics*, volume 1, page 239.

Horvath, H. (2014). Photophoresis — a forgotten force?? *KONA Powder and Particle Journal*, **31**(0):181–199.

Hughes, D. W. (1978). A disaggregation and thin section analysis of the size and mass distribution of the chondrules in the bjurbole and chainpur meteorites. *Earth and Planetary Science Letters*, **38**:391–400.

Hurlbut, F. C. (1986). Gas/surface scattering models for satellite applications. In Roussos, L. A., Heitman, K. E., and Rucker, C. E., editors, *Thermophysical Aspects of Re-entry Flows*, pages 97–119.

Hurlbut, F. C. (1989). Particle surface interaction in the orbital context: A survey. In *Rarefied gas dynamics: Space-related studies*, volume 116 of *Progress in Astronautics and Aeronautics*, pages 419–450.

Ivchenko, I. N., Loyalka, S. K., and Tompson, R. V. (1993). A boundary model for the thermal creep problem. *Fluid Dynamics*, **28**(6):876–878.

Ivchenko, I. N., Loyalka, S. K., and Tompson, R. V. (2007). *Analytical methods for problems of molecular transport*, volume 83 of *Fluid Mechanics and Its Applications*. Springer.

Keh, H. J. (2001). Photophoresis of an aerosol sphere in a spherical cavity. *Aerosol and Air Quality Research*, **1**(1):21–30.

Keh, H. J. and Hsu, F. C. (2005). Photophoresis of an aerosol sphere normal to a plane wall. *Journal of Colloid and Interface Science*, **289**(1):94–103.

Keller, C. and Gail, H.-P. (2004). Radial mixing in protoplanetary accretion disks. VI. Mixing by large-scale radial flows. *A&A*, **415**:1177–1185.

Kelling, T. and Wurm, G. (2011). A Mechanism to Produce the Small Dust Observed in Protoplanetary Disks. *ApJ*, **733**:120–125.

Kelling, T. and Wurm, G. (2013). Accretion through the Inner Edges of Protoplanetary Disks by a Giant Solid State Pump. *ApJ*, **774**:L1.

Kelling, T., Wurm, G., and Dürmann, C. (2011). Ice particles trapped by temperature gradients at mbar pressure. *Review of Scientific Instruments*, **82**(11):115105.

Kerker, M. and Cooke, D. D. (1982). Photophoretic force on aerosol particles in the free-molecule regime. *Journal of the Optical Society of America (1917-1983)*, **72**:1267–1272.

Ketcham, R. (2005). Computational methods for quantitative analysis of three-dimensional features in geological specimens. *Geosphere*, **1**(1):32–41.

Klahr, H. H. and Lin, D. N. C. (2001). Dust Distribution in Gas Disks: A Model for the Ring around HR 4796A. *ApJ*, **554**:1095–1109.

Klahr, H. H. and Lin, D. N. C. (2005). Dust Distribution in Gas Disks. II. Self-induced Ring Formation through a Clumping Instability. *ApJ*, **632**:1113–1121.

Klačka, J. and Kocifaj, M. (2002). On applicability of Poynting-Robertson effect. In Warmbein, B., editor, *Asteroids, Comets, and Meteors: ACM 2002*, volume 500 of *ESA Special Publication*, pages 169–171.

Klerner, S. and Palme, H. (1999). Origin of Chondrules and Matrix in Carbonaceous Chondrites. In *Lunar and Planetary Institute Science Conference Abstracts*, volume 30 of *Lunar and Planetary Institute Science Conference Abstracts*, page 1272.

Knudsen, M. (1911). Die molekulare Wärmeleitung der Gase und der Akkommodationskoeffizient. *Annalen der Physik*, **339**(4):593–656.

Kothe, S., Gttler, C., and Blum, J. (2011). The physics of protoplanetesimal dust agglomerates. v. multiple impacts of dusty agglomerates at velocities above the fragmentation threshold. In *EPSC-DPS Joint Meeting 2011, held 2-7 October 2011 in Nantes, France*, page 412.

Krause, M., Blum, J., Skorov, Y. V., and Trieloff, M. (2011). Thermal conductivity measurements of porous dust aggregates: I. technique, model and first results. *Icarus*, **214**:286–296.

Krauss, O. and Wurm, G. (2005). Photophoresis and the pile-up of dust in young circumstellar disks. *ApJ*, **630**:1088–1092.

Krauss, O., Wurm, G., Mousis, O., Petit, J.-M., Horner, J., and Alibert, Y. (2007). The photophoretic sweeping of dust in transient protoplanetary disks. *A&A*, **462**:977–987.

Krot, A., Amelin, Y., Cassen, P., and Meibom, A. (2005). Young chondrules in cb chondrites from a giant impact in the early solar system. *Nature*, **436**(7053):989–992.

Kuebler, K. E., McSween, H. Y., Carlson, W. D., and Hirsch, D. (1999). Sizes and masses of chondrules and metal-troilite grains in ordinary chondrites: Possible implications for nebular sorting. *Icarus*, **141**:96–106.

Kuepper, M., de Beule, C., Wurm, G., Matthews, L. S., Kimery, J. S., and Hyde, T. W. (2014). Photophoresis on polydisperse basalt microparticles under microgravity. *Journal of Aerosol Science*, **76**:126–137.

Kuhlthau, A. R. and Bishara, M. N. (1965). On the Nature of the Surface Interaction between Inert Gas Molecules and Engineering Surfaces. In de Leeuw, J. H., editor, *Rarefied Gas Dynamics*, volume 2, page 518.

Kundt, A. and Warburg, E. (1875). Ueber Reibung und Wärmeleitung verdünnter Gase. *Annalen der Physik*, **231**(7):337–365.

Kuščer, I. (1971). Reciprocity in scattering of gas molecules by surfaces. *Surface Science*, **25**(2):225–237.

Letfulova, L. B., Starinov, A. V., and Beresnev, S. A. (2001). Absorbing properties of atmospheric aerosol: analysis of microphysical optical characteristics. *ATMOSPHERIC AND OCEANIC OPTICS C/C OF OPTIKA ATMOSFERY I OKEANA*, **14**(1):62–68.

Li, W. K., Tzeng, P. Y., Soong, C. Y., and Liu, C. H. (2010). Absorption Center of Photophoresis within Micro-Sized and Spheroidal Particles in a Gaseous Medium. **4**(5):328–332.

Liffman, K. (2005). Chondrule and metal grain size sorting from jet flows. *Meteoritics and Planetary Science*, **40**:123–138.

Lin, H.-B. (1985). Infrared absorption spectroscopy of single particles using photophoresis. *Optics Letters*, **10**:68–70.

Loesche, C., Friedrich, J. M., Teiser, J., and Wurm, G. (2011). Calculations on Photophoretic Motion of Chondrules in the Early Solar System and Temperature Distributions in Illuminated Chondrules. In *Meteoritics and Planetary Science Supplement*, volume 74, page 5260.

Loesche, C., Teiser, J., Wurm, G., Hesse, A., Friedrich, J. M., and Bischoff, A. (2014). Photophoretic Strength on Chondrules. 2. Experiment. *ApJ*, **792**(1):73.

Loesche, C. and Wurm, G. (2012). Thermal and photophoretic properties of dust mantled chondrules and sorting in the solar nebula. *A&A*, **545**:A36.

Loesche, C., Wurm, G., and Teiser, J. (2012). Moving and Sorting Chondrules by Photophoresis. In *Joint meeting 'Paneth Kolloquium', 'The first 10 million years of the solar system' (DFG SPP 1385)*.

Loesche, C., Wurm, G., Teiser, J., Friedrich, J. M., and Bischoff, A. (2013). Photophoretic Strength on Chondrules. 1. Modeling. *ApJ*, **778**(2):101.

Lord, R. G. (1991). Some extensions to the Cercignani-Lampis gas-surface scattering kernel. *Physics of Fluids A: Fluid Dynamics (1989-1993)*, **3**(4):706–710.

Mackowski, D. W. (1989). Photophoresis of aerosol particles in the free molecular and slip-flow regimes. *International Journal of Heat and Mass Transfer*, **32**(5):843–854.

Mackowski, D. W., Altenkirch, R. A., and Menguc, M. P. (1989). A comparison of electromagnetic wave and radiative transfer equation analyses of a coal particle surrounded by a soot cloud. *Combustion and Flame*, **76**(3-4):415–420.

Mavromatis, H. A. and Alassar, R. S. (1999). A generalized formula for the integral of three associated legendre polynomials. *Applied Mathematics Letters*, **12**(3):101–105.

Maxwell, J. C. (1878). On stresses in rarefied gases arising from inequalities of temperature. [abstract]. *Proceedings of the Royal Society of London*, **27**:304–308.

Maxwell, J. C. (1879). On stresses in rarified gases arising from inequalities of temperature. *Philosophical Transactions of the Royal Society of London*, **170**:231–256.

Maxwell, J. C. (1890). *The scientific papers of James Clerk Maxwell*, volume 2. Cambridge University Press.

McNally, C. P., Hubbard, A., Yang, C.-C., and Mac Low, M.-M. (2014). Temperature Fluctuations Driven by Magnetorotational Instability in Protoplanetary Disks. *ApJ*, **791**:62.

Metzler, K., Bischoff, A., and Morfill, G. (1991). Accretionary dust mantles in cm chondrites: Chemical variations and calculated time scales of formation. *LPI Contributions*, **766**:155.

Metzler, K., Bischoff, A., and Stoeffler, D. (1992). Accretionary dust mantles in cm chondrites - evidence for solar nebula processes. *Geochim. Cosmochim. Acta*, **56**:2873–2897.

Moe, K. and Moe, M. M. (2005). Gas surface interactions and satellite drag coefficients. *Planet. Space Sci.*, **53**:793–801.

Morfill, G. E., Durisen, R. H., and Turner, G. W. (1998). Note: an accretion rim constraint on chondrule formation theories. *Icarus*, **134**:180–184.

Moudens, A., Mousis, O., Petit, J.-M., Wurm, G., Cordier, D., and Charnoz, S. (2011). The role of photophoresis in the radial transport of hot minerals in the solar nebula. In *Lunar and Planetary Institute Science Conference Abstracts*, volume 42 of *Lunar and Planetary Inst. Technical Report*, page 1409.

Mousis, O., Petit, J.-M., Wurm, G., Krauss, O., Alibert, Y., and Horner, J. (2007). Photophoresis as a source of hot minerals in comets. *A&A*, **466**:L9–L12.

Najita, J. R., Carr, J. S., Glassgold, A. E., and Valenti, J. A. (2007). Gaseous inner disks. In Reipurth, B., Jewitt, D., and Keil, K., editors, *Protostars and Planets V*, pages 507–522. University of Arizona Press, Tucson, AZ.

Oloff, R. (2010). *Geometrie in der Raumzeit. Eine mathematische Einführung in die Relativitätstheorie.* Springer (Heidelberg, Berlin), 5 edition.

Opeil, C. P., Consolmagno, G. J., and Britt, D. T. (2010). The thermal conductivity of meteorites: New measurements and analysis. *Icarus*, **208**:449–454.

Opeil, C. P., Consolmagno, G. J., Safarik, D. J., and Britt, D. T. (2012). Stony meteorite thermal properties and their relationship with meteorite chemical and physical states. *Meteoritics and Planetary Science*, **47**:319–329.

Ormel, C. W., Cuzzi, J. N., and Tielens, A. G. G. M. (2008). Co-accretion of chondrules and dust in the solar nebula. *ApJ*, **679**:1588–1610.

Orr, Jr., C. and Keng, E. Y. H. (1964). Photophoretic Effects in the Stratosphere. *Journal of Atmospheric Sciences*, **21**:475–478.

Ou, C. L. and Keh, H. J. (2005). Low-Knudsen-number photophoresis of aerosol spheroids. *Journal of Colloid and Interface Science*, **282**(1):69–79.

Parankiewicz, I. (1918). Über die lichtpositive und die lichtnegative Photophorese. *Annalen der Physik*, **362**:489–518.

Pluchino, A. B. (1983). Photophoretic force on particles for low Knudsen number. *Appl. Opt.*, **22**:103–106.

Presley, M. A. and Christensen, P. R. (1997a). Thermal conductivity measurements of particulate materials 1. A review. *J. Geophys. Res.*, **102**:6535–6550.

Presley, M. A. and Christensen, P. R. (1997b). Thermal conductivity measurements of particulate materials 2. results. *J. Geophys. Res.*, **102**:6551–6566.

Rakhmanov, E. A., Saff, E. B., and Zhou, Y. M. (1994). Minimal discrete energy on the sphere. *Math. Res. Lett*, **1**(6):647–662.

Reed, L. D. (1977). Low knudsen number photophoresis. *Journal of Aerosol Science*, **8**(2):123–131.

Robie, R. and Hemingway, B. (1984). Heat capacity and entropy of Ni2SiO4-olivine from 5 to 1000K and heat capacity of Co2SiO4 from 360 to 1000K. *American Mineralogist*, **69**:1069–1101.

Rohatschek, H. (1956a). Über die Kräfte der reinen Photophorese und der Gravitophotophorese (On the forces of pure and gravito-photophoresis). *Acta Physica Austriaca*, **10**:267–286.

Rohatschek, H. (1956b). Zur Theorie der Gravitophotophorese. *Acta Physica Austriaca*, **10**:227–238.

Rohatschek, H. (1984). The role of gravitophotophoresis for stratospheric and mesospheric particulates. *Journal of Atmospheric Chemistry*, **1**(4):377–389.

Rohatschek, H. (1985). Direction, magnitude and causes of photophoretic forces. *Journal of Aerosol Science*, **16**(1):29–42.

Rohatschek, H. (1989). Photophoretic levitation of carbonaceous aerosols. *Journal of Aerosol Science*, **20**(8):903–906.

Rohatschek, H. (1995). Semi-empirical model of photophoretic forces for the entire range of pressures. *Journal of Aerosol Science*, **26**(5):717–734.

Rohatschek, H. and Horvath, H. (2010). Magneto-photophoresis and mesospheric particles. *Journal of Geophysical Research (Atmospheres)*, **115**(D14):24208.

Rohatschek, H. and Zulehner, W. (1985). The photophoretic force on nonspherical particles. *Journal of Colloid and Interface Science*, **108**(2):457–461.

Rohatschek, H. and Zulehner, W. (1987). The resistance force on nonspherical bodies in the free molecule regime. *Journal of Colloid and Interface Science*, **119**(2):378–382.

Rosen, M. H. and Orr, Jr., C. (1964). The photophoretic force. *Journal of Colloid Science*, **19**(1):50–60.

Rubincam, D. P. (1995). Asteroid orbit evolution due to thermal drag. *J. Geophys. Res.*, **100**:1585–1594.

Sasso, M. R., Macke, R. J., Boesenberg, J. S., Britt, D. T., Rivers, M. L., Ebel, D. S., and Friedrich, J. M. (2009). Incompletely compacted equilibrated ordinary chondrites. *Meteoritics and Planetary Science*, **44**:1743–1753.

Sazhin, O., Kulev, A., Borisov, S., and Gimelshein, S. (2008). Numerical analysis of gas–surface scattering effect on thermal transpiration in the free molecular regime. *Vacuum*, **82**(1):20–29.

Scott, E. R. D. (2007). Chondrites and the Protoplanetary Disk. *Annual Review of Earth and Planetary Sciences*, **35**:577–620.

Scott, E. R. D., Love, S. G., and Krot, A. N. (1996). Formation of chondrules and chondrites in the protoplanetary nebula. In Hewins, R. H., Jones, R. H., and Scott, E. R. D., editors, *Chondrules and the Protoplanetary Disk*, pages 87–96. Cambridge University Press, Cambridge, U.K.

Sharipov, F. (2001). Application of the Cercignani-Lampis Scattering Kernel to Channel Gas Flows. In Bartel, T. J. and Gallis, M. A., editors, *Rarefied Gas Dynamics: 22nd International Symposium*, pages 347–353.

Sharipov, F. (2002). Application of the Cercignani-Lampis scattering kernel to calculations of rarefied gas flows. I. Plane flow between two parallel plates. *European Journal of Mechanics - B/Fluids*, **21**(1):113–123.

Sharipov, F. (2003a). Application of the Cercignani-Lampis scattering kernel to calculations of rarefied gas flows. II. Slip and jump coefficients. *European Journal of Mechanics - B/Fluids*, **22**(2):133–143.

Sharipov, F. (2003b). Application of the Cercignani-Lampis scattering kernel to calculations of rarefied gas flows. III. Poiseuille flow and thermal creep through a long tube. *European Journal of Mechanics - B/Fluids*, **22**(2):145–154.

Sharipov, F. (2004). Heat transfer in the Knudsen layer. *Phys. Rev. E*, **69**(6):061201.

Shu, F. H., Shang, H., and Lee, T. (1996). Toward an Astrophysical Theory of Chondrites. *Science*, **271**:1545–1552.

Shu, F. H., Shang, H., Lee, T., and Glassgold, A. E. (1997). The Origin of Chondrites and Extinct Radioactivities in the Solar System. In *Bulletin of the American Astronomical Society*, volume 29, page 845ff.

Shvedov, V. G., Hnatovsky, C., Eckerskorn, N., Rode, A. V., and Krolikowski, W. (2012). Polarization-sensitive photophoresis. *Applied Physics Letters*, **101**(5):051106.

Sicilia-Aguilar, A., Henning, T., Juhász, A., Bouwman, J., Garmire, G., and Garmire, A. (2008). Very low mass objects in the coronet cluster: The realm of the transition disks. *ApJ*, **687**:1145–1167.

Sitko, M. L., Lynch, D. K., Russell, R. W., and Hanner, M. S. (2004). 3-14 Micron Spectroscopy of Comets C/2002 O4 (Hönig), C/2002 V1 (NEAT), C/2002 X5 (Kudo-Fujikawa), C/2002 Y1 (Juels-Holvorcem), and 69P/Taylor and the Relationships among Grain Temperature, Silicate Band Strength, and Structure among Comet Families. *ApJ*, **612**:576–587.

Smoluchowski von Smolan, M. (1898a). Ueber Wärmeleitung in verdünnten Gasen. *Annalen der Physik*, **300**(1):101–130.

Smoluchowski von Smolan, M. (1898b). XIV. On conduction of heat by rarefied gases. *Philosophical Magazine Series 5*, **46**(279):192–206.

Soong, C. Y., Li, W. K., Liu, C. H., and Tzeng, P. Y. (2010). Theoretical analysis for photophoresis of a microscale hydrophobic particle in liquids. *Optics express*, **18**(3):2168–2182.

Steinbach, J., Blum, J., and Krause, M. (2004). Development of an optical trap for microparticle clouds in dilute gases. *The European Physical Journal E: Soft Matter and Biological Physics*, **15**(3):287–291.

Stoffels, W. W., Stoffels, E., Kroesen, G. M. W., and de Hoog, F. J. (1996). Detection of dust particles in the plasma by laser-induced heating. *Journal of Vacuum Science Technology*, **14**(2):588–594.

Struchtrup, H. (2013). Maxwell boundary condition and velocity dependent accommodation coefficient. *Physics of Fluids*, **25**(11):112001.

Takeuchi, T. and Krauss, O. (2008). Photophoretic structuring of circumstellar dust disks. *ApJ*, **677**:1309–1323.

Tehranian, S., Giovane, F., Blum, J., Xu, Y. L., and Gustafson, B. Å. S. (2001). Photophoresis of micrometer-sized particles in the free-molecular regime. *International Journal of Heat and Mass Transfer*, **44**(9):1649–1657.

Teiser, J., Engelhardt, I., and Wurm, G. (2011). Porosities of Protoplanetary Dust Agglomerates from Collision Experiments. *ApJ*, **742**:5.

Tipler, P., Mosca, G., Basler, M., Dohmen, R., Heinisch, C., Schleitzer, A., and Zillgitt, M. (2009a). *Physik: Für Wissenschaftler und Ingenieure*, page 340. Spektrum Lehrbuch. Spektrum Akademischer Verlag.

Tipler, P., Mosca, G., Basler, M., Dohmen, R., Heinisch, C., Schleitzer, A., and Zillgitt, M. (2009b). *Physik: Für Wissenschaftler und Ingenieure*, page 547. Spektrum Lehrbuch. Spektrum Akademischer Verlag.

Tong, N. T. (1973). Photophoretic force in the free molecule and transition regimes. *Journal of Colloid and Interface Science*, **43**(1):78–84.

Tong, N. T. (1975). Experiments on photophoresis and thermophoresis. *Journal of Colloid and Interface Science*, **51**(1):143–151.

van den Heuvel, F. (2006). Decomposition analysis of differential dose volume histograms. *Medical Physics*, **33**:297–307.

van Eymeren, J. and Wurm, G. (2012). The implications of particle rotation on the effect of photophoresis. *MNRAS*, **420**:183–186.

von Borstel, I. and Blum, J. (2012). Photophoresis of dust aggregates in protoplanetary disks. *A&A*, **548**:A96.

von Smoluchowski, M. (1911). Zur Theorie der Wärmeleitung in verdünnten Gasen und der dabei auftretenden Druckkräfte. *Annalen der Physik*, **340**:983–1004.

Wachman, H. Y. (1962). The thermal accommodation coefficient: a critical survey. *American Rocket Society Journal*, **32**(1):2–12.

Wadhwa, M., Amelin, Y., Davis, A. M., Lugmair, G. W., Meyer, B., Gounelle, M., and Desch, S. J. (2007). From Dust to Planetesimals: Implications for the Solar Protoplanetary Disk from Short-lived Radionuclides. In Reipurth, B., Jewitt, D., and Keil, K., editors, *Protostars and Planets V*, pages 835–848. University of Arizona Press, Tucson, AZ.

Weidenschilling, S. J. (1977). Aerodynamics of solid bodies in the solar nebula. *MNRAS*, **180**:57–70.

Weisberg, M., Prinz, M., Clayton, R., Mayeda, T., Grady, M., and Pillinger, C. (1995). The cr chondrite clan. *Antarctic Meteorite Research*, **8**:11.

Weisberg, M., Prinz, M., Clayton, R., Mayeda, T., Sugiura, N., Zashu, S., and Ebihara, M. (2010). A new metal-rich chondrite grouplet. *Meteoritics & Planetary Science*, **36**(3):401–418.

Wooden, D. H., Woodward, C. E., and Harker, D. E. (2004). Discovery of Crystalline Silicates in Comet C/2001 Q4 (NEAT). *ApJ*, **612**:L77–L80.

Woronowicz, M. S. and Rault, D. F. G. (1994). Cercignani-Lampis-Lord gas-surface interaction model: Comparisons between theory and simulation. *Journal of Spacecraft and Rockets*, **31**:532–534.

Wurm, G. (2007). Light-induced disassembly of dusty bodies in inner protoplanetary discs: implications for the formation of planets. *MNRAS*, **380**:683–690.

Wurm, G. and Haack, H. (2009). Outward transport of CAIs during FU-Orionis events. *Meteoritics and Planetary Science*, **44**:689–699.

Wurm, G. and Krauss, O. (2006). Concentration and sorting of chondrules and cais in the late solar nebula. *Icarus*, **180**:487–495.

Wurm, G. and Krauss, O. (2008). Experiments on negative photophoresis and application to the atmosphere. *Atmospheric Environment*, **42**(11):2682–2690.

Wurm, G., Krauss, O., and Haack, H. (2006). Planetesimal Formation Induced by Photophoresis at the Inner Edge of the Solar Nebula. volume 41, page 5115.

Wurm, G., Teiser, J., Bischoff, A., Haack, H., and Roszjar, J. (2010). Experiments on the photophoretic motion of chondrules and dust aggregates — Indications for the transport of matter in protoplanetary disks. *Icarus*, **208**:482–491.

Wurm, G., Trieloff, M., and Rauer, H. (2013). Photophoretic Separation of Metals and Silicates: The Formation of Mercury-like Planets and Metal Depletion in Chondrites. *ApJ*, **769**:78.

Xu, Y.-L., Gustafson, B. Å. S., Giovane, F., Blum, J., and Tehranian, S. (1999). Calculation of the heat-source function in photophoresis of aggregated spheres. *Phys. Rev. E*, **60**:2347–2365.

Yalamov, Y. I. and Khasanov, A. S. (1998). Photophoresis of coarse aerosol particles with nonuniform thermal conductivity. *Journal of Technical Physics*, **43**:347–352.

Yalamov, Y. I., Kutukov, V. B., and Shchukin, E. R. (1976a). Motion of small aerosol particle in a light field. *Journal of Engineering Physics*, **30**:648–652.

Yalamov, Y. I., Kutukov, V. B., and Shchukin, E. R. (1976b). Theory of the photophoretic motion of the large-size volatile aerosol particle. *Journal of Colloid and Interface Science*, **57**(3):564–571.

Yalamov, Y. I., Shchukin, E. R., Kutukov, V. B., Myagkov, A. V., and Gretskii, A. V. (1978). Effect of thermal diffusion on photophoretic motion of aerosol particles. *Journal of Engineering Physics*, **33**:1082–1084.

Zolensky, M. E., Zega, T. J., Yano, H., Wirick, S., Westphal, A. J., Weisberg, M. K., Weber, I., Warren, J. L., Velbel, M. A., Tsuchiyama, A., Tsou, P., Toppani, A., Tomioka, N., Tomeoka, K., Teslich, N., Taheri, M., Susini, J., Stroud, R., Stephan, T., Stadermann, F. J., Snead, C. J., Simon, S. B., Simionovici, A., See, T. H., Robert, F., Rietmeijer, F. J. M., Rao, W., Perronnet, M. C., Papanastassiou, D. A., Okudaira, K., Ohsumi, K., Ohnishi, I., Nakamura-Messenger, K., Nakamura, T., Mostefaoui, S., Mikouchi, T., Meibom, A., Matrajt, G., Marcus, M. A., Leroux, H., Lemelle, L., Le, L., Lanzirotti, A., Langenhorst, F., Krot, A. N., Keller, L. P., Kearsley, A. T., Joswiak, D., Jacob, D., Ishii, H., Harvey, R., Hagiya, K., Grossman, L., Grossman, J. N., Graham, G. A., Gounelle, M., Gillet, P., Genge, M. J., Flynn, G., Ferroir, T., Fallon, S., Ebel, D. S., Dai, Z. R., Cordier, P., Clark, B., Chi, M., Butterworth, A. L., Brownlee, D. E., Bridges, J. C., Brennan, S., Brearley, A., Bradley, J. P., Bleuet, P., Bland, P. A., and Bastien, R. (2006). Mineralogy and Petrology of Comet 81P/Wild 2 Nucleus Samples. *Science*, **314**:1735–1739.

Zulehner, W. and Rohatschek, H. (1990). Photophoresis of nonspherical bodies in the free molecule regime. *Journal of Colloid and Interface Science*, **138**(2):555–564.

Zulehner, W. and Rohatschek, H. (1995). Representation and calculation of photophoretic forces and torques. *Journal of Aerosol Science*, **26**(2):201–210.

Danksagung

Mein aufrichtiger Dank geht an **Professor Dr. Gerhard Wurm** für die Chance bei ihm zu promovieren, die gute Ausstattung, und die vielen Freiheiten, die er mir gab. Ich danke ihm ebenso für seine Geduld.

Das **SPP 1385 der DFG** ermöglichte die Finanzierung meiner Doktorandenstelle, deswegen danke ich allen Beteiligten recht herzlich. Dem **American Museum of Natural History** gebührt ebenso mein Dank für das **KADE Fellowship**, welches ich erhalten durfte. Meiner **Arbeitsgruppe** danke ich für die gute Atmosphäre. Der **FEMET GmbH** und **3D Systems** möchte ich meinen Dank aussprechen für die Bereitstellung einer voll funktionsfähigen Testversion von Geomagic Studio 12.

Ich möchte mich ebenso bei meinem Kollegen **Dr. Jens Teiser** für die Planung der Fallturmkampagne, die Anschubhilfe und konstruktive Kritik bedanken. **Jon M. Friedrich** einen herzlichen Dank für die Chondrentomographien und unsere Meßzeit am Argonne National Laboratory sowie **Denton Ebel** für die Aufnahme in seine Arbeitsgruppe während meines Gastaufenthaltes am AMNH.

Meine große Dankbarkeit geht auch an meine **Eltern** für die gute, tatkräftige und finanzielle Unterstützung, die mir überhaupt erst mein Studium ermöglicht hat. Ein herzliches Dankeschön auch an **Yue Yu**, **Chengeng Zeng**, **Caroline de Beule** und **Rosa Esteban Garcia** für ihre Ermutigungen, Anregungen und die vielen angenehmen und erheiternden Gespräche. Caroline danke ich auch für das mehrfache Lesen eines Kapitels dieser Arbeit, **Tim Jankowski** für das Mitbeschaffen meiner Workstation, und Geng für seine Mithilfe bezüglich des KADE Fellowship. Yue bitte ich um Nachsicht für die vielen Tage und Wochen, an denen ich zu unmöglichen Stunden an meiner Doktorarbeit arbeitete, und danke ihm für die Zeit an meiner Seite.

Erklärung

Die vorliegende Dissertation wurde von mir selbstständig verfasst. Bei der Abfassung der Dissertation wurden nur die angegebenen Hilfsmittel benutzt und alle wörtlich oder inhaltlich übernommenen Stellen sind als solche gekennzeichnet. Die Dissertation ist nur in diesem Promotionsverfahren eingereicht und es wird der Doktorgrad Dr. rer. nat. angestrebt.

_____

Ort, Datum, Unterschrift